Exploring the Synthesis and Characterisation of Oxychalcogenide, Oxypnictide and Chalcogenide Materials

Bradley Carl Sheath

A thesis submitted in part fulfilment of the requirements for the degree of Doctor of Philosophy at the University of Oxford

St Catherine's College

University of Oxford

May 2023



Abstract

Exploring the Synthesis and Characterisation of Oxychalcogenide, Oxypnictide and Chalcogenide Materials

Bradley Carl Sheath DPhil Thesis May 2023

This thesis details various studies of the structure, characterisation and physical properties of some oxychalcogenide, oxypnictide and chalcogenide materials, with a particular focus on the long-range magnetic ordering of the local 3*d* transition metal moments.

A wide range of characterisation methods are used to investigate the crystal structure of the $Ca_2FeO_2Fe_{1.6}OS_2$ oxysulfide, including synchrotron XRPD, high-resolution NPD, XANES, XPS and Mössbauer spectroscopy. The 'Fe1' layer hosts Fe^{3+} in FeO_4S_2 distorted octahedra and the 'Fe2' layer contains Fe^{2+} in FeO_2S_4 distorted octahedra. Long-range Fe vacancy ordering exists in the 'Fe2' layer, resulting in a supercell which is a $2\sqrt{2}a_{nuc} \times 2\sqrt{2}a_{nuc} \times 2c_{nuc}$ expansion of the basic nuclear unit cell. This vacancy ordering is accompanied by movement of the Fe and O atoms in this layer, all of which can be described using the *Aea*2 space group. Long-range ordering of the two Fe sublattices occurs simultaneously at 330(10) K and analysis of NPD data reveals that the Fe moments order in the *ab*-plane in a manner which ensures all Fe-O-Fe superexchange pathways contain antiferromagnetic coupling of spins. A second antiferromagnetic ordering transition occurs at 70(2) K, which can be modelled by canting of the spins in both Fe layers.

The $Ca_2FeO_2Fe_{1.65}OS_{1.5}Se_{0.5}$, $Ca_2FeO_2Fe_{1.7}OSSe$ and $Ca_2FeO_2Fe_{1.75}OS_{0.5}Se_{1.5}$ solid solution phases are isostructural to the $Ca_2FeO_2Fe_{1.6}OS_2$ material but do not exhibit long-range ordering of the Fe vacancies in the 'Fe2' FeO_2Ch_4 layer. The long-range magnetic ordering models obtained from NPD data are comparable to that deduced for $Ca_2FeO_2Fe_{1.6}OS_2$, where all Fe-O-Fe superexchange pathways have antiferromagnetic interactions of the Fe moments. The most selenide-rich $Ca_2FeO_2Fe_{1.75}OS_{0.5}Se_{1.5}$ compound undergoes spin-reorientations of the Fe^{3+} spins on the 'Fe1' sublattice with changing temperature.

First reports of the structure and properties of the newly synthesised $Sr_2CrO_2Cr_2OAs_2$ phase are also presented. This material is again isostructural to the $Ca_2FeO_2Fe_{1.6}OS_2$ material, however in this case no transition metal vacancies or any deviations from the formula stoichiometry are evident. Another contrast to the $Ca_2FeO_2Fe_{1.6}OS_2$ material is that Cr^{2+} is present in the 'Cr1' CrO_4As_2 layers and the 'Cr2' CrO_2As_4 layers host Cr^{3+} (i.e., the transition metal oxidation state site preferences are reversed). The Cr sublattices order independently, with the 'Cr2' (Cr^{3+} d^3) moments ordering just above 600 K and the 'Cr1' (Cr^{2+} d^4) moments ordering at 530(10) K, all parallel to the *c*-axis. It is likely that antiferromagnetic direct exchange interactions between Cr centres in the 'Cr2' sublattice are the driving force behind the nature of the ordering observed in this layer, whereas antiferromagnetic Cr-O-Cr superexchange interactions dictate the checkerboard ordering adopted by the 'Cr1' sublattice.

Long-range magnetic ordering of the Fe^{3+} spins in the Ba_2FeSbS_5 and Ba_2FeBiS_5 quaternary sulfides is modelled from NPD data and the arrangement of the moments can be explained by Fe-S…S-Fe super-superexchange (SSE) pathways. These ensure that Fe centres coupling over the shortest distance are antiferromagnetic and the relatively weak interactions between the Fe spins via these pathways results in the very low Néel temperatures of 12.1(10) K and 34.5(10) K observed for Ba_2FeSbS_5 and Ba_2FeBiS_5 respectively. Small magnetic Bragg peaks in the NPD pattern of Ba_2FeSbS_5, which are not positioned on a commensurate *k*-vector, suggest an additional incommensurately modulated component is present in the long-range ordering of the Fe moments.

Acknowledgements

I have had the most incredible 8 years here in Oxford and the people I have met have made all the difference to how great this time has been.

I owe a huge amount of gratitude to Prof. Simon Clarke who has given me guidance whenever I have sought it and from whom I have learnt a great deal. I very much appreciate the opportunity to have been a part of the Clarke group, which I feel has been an invaluable experience and one which has set me up well for whatever I pursue in the future.

I have been very fortunate to work with many people throughout my time here, many of whom have become very good friends. It all started off with Penny and Mahmoud during Part II, who have both been constant sources of memes, laughs and occasionally science chat during the last 5 years. I thank them for being so supportive from the very beginning. I thank Bob for being the other half of the SQUID maintenance crew (aka dumb and dumb) and for all the fun nights at Catz bar. I thank Souvik for teaching me how to be 'truly drunk' and for his fun ringtones and jumpers. I thank Katie for being LEAF champion and being the other group member who enjoys a later start to the day. I thank Mila for many chats about trash TV, musicals and all things unrelated to work, which were definitely needed sometimes. I thank Lemuel 'Crenz' for sharing his music and being such a chill presence in the office. I thank Lexy for her fantastic baking and for carrying some of my work forward too.

I thank Dr Simon Cassidy for teaching me the ways of the Clarke group, especially in terms of his TOPAS wizardry. I thank Dr Machteld Kamminga for her unrivalled enthusiasm and questionable waterproof attire. I thank Dr Shunsuke Sasaki for getting me through the COVID times with his funny impressions and stripy t-shirts. I thank Dr Viktoria Falkowski for her crystal expertise and the many wine and board game evenings. I thank Dr Nicola Kelly for her ability to always tell stories which get me chuckling. I thank Dr Xabier Martinez de Irujo-Labalde for being the best hermano one could ask for.

I would also like to thank the numerous other group members with whom I shared many good moments- Dr Xiaoyu Xu, Dr Bertold Rasche, Cristina, James, Max, Ben, Billy, Emily, Fergus, Henry, Saumitra, Adam and Jamie (J).

I would like to thank all the people who collaborated with me on my research projects, especially Dr Pascal Manuel and Dr Fabio Orlandi (WISH) and Dr Stanislav Savvin (D1B and D2B) who provided an excellent mail-in service for NPD experiments during COVID. Without these experiments my thesis would be a shell of what it is today.

Finally, I thank my family and friends for always being there for me.

"Been around the world, don't speak the language

But your science don't need explaining

.

.

Talk science with me"

Table of Contents

1 Introduction 1
1.1 Solid-State Chemistry 1
1.2 Mixed-Anion and Non-Oxide Solids 4
1.2.1 Oxychalcogenides and Oxypnictides 4
1.2.2 Sulfides 5
1.3 Structure Types 6
1.3.1 The $Ae_2MO_2M_2OX_2$ Structure Type 6
1.3.2 The $Ae_2M_AM_BCh_5$ Structure Type 9
1.4 Magnetism 11
1.4.1 Diamagnetism 11
1.4.2 Paramagnetism 12
1.4.2.1 Curie Paramagnetism 12
1.4.2.2 Curie-Weiss Paramagnetism 13
1.4.2.3 Pauli Paramagnetism 14
1.4.2.4 Temperature Independent Paramagnetism 15
1.4.3 Ferromagnetism 15
1.4.4 Antiferromagnetism 16
1.4.5 Ferrimagnetism 17
1.4.6 Spin-Glass Behaviour 18
1.5 Magnetic Exchange 20
1.5.1 Direct Exchange 20
1.5.2 Superexchange 21
1.5.3 Super-Superexchange 23
1.6 Aims of the Thesis 24
References 26
2 Experimental Methods 32
2.1 Synthetic Techniques 32
2.1.1 Handling Air/Moisture-Sensitive Materials 32
2.1.2 Solid-State Synthesis 33
2.1.3 Preparation of SrO 34
2.2 Characterisation Techniques 35
2.2.1 X-Ray Powder Diffraction (XRPD) 35
2.2.1.1 In-House Diffractometers 39
2.2.1.2 Bruker D8 Advance Eco 40

2.2.1.3 Malvern Panalytical Empyrean Alpha 1 40
2.2.1.4 Diamond Light Source 41
2.2.1.5 I11 Beamline, Diamond Light Source (MAC and VT) 42
2.2.2 Neutron Powder Diffraction (NPD) 43
2.2.2.1 WISH, ISIS 44
2.2.2.2 D2B, ILL 45
2.2.2.3 D1B, ILL 46
2.2.3 Rietveld Refinement 48
2.2.4 SQUID Magnetometry 49
2.2.4.1 DC SQUID Magnetometry 50
2.2.5 Electron Microscopy 52
2.2.5.1 Selected Area Electron Diffraction (SAED) and Tomography 52
2.2.5.2 Energy Dispersive X-Rays (EDX) 52
2.2.6 X-ray Absorption Near Edge Spectroscopy (XANES) 54
2.2.6.1 B18 Beamline, Diamond Light Source 54
2.2.7 X-Ray Photoelectron Spectroscopy (XPS) 55
2.2.8 Resistivity 56
2.2.9 Specific Heat Capacity 57
2.2.10 Mössbauer Spectroscopy 58
2.2.11 Single Crystal X-Ray Diffraction (SCXRD) 60
References 61
3 Synthesis and Characterisation of $Ca_2FeO_2Fe_{1.6}OS_2$ 63
3.1 Introduction 63
3.2 Synthesis 64
3.3 Characterisation 64
3.3.1 Superstructure Determination 64
3.3.2 Room Temperature XRPD 69
3.3.3 High Temperature NPD 77
3.3.4 SQUID Magnetometry 81
3.3.5 XANES Measurements 84
3.3.6 XPS Measurements 85
3.3.7 TEM-EDX 86
3.3.8 Variable Temperature NPD 89
3.3.9 Variable Temperature XRPD 105
3.3.10 Heat Capacity 109
3.3.11 Resistivity 111

3.3.12 Mössbauer Spectroscopy 113
3.4 Discussion 118
3.4.1 Crystal Structure 118
3.4.2 Magnetic Structure 120
3.5 Conclusions 122
References 125
4 Synthesis and Characterisation of $Ca_2FeO_2Fe_{1.65}OS_{1.5}Se_{0.5}$, $Ca_2FeO_2Fe_{1.7}OSSe$ and $Ca_2FeO_2Fe_{1.75}OS_{0.5}Se_{1.5}$ 127
4.1 Introduction 127
4.2 Synthesis 128
4.3 Characterisation 129
4.3.1 Room Temperature XRPD 129
4.3.2 Room Temperature NPD 134
4.3.3 SQUID Magnetometry 138
4.3.4 XANES Measurements 141
4.3.5 Variable Temperature NPD 143
4.3.5.1 $Ca_2FeO_2Fe_{1.65}OS_{1.5}Se_{0.5}$ 143
4.3.5.2 $Ca_2FeO_2Fe_{1.7}OSSe$ 145
4.3.5.3 $Ca_2FeO_2Fe_{1.75}OS_{0.5}Se_{1.5}$ 147
4.3.6 Mössbauer Spectroscopy 159
4.4 Discussion 163
4.4.1 Crystal Structure 163
4.4.2 Magnetic Structure 164
4.5 Conclusions 166
References 168
5 Synthesis and Characterisation of $Sr_2CrO_2Cr_2OAs_2$ 169
5.1 Introduction 169
5.2 Synthesis 170
5.3 Characterisation 171
5.3.1 Room Temperature XRPD 171
5.3.2 Room Temperature NPD 173
5.3.3 SQUID Magnetometry 176
5.3.4 Variable Temperature NPD 177
5.3.5 Variable Temperature XRPD 182
5.3.6 High Temperature Resistance Measurements 186
5.4 Discussion 187

5.4.1 Crystal Structure....187
5.4.2 Magnetic Structure....189
5.5 Conclusions....192
References....194
6 Structure and Magnetism of Ba_2FeSbS_5 and Ba_2FeBiS_5....196
6.1 Introduction....196
6.2 Synthesis....196
6.3 Characterisation....197
6.3.1 Room Temperature XRPD....197
6.3.2 SQUID Magnetometry....201
6.3.3 Variable Temperature NPD....204
6.4 Discussion....217
6.4.1 Crystal Structure....217
6.4.2 Magnetic Structure....220
6.5 Conclusions....222
References....224
7 Final Conclusions....226
References....230
Appendix....231
Further Rietveld Refinement Details....236

Chapter 1

1 Introduction

1.1 Solid-State Chemistry

The field of solid-state chemistry is one which explores the structures and properties of materials which exist as solids. Many materials which fall into this category occur naturally on Earth, such as the metal oxides found in ores, however many are also synthesised in laboratories using a number of different methods. There is now a vast array of known solids, each with a particular composition and arrangement of atoms. Some solids may be considered as 'crystalline' if there is long-range ordering of the constituent atoms or as 'amorphous' if there is only short-range order or indeed no order of the atoms at all. The structure of crystalline solids can be investigated using x-ray crystallography, first introduced by Max von Laue and W.H. and W.L. Bragg, and each can be represented by a repeating 'unit cell' containing atoms in specific positions.

In recent years, the search for new materials and subsequent investigation of their structures and properties has been driven by the use of solid-state compounds in technology. One current issue of great importance is energy storage, due to the need to move towards renewable sources of energy and away from using fossil fuels, which are both a finite resource and contribute to global warming when used in the production of electricity. The discovery of $LiCoO_2$ as a high voltage cathode material in the 1980s[1] has revolutionised energy storage over the last few decades, along with being a driving force for the development of portable technology. However, there are issues with respect to degradation of the battery from Li dendrite formation[2] and sourcing of the cobalt metal from the Democratic Republic of the Congo.[3] Recently, there has also been the need for batteries to give a greater power output because of the shift of this technology into the automotive sector and a higher capacity for the storage of large amounts of energy produced from renewable sources. These issues and aspirations have led to the search for other solid-state cathode materials, examples of which

include $Li_{1.2}Ni_{0.13}Mn_{0.54}Co_{0.13}O_2$,[4] Li_xCoPO_4[5] and Li_2MnO_2F.[6] Alternative approaches include the development of solid-state batteries[7,8] and Na-ion batteries.[7,9]

Another area of technological importance is the study of superconducting materials. These are materials which have zero resistivity and behave as perfect diamagnets below certain critical temperatures, magnetic fields and electrical currents. They are used in MRI scanners in hospitals and more recently have been employed to contain the plasma in fusion reactors. The major breakthrough for using superconductors for these applications was the discovery of the YBCO materials of formulae $YBa_2Cu_3O_{7-\delta}$ (T_c up to $\sim$ 90 K) [10] and analogous materials such as the $Hg_{0.8}Bi_{0.2}Ba_2Ca_2Cu_3O_{8+\delta}$ phases ($T_c \sim 130$ K).[11] The significance of these is that the critical temperatures are higher than the boiling point of liquid nitrogen ($\sim$77 K) and so these cuprates become superconducting when cooled in liquid nitrogen. Currently, the YBCO compounds are used as the central part of the magnets in NMR instruments because of this desirable property. Other exciting superconductors are the iron-based arsenides, such as $BaFe_2As_2$,[12] LaOFeAs[13] and $CaKFe_4As_4$,[14] however these have considerably lower critical temperatures.

As previously mentioned, renewable sources of energy are becoming increasingly important to reduce the consumption of fossil fuels and minimise global warming. Semiconducting compounds are the key components of solar cells which convert the photon energy from the sun into electrical energy. At the junction between a p-type and an n-type semiconductor, electron-hole pairs are created by radiation with a higher energy than the bandgap, which ultimately recombine and generate a current. Si is most commonly used due to its low cost and high abundance, however a much higher efficiency can be achieved if multi-junction solar cells are used and more of the spectral range from the sun can be transferred into electrical energy. Materials such as Ge, InGaAs and InGaP can be utilised here.[15]

Data storage is achieved using ferromagnetic materials. Alternating thin sheets of ferromagnetic and non-ferromagnetic metals can result in giant magnetoresistance- a significant change in the resistance of the device depending whether there is an applied magnetic field or not. This is used in the hard

drives of computers. Materials such as the $La_{1-x}Sr_xMnO_3$[16] and $La_{1-x}Ca_xMnO_3$[17] solid solution perovskites exhibit a larger "colossal magnetoresistance" due the stabilisation of a ferromagnetic-metallic state in an applied field over a paramagnetic-insulating state, which is accompanied by a drastic reduction in the resistivity.[18]

Other than the applications discussed so far, solid-state compounds have also been widely used in catalysis. Materials which can be described as porous frameworks with large cavities, such as zeolites[19,20] and metal-organic frameworks (MOFs),[19,21] have been proven as successful materials for heterogeneous catalysis. GaN-based light-emitting diodes (LEDs) are used in lighting and displays, which produce light with a much greater efficiency than the more traditional methods, such as filament light bulbs.[22] The semiconducting properties of silicon mean that is has also been used for microchips and this has enabled the great advances in computing over the past decades.[23]

Solid-state materials have played vital roles in many technological developments throughout the last century and they are likely to continue to be crucial to further advances in the future. Therefore, the study of new materials and their properties is key to finding solid compounds which can improve current, as well as enabling novel, technologies.

1.2 Mixed-Anion and Non-Oxide Solids

The exploration of solid-state materials has moved away from the well-studied oxides and more focus is now on mixed-anion and non-oxide materials. Compared to the oxides, these compounds have different coordination environments around the metal; varying degrees of covalency in the metal-anion bonding; a change in the band structure of the solid and can lead to different structures with different dimensionalities. These all result in materials with properties which differ from those exhibited by oxides, making mixed-anion and non-oxide solids exciting materials to investigate.

1.2.1 Oxychalcogenides and Oxypnictides

The introduction of chalcogenide (sulfide, selenide, telluride) or pnictide (phosphide, arsenide, antimonide) anions to create a mixed-anion system can often result in layered structures with long-range anion order due to the contrast in size and polarizability of these anions with the O^{2-} ions. The band gap often decreases as the filled chalcogenide or pnictide valence band lies higher and closer in energy to the partially-filled metal *d* states. Interactions between magnetic transition metal cations can be affected as the metal-anion bonds are more covalent, increasing the electron density on the metal and altering the nature of any exchange pathways. In addition to this, different coordination environments around the metal centres and the potential to stabilise different metal oxidation states can tune the magnetic interactions present in a solid. The promising potential of mixed-anion materials are well documented by Kageyama *et al*.[24]

In terms of their synthesis, a popular approach to the design of new materials has been to treat each different layer type as "building blocks" which can be combined with different blocks or in different arrangements.[25] Different structure types can also be related to each other, whether that be through the occupancy of a van der Waals gap or the filling of interstitial sites or via an anti-type relationship. This has led to the discovery of a whole host of mixed-anion structures, the properties of which have been investigated deeply.[26]

1.2.2 Sulfides

Sulfides, like oxides, are found naturally as metal ores, examples including Ag_2S, PbS and FeS_2. Sulfides differ from oxides in terms of both structure and property. They often form layered structures meaning they are useful as lubricants (eg MoS_2[27]) and prototypical battery cathodes (eg TiS_2[28]). The introduction of the larger and more polarisable S^{2-} anion rather than the O^{2-} anion results in changes to the band gaps and magnetic interactions, as described in section 1.2.1. The lower band gap inherent to sulfides (compared to oxides) means they are often electrical semiconductors which can be used in photovoltaic[29] and thermoelectric[30,31,32] applications. Also, the change in magnetic interactions can lead to new magnetic phenomena.

Binary metal sulfides commonly form materials with *M*S, M_2S, M_2S_3, M_3S_4 and MS_2 (*M* = metal) stoichiometries, examples of which are ZnS, Cu_2S, Bi_2S_3, Sn_3S_4 and TaS_2. These can exist as various structure types including rock-salt (MnS[33]), pyrite (FeS_2[34]) and spinel ($CdIn_2S_4$[35]). Ternary and quaternary sulfides have also been extensively studied and these often have structures comprising 1D chains (eg Ba_3CrS_5[36]) or 2D sheets (eg $CuSbS_2$[37]). In terms of their properties, the band gaps of ternary sulfides tend to fall between the band gaps of the binary sulfides which make up the ternary materials, with band gap values of around 0.5-2.0 eV.[38] Interestingly, the MS_4 (*M* = metal) tetrahedral ligand field was reported to produce the first low-spin configuration of a transition metal ion in such a ligand field, determined using the magnetometry results of the $CsFeS_2$ ternary phase.[39]

1.3 Structure Types

1.3.1 The $Ae_2MO_2M_2OX_2$ Structure Type

Materials adopting the $Ae_2MO_2M_2X_2$ structure type, first reported for $Ae_2MnO_2Mn_2X_2$ (*Ae* = Sr, Ba and *X* = As, Sb, Bi) by Brechtel et al in 1979,[40] are currently well established. The $[MO_2]^{2-}$ layers comprise M^{2+} cations in MO_4 square-planar coordination or could equally be described as axially elongated MO_4X_2 octahedra. The $[M_2X_2]^{2-}$ layers contain M^{2+} cations in MX_4 tetrahedra. More recently there has been the discovery of compounds adopting the $Ae_2MO_2M_2OX_2$ structure type, which can be viewed as a formal "oxidative insertion" of oxygen into the $[M_2X_2]^{2-}$ anti-fluorite type layers of the $Ae_2MO_2M_2X_2$ structure type, resulting in partial oxidation of the metal species and a relative shifting of the layers by vector (½, ½, 0), therefore this shift is in the *ab*-plane. This is illustrated in Figure 1.1.

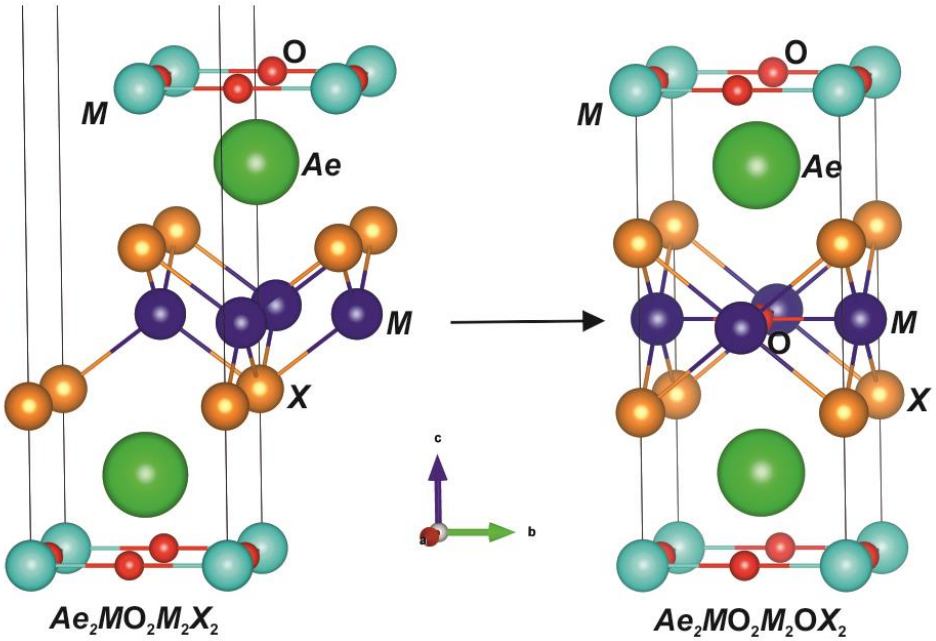


Figure 1.1: The structure of $Ae_2MO_2M_2X_2$ (left) and $Ae_2MO_2M_2OX_2$ (right). The structure of $Ae_2MO_2M_2OX_2$ may be formally derived from the oxidation of the $[M_2X_2]$ layers in $Ae_2MO_2M_2X_2$ accompanied by a relative shift of (½, ½, 0) by the $[Ae_2MO_2]$ layers.

In recent years, various materials adopting the $Ae_2MO_2M_2X_2$ structure type have been studied. Analysis of neutron powder diffraction data has led to the determination of magnetic models for the long-range ordering of the moments on the metal centres. This has uncovered some very interesting results. One example is the $Sr_2CrO_2Cr_2As_2$ compound,[41,42,43] where the moments within each Cr containing layer order independently. Below 600 K, the Cr^{2+} moments in the Cr_2As_2 layer order antiferromagnetically and align along the *c*-axis. Then, below 348 K, the Cr^{2+} moments in the CrO_2 layer also order antiferromagnetically. As the temperature is decreased further there is a spin-reorientation in both layers, so that the moments in the Cr_2As_2 layer lie in the *ab*-plane and the moments in the CrO_2 layer are aligned with the *c*-axis. These findings are depicted in Figure 1.2. It appears that the orientation of the moment within one layer influences that in the other layer. In contrast, the Ba analogue of this compound does not exhibit a spin-reorientation.

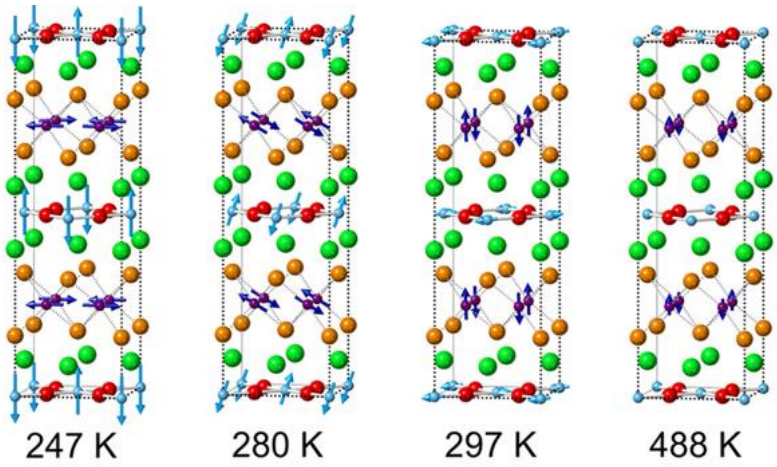


Figure 1.2: Magnetic models for the $Sr_2CrO_2Cr_2As_2$ compound at different temperatures, depicting the cooperative spin-reorientation of the two Cr sublattices. Figure by X. Xu *et al*.[44]

So far there is only one family of compounds which are reported to adopt the $Ae_2MO_2M_2OX_2$ structure type. These are the $Ca_2FeO_2Fe_{2-\delta}O(S_{1-x}Se_x)_2$ compounds, reported by Zhang *et al*. in 2016.[45] However, there are also a number of materials which do contain the "oxidised" layer containing MO_2X_4 distorted octahedra. These include $La_2O_2Fe_2OCh_2$ (Ch = S, Se),[46,47,48,49] $A_2F_2Fe_2OQ_2$ (A = Sr, Ba; Q = S, Se),[50] $La_2O_2Mn_2OSe_2$[46,51] and $La_2O_2Co_2OSe_2$.[52,53,54] It can be seen that these all contain an anti-fluorite type layer between the MO_2X_4 layer of interest and have perhaps been some of the first reported compounds with this MO_2X_4 layer as the transition metal is only present in the mixed-anion layer. The structure of these related compounds, of general formula $A_2B_2M_2OX_2$, is depicted in Figure 1.3.

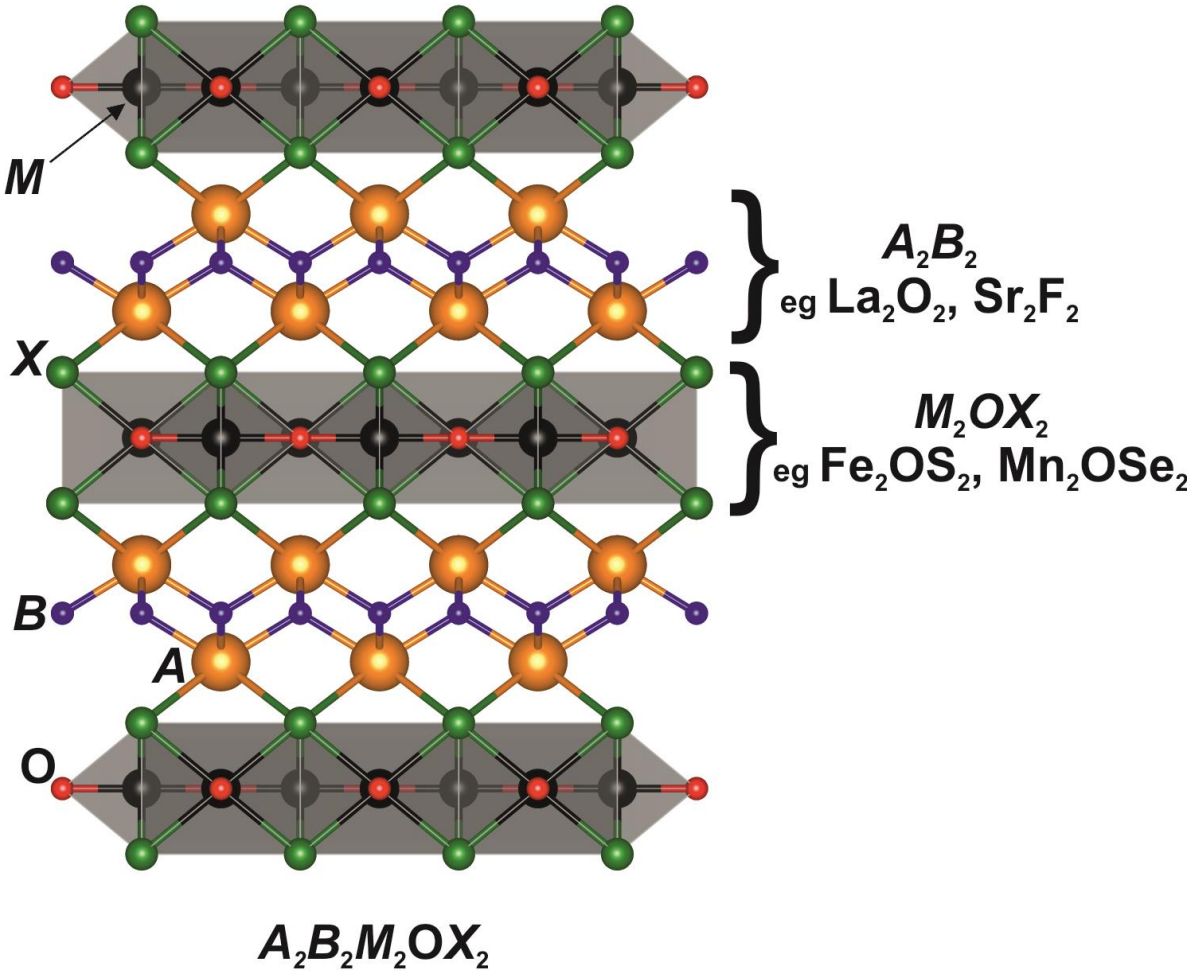


Figure 1.3: Structure of the $A_2B_2M_2OX_2$ family of compounds.

1.3.2 The $Ae_2M_AM_BCh_5$ Structure Type

This quaternary chalcogenide system contains infinite $[M_AM_BCh_5]^{4-}$ chains, with M_A in M_ACh_4 edge-sharing tetrahedra and M_B in M_BCh_6 edge-sharing octahedra, with the compounds studied in this thesis crystallising in the *Pnma* space group. The *Pnma* structure is illustrated in Figure 1.4. The identity of the M_A cation tends to be a 3*d* transition metal or triel (group 13) and the M_B cation is usually a pnictogen (group 15) possessing a stereoactive lone pair. Examples of compounds which crystallise in this structure are Ba_2GaBiS_5,[55] $Ba_2GaLaSe_5$,[56] $Ba_2FeSbSe_5$[57] and $Ba_2FeBiSe_5$.[57]

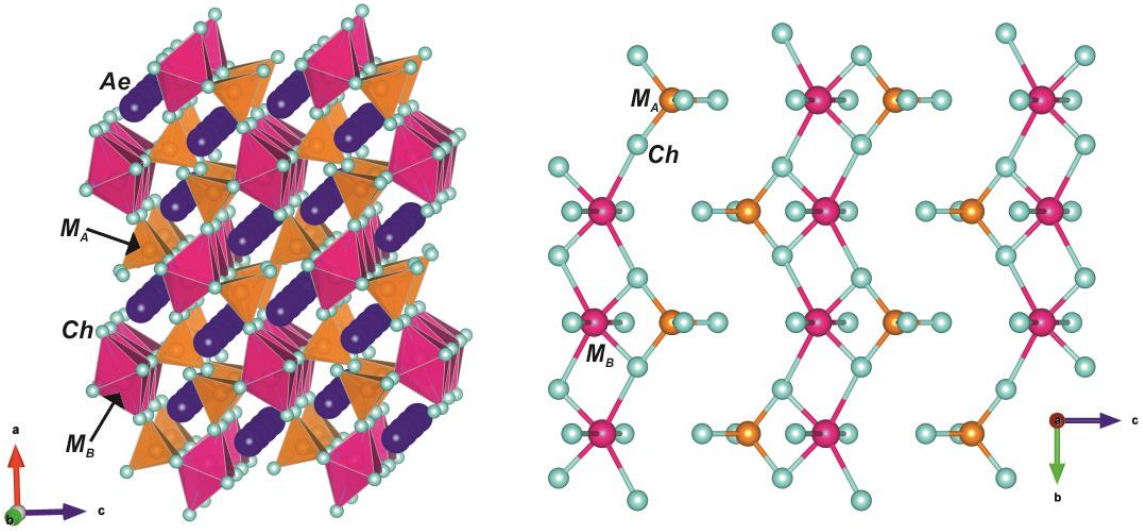


Figure 1.4: The structure of $Ae_2M_AM_BCh_5$ highlighting the M_ACh_4 and M_BCh_6 polyhedra (left) and the infinite 1D $[M_AM_BCh_5]^{4-}$ chains (right).

Interestingly Ba_2InBiS_5[55] forms a structure which is very similar but with an alternative arrangement of the $[M_AM_BCh_5]^{4-}$ chains- one which results in the structure being non-centrosymmetric (space group $Cmc2_1$) rather than centrosymmetric. The Ca_2CdSb_2 (space group *Pnma*) and Yb_2CdSb_2 (space group $Cmc2_1$) are another pair of compounds which exhibit this, perhaps unexpected, difference in structure upon changing of a constituent cation while maintaining the same corner-sharing $CdSb_4$ building blocks.[58]

The lone pair on the pnictogen cation can be modelled in a number of different ways, as detailed by Brown.[59] The lone pair may be 'inactive' and not affect the coordination geometry of the anions around a metal centre, such as in TlCl,[60] where the Tl^+ is in a highly symmetric $TlCl_6$ (low temperature) or $TlCl_8$ (room temperature) coordination. On the other hand, the lone pair may be 'stereoactive' and influence the coordination geometry, such as in Tl_3BO_3,[61] where the Tl^+ effectively has a tetrahedral arrangement of ligands, where one of these ligands is the electron lone pair. Commonly, the geometry of ligands and stereoactive lone pairs around a metal centre are modelled using valence shell electron pair repulsion theory (VSEPR) which aims to minimise the energy of the system by positioning the electron density in the metal-ligand bond and any lone pairs as far apart as possible. Rather than deciding if the stereoactivity of a lone pair is "on" or "off," the presence of a lone pair on a metal centre is perhaps better treated on a scale from completely 'inactive' to completely 'active', where a 'partially active' lone pair results in some shorter (primary) bonds and some longer (secondary) bonds.[59] This scale is illustrated by the diagrams in Figure 1.5.

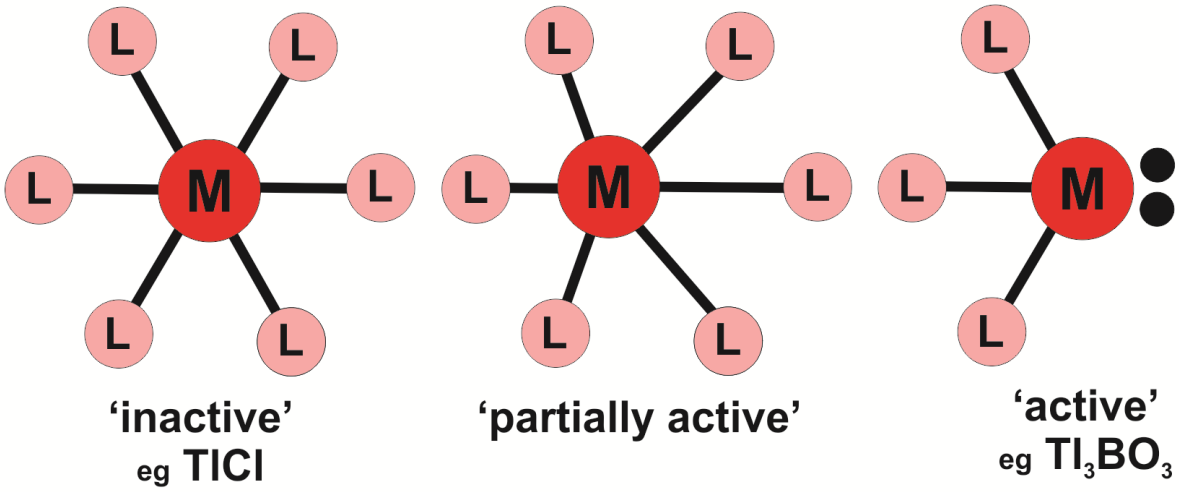


Figure 1.5: Models for the scale of participation of a lone pair towards determining the coordination geometry of a metal centre, usually predicted using VSEPR.

1.4 Magnetism

Structure-property relationships are crucial to the fundamental understanding of materials and the development of novel materials with desired properties. The crystal structure of a solid can affect properties which are magnetic, electronic and physical in nature, however this thesis will primarily focus on magnetic behaviour. Often a crystal structure of a certain crystal dimensionality will display magnetism of the same dimensionality. However, it should be noted that lattice and magnetic dimensionality are not the same in every system and in some cases the magnetism may be quite complex. A good example of this is in the $Sr_2MnO_2Ag_{1.5}Se_2$ material,[62] which adopts a layered crystal structure with alternating $[MnO_2]^{1.5-}$ and $[Ag_{1.5}Se_2]^{2.5-}$ sheets but exhibits low temperature 3D magnetic ordering as there is long-range order both within and between the 2D sheets. However, the magnetism could equally be viewed as 2D as the intralayer magnetic interactions are much stronger than the interlayer interactions.

1.4.1 Diamagnetism

Diamagnetism is the repulsion of an applied magnetic field by the paired electrons belonging to the closed-shell atoms in a material, whether they are valence electrons or core electrons. Lenz's law states that when a magnetic field induces a current in a wire, the magnetic field generated by this induced current will oppose the magnetic field that created it. It is this law that is the origin of diamagnetism. When an external field is applied to a material, the motion of electrons in atomic orbitals results in induced magnetic fields which repel the external field. This phenomenon is small in magnitude (-1 to -100 x 10^{-6} emu mol^{-1}) and the contributions from each atom in the sample are approximately accumulative. When studying paramagnetic, ferromagnetic or antiferromagnetic materials the diamagnetic contributions are usually treated as insignificant, although the magnitude may be comparable to the Pauli paramagnetism of metals. Known diamagnetic materials include TaAs[63] and Ca_3PN.[64]

1.4.2 Paramagnetism

There are 4 types of paramagnetism: Curie paramagnetism, Curie-Weiss paramagnetism, Pauli paramagnetism and temperature independent paramagnetism.

1.4.2.1 Curie Paramagnetism

Curie paramagnetism is exhibited by materials containing unpaired electrons, which are randomly oriented due to thermal fluctuations but then align their angular momenta with in the presence of an applied magnetic field. This happens when the spins are not interacting strongly with one another and so the coupling between adjacent moments is weak. Unlike in the case of diamagnetism, here flux is produced in the same direction as the external field. The magnetisation of the spin, *M*, is given by:

$$M = \frac{Nm^2}{3k_B}\frac{H}{T} \qquad \text{Eqn 1.1}$$

Where *N* is Avogadro's constant, *m* is the magnitude of the magnetic moment, k_B is the Boltzmann constant, *H* is the applied magnetic field and *T* is the temperature. The magnetic susceptibility, χ, is given by:

$$\chi = \frac{M}{H} = \frac{Nm^2}{3k_BT} = \frac{C}{T}\left(where\ the\ Curie\ constant, C = \frac{Nm^2}{3k_B}\right) \qquad \text{Eqn 1.2}$$

Taking into account spatial quantisation, the susceptibility is given by:

$$\chi = \frac{N{\mu_{eff}}^2{\mu_B}^2}{3k_BT} = \frac{C}{T} \qquad \text{Eqn 1.3}$$

Where μ_{eff} is the effective magnetic moment and μ_B is the Bohr magneton. This equation reduces down to:

$$\mu_{eff} \approx \sqrt{8C} \qquad \text{Eqn 1.4}$$

This effective magnetic moment can also be expressed in terms of the total angular momentum, *J*, and the Landé g-factor, *g*:

$$\mu_{eff} = g\sqrt{J(J+1)} \qquad \text{Eqn 1.5}$$

$$g = 1 + \frac{J(J+1)+S(S+1)-L(L+1)}{2J(J+1)} \qquad \text{Eqn 1.6}$$

Where *L* is the orbital momentum, *S* is the spin momentum and *J* is the sum of *L* and *S*. When considering first-row transition metals, the orbital angular momentum is mostly quenched as the ligand field removes the degeneracy of the 3*d* orbitals. For these cases, *L* = 0 resulting in *S* = *J* and *g* = 2, therefore the spin-only effective moment is given by:

$$\mu_{eff} = 2\sqrt{S(S+1)} \qquad \text{Eqn 1.7}$$

Combining Eqn 1.4 and Eqn 1.7 gives:

$$C \approx \frac{S(S+1)}{2} \qquad \text{Eqn 1.8}$$

This means that the number of unpaired electrons can be found by calculating the Curie constant, *C* from the gradient of a plot of $1/\chi$ vs *T*. The room temperature susceptibility values for Curie paramagnets are relatively large (1 to 100 x 10^{-4} emu mol^{-1}).

1.4.2.2 Curie-Weiss Paramagnetism

Moving on to the case where the magnetic moments are now interacting with one another, the Curie-Weiss law is given by:

$$\chi = \frac{C}{T-\theta} \qquad \text{Eqn 1.9}$$

Where the Weiss constant, θ, is positive for spins which are aligned parallel (ferromagnetic) and negative for spins which are aligned antiparallel (antiferromagnetic). Typical Curie-Weiss plots of $1/\chi$ vs *T* are given in Figure 1.6. The magnitude of the Weiss constant, θ, infers the strength of these interactions. At the point where $T \approx \theta$, long-range order occurs in ferromagnets (Curie temperature T_C) and antiferromagnets (Néel temperature T_N). One exception to this is when the magnetic ordering is suppressed by frustration within the system. When calculating the Curie constant, *C*, data must be analysed from well above the Weiss temperature in the region where thermal fluctuations are much

greater than the magnetic interactions. Curie-Weiss paramagnetism is reported for materials such as $BaTiO_3$[65] and $Cs_3GdSi_4O_{10}F_2$.[66]

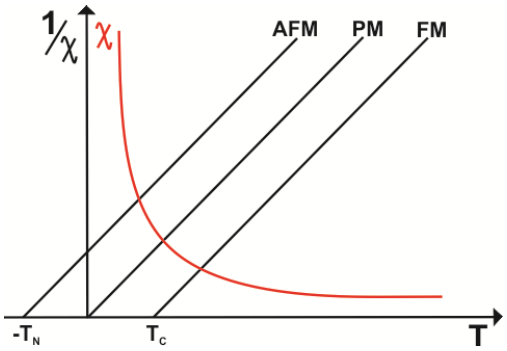


Figure 1.6: Ideal Curie-Weiss plots for antiferromagnetic (AFM), paramagnetic (PM) and ferromagnetic (FM) materials.

1.4.2.3 Pauli Paramagnetism

Pauli paramagnetism arises when valence electron are no longer localised, but are instead itinerant. An example of itinerant electrons are those in a metal which are involved in the metallic band. When an external magnetic field is applied, the spin state which is aligned parallel to this field becomes energetically favoured, where before the field was applied there were equal 'up' and 'down' spins, as the two spin states were degenerate (see Figure 1.7). As the preferred spin state of lower energy is preferentially occupied, a net magnetisation in the same direction as the applied field is produced. Only spins close to the Fermi level, E_F, partake in this phenomenon, so the magnitude is small (1 to 100 x 10^{-7} emu mol^{-1}). Pauli paramagnetism is exhibited by Li_xCoO_2 ($x \leq 0.35$).[67]

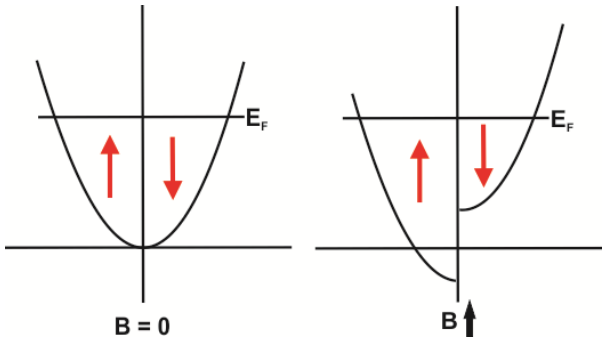


Figure 1.7: Distribution of itinerant electrons in a Pauli paramagnet without an external magnetic field (left) and with an external magnetic field, B (right).

1.4.2.4 Temperature Independent Paramagnetism

Some closed-shell systems, expected only to exhibit diamagnetism, also show weak paramagnetic behaviour. Low-lying excited states, which are not thermally populated, can mix with the ground state resulting in a small paramagnetic contribution- the magnitude of which is temperature independent. This is known as Van Vleck paramagnetism and it is one common type of temperature independent paramagnetism, exhibited by compounds such as Eu_2O_3.[68] It should also be noted that Pauli paramagnetism is another common type of temperature independent paramagnetism.

1.4.3 Ferromagnetism

Ferromagnetism can occur in both metallic spin-polarised systems (eg Fe and CrO_2) and localised moment systems (eg $LaMn_{1-x}Ga_xO_{3+\delta}$[69]). For metallic spin-polarised systems, one spin state is energetically preferred over the other at the Fermi Level, E_F, therefore one spin state is more populated and this results in an overall ferromagnetic system. In terms of localised moment systems, ferromagnetism arises when it is energetically favourable for magnetic moments on neighbouring atoms to align parallel to each other. These moments are grouped into domains which are orientated in different directions to their neighbouring domains. The origin of this domain formation is that a lower energy state is attained when domains are created which have magnetic moments in different directions, rather than having all the moments pointing along the same direction. This results in the total magnetic moment of the solid being zero, however when an external field is applied the domains align and flux is produced in the same direction as the applied field. At temperatures above the Curie temperature, T_C, thermal energy overcomes the magnetic interactions and the sample behaves as a paramagnet. Large susceptibility values are usually achieved for localised spin ferromagnets (1 to 100 x 10^{-2} emu mol^{-1}) and saturation of the magnetisation of these materials is achieved at much lower applied fields than with paramagnets due to the energetic stabilisation of the magnetic state which sees the moments aligned parallel with each other and with the external field. Ideal magnetometry results for localised spin ferromagnets are given in Figures 1.8 and 1.9.

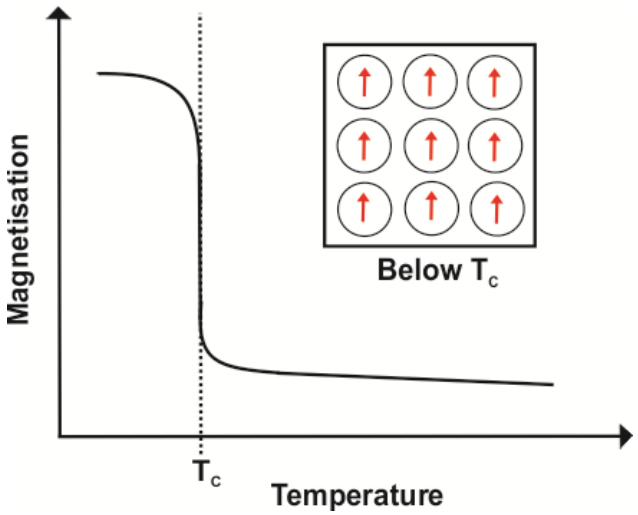


Figure 1.8: Ideal magnetisation vs temperature curve for a ferromagnetic material.

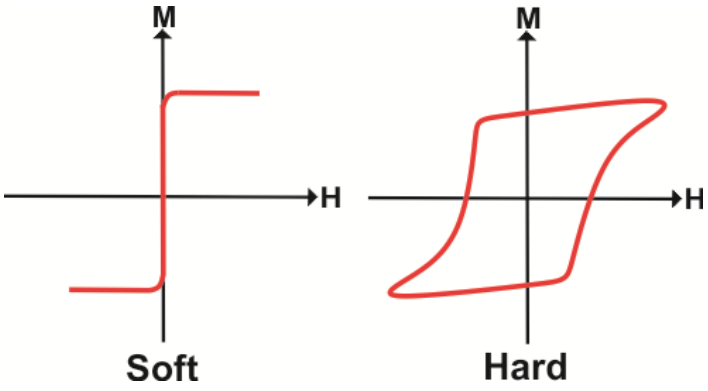


Figure 1.9: Ideal magnetisation vs field hysteresis for a soft and hard ferromagnetic material.

1.4.4 Antiferromagnetism

Antiferromagnetism arises when it is energetically favourable for magnetic moments on neighbouring atoms to align antiparallel to each other. The total magnetic moment of the material is therefore zero. At temperatures above the Néel temperature, T_N, thermal energy overcomes the magnetic interactions and the sample behaves as a paramagnet. When in an external field, moments on the magnetic atoms will align with the field causing a net magnetisation in the sample and overcoming a fraction of the antiferromagnetic interactions present. Below T_N, as temperature is decreased, the susceptibility will decrease because the antiferromagnetic coupling becomes stronger relative to the thermal energy and so there are fewer thermally randomised moments which can align parallel to the

external field. Materials which exhibit long-range antiferromagnetic order include MnO,[70] $Ca_4Mn_3O_{10}$[71] and $Ba_3Fe_2O_5Cu_2Se_2$,[72] along with all the compounds investigated in this thesis. An ideal magnetisation against temperature curve for antiferromagnets is given in Figure 1.10.

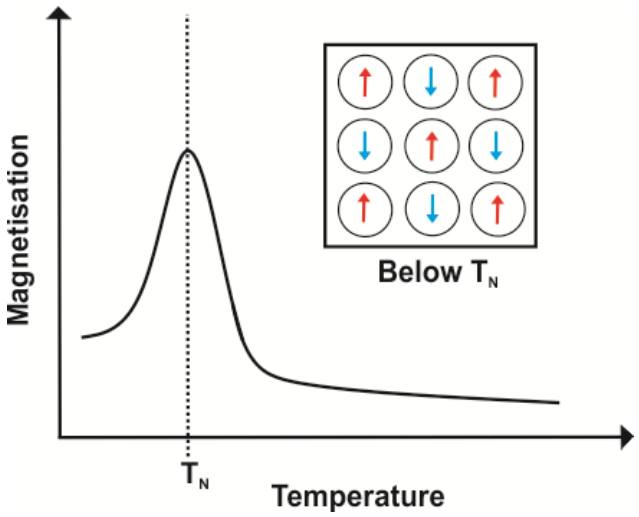


Figure 1.10: Ideal magnetisation vs temperature curve for an antiferromagnetic material.

1.4.5 Ferrimagnetism

Ferrimagnetism results when it is favourable for neighbouring spins to align antiparallel to each other, but the moments directed in each orientation differ in magnitude. This means the material has magnetic moments which are antiferromagnetically aligned, however overall there is a net magnetic moment in the material, and so the material exhibits ferromagnetic-like behaviour. Classic examples of compounds which contain ferrimagnetic order are the spinels, such as $NiCo_2O_4$, which contains mostly Ni^{3+} on the tetrahedral metal site (spin up) and approximately half $Ni^{3.5+}$ and half $Co^{2.5+}$ on the octahedral metal site (spin down).[73] The $Ca_2FeO_2Fe_{1.6}OS_2$ material studied in Chapter 3 exhibits ferrimagnetism.

1.4.6 Spin-Glass Behaviour

Spin-glass behaviour occurs due to frustration and disorder present in a system containing magnetic moments. This can be due to competing interactions or geometrical constraints, such as exchange triangles or tetrahedra, as illustrated in Figure 1.11.

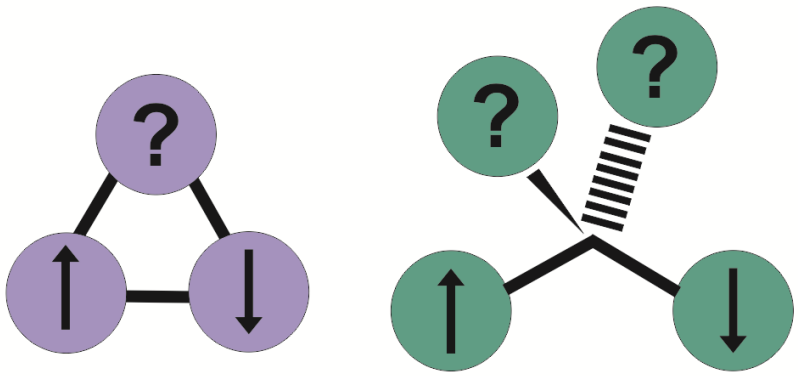


Figure 1.11: Magnetic frustration can occur in exchange triangles (left) and tetrahedra (right).

There is random, yet cooperative, freezing of the magnetic moments as the temperature decreases towards the freezing temperature, T_g, at which point the spins freeze into one of a number of possible ground states. At temperatures well above T_g thermal fluctuations overcome interaction between spins and the material behaves much like a paramagnet, however as the temperature drops towards T_g clusters of spins with a disordered nature will form and bridging spins will mediate interactions between the clusters until eventually T_g is reached and the spins become locked without any long-range order. There will be a difference in the field cooled (FC) and zero field cooled (ZFC) curves as the pattern of the spins will be affected by the presence of an external field as the sample is cooled. The hysteresis of a spin glass below T_g will look similar to that for a ferromagnet, however the hysteresis loop may not end up at the same magnetisation value that it started, it may be displaced from the origin and the curve may contain steps as the magnetisation changes direction. This is because, unlike the case of an antiferromagnet, the frozen state is dependent on its thermal history. Known spin-glasses include $CoAl_2O_4$[74] and $BiFeO_3$.[75] Ideal magnetometry results for spin-glasses are given in Figures 1.12 and 1.13.

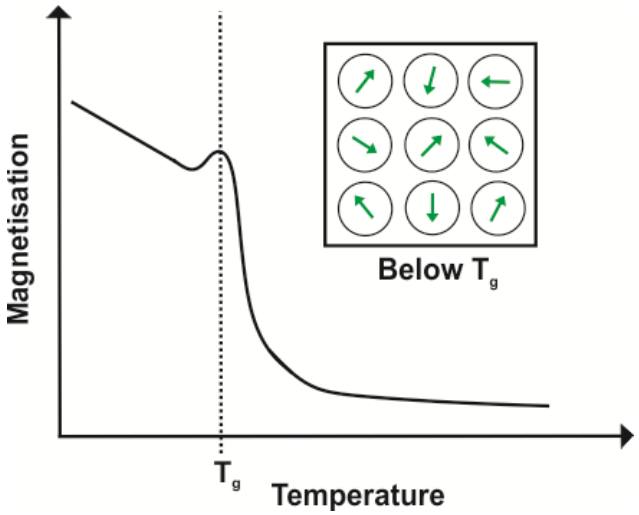


Figure 1.12: Ideal magnetisation vs temperature curve for a spin glass material.

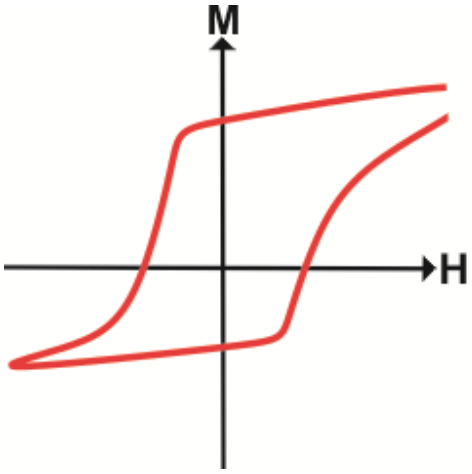


Figure 1.13: Ideal magnetisation vs field hysteresis for a spin glass material.

1.5 Magnetic Exchange

The magnetic ions in a solid- those with unpaired electrons in their frontier orbitals - can interact with each other through various magnetic exchanges. If these exchanges act throughout a crystallographically ordered system, long-range magnetic ordering arises in the material and magnetic Bragg peaks appear in the diffraction data of neutron scattering experiments (see section 2.2.2) when the system enters the ordered state (antiferro-, ferro- or ferri-magnetic states).

1.5.1 Direct Exchange

Direct exchange happens when the orbitals of neighbouring magnetic ions (where these orbitals must contain unpaired electrons) overlap and interact directly. This mechanism therefore only acts over short distances and has a magnitude inversely proportional to r^{12}, where r is the distance between interacting ions and so the strength of the interaction decreases rapidly with increasing distance. Direct exchange can result in either ferromagnetic or antiferromagnetic coupling (see Figure 1.14).

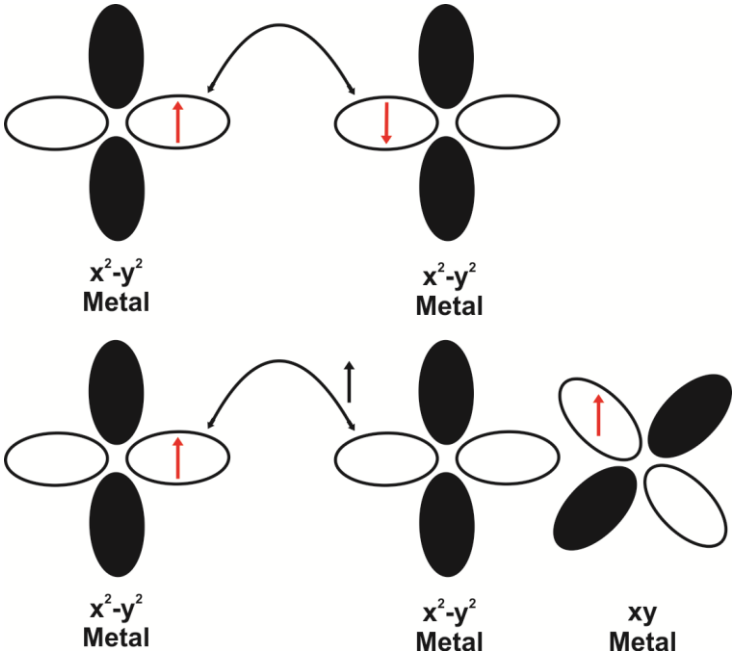


Figure 1.14: Direct exchange, involving two filled orbitals interacting (top) and one filled and one empty orbital interacting (bottom).

1.5.2 Superexchange

Superexchange between two magnetic ions occurs via a mediating, intermediate, non-magnetic ion. It commonly involves a chain of the form M^{n+}-O-M^{n+} with M^{n+} being a transition metal cation of +n valence. There is donation, through covalency, of some electron density from the O^{2-} *p* orbital to the M^{n+} *d* orbitals through the M-O bond, where there will be a preference in the spin state of this transferred electron density depending on the spin state of the unpaired electrons in the metal *d* orbitals.

For the case when this chain is linear, the two metal *d* orbitals overlap with the intermediate oxygen 2*p*(σ) orbital, forming a pathway along which the spins interact and where electron density delocalisation is favourable as this lowers the energy of the system. The filled oxygen 2*p*(σ) orbital must contain electrons of opposite spins in its two lobes (Hund's rules) and the electron density donated to each metal centre must have an opposite spin state to that present in the metal *d* orbital (Pauli exclusion principle). Thus a 180° M^{n+}-O-M^{n+} superexchange usually leads to antiferromagnetic coupling of the magnetic moments, however ferromagnetic coupling can arise for the less common case when orbitals with different electron occupancies interact (see Figure 1.15).

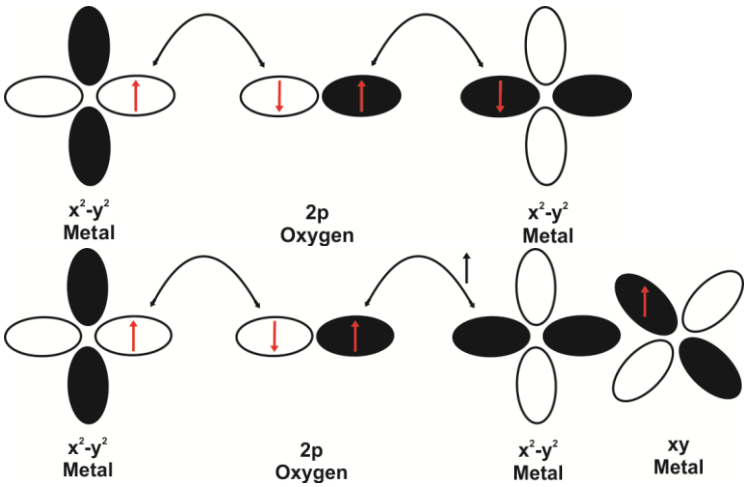


Figure 1.15: M-O-M superexchange, involving the same metal *d* orbital (top) and different metal *d* orbitals with different electron occupancies (bottom).

There may also be the case where the M^{n+}-O-M^{n+} pathway forms a 90° angle instead of 180°. This can result in ferromagnetic or antiferromagnetic coupling depending on the metal orbitals involved. In the ferromagnetic case, there is spin correlation between the electrons in the different *p* orbitals of the intermediate oxygen. In the antiferromagnetic case, there is also spin correlation between the electron density transferred to the empty *d* orbital and those electrons in different *d* orbitals.

The likely dominant metal-metal magnetic coupling can be predicted using Goodenough-Kanamori rules. One extra consideration is for the case when two different metal orbitals are involved, such as in Rb_2CrCl_4[76] as depicted in Figure 1.16.

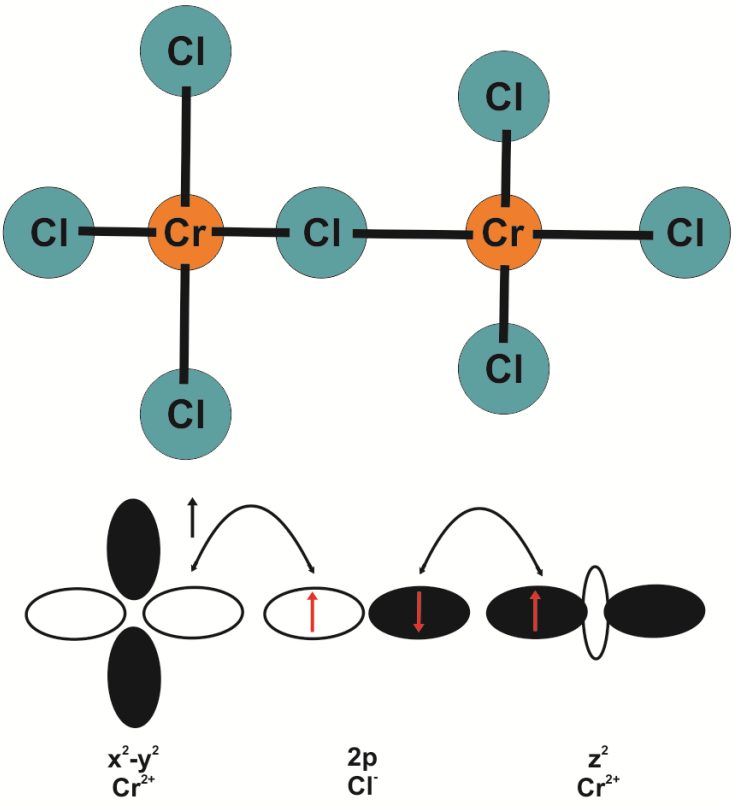


Figure 1.16: Orbital ordering in Rb_2CrCl_4 gives rise to long-range, localised moment ferromagnetism.

1.5.3 Super-Superexchange

Super-superexchange uses the same mechanism as superexchange but over a longer pathway involving more atoms. Often these pathways contain four atoms in an M-O-O-M arrangement, such as the Fe-O-O-Fe super-superexchange in $Li_3Fe_2(PO_4)_3$ which mediates antiferromagnetic coupling between the Fe^{3+} ions.[77] An example of an M-O-O-M super-superexchange pathway is depicted in Figure 1.17. Even super-superexchange chains containing five atoms in an M-O-M-O-M fashion are proposed to mediate spin interactions, examples of which can be seen in some double perovskites, including Os-O-Mg-O-Os chains in Sr_2MgOsO_6[78] and Fe-O-W-O-Fe chains in Sr_2FeWO_6.[79]

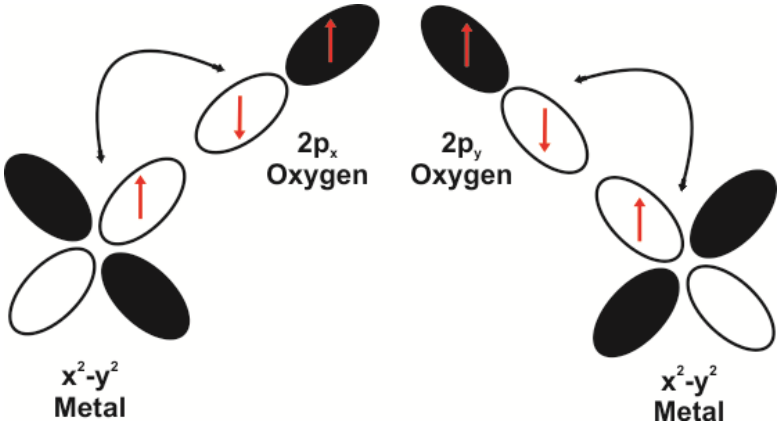


Figure 1.17: Example of an M-O-O-M super-superexchange pathway.

1.6 Aims of the Thesis

This thesis details the studies performed on a number of compounds in order to investigate their structures and properties. The discoveries made will further understanding of how certain properties arise in these materials, in the hope that this knowledge may be used to synthesise materials with specific properties for select applications. These studies can be compared to the results of the many others carried out on other solid-state systems to gain a more holistic view of the field.

Chapter 3 explores the synthesis and characterisation of the $Ca_2FeO_2Fe_{1.6}OS_2$ oxysulfide material. The superstructure present due to Fe-vacancy ordering will be explored, along with the nature of the long-range magnetic ordering present on the two Fe sublattices. Many other characterisation techniques will be employed in order to probe the magnetic and electronic properties of this material, as well as provide further information about the possible distribution of Fe oxidation states. This compound is of particular interest as it is predicted to be close to a superconducting parent phase, as calculations suggest the vacancy-free $Ca_2FeO_2Fe_2OS_2$ material is a superconducting 'bad metal'.[80]

Chapter 4 explores the synthesis and characterisation of the $Ca_2FeO_2Fe_{1.65}OS_{1.5}Se_{0.5}$, $Ca_2FeO_2Fe_{1.7}OSSe$ and $Ca_2FeO_2Fe_{1.75}OS_{0.5}Se_{1.5}$ solid solution phases. Again, the focus of the study will be on the nature of the long-range magnetic ordering in these compounds. A comparison between these phases and also with the $Ca_2FeO_2Fe_2OS_2$ phase will be made, in terms of both structure and properties. The most selenide-rich phase, $Ca_2FeO_2Fe_{1.75}OS_{0.5}Se_{1.5}$, exhibits intriguing spin-reorientation transitions at temperatures between 5-100 K and 100-200 K.

Chapter 5 explores the synthesis and characterisation of the oxypnictide $Sr_2CrO_2Cr_2OAs_2$. This is a novel compound and so the first reports of its structure and properties will be documented. The evolution of the long-range magnetic ordering present on the two Cr sublattices will be detailed using neutron powder diffraction results and a subtle structural distortion between 400 and 500 K will also be discussed. This work has been published in *Inorganic Chemistry*.[81]

Chapter 6 explores the synthesis and magnetic behaviour of the quaternary sulfides Ba_2FeSbS_5 and Ba_2FeBiS_5. These materials exhibit antiferromagnetic ordering of the Fe^{3+} spins below relatively low Néel temperatures of 13 K (Ba_2FeSbS_5) and 35 K (Ba_2FeBiS_5). The presence of incommensurately modulated magnetic Bragg peaks in the neutron powder data for Ba_2FeSbS_5 adds complexity to the magnetic model for this material and may arise due to the higher degree of magnetic frustration occurring in the system.

Chapter 7 summarises the findings of the all the projects in this thesis.

References

(1) Mizushima, K.; Jones, P. C.; Wiseman, P. J.; Goodenough, J. B. Li_xCoO_2 ($0<x\leq1$): A New Cathode Material for Batteries of High Energy Density. *Solid State Ionics* **1981**, *3–4* (C), 171–174. https://doi.org/10.1016/0167-2738(81)90077-1.

(2) Xiao, J. How Lithium Dendrites Form in Liquid Batteries: Studies of Interfacial Reactions and Mass Transport May Allow Safe Use of Lithium Metal Anodes. *Science*. American Association for the Advancement of Science October 25, 2019, pp 426–427. https://doi.org/10.1126/science.aay8672.

(3) Prause, L. Conflicts Related to Resources: The Case of Cobalt Mining in the Democratic Republic of Congo. In *The Material Basis of Energy Transitions*; Academic Press, 2020; pp 153–167. https://doi.org/10.1016/b978-0-12-819534-5.00010-6.

(4) Shakoor, R. A.; Abraham, J. J.; Monawwar, H.; Quddus, A. A.; Tariq, H.; Saleh, I.; Kahraman, R.; Al-Qaradawi, S. Y. Synthesis and Performance Evaluation of SiO_2 Coated Li-Rich $Li_{1.2}Ni_{0.13}Mn_{0.54}Co_{0.13}O_2$ Cathode Materials for Li-Ion Batteries. *ECS Meet. Abstr.* **2020**, *MA2020-01* (2), 399–399. https://doi.org/10.1149/ma2020-012399mtgabs.

(5) Xu, J.; Chou, S. L.; Avdeev, M.; Sale, M.; Liu, H. K.; Dou, S. X. Lithium Rich and Deficient Effects in Li_xCoPO_4 (x = 0.90, 0.95, 1, 1.05) as Cathode Material for Lithium-Ion Batteries. *Electrochim. Acta* **2013**, *88*, 865–870. https://doi.org/10.1016/j.electacta.2012.10.048.

(6) Natsui, R.; Ikeuchi, I.; Ohuchi, S.; Nakura, K. Disordered Rocksalt Type Li-Rich Manganese Oxyfluoride As High-Capacity Cathode Material for Rechargeable Lithium Ion Batteries. *ECS Meet. Abstr.* **2018**, *MA2018-02* (4), 202–202. https://doi.org/10.1149/ma2018-02/4/202.

(7) Zhou, W.; Li, Y.; Xin, S.; Goodenough, J. B. Rechargeable Sodium All-Solid-State Battery. *ACS Cent. Sci.* **2017**, *3* (1), 52–57. https://doi.org/10.1021/acscentsci.6b00321.

(8) Li, C.; Wang, Z. yu; He, Z. jiang; Li, Y. jiao; Mao, J.; Dai, K. hua; Yan, C.; Zheng, J. chao. An Advance Review of Solid-State Battery: Challenges, Progress and Prospects. *Sustainable Materials and Technologies*. Elsevier September 1, 2021, p e00297. https://doi.org/10.1016/j.susmat.2021.e00297.

(9) Palomares, V.; Casas-Cabanas, M.; Castillo-Martínez, E.; Han, M. H.; Rojo, T. Update on Na-Based Battery Materials. A Growing Research Path. *Energy and Environmental Science*. Royal Society of Chemistry July 17, 2013, pp 2312–2337. https://doi.org/10.1039/c3ee41031e.

(10) Wu, M. K.; Ashburn, J. R.; Torng, C. J.; Hor, P. H.; Meng, R. L.; Gao, L.; Huang, Z. J.; Wang, Y. Q.; Chu, C. W. Superconductivity at 93 K in a New Mixed-Phase Yb-Ba-Cu-O Compound System at Ambient Pressure. *Phys. Rev. Lett.* **1987**, *58* (9), 908–910. https://doi.org/10.1103/PhysRevLett.58.908.

(11) Raveau, B.; Michel, C.; Mercey, B.; Hamet, J. F.; Hervieu, M. Crystal Chemistry of Superconducting Copper Oxycarbonates. *J. Alloys Compd.* **1995**, *229* (1), 134–143. https://doi.org/10.1016/0925-8388(95)01679-1.

(12) Mandrus, D.; Sefat, A. S.; McGuire, M. A.; Sales, B. C. Materials Chemistry of $BaFe_2As_2$: A Model Platform for Unconventional Superconductivity. *Chemistry of Materials*. American Chemical Society February 9, 2010, pp 715–723. https://doi.org/10.1021/cm9027397.

(13) Gupta, A.; Huhtinen, H.; Shekhar, C.; Schlesier, K.; Srivastava, P.; Srivastava, A.; Srivastava, O. N.; Laiho, R.; Narlikar, A. V. Occurrence of Superconductivity and Magnetism in Nominally Undoped LaOFeAs. *J. Supercond. Nov. Magn.* **2010**, *23* (8), 1461–1466. https://doi.org/10.1007/s10948-010-0795-8.

(14) Singh, S. J.; Cassidy, S. J.; Bristow, M.; Blundell, S. J.; Clarke, S. J.; Coldea, A. I. Optimization of Superconducting Properties of the Stoichiometric $CaKFe_4As_4$. *Supercond. Sci. Technol.* **2019**, *33* (2), 025003. https://doi.org/10.1088/1361-6668/ab58be.

(15) Nishioka, K.; Takamoto, T.; Agui, T.; Kaneiwa, M.; Uraoka, Y.; Fuyuki, T. Annual Output Estimation of Concentrator Photovoltaic Systems Using High-Efficiency InGaP/InGaAs/Ge Triple-Junction Solar Cells Based on Experimental Solar Cell's Characteristics and Field-Test Meteorological Data. *Sol. Energy Mater. Sol. Cells* **2006**, *90* (1), 57–67. https://doi.org/10.1016/j.solmat.2005.01.011.

(16) Takemoto, S.; Takumi, O.; Takeuchi, H.; Koizumi, Y. The Sr Compositions Dependence of Magnetoresistance of Perovskite-Type Compounds $La_{1-x}Sr_xMnO_3$. *Funtai Oyobi Fummatsu Yakin/Journal Japan Soc. Powder Powder Metall.* **2001**, *48* (12), 1107–1111. https://doi.org/10.2497/jjspm.48.1107.

(17) Cong, B. T.; Anh Huy, P. N.; Long, N. H. The Concentration Dependence of the Curie Temperature of the Colossal Magnetoresistance Perovskite $La_{1-x}Ca_xMnO_3$. In *Journal of Magnetism and Magnetic Materials*; 2003; Vol. 262, pp 437–440. https://doi.org/10.1016/S0304-8853(03)00086-6.

(18) Rao, C. N. R.; Raveau, B. *Colossal Magnetoresistance, Charge Ordering and Related Properties of Manganese Oxides*; WORLD SCIENTIFIC, 1998. https://doi.org/10.1142/3605.

(19) Liang, J.; Liang, Z.; Zou, R.; Zhao, Y. Heterogeneous Catalysis in Zeolites, Mesoporous Silica, and Metal–Organic Frameworks. *Advanced Materials*. John Wiley & Sons, Ltd August 1, 2017, p 1701139. https://doi.org/10.1002/adma.201701139.

(20) Weitkamp, J. Zeolites and Catalysis. *Solid State Ionics* **2000**, *131* (1), 175–188. https://doi.org/10.1016/S0167-2738(00)00632-9.

(21) Wu, C. De; Zhao, M. Incorporation of Molecular Catalysts in Metal–Organic Frameworks for Highly Efficient Heterogeneous Catalysis. *Advanced Materials*. John Wiley & Sons, Ltd April 1, 2017, p 1605446. https://doi.org/10.1002/adma.201605446.

(22) Denbaars, S. P.; Feezell, D.; Kelchner, K.; Pimputkar, S.; Pan, C. C.; Yen, C. C.; Tanaka, S.; Zhao, Y.; Pfaff, N.; Farrell, R.; Iza, M.; Keller, S.; Mishra, U.; Speck, J. S.; Nakamura, S. Development of Gallium-Nitride-Based Light-Emitting Diodes (LEDs) and Laser Diodes for Energy-Efficient Lighting and Displays. *Acta Mater.* **2013**, *61* (3), 945–951. https://doi.org/10.1016/j.actamat.2012.10.042.

(23) Akinwande, D.; Huyghebaert, C.; Wang, C. H.; Serna, M. I.; Goossens, S.; Li, L. J.; Wong, H. S. P.; Koppens, F. H. L. Graphene and Two-Dimensional Materials for Silicon Technology. *Nature*. Nature Publishing Group September 25, 2019, pp 507–518. https://doi.org/10.1038/s41586-019-1573-9.

(24) Kageyama, H.; Hayashi, K.; Maeda, K.; Attfield, J. P.; Hiroi, Z.; Rondinelli, J. M.; Poeppelmeier, K. R. Expanding Frontiers in Materials Chemistry and Physics with Multiple Anions. *Nature Communications*. 2018, p 772. https://doi.org/10.1038/s41467-018-02838-4.

(25) Cario, L.; Lafond, A.; Morvan, T.; Kabbour, H.; André, G.; Palvadeau, P. Design and Magnetic Properties of New Compounds Containing Iron 2D Building Blocks of the Perovskite Type. *Solid State Sci.* **2005**, *7* (8), 936–944. https://doi.org/10.1016/j.solidstatesciences.2005.04.016.

(26) Clarke, S. J.; Adamson, P.; Herkelrath, S. J. C.; Rutt, O. J.; Parker, D. R.; Pitcher, M. J.; Smura, C. F. Structures, Physical Properties, and Chemistry of Layered Oxychalcogenides and

Oxypnictides. *Inorganic Chemistry*. 2008, pp 8473–8486. https://doi.org/10.1021/ic8009964.

(27) Vazirisereshk, M. R.; Martini, A.; Strubbe, D. A.; Baykara, M. Z. Solid Lubrication with MoS_2: A Review. *Lubricants*. Multidisciplinary Digital Publishing Institute July 2, 2019, p 57. https://doi.org/10.3390/LUBRICANTS7070057.

(28) Whittingham, M. S. Chemistry of Intercalation Compounds: Metal Guests in Chalcogenide Hosts. *Progress in Solid State Chemistry*. 1978, pp 41–99. https://doi.org/10.1016/0079-6786(78)90003-1.

(29) Moon, D. G.; Rehan, S.; Yeon, D. H.; Lee, S. M.; Park, S. J.; Ahn, S. J.; Cho, Y. S. A Review on Binary Metal Sulfide Heterojunction Solar Cells. *Sol. Energy Mater. Sol. Cells* **2019**, *200*, 109963. https://doi.org/10.1016/j.solmat.2019.109963.

(30) Powell, A. V. Recent Developments in Earth-Abundant Copper-Sulfide Thermoelectric Materials. *J. Appl. Phys.* **2019**, *126* (10). https://doi.org/10.1063/1.5119345.

(31) Wang, H.; Ma, H.; Duan, B.; Geng, H.; Zhou, L.; Li, J.; Zhang, X.; Yang, H.; Li, G.; Zhai, P. High-Pressure Rapid Preparation of High-Performance Binary Silver Sulfide Thermoelectric Materials. *ACS Appl. Energy Mater.* **2021**, *4* (2), 1610–1618. https://doi.org/10.1021/acsaem.0c02810.

(32) Wu, H.; Lu, X.; Wang, G.; Peng, K.; Chi, H.; Zhang, B.; Chen, Y.; Li, C.; Yan, Y.; Guo, L.; Uher, C.; Zhou, X.; Han, X. Sodium-Doped Tin Sulfide Single Crystal: A Nontoxic Earth-Abundant Material with High Thermoelectric Performance. *Adv. Energy Mater.* **2018**, *8* (20), 1800087. https://doi.org/10.1002/aenm.201800087.

(33) Yang, X.; Wang, Y.; Sui, Y.; Huang, X.; Cui, T.; Wang, C.; Liu, B.; Zou, G.; Zou, B. Size-Controlled Synthesis of Bifunctional Magnetic and Ultraviolet Optical Rock-Salt MnS Nanocube Superlattices. *Langmuir* **2012**, *28* (51), 17811–17816. https://doi.org/10.1021/la304228w.

(34) Utyuzh, A. N. Influence of Temperature on Raman Spectra of the FeS_2 Single Crystal with Pyrite Structure. *Phys. Solid State* **2014**, *56* (10), 1985–1990. https://doi.org/10.1134/S1063783414100321.

(35) Kale, B. B.; Baeg, J. O.; Lee, S. M.; Chang, H.; Moon, S. J.; Lee, C. W. $CdIn_2S_4$ Nanotubes and "Marigold" Nanostructures: A Visible-Light Photocatalyst. *Adv. Funct. Mater.* **2006**, *16* (10), 1349–1354. https://doi.org/10.1002/adfm.200500525.

(36) Fukuoka, H.; Miyaki, Y.; Yamanaka, S. High-Pressure Synthesis and Structures of Novel Chromium Sulfides, Ba_3CrS_5 and $Ba_3Cr_2S_6$ with One-Dimensional Chain Structures. *J. Solid State Chem.* **2003**, *176* (1), 206–212. https://doi.org/10.1016/S0022-4596(03)00398-0.

(37) Ramasamy, K.; Sims, H.; Butler, W. H.; Gupta, A. Mono-, Few-, and Multiple Layers of Copper Antimony Sulfide ($CuSbS_2$): A Ternary Layered Sulfide. *J. Am. Chem. Soc.* **2014**, *136* (4), 1587–1598. https://doi.org/10.1021/ja411748g.

(38) Boldish, S. I.; White, W. B. Optical Band Gaps of Selected Ternary Sulfide Minerals. *Am. Mineral.* **1998**, *83* (7–8), 865–871. https://doi.org/10.2138/am-1998-7-818.

(39) Bronger, W. Ternary Sulfides: Model Compounds for the Correlation of Crystal Structure and Magnetic Properties. *Angewandte Chemie International Edition in English*. John Wiley & Sons, Ltd January 1, 1981, pp 52–62. https://doi.org/10.1002/anie.198100521.

(40) Brechtel, E.; Cordier, G.; Schäfer, H. On Oxidpnictides: Preparation and Crystal Structure of $A_2Mn_3B_2O_2$ with A = Sr, Ba and B = As, Sb, Bi. *Zeitschrift fur Naturforsch. - Sect. B J. Chem. Sci.* **1979**, *34* (6), 777–780. https://doi.org/10.1515/znb-1979-0603.

(41) Xu, X.; Jones, M. A.; Cassidy, S. J.; Manuel, P.; Orlandi, F.; Batuk, M.; Hadermann, J.; Clarke, S. J. Magnetic Ordering in the Layered Cr(II) Oxide Arsenides $Sr_2CrO_2Cr_2As_2$ and $Ba_2CrO_2Cr_2As_2$. *Inorg. Chem.* **2020**, *59* (21), 15898–15912. https://doi.org/10.1021/acs.inorgchem.0c02415.

(42) Jiang, H.; Bao, J. K.; Zhai, H. F.; Tang, Z. T.; Sun, Y. L.; Liu, Y.; Wang, Z. C.; Bai, H.; Xu, Z. A.; Cao, G. H. Physical Properties and Electronic Structure of $Sr_2Cr_3As_2O_2$ Containing CrO_2 and Cr_2As_2 Square-Planar Lattices. *Phys. Rev. B - Condens. Matter Mater. Phys.* **2015**, *92* (20), 205107. https://doi.org/10.1103/PhysRevB.92.205107.

(43) Liu, J.; Wang, J.; Sheng, J.; Ye, F.; Taddei, K. M.; Fernandez-Baca, J. A.; Luo, W.; Sun, G. A.; Wang, Z. C.; Jiang, H.; Cao, G. H.; Bao, W. Neutron Diffraction Study on Magnetic Structures and Transitions in $Sr_2Cr_3As_2O_2$. *Phys. Rev. B* **2018**, *98* (13), 134416. https://doi.org/10.1103/PhysRevB.98.134416.

(44) Xu, X.; Jones, M. A.; Cassidy, S. J.; Manuel, P.; Orlandi, F.; Batuk, M.; Hadermann, J.; Clarke, S. J. Magnetic Ordering in the Layered Cr(II) Oxide Arsenides $Sr_2CrO_2Cr_2As_2$ and $Ba_2CrO_2Cr_2As_2$. *Inorg. Chem.* **2020**, *59* (21), 15898–15912. https://doi.org/10.1021/acs.inorgchem.0c02415.

(45) Zhang, H.; Wu, X.; Li, D.; Jin, S.; Chen, X.; Zhang, T.; Lin, Z.; Shen, S.; Yuan, D.; Chen, X. $Ca_2O_3Fe_{2.6}S_2$: An Antiferromagnetic Mott Insulator at Proximity to Bad Metal. *J. Phys. Condens. Matter* **2016**, *28* (14), 145701. https://doi.org/10.1088/0953-8984/28/14/145701.

(46) Free, D. G.; Withers, N. D.; Hickey, P. J.; Evans, J. S. O. Synthesis, Structure and Properties of Several New Oxychalcogenide Materials with the General Formula $A_2O_2M_2OSe_2$ (A = La-Sm, M = Fe, Mn). *Chem. Mater.* **2011**, *23* (6), 1625–1635. https://doi.org/10.1021/cm1035453.

(47) Free, D. G.; Evans, J. S. O. Low-Temperature Nuclear and Magnetic Structures of $La_2O_2Fe_2OSe_2$ from x-Ray and Neutron Diffraction Measurements. *Phys. Rev. B - Condens. Matter Mater. Phys.* **2010**, *81* (21). https://doi.org/10.1103/PhysRevB.81.214433.

(48) Oogarah, R. K.; Suard, E.; McCabe, E. E. Magnetic Order and Phase Transition in the Iron Oxysulfide $La_2O_2Fe_2OS_2$. *J. Magn. Magn. Mater.* **2018**, *446*, 101–107. https://doi.org/10.1016/j.jmmm.2017.09.024.

(49) Zhu, J. X.; Yu, R.; Wang, H.; Zhao, L. L.; Jones, M. D.; Dai, J.; Abrahams, E.; Morosan, E.; Fang, M.; Si, Q. Band Narrowing and Mott Localization in Iron Oxychalcogenides $La_2O_2Fe_2O(Se,S)_2$. *Phys. Rev. Lett.* **2010**, *104* (21). https://doi.org/10.1103/PhysRevLett.104.216405.

(50) Kabbour, H.; Janod, E.; Corraze, B.; Danot, M.; Lee, C.; Whangbo, M. H.; Cario, L. Structure and Magnetic Properties of Oxychalcogenides $A_2F_2Fe_2OQ_2$ (A = Sr, Ba; Q = S, Se) with Fe_2O Square Planar Layers Representing an Antiferromagnetic Checkerboard Spin Lattice. *J. Am. Chem. Soc.* **2008**, *130* (26), 8261–8270. https://doi.org/10.1021/ja711139g.

(51) Ni, N.; Climent-Pascual, E.; Jia, S.; Huang, Q.; Cava, R. J. Physical Properties and Magnetic Structure of the Layered Oxyselenide $La_2O_3Mn_2Se_2$. *Phys. Rev. B - Condens. Matter Mater. Phys.* **2010**, *82* (21). https://doi.org/10.1103/PhysRevB.82.214419.

(52) Wu, H. Electronic Structure, Spin State, and Magnetism of the Square-Lattice Mott Insulator $La_2Co_2Se_2O_3$ from First Principles. *Phys. Rev. B - Condens. Matter Mater. Phys.* **2010**, *82* (2). https://doi.org/10.1103/PhysRevB.82.020410.

(53) Wang, C.; Tan, M. Q.; Feng, C. M.; Ma, Z. F.; Jiang, S.; Xu, Z. A.; Cao, G. H.; Matsubayashi, K.; Uwatoko, Y. $La_2Co_2Se_2O_3$: A Quasi-Two-Dimensional Mott Insulator with Unusual Cobalt Spin State and Possible Orbital Ordering. *J. Am. Chem. Soc.* **2010**, *132* (20), 7069–7073. https://doi.org/10.1021/ja1001295.

(54) Fuwa, Y.; Endo, T.; Wakeshima, M.; Hinatsu, Y.; Ohoyama, K. Orthogonal Spin Arrangement in

Quasi-Two-Dimensional $La_2Co_2O_3Se_2$. *J. Am. Chem. Soc.* **2010**, *132* (51), 18020–18022. https://doi.org/10.1021/ja109007g.

(55) Geng, L.; Cheng, W. D.; Lin, C. S.; Zhang, W. L.; Zhang, H.; He, Z. Z. Syntheses and Characterization of New Mid-Infrared Transparency Compounds: Centric Ba_2BiGaS_5 and Acentric Ba_2BiInS_5. *Inorg. Chem.* **2011**, *50* (12), 5679–5686. https://doi.org/10.1021/ic2004358.

(56) Yin, W.; Zhang, D.; Zhou, M.; Iyer, A. K.; Pöhls, J. H.; Yao, J.; Mar, A. Quaternary Rare-Earth Selenides $Ba_2REGaSe_5$ and $Ba_2REInSe_5$. *J. Solid State Chem.* **2018**, *265*, 167–175. https://doi.org/10.1016/j.jssc.2018.05.041.

(57) Wang, J.; Greenfield, J. T.; Kovnir, K. Synthesis, Crystal Structure, and Magnetic Properties of Quaternary Iron Selenides: $Ba_2FePnSe_5$ (Pn=Sb, Bi). *J. Solid State Chem.* **2016**, *242*, 22–27. https://doi.org/10.1016/j.jssc.2015.12.030.

(58) Xia, S. Q.; Bobev, S. Cation-Anion Interactions as Structure Directing Factors: Structure and Bonding of Ca_2CdSb_2 and Yb_2CdSb_2. *J. Am. Chem. Soc.* **2007**, *129* (13), 4049–4057. https://doi.org/10.1021/ja069261k.

(59) Brown, I. D. View of Lone Electron Pairs and Their Role in Structural Chemistry. *J. Phys. Chem. A* **2011**, *115* (45), 12638–12645. https://doi.org/10.1021/jp203242m.

(60) Blackman, M.; Khan, I. H. The Polymorphism of Thallium and Other Halides at Low Temperatures. *Proc. Phys. Soc.* **1961**, *77* (2), 471–475. https://doi.org/10.1088/0370-1328/77/2/331.

(61) PIFFARD, Y.; R, M.; M, T. STRUCTURE ET FILIATION STRUCTURALE DES PHASES $TL_6SI_2O_7$ ET TL_3BO_3. *Struct. Filiat. Struct. DES PHASES TL6SI2O7 TL3BO3.* **1975**.

(62) Blandy, J. N.; Boskovic, J. C.; Clarke, S. J. Synthesis and Magnetic Structure of the Layered Manganese Oxide Selenide $Sr_2MnO_2Ag_{1.5}Se_2$. *J. Solid State Chem.* **2017**, *245*, 61–66. https://doi.org/10.1016/j.jssc.2016.10.010.

(63) Liu, Y.; Li, Z.; Guo, L.; Chen, X.; Yuan, Y.; Liu, F.; Prucnal, S.; Helm, M.; Zhou, S. Intrinsic Diamagnetism in the Weyl Semimetal TaAs. *Journal of Magnetism and Magnetic Materials*. North-Holland June 15, 2016, pp 73–76. https://doi.org/10.1016/j.jmmm.2016.01.100.

(64) Chern, M. Y.; Vennos, D. A.; Disalvo, F. J. Synthesis, Structure, and Properties of Anti-Perovskite Nitrides Ca_3MN, M=P, As, Sb, Bi, Ge, Sn, and Pb. *J. Solid State Chem.* **1992**, *96* (2), 415–425. https://doi.org/10.1016/S0022-4596(05)80276-2.

(65) Flores-Ramirez, R.; Huanosta, A.; Amano, E.; Valenzuela, R.; Westi, A. R. Curie-Weiss Behavior In Polycrystalline Barium Titanate From AC Measurements. *Ferroelectrics* **1989**, *99* (1), 195–201. https://doi.org/10.1080/00150198908221452.

(66) Morrison, G.; Latshaw, A. M.; Spagnuolo, N. R.; Zur Loye, H. C. Observation of Intense X-Ray Scintillation in a Family of Mixed Anion Silicates, $Cs_3RESi_4O_{10}F_2$ (RE = Y, Eu-Lu), Obtained via an Enhanced Flux Crystal Growth Technique. *J. Am. Chem. Soc.* **2017**, *139* (41), 14743–14748. https://doi.org/10.1021/jacs.7b08559.

(67) Motohashi, T.; Ono, T.; Sugimoto, Y.; Masubuchi, Y.; Kikkawa, S.; Kanno, R.; Karppinen, M.; Yamauchi, H. Electronic Phase Diagram of the Layered Cobalt Oxide System Li_xCoO_2 ($0.0 \leq x \leq 1.0$). *Phys. Rev. B - Condens. Matter Mater. Phys.* **2009**, *80* (16). https://doi.org/10.1103/PhysRevB.80.165114.

(68) Takikawa, Y.; Ebisu, S.; Nagata, S. Van Vleck Paramagnetism of the Trivalent Eu Ions. *J. Phys.*

Chem. Solids **2010**, *71* (11), 1592–1598. https://doi.org/10.1016/j.jpcs.2010.08.006.

(69) Goodenough, J. B.; Wold, A.; Arnott, R. J.; Menyuk, N. Relationship between Crystal Symmetry and Magnetic Properties of Ionic Compounds Containing Mn^{3+}. *Phys. Rev.* **1961**, *124* (2), 373–384. https://doi.org/10.1103/PhysRev.124.373.

(70) Shull, C. G.; Strauser, W. A.; Wollan, E. O. Neutron Diffraction by Paramagnetic and Antiferromagnetic Substances. *Phys. Rev.* **1951**, *83* (2), 333–345. https://doi.org/10.1103/PhysRev.83.333.

(71) Battle, P. D.; Green, M. A.; Lago, J.; Millburn, J. E.; Rosseinsky, M. J.; Vente, J. F. Crystal and Magnetic Structures of $Ca_4Mn_3O_{10}$, an n = 3 Ruddlesden-Popper Compound. *Chem. Mater.* **1998**, *10* (2), 658–664. https://doi.org/10.1021/cm970647r.

(72) Smyth, R. D.; Wilson, J. A. D.; Manuel, P.; Clarke, S. J. Synthesis, Structure, Magnetism and Cation Ordering in $Ba_{3-x}Sr_xFe_2O_5Cu_2Ch_2$ (x = 0, 1, 2; Ch = S, Se) and $BaCa_2Fe_2O_5Cu_2S_2$. *J. Solid State Chem.* **2022**, *307*, 122841. https://doi.org/10.1016/j.jssc.2021.122841.

(73) Marco, J. F.; Gancedo, J. R.; Gracia, M.; Gautier, J. L.; Ríos, E. I.; Palmer, H. M.; Greaves, C.; Berry, F. J. Cation Distribution and Magnetic Structure of the Ferrimagnetic Spinel $NiCo_2O_4$. *J. Mater. Chem.* **2001**, *11* (12), 3087–3093. https://doi.org/10.1039/b103135j.

(74) Hanashima, K.; Kodama, Y.; Akahoshi, D.; Kanadani, C.; Saito, T. Spin Glass Order by Antisite Disorder in the Highly Frustrated Spinel Oxide $CoAl_2O_4$. *J. Phys. Soc. Japan* **2013**, *82* (2). https://doi.org/10.7566/JPSJ.82.024702.

(75) Singh, M. K.; Prellier, W.; Singh, M. P.; Katiyar, R. S.; Scott, J. F. Spin-Glass Transition in Single-Crystal $BiFeO_3$. *Phys. Rev. B - Condens. Matter Mater. Phys.* **2008**, *77* (14). https://doi.org/10.1103/PhysRevB.77.144403.

(76) Day, P.; Hutchings, M. T.; Janke, E.; Walker, P. J. Co-Operative Jahn-Teller Ordering in the Crystal Structure of Rb_2CrCl_4: A Two-Dimensional Easy-Plane Ionic Ferromagnet. *J. Chem. Soc. Chem. Commun.* **1979**, No. 16, 711–713. https://doi.org/10.1039/C39790000711.

(77) Rousse, G.; Rodríguez-Carvajal, J.; Wurm, C.; Masquelier, C. Magnetic Structural Studies of the Two Polymorphs of $Li_3Fe_2(PO_4)_3$: Analysis of the Magnetic Ground State from Super-Super Exchange Interactions. *Chem. Mater.* **2001**, *13* (12), 4527–4536. https://doi.org/10.1021/cm011054q.

(78) Yuan, Y.; Feng, H. L.; Ghimire, M. P.; Matsushita, Y.; Tsujimoto, Y.; He, J.; Tanaka, M.; Katsuya, Y.; Yamaura, K. High-Pressure Synthesis, Crystal Structures, and Magnetic Properties of 5d Double-Perovskite Oxides Ca_2MgOsO_6 and Sr_2MgOsO_6. *Inorg. Chem.* **2015**, *54* (7), 3422–3431. https://doi.org/10.1021/ic503086a.

(79) Kawanaka, H.; Hase, I.; Toyama, S.; Nishihara, Y. Electronic State of Fe in Double Perovskite Oxide Sr_2FeWO_6. *J. Phys. Soc. Japan* **1999**, *68* (9), 2890–2893. https://doi.org/10.1143/JPSJ.68.2890.

(80) Craco, L.; Freelon, B.; Alafailakawi, A. M.; Karki, B.; Leoni, S. Site-Selective Electronic Structure of Pure and Doped $Ca_2O_3Fe_3S_2$. *Phys. Rev. B* **2018**, *98* (4), 45130. https://doi.org/10.1103/PhysRevB.98.045130.

(81) Sheath, B. C.; Xu, X.; Manuel, P.; Hadermann, J.; Batuk, M.; O'Sullivan, J.; Bonilla, R. S.; Clarke, S. J. Structures and Magnetic Ordering in Layered Cr Oxide Arsenides $Sr_2CrO_2Cr_2OAs_2$ and Sr_2CrO_3CrAs. *Inorg. Chem.* **2022**, *61* (31), 12373–12385. https://doi.org/10.1021/acs.inorgchem.2c01773.

Chapter 2

2 Experimental Methods

2.1 Synthetic Techniques

This section details the procedures employed in the synthesis of the materials studied in this thesis.

2.1.1 Handling Air/Moisture-Sensitive Materials

Although the materials synthesised in this thesis were not highly sensitive to either air or moisture, they were treated as such and the synthetic route to attain these products needed air and moisture levels to be very low. A Glovebox Technology argon-filled dry box was used throughout the synthesis of the materials studied in this thesis. This contains an argon atmosphere, where the oxygen level is continually monitored by an oxygen sensor and should always be below 1 ppm when working inside it. The argon atmosphere circulates around the box and through a purification system in which any O_2 or H_2O are removed by Cu catalysts and molecular sieves. The glove box is regenerated regularly in order to replenish the Cu catalysts (by passing a H_2/N_2 gaseous mixture over them to reduce any CuO back to Cu) and dry out the molecular sieves (by heating them up). Pre-drying equipment and leaving this under vacuum inside the antechamber further helps to maintain the very low oxygen and moisture levels inside the box.

The reagents used are air-sensitive and so these were stored inside the glove box, along with the products synthesised for this thesis. These reagents were weighed and ground inside the glove box. Two argon-filled polythene bags maintained the inert atmosphere while the pellets were being pressed outside the glove box. A Young's tap fitted to the end of the silica tube works by putting pressure on a rubber O-ring which keeps the setup air-tight, thus the tube is either filled with argon or is attached to the vacuum line. The reactions took place inside evacuated silica ampoules and preparation of the products for analysis was generally also carried out inside the glove box. All

equipment used, including the silica tubes and alumina crucibles, was pre-dried in furnaces and/or drying ovens to remove moisture.

2.1.2 Solid-State Synthesis

Stoichiometric amounts of reagents were accurately weighed and ground together using an agate pestle and mortar until an homogeneous mixture was obtained, usually after 20-30 mins of grinding. The powder was then transferred into a 13mm diameter pellet die, placed inside two argon-filled polythene bags and the pellet pressed under 3-5 tonnes of force. Pellets were then extracted inside the glovebox and either placed straight into a silica tube or into an alumina crucible and then into a silica tube, with the alumina crucible sitting on top of a silica spacer. A Young's tap was then fitted to the open end of the tube and this was put under dynamic vacuum (of the order of 10^{-2} mbar). The tube was sealed using a blow torch. A typical setup for sealing a sample inside an evacuated silica ampoule is illustrated in Figure 2.1. This was then placed inside a furnace and heated to high temperatures, typically around 1000 °C.

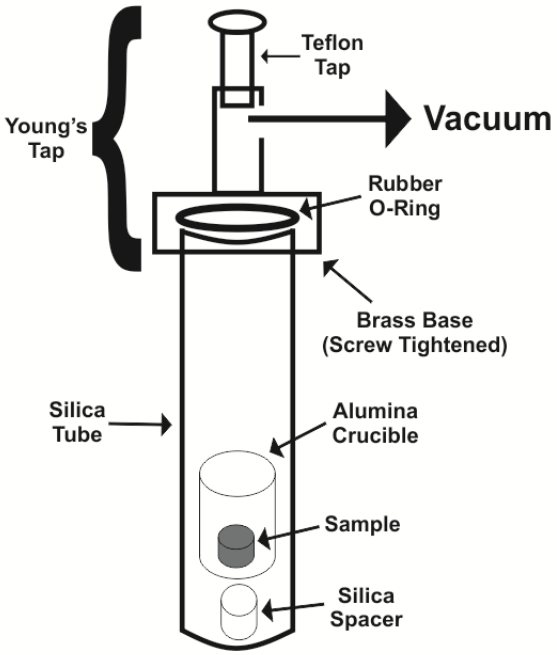


Figure 2.1: The experimental setup used to seal a sample in a silica tube under dynamic vacuum.

The diffusion of ions in a solid-state reaction is very slow and has a high activation barrier. Steps are taken in the synthesis of solids in order to overcome this. Very high temperatures are used to give the ions energy to overcome the activation barrier and diffuse faster. Mixing the initial starting materials by grinding until they are homogenous gives smaller particles that are well distributed, minimising the distance between particles and promoting contact between a particle and the other reagents. Pelletising the starting mixture increases contact between the grains, helping diffusion of the ions. Regrinding and reheating can be important if the mixture contains ions with low mobility, however in the cases involving chalcogenides and pnictides this issue does not usually arise.

2.1.3 Preparation of SrO

SrO was synthesised as a reagent for the strontium containing product in this thesis. It was made via thermal decomposition of $SrCO_3$ (Alfa Aesar, 99.99 %), as given by:

$$SrCO_3 \rightarrow SrO + CO_2 \uparrow$$

Two alumina boats were filled with loosely packed $SrCO_3$ and these boats placed in the centre of a silica tube, fitted with an end-cap at one end and a Young's tap attached to an end-cap on the other end. The Young's tap was connected up to a dynamic vacuum (of the order of 10^{-2} mbar) and the tube placed into a split-tube furnace. A cooling fan was placed under each end-cap to prevent the O-ring from heating up and degrading. The tube was heated up to 840 °C for 18 h (10 °C min^{-1}) and then to 1100 °C for 4 h (5 °C min^{-1}). The setup was left to cool naturally back down to room temperature, at which point the whole assembly was transferred to the glove box. The purity of the SrO was checked using in-house XRPD.

2.2 Characterisation Techniques

This section details the various techniques employed in the characterisation of the structure and investigation of the properties of the compounds studied in this thesis.

2.2.1 X-Ray Powder Diffraction (XRPD)

X-ray powder diffraction[1,2] is a key technique used to probe the structure of crystalline solids. Due to the fact that the wavelength of x-ray radiation (0.1 – 10 Å) and the distances between atoms in these solids (typically 1 – 2 Å) are comparable, a crystalline material will act as a diffraction grating when irradiated with x-ray radiation. As crystalline solids are comprised of a periodic array of repeating unit cells in 3D space, the many diffracted x-ray waves will constructively interfere along certain directions.

Laue first introduced the idea of a lattice scattering monochromatic radiation. An example of this using a 1D lattice is shown in Figure 2.2.

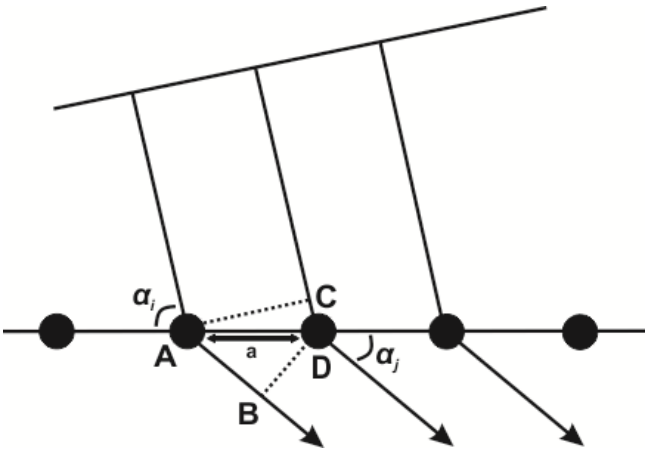


Figure 2.2: The Laue scattering of monochromatic radiation by a 1D crystal lattice.

The incident, monochromatic radiation hits the row of atoms with an incident angle of α_i. In order to observe maximum constructive interference, the path difference between the x-ray waves after diffraction, exiting with an angle of α_j, must be equal to an integer number (n) of wavelengths (λ). Therefore:

$$AB - CD = a(cos\alpha_j - cos\alpha_i) = n\lambda \qquad \text{Eqn 2.1}$$

Now moving to a 3D lattice, there are three Laue equations- one for each dimension *x*, *y* and *z*:

$$a(cos\alpha_j - cos\alpha_i) = n_x\lambda \qquad \text{Eqn 2.2}$$

$$b(cos\beta_j - cos\beta_i) = n_y\lambda \qquad \text{Eqn 2.3}$$

$$c(cos\gamma_j - cos\gamma_i) = n_z\lambda \qquad \text{Eqn 2.4}$$

However, there are many variables that need to be determined when using these equations and in 1912, father and son W. H. Bragg and W. L. Bragg developed Bragg's law. This describes the structure of a crystalline solid as a series of planes of atoms, which are able to reflect radiation. These planes are denoted by Miller indices *h k l*, where a certain plane will intersect the edges of the unit cell with dimensions *a b c* at positions *a/h b/k c/l*. Figure 2.3 depicts x-rays being reflected by these Miller planes, which are separated by distance d_{hkl}. In order for maximum constructive interference after reflection the radiation that is reflected by different planes must travel with a path length difference equal to an integer number of wavelengths. Therefore:

$$(AB + BC) = 2d_{hkl}sin\theta = n\lambda \qquad \text{Eqn 2.5}$$

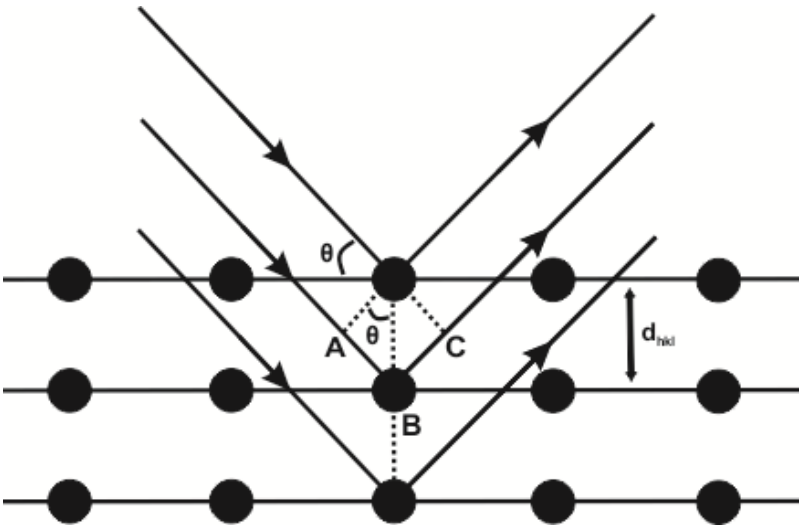


Figure 2.3: The Bragg scattering of monochromatic radiation by a 3D crystal lattice.

As angles are scanned, a diffraction pattern is recorded with peaks which correspond to various values of 2θ, which in turn relate to specific values of d_{hkl}. These *d*-spacings correlate to the planes of lattice points in the structure where there is constructive interference and the specific values relate to the specific interplanar distances. These values therefore give information about the translational periodicity of the atoms within the structure. Peaks can be indexed by assigning the Miller indices (*hkl*) to them, which lead to the determination of lattice parameters and symmetry within the structure, by considering their *d*-spacing values and assessing any systematic absences, respectively. The intensities of Bragg reflections I_{hkl} in a diffraction pattern are related to a structure factor F_{hkl} by:

$$I_{hkl} \propto |F_{hkl}|^2 \qquad \text{Eqn 2.6}$$

Where the structure factor F_{hkl} is due to waves scattered in the $2\theta_{hkl}$ direction by all atoms in the unit cell, and is given by:

$$F_{hkl} = \sum_{n=1}^{N} f_n(\theta)[\cos 2\pi (hx_n + ky_n + lz_n)]q + i\sum_{n=1}^{N} f_n(\theta)[\sin 2\pi (hx_n + ky_n + lz_n)]q \qquad \text{Eqn 2.7}$$

Where *N* is the number of atoms in the unit cell, $f_n(\theta)$ is the atomic scattering factor for atom *n*, *q* is the Debye-Waller factor and x_n, y_n and z_n are the coordinates of atom *n* in the unit cell.

The Debye-Waller factor *q* takes into account the thermal displacement of atoms. As temperature increases, the electron density of atoms becomes more disperse and the important result of this phenomenon is that there is a fall-off in intensity of Bragg peaks as 2θ increases. The relationship between the intensity of Bragg peaks, *I*, and the scattering angle of Bragg peaks, 2θ is shown in Figure 2.4. The origin of the angular dependency is that, as the electron cloud cannot be viewed as a point scatterer relative to the wavelength of the x-ray radiation, two photons can be scattered with slightly different path lengths if they are scattered by a core electron or an outer-shell electron and the degree of destructive interference this introduces increases with increasing 2θ.

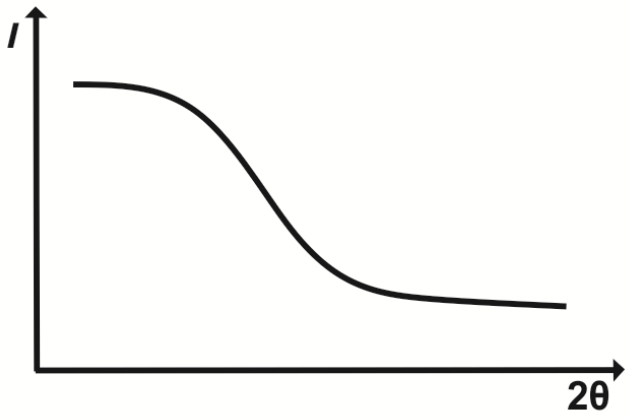


Figure 2.4: The relationship between the intensity of Bragg peaks, I, and the scattering angle of Bragg peaks, 2θ, for the scattering of x-rays during an XRPD experiment.

If the thermal displacement is treated as isotropic, then q_{iso} is given by:

$$q_{iso} = e^{\left[\frac{-8\pi^2 U_{iso} sin^2(\theta)}{\lambda^2}\right]} \qquad \text{Eqn 2.8}$$

Where U_{iso} is the isotropic temperature factor determined by experiment (or alternatively $B_{iso} = 8\pi^2 U_{iso}$).

The atomic scattering factor, $f_n(\theta)$, for an atom can be given by:

$$f_n(\theta) \propto \frac{Z}{2}[1 + \cos(2\theta)] \qquad \text{Eqn 2.9}$$

Where Z is the atomic number of the atom. The dependency of the reflection intensities on Z arises because a higher value of Z means an atom has more electrons and so scatters x-rays more strongly.

When collecting XRPD data the crystallites which make up the sample will be oriented randomly. This means that at angles where Bragg's Law is satisfied, cones of diffracted x-rays are produced (known as Debye-Scherrer cones). These are detected on a flat detector as rings, as depicted in Figure 2.5. This results in the typical intensity vs 2θ diffraction patterns used for structure refinement, where the intensities can be obtained by integrating the intensity of the whole ring or by taking a cut through the ring. The former gives higher intensities, whereas the latter produces higher resolution.

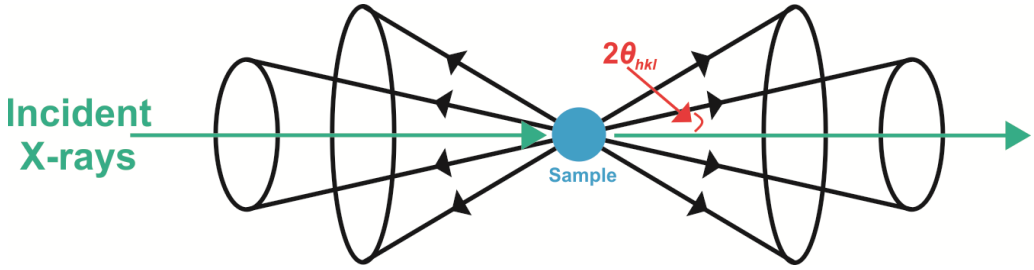


Figure 2.5: The Debye-Scherrer cones produced by diffraction of a powder sample.

A significant limitation of powder diffraction data compared to single crystal diffraction data is the loss of the phase of each reflection, where the 'phase' is the position of the wave used to describe each Bragg reflection. This is known as the phase problem and arises due to the relationship described in Eqn 2.6- the sign of F_{hkl} is unknown when analysing powder diffraction data. However, techniques such as direct methods[3] and charge-flipping[4] can be used to solve the phase problem. This problem is also solved much easier if the intensities of many independent Bragg reflections can be determined. Two ways this can be achieved is either by using very high-resolution powder diffraction (e.g. synchrotron XRPD) or using single crystal diffraction.

2.2.1.1 In-House Diffractometers

Day-to-day XRPD data were gathered on in-house x-ray diffractometers. A tungsten filament is heated to produce electrons via thermionic emission. These are then accelerated under a voltage of 40 kV towards a Cu anode, where the incident electrons collide with and eject core 1s electrons from the Cu atoms. Electrons in higher energy orbitals drop down to fill the holes and the energy lost by these electrons is emitted as x-rays with specific values of λ. K_α radiation is produced when electrons drop from L to K shells and K_β radiation is produced when electrons drop from M to K shells (where $\Delta E_\beta > \Delta E_\alpha$ and so $\lambda_\beta < \lambda_\alpha$). K_α radiation is usually the one selected for XRPD as it is much more intense than K_β radiation. There are also two types of K_α radiation- $K_{\alpha1}$ and $K_{\alpha2}$- produced because spin-orbit coupling results in two different spin states in the 2*p* orbital ($^2P_{1/2}$ and $^2P_{3/2}$). The production of these 3 types of radiation is depicted in Figure 2.6. In order to obtain monochromatic radiation, a nickel filter or energy-discriminating detectors can be fitted to remove K_β x-rays and monochromator crystals can

isolate just the $K_{\alpha 1}$ x-rays. These filters also remove the "white" Bremsstrahlung radiation (radiation emitted when a charged particle decelerates due to being deflected by another charged particle).

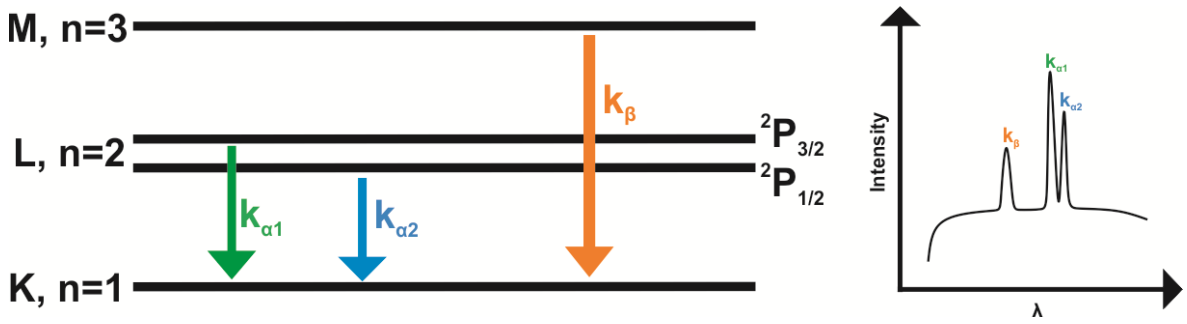


Figure 2.6: The types of x-ray radiation emitted from an in-house, Cu-anode diffractometer.

2.2.1.2 Bruker D8 Advance Eco

This diffractometer uses Bragg-Brentano geometry with a fixed sample position and a rotating incident beam and detector. The beam is produced using a Cu anode and is not monochromated, containing both $K_{\alpha 1}$ and $K_{\alpha 2}$ radiation. Although this lowers the resolution of the diffraction pattern obtained, this instrument has a relatively high x-ray intensity and the detector is able to scan a 2θ range of 3° at the same time, meaning a good signal-to-noise ratio is obtained for even short scans (~ 30 mins). This instrument also has the benefit of using a detector with energy discrimination which removes undesirable scattered radiation, such as fluorescence from atoms with an absorption edge close to the Cu K_α wavelength. The data were useful for determining phase purity and the identity of any impurity phases.

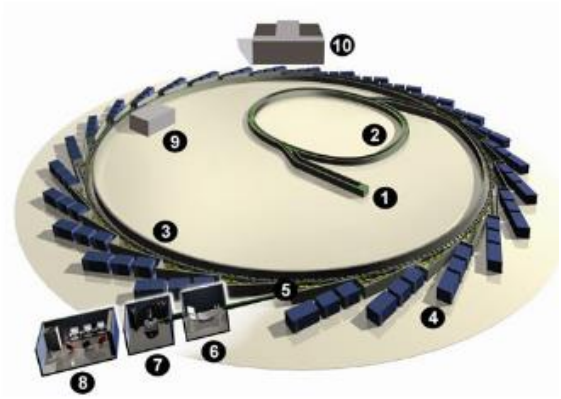
2.2.1.3 Malvern Panalytical Empyrean Alpha 1

This diffractometer uses Bragg-Brentano geometry with a fixed incident beam and a rotating sample position and detector. The beam is produced using a Cu anode and, unlike the Bruker D8 Advance Eco, is fitted with a Ge crystal (111) monochromator, so only contains $K_{\alpha 1}$ radiation upon reaching the sample. This gives a good resolution and a more symmetrical instrumental contribution to the peak shape, and again the detector is able to scan a 2θ range of 3° at the same time, meaning a good

signal-to-noise ratio is obtained for even short scans (~ 30 mins). The data were useful for determining phase purity and the identity of any impurity phases.

2.2.1.4 Diamond Light Source

XRPD data of very high intensity and resolution were collected using the I11 beamline[5] at Diamond Light Source, pictured in Figure 2.7. This is a synchrotron radiation facility which generates intense radiation by accelerating particles around a curved path. An electron gun is used to produce electrons via thermionic emission, which are then accelerated in the linear accelerator (linac) and fed into a booster synchrotron to take their energies from MeV to GeV. These electrons with GeV energies are then fed into the main storage ring which accelerates them around a circular path using strong magnets. Kicker magnets are used to give the electrons back the energy they lose as they emit radiation when travelling around the ring. The storage ring has to be refilled every 12-24 hours to counteract the decaying electron count inside the ring, which occurs due to collisions between electrons and the very few molecules present in the very high vacuum ($< 10^{-10}$ mbar). The photon flux at the sample is around 10^{13} photons/s,[6] resulting in Bragg peaks having 10x the intensity of those recorded on an in-house diffractometer.



1) Injection System and Linac **2)** Booster Synchrotron **3)** Storage Ring **4)** Beamline
5) Front End **6)** Optics Hutch **7)** Experimental Hutch **8)** Control Cabin

Figure 2.7: Diagram of Diamond Light Source and its constituent parts.[7]

The radiation used in each beamline is produced using either bending magnets or insertion devices. When bending magnets force the electrons to follow the curvature of the path, this results in the electrons being accelerated and so radiation is emitted. Even though the storage ring is curved overall, it does contain some straight sections. In these sections, insertion devices called wigglers and undulators[8] (possessing magnets which produce magnetic fields in the path of the electron beams) are used to change the path of the electron beams so that they produce radiation.

2.2.1.5 I11 Beamline, Diamond Light Source (MAC and VT)

The I11 beamline[5] is used for high-resolution XRPD. The x-ray beam that is incident on samples originates from an in-vacuum undulator (IVU) insertion device and this is monochromated using a double-bounce Si (111) monochromator, with higher energy harmonic waves removed using harmonic rejection mirrors. The beam is very intense and has an x-ray wavelength of 0.82 Å. Samples are diluted using amorphous ground glass to reduce beam absorption and preferred orientation and sealed inside borosilicate capillaries (or quartz capillaries for high T measurements) using a blow torch. This capillary is glued onto a brass holder, which is loaded onto the sample stage by a robotic arm inside the experiment hutch.

There are two different detectors utilised for different experiments- the MAC and the PSD detector. The Multi-Analyser Crystal (MAC) detector is used for collecting data with extremely high resolution and very good signal-to-noise ratio. It has 9 Si (111) analyser crystals on each of its 5 arms and by rotating through just 40° this detector is able to scan a 2θ range of 5-150° with overlap between neighbouring detectors. The position-sensitive detector (PSD) is used for collecting variable temperature data, with a good resolution but lower than that of the MAC detector. Its 90° aperture allows it to collect diffraction patterns fast (in a few seconds) but still with a higher resolution than on a lab diffractometer and good signal-to-noise ratio despite the lack of analyser crystals to remove fluorescence.

2.2.2 Neutron Powder Diffraction (NPD)

Like x-rays, neutrons are diffracted by crystalline solids[9] as they too have a wavelength comparable to the distances between the atoms. Neutrons interact with the nuclei of atoms (rather than electrons, which is the case for x-rays) and this results in a seemingly random trend of scattering length across the periodic table. An advantage of neutron scattering over x-ray scattering is that atoms which are close in atomic number can sometimes be distinguished and also atoms of low atomic number can be detected, both of which are a consequence of the lack of trend in scattering ability with the atomic number, *Z*. The form factor does not decrease in angle as the x-ray form factor does, because now the size of the scattering object (the nucleus) is much smaller than the waves being diffracted (the neutrons) and so the nucleus acts as a point scatterer.

Neutrons can be utilised to probe the magnetism of solids, as well their nuclear structure, because they are spin-$\frac{1}{2}$ particles which interact with magnetic moments of atoms. Analogous to the way in which x-rays and neutrons are diffracted by the long-range ordering of atoms, giving rise to Bragg reflections at specific *d*-spacings, the long-range ordering of magnetic moments also diffract neutrons to give rise to magnetic Bragg peaks. The magnetic scattering of neutrons is only dependent on component of the moment which lies perpendicular to the wavevector transfer, Q. The upshot of this is that long-range ordered magnetic moments give rise to intensity on reflections which are indexed perpendicular to the moment direction. Neutrons are diffracted by a magnetic lattice by an amount proportional to the square of the magnitude of the ordered magnetic moment. The form factor once again falls off as angle increases, like for XRPD, because the scatterer is again the electron cloud. The fall off is even more drastic for the magnetic form factor, however, as only the valence electrons affect the scattering of the neutrons whereas valance and core electrons affect the scattering of x-rays. There are two types of neutron scattering facilities: nuclear reactor sources and spallation sources.

2.2.2.1 WISH, ISIS

The WISH instrument[10] uses neutrons generated from a spallation source. H^- ions are accelerated, ionised to protons, sent around a synchrotron and finally directed at a tungsten target, resulting in the production of neutrons. At ISIS, proton bunches with a 50 Hz frequency are sent towards two target stations. Target Station 1 (TS1) receives 4/5 of the proton pulses and Target Station 2 receives every 5th pulse. The neutrons produced are slowed down using various moderators appropriate to the instruments which receive neutrons from each moderator (WISH uses a methane moderator) and this white beam is directed towards samples on each instrument. The scattering of the neutrons from each pulse are detected in time-of-flight (ToF) experiments. The neutron λ is related to the ToF:

$$\lambda = \frac{h}{p} = \frac{h}{m_n v} = \frac{h}{m_n}\frac{ToF}{d} \qquad \text{Eqn 2.10}$$

Where *h* is the Planck constant, *p* is momentum, m_n is the mass of the neutron, *v* is the neutron velocity and *ToF* is the time of flight of the neutron along the fixed path length, *d*. The *d*-spacings are investigated here by fixing the angle of the detector, θ, but varying the incident λ by using a white beam with neutrons of varying velocities.

WISH (WIde angle in a Single Histogram) has very high resolution at long *d*-spacings, which makes it ideal for probing large nuclear and magnetic unit cells. The ^{3}He detectors (^{3}He is a strong neutron absorber) are arranged around the sample with 5 detectors on each side, covering scattering angles of 10° to 170°, as depicted in Figure 2.8. The pairs of detectors which cover the same range of angles are coupled together when analysing the data (banks 1_10, 2_9, 3_8, 4_7, 5_6) and refinements are typically carried out using all 5 pairs of banks simultaneously. High-resolution data can be gathered for *d*-spacings of 0.7-17 Å. The resolution, $\Delta d/d$, is effectively constant for all *d*-spacings, which is an advantage of WISH over a single wavelength instrument (e.g. D2B, section 2.2.2.2) where the resolution is relatively poor at longer *d*-spacings.

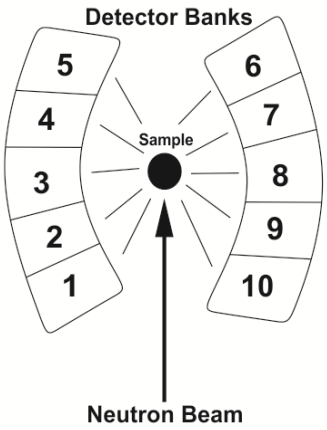


Figure 2.8: Simplified diagram of the WISH instrument setup.

The resolutions of different ToF diffractometers, *R*(*d*), can be compared by evaluating the width of a certain reflection, Δd, divided by the *d*-spacing value of that reflection:

$$R(d) = \frac{\Delta d}{d} = \sqrt{\Delta\theta^2 cot^2\theta + \left(\frac{\Delta t}{t}\right)^2 + \left(\frac{\Delta L}{L}\right)^2} \qquad \text{Eqn 2.11}$$

Where $\Delta\theta$ is the uncertainty in the diffracted angle θ, Δt is the uncertainly in the time-of-flight *t* and ΔL is the uncertainty in the neutron flight path *L*. This dependency on the scattering angle, θ, means that higher resolution is obtained at higher angles, however a detector bank placed at around 90° gives a good compromise between resolution and *d*-spacing range, which is why bank 3_8 (average 2θ = 90°) is the bank shown in this thesis. WISH data were collected by Dr. Pascal Manuel.

2.2.2.2 D2B, ILL

The D2B instrument[11] uses neutrons generated from a nuclear reactor source. The controlled fission of ^{235}U is the process which releases the neutrons, which are then all slowed down to similar speeds using heavy-water moderators and then finally the resultant white beam is highly-monochromated using a germanium crystal (115) at a high take-off angle of 135° so that high resolution data can be obtained. 128 ^{3}He detectors, spaced at intervals of 1.25°, cover scattering angles of 4° to 160°. The experiment setup is illustrated in Figure 2.9. A shorter 1.59 Å wavelength can be used to focus on shorter *d*-spacings (crystal structure analysis) and a longer 2.39 Å wavelength can be used to focus on longer *d*-spacings (magnetic structure analysis). All data in this thesis were collected at 1.59 Å to allow

for analysis of crystal and magnetic structure, where further magnetic structure analysis was performed using D1B (section 2.2.2.3).

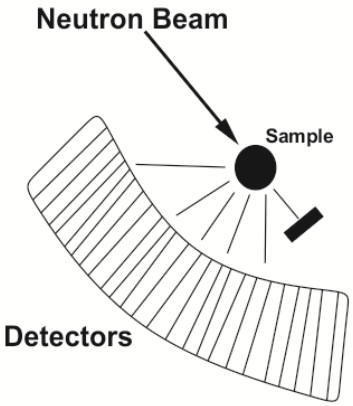


Figure 2.9: Simplified diagram of the D2B instrument setup.

The resolutions of different constant wavelength diffractometers, σ^2, can be compared by evaluating the square of full width at half maximum of a certain reflection, FWHM^2, divided by a constant:

$$\sigma^2 = \frac{FWHM^2}{8ln2} = Utan^2\theta + Vtan\theta + W \qquad \text{Eqn 2.12}$$

Where the parameters U, V and W are influenced by instrumental factors, as well as the sample being measured. This is known as the Caglioti function.[12] D2B data were collected by Dr. Stanislav Savvin.

2.2.2.3 D1B, ILL

The D1B instrument[13] is another based at the ILL and is useful for variable temperature NPD. The white beam is highly monochromated using a germanium crystal (311) at a take-off angle of 44.22° for high resolution data collection over short scans of 1-5 minutes. The high neutron flux coupled with a multidetector containing 1280 ^{3}He cells allows for the collection of diffraction patterns with good counting statistics over such a short collection time. The instrument uses a neutron wavelength of 2.52 Å to obtain a high spatial resolution at long *d*-spacings (FWHM at 2θ = 10° is around 0.3° whereas at 2θ = 100° is around 1.4° using a certain 5mm diameter sample[14]) and so is tailored towards magnetic structure analysis, where data can be gathered from 1.5 K to 300 K in 1 K steps over 3-5 h. D1B data were collected by Dr. Stanislav Savvin.

In order to compare the data collected on D1B and D2B, the (011) nuclear Bragg peak of Ba_2FeSbS_5 measured on each of these instruments is shown in Figure 2.10. Note that both peaks are plotted so as to cover a 2° range of 2θ values. At these low angle (high *d*-spacing) values, the FWHM is smaller for the sharper peak measured on D1B than D2B, illustrating how the resolution is greater on D1B in this 2θ range. The intensity of the peak measured on D1B is much greater than that measured on D2B, owing to the much higher neutron flux of D1B compared to D2B.

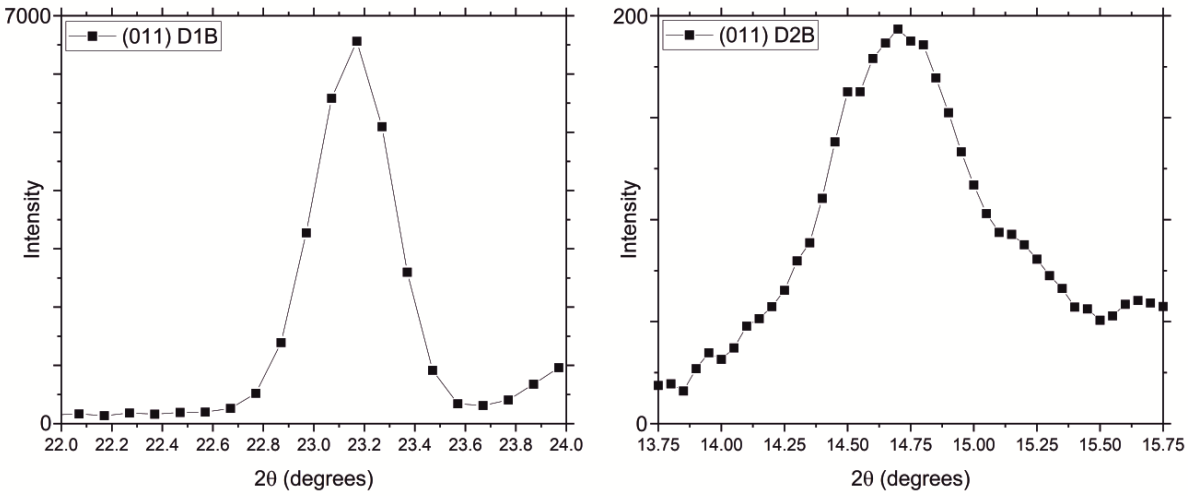


Figure 2.10: Comparison of the (011) nuclear Bragg peak of Ba_2FeSbS_5 (studied in Chapter 6) measured on the D1B (left) and D2B (right) instruments at the ILL. It is clear that the low angle peaks measured on D1B are of higher resolution and higher intensity compared to those measured on D2B.

2.2.3 Rietveld Refinement

Analysis of powder diffraction data can be performed using a Rietveld refinement.[9] This is a least-squares refinement of a preliminary structural model against experimental data. It is not a solution technique and the phase problem is avoided by supplying a satisfactory starting model. This starting model, which should be a good approximation to avoid refinement to a local minimum rather than the global minimum, is input with variables which are refined using a least-squares minimisation to values that result in the best match between the calculated pattern and the observed pattern. The calculated intensity, y_{ci}, at point *i* in a diffraction pattern is determined by a number of factors:

$$y_{ci} = s \sum_{hkl} L_{hkl} P_{hkl} A |F_{hkl}|^2 \Phi(2\theta_i - 2\theta_{hkl}) + y_{bi} \qquad \text{Eqn 2.13}$$

Where *s* is a scaling factor, L_{hkl} is the Lorentz polarisation factor, P_{hkl} is the preferred orientation, *A* is the absorption factor, F_{hkl} is the structure factor, Φ is the reflection profile function and y_{bi} accounts for the background at point *i*. These factors all affect the intensity of a reflection. The residual fuction, S_y, gives the difference between the observed and calculated diffraction patterns:

$$S_y = \sum_i w_i (y_i - y_{ci})^2 \qquad \text{Eqn 2.14}$$

Where w_i is the normalisation factor, y_i is the observed intensity and y_{ci} is the calculated intensity. The quality of the refinement is quantified by R-factors, such as R_{wp}:

$$R_{wp} = \sqrt{\frac{\sum_i w_i (y_i - y_{ci})^2}{\sum_i w_i y_i^2}} = \sqrt{\frac{S_y}{\sum_i w_i y_i^2}} \qquad \text{Eqn 2.15}$$

R_{wp} can be compared to the statistically expected value, R_{exp}:

$$R_{exp} = \sqrt{\frac{N_{obs} - N_{var}}{\sum_i w_i y_i^2}} \qquad \text{Eqn 2.16}$$

Where N_{obs} and N_{var} are the number of observables and refined variables respectively. This means that the goodness-of-fit parameter, χ, is the ratio between the obtained and expected R-values:

$$\chi = \frac{R_{wp}}{R_{exp}} = \sqrt{\frac{S_y}{N_{obs} - N_{var}}} \qquad \text{Eqn 2.17}$$

The TOPAS Academic software[15] was used in refinements against all XRPD and NPD data in this thesis.

For assessing possible magnetic modes and structural displacement modes, the ISODISTORT software[16] was also incorporated. When studying a symmetry-lowering transition, such as the ordering of magnetic moments or the distortion of the crystal structure, one must consider all the distortion symmetries available to the parent structure. This software uses both crystallography and group-theory in order to determine the possible parameters (called 'modes') which are available to this superstructure which has been derived from the original, undistorted parent structure. These 'modes' can then be refined against XRPD and NPD data, using the TOPAS Academic software,[15] to predict the most likely nature of the distortion. One crucial point to highlight is that chemical intuition should also play a role when deciding the most likely nature of the distortion, as the model which best fits the diffraction data may not be chemically viable.

2.2.4 SQUID Magnetometry

An in-house Quantum Design MPMS-3 SQUID magnetometer was employed to measure the magnetisation of samples. A Superconducting QUantum Interference Device (SQUID)[17,18] is a closed ring with two Josephson junctions (two superconducting materials separated by a thin, insulating material) which is used to measure magnetic fields by detecting changes to the voltage across the junctions. When a small current is applied across these junctions, Cooper pairs of electrons tunnel through the insulating material with zero resistance, however a resistance and a voltage across the junction will arise if the critical current is exceeded. Any applied magnetic field will affect this critical current and so the voltage across the junction relates to changes in the applied magnetic field. When the sample moves through an induction coil, it generates a current in the coil which is used by the SQUID to give the magnetic moment of the sample.

When the sample is in the presence of an external field *H*, supplied by He-cooled superconducting magnets, a magnetic induction *B* arises in the material:

$$B = H + 4\pi M \qquad \text{Eqn 2.18}$$

Where M is the magnetisation of the material. The molar magnetic susceptibility χ_{mol} is defined as:

$$\chi_{mol} = \frac{M}{B_0 n} \qquad \text{Eqn 2.19}$$

Where B_0 is the applied magnetic flux and n is the number of moles of material present.

For the measurement, around 20-30 mg of material was accurately weighed and placed inside a gelatine capsule. This capsule was secured inside a plastic straw using other gelatine capsules, diamagnetic tape and a plastic plug. Holes were made in the straw and capsules so that air could be removed from them (O_2 is paramagnetic and gives signals in this highly sensitive SQUID setup). Finally, the straw was lowered into the SQUID on the end of a rod so that a purge/seal routine could be performed, the sample centred in the instrument and the measurement carried out.

2.2.4.1 DC SQUID Magnetometry

Zero-Field Cooled (FC) and Field Cooled (FC) measurements were performed to help identify magnetic transitions and deduce the magnetic behaviour of samples over a given low temperature range. The sample was cooled down to a base temperature (usually 2 K or 5 K) either in no field (ZFC) or in a field of 100 or 1000 Oe (FC) and then the magnetisation measured as a function of temperature upon warming, with a field of 100 or 1000 Oe applied to the sample. Variable temperature hysteresis loops (isotherms of M vs H) were also performed by cooling the sample in a field of 7 T and then measuring from 7 T to -7 T and then back up to 7 T.

Magnetisation of the sample against field, from 0-7 T, was measured to observe the behaviour of the magnetisation of the sample with changing field, as well as assess if any paramagnetic or ferromagnetic impurities were present, which would be indicated by a sharp rise in magnetisation at low fields before a shallower, steady gradient up to higher fields as illustrated in Figure 2.11.

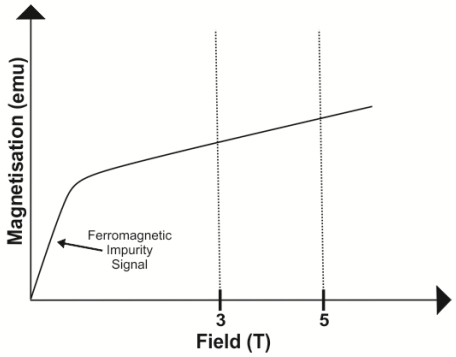


Figure 2.11: M vs H curve for an antiferromagnetic material with a ferromagnetic impurity.

If this indicated the presence of such impurities, measurement of the magnetisation at 3 different fields well above the paramagnetic or ferromagnetic regime (3 T, 4 T, 5 T in the case of this thesis) was performed in order to deduce the susceptibility at each temperature- the gradient of the magnetisation against field:

$$\chi_{mol} = \frac{M(H_2) - M(H_1)}{(H_2 - H_1)n} \qquad \text{Eqn 2.20}$$

Where *M(H)* is the magnetisation at a certain field *H* and *n* is the number of moles of material measured. The gradient between each pair of field values was calculated and an average taken for the value of the molar susceptibility at each temperature. It should be enough to measure the magnetisation of the sample at two fields for this calculation, as the change in magnetisation with field should be truly linear in this region, however three fields were used in this thesis to improve the reliability of the analysis.

High temperature magnetisation vs temperature measurements were performed by securing a piece of material (cut off from a pressed pellet) to a temperature-controlled heater stick using Zicar cement. Copper foil was then wrapped around the sample to reduce radiative heat loss. During the measurement, the sample chamber was kept under a higher vacuum than for low temperature operation, in order to reduce heat transfer away from the sample via exchange gas. The magnetisation was measured as the sample was warmed up from room temperature (ZFC-like) and then as the sample was cooled back down to room temperature immediately after (FC-like), all in a field of 100 Oe.

2.2.5 Electron Microscopy

Electrons interact with the atoms in a sample mainly via Coulombic forces and when an electron beam is fired at the sample the electron scattering factor f_e is given by:

$$f_e(\theta) \propto Z - f_x \qquad \text{Eqn 2.21}$$

Where Z is the charge of the nucleus and f_x is the extent of shielding by the electron density around the nucleus. There are two different types of electron microscopy[19] measurement: Scanning Electron Microscopy (SEM) and Transmission Electron Microscopy (TEM). SEM measures the x-rays and electrons emitted when the electron beam interacts with the sample, creating a magnified image and detecting the different elements in the process. TEM measures the electrons from the electron beam that are transmitted through the sample, which can be used to create a much more magnified image of the sample (down to the atomic level) and to obtain diffraction patterns.

2.2.5.1 Selected Area Electron Diffraction (SAED) and Tomography

Selected Area Electron Diffraction (SAED) gathers diffraction images of specific directions along the crystal using TEM. By indexing the diffraction spots and analysing the reflection conditions, one can determine the possible space group symmetries for a system. Collecting many SAED patterns by tilting the crystal over a range of angles gives rise to tomography images which help in the analysis of reflection conditions, and increasingly enable structure solution. The electron diffraction patterns were collected by Prof. Joke Hadermann and Dr. Maria Batuk at the Electron Microscopy for Materials Science (EMAT) institute, University of Antwerp, Belgium. A Tecnai TEM was used, operating at 200 kV. Samples were ground in ethanol and a few drops were deposited onto a copper grid covered by a holey carbon layer.

2.2.5.2 Energy Dispersive X-Rays (EDX)

This technique uses TEM or SEM to image crystals, map the distribution of the different elements and collect spectra which give the relative atomic percentages of the elements on the surface of the

crystals. Core electrons in the atoms are ejected when the electrons from the beam in the instrument collide with them, resulting in an electron dropping down from a higher energy shell to fill the vacancy. This is shown in Figure 2.12. The spectrum of the emitted X-rays is specific to the elements and their ratio in the sample. EDX was performed by Daphne Vandemeulebroucke at the Electron Microscopy for Materials Science (EMAT) institute, University of Antwerp, Belgium.

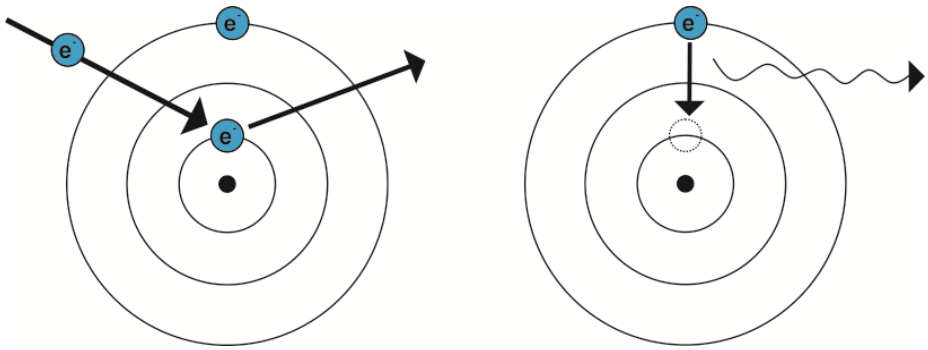


Figure 2.12: Diagrams showing the principle behind EDX spectroscopy.

2.2.6 X-ray Absorption Near Edge Spectroscopy (XANES)

X-ray Absorption Spectroscopy (XAS)[20] focusses on the sharp change in the degree of absorption by an element at a photon energy equal to the energy needed to excite a core electron to the first excited state. This is the absorption edge and is known by different names depending on the principle quantum number of the shell from which the excited electron originates (K-edge when n=1, L-edge when n=2, M-edge when n=3). X-ray Absorption Near Edge Spectroscopy (XANES) specifically considers the position of this edge, as highlighted in Figure 2.13. The position for a certain element and a certain edge can be influenced by the oxidation state and coordination environment of the atoms.

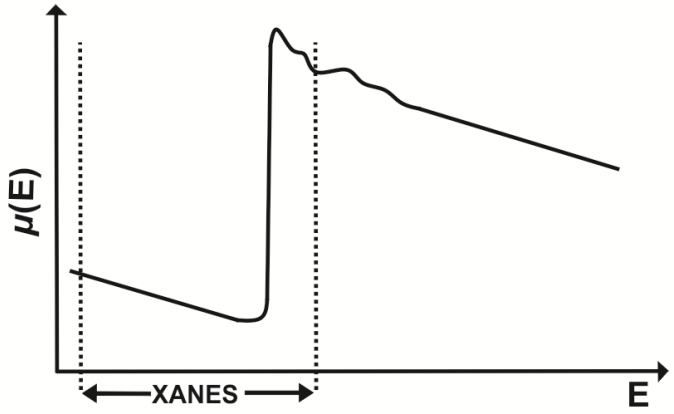


Figure 2.13: Typical XANES edge measured during an XAS experiment.

2.2.6.1 B18 Beamline, Diamond Light Source

The B18 instrument[21] is used for XAS and the XANES data presented in this thesis were collected by our collaborator on the instrument, Dr Giannantonio Cibin. The beam travels through a collimating mirror, a Si (311 and 111) monochromator and finally a focussing mirror, before reaching the sample. It has an energy range of 2.05-35 keV. 20 mg of sample was ground together with 80 mg of cellulose in order to dilute the sample and reduce beam absorption. This was pressed in a 13 mm pellet die to produce a thin pellet, which was then taped onto a plastic grid using diamagnetic tape. The K-edge of Fe was then measured on the instrument. The data files were calibrated using an Fe foil standard.

2.2.7 X-Ray Photoelectron Spectroscopy (XPS)

The XPS technique[22] probes the ions on the surface of crystals. X-rays of a known λ are fired at the sample and then electrons are emitted from the atoms on the surface of the sample having absorbed the energy of the incident photon. The kinetic energy of these electrons is recorded and, due to the conservation of energy in this process, the binding energy of those electrons emitted can be calculated:

$$E_{binding} = E_{photon} - (E_{kinetic} + \Phi) \qquad \text{Eqn 2.22}$$

Where $E_{binding}$ is the binding energy of the detected electron, E_{photon} is the energy of the incident x-rays, $E_{kinetic}$ is the recorded electron kinetic energy and Φ is a correction factor for the instrument setup. The binding energy will depend not only on the identity of the atom and the orbital the electron originated from, but will also be affected by the oxidation state and coordination environment of the atom. In terms of Fe, which is the element studied using XPS in this thesis, high spin Fe^{2+} and Fe^{3+} produce multiplets whereas low spin Fe^{2+} produces a singlet in the $2p_{3/2}$ spectra.[23] Typical examples of these spectra are shown in Figure 2.14. The photoemission process caused by the incident x-rays is accompanied by valence electron redistribution- which is the origin of the multiplet signals- however this does not happen when there are no unpaired electrons (i.e. low spin Fe^{2+}). Unfortunately, the peaks arising from high spin Fe^{2+} and high spin Fe^{3+} can overlap to a high degree and can therefore be difficult to distinguish. XPS measurements were performed on a Thermo k_α spectrometer by Prof. Robert Palgrave at University College London. Powder samples were attached to the sample stage using carbon tape and a dual beam flood gun was used for charge compensation.

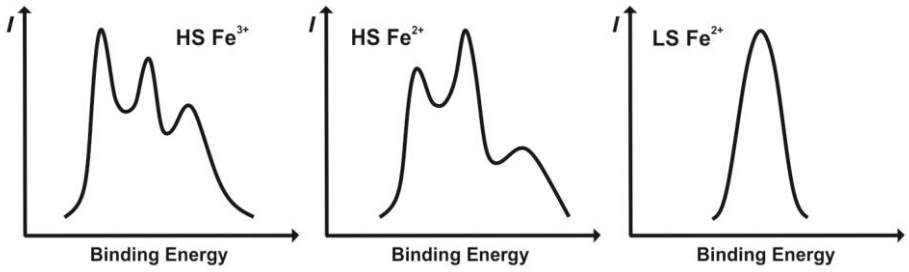


Figure 2.14: Typical $2p_{3/2}$ XPS spectra for different Fe electron configurations.

2.2.8 Resistivity

Resistivity measurements can give an indication of the electronic behaviour of a material.[24] Figure 2.15 shows typical changes in resistivity for compounds which can be categorised as a metal, semiconductor or insulator. As a metal is warmed up, the ions vibrate more, making collisions between conduction electrons and these ions more probable as the electrons travel through the lattice. When a semiconductor is heated, more electrons have the energy needed to be promoted to the conduction band from the valence band and so resistivity decreases. Temperature has very little effect on strongly insulating materials. Variable temperature resistivity measurements can be important when studying a magnetic transition because both magnetic and electronic properties are determined by the behaviour of electrons in the material. One might expect that when the magnetic moments on transition metals undergo a long-range ordering transition, the electrons in the material become more localised and so the compound may simultaneously undergo a metal to insulator transition.

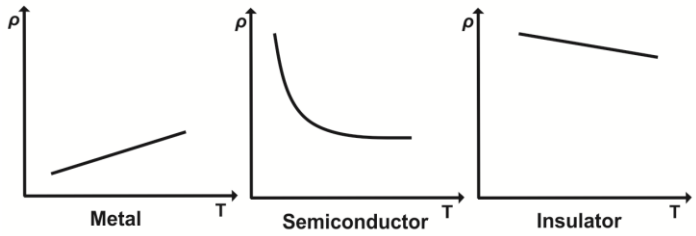


Figure 2.15: General behaviour of resistivity vs T for different classes of materials.

Resistivity measurements were performed on a small piece of a sintered pellet, using the 4-probe setup depicted in Figure 2.16 and data collected on a Quantum Design PPMS with the help of Dr Dharmalingam Prabhakaran in the Oxford University Physics Department.

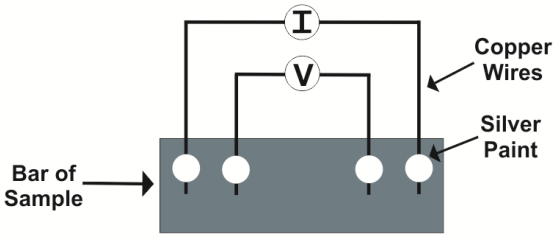


Figure 2.16: The 4-probe setup used to measure the resistivity of samples in a PPMS.

2.2.9 Specific Heat Capacity

Formally the specific heat capacity, C_p, of a material is the amount of energy needed to raise its temperature. The Einstein[25] and Debye[25,26] models of solids are used when considering the specific heat capacity of lattice vibrations. The Einstein model treats the vibrating atoms in a solid as quantum harmonic oscillators, whereas the Debye model couples these individual harmonic oscillators and approximates them as phonons in a box. The Debye model is slightly superior and the result is that heat capacity is proportional to T^3, which agrees with experimental data very well at low values of T.

Any deviations away from the heat capacity due to the lattice vibrations tend to be due to structural or magnetic transitions. The enthalpy and entropy changes during these transitions can be calculated using the following integrals:

$$\Delta H = \int_{T_1}^{T_2} C_p \, dT \qquad \text{Eqn 2.23}$$

$$\Delta S = \int_{T_1}^{T_2} \frac{C_p}{T} \, dT \qquad \text{Eqn 2.24}$$

Where, in these cases, the areas under the curve are taken with the lattice vibration contribution subtracted, as illustrated in Figure 2.17. Heat capacity measurements were performed on a small piece of a sintered pellet, secured onto a sample stage using grease and data collected on a Quantum Design PPMS with the help of Dr Dharmalingam Prabhakaran in the Oxford Physics Department.

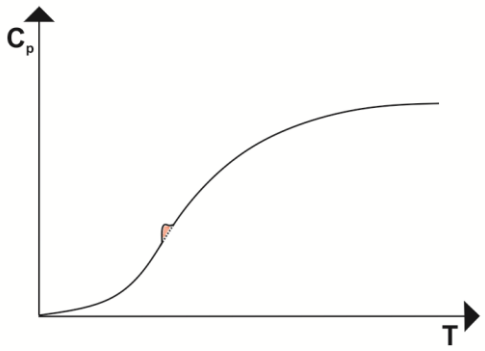


Figure 2.17: General behaviour of C_p vs T for a solid, where the red shaded area represents the enthalpy change of a structural or magnetic transition.

2.2.10 Mössbauer Spectroscopy

The Mössbauer effect[27] is the emission and absorption of radiation by an atom without any recoil and this effect is made use of in Mössbauer spectroscopy.[28] A solitary atom emitting or absorbing radiation must recoil to conserve momentum, however in the case where this atom belongs to part of an extended crystal lattice, the atom involved in emitting or absorbing radiation instead transfers its recoil energy to the rest of the lattice. This is therefore known as 'recoilless emission/absorption' as the kinetic energy is transferred from the individual atom to the surrounding crystal lattice. This effect can be used to study very subtle differences between the atoms in a solid, as different electric and magnetic fields affect the magnitudes and splitting of the orbital energy levels in these atoms.

During the experiment, γ-rays are directed at the sample and a detector measures those transmitted after travelling through the sample, as some will be absorbed by nuclei in the material being studied (in the case of this thesis, this is always ^{57}Fe nuclei). The source is accelerated over a range of velocities in order to cover a range of energies via the Doppler effect. The γ-rays will be absorbed at different velocities (energies) depending on factors such as the symmetry of the site (centre shift, CS), the distribution of charge around the nucleus (quadrupole splitting, QS) or the extent of magnetic ordering between the nuclei (hyperfine magnetic splitting, H). Typical Mössbauer spectra produced by a certain isotope when considering different orbital energy level splitting are shown in Figure 2.18. Mössbauer experiments were performed by Dr. Alex Scrimshire at Sheffield Hallam University.

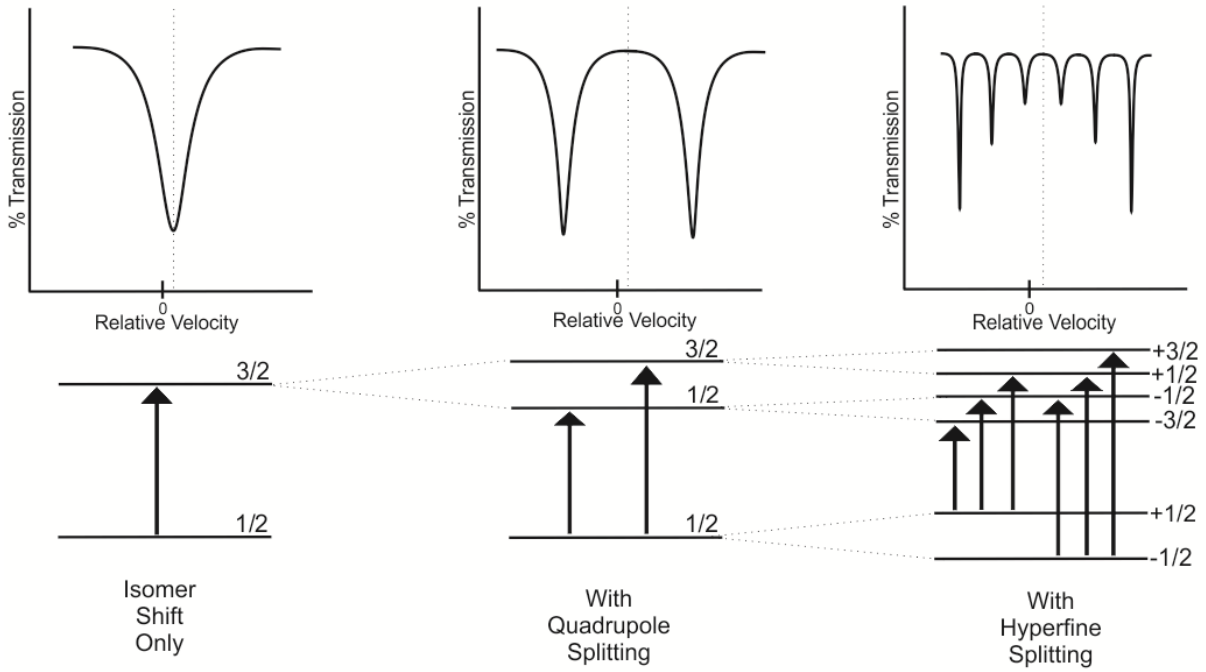


Figure 2.18: Mössbauer spectra for atoms in a sample when only the isomer shift is considered (left) and when either quadrupole splitting (centre) or hyperfine splitting (right) is also present.

2.2.11 Single Crystal X-Ray Diffraction (SCXRD)

In this type of x-ray diffraction, it is a single crystal which is mounted in the path of a monochromatic x-ray beam, as supposed to the case of XRPD where a thin layer of powder is placed in the path of the beam (as discussed in section 2.2.1). The crystal is rotated and the resulting diffraction patterns are collected by an area detector, resulting in a three-dimensional (usually a half or full sphere) set of diffraction peaks in reciprocal space. During data collection, the crystal is often cooled to low temperatures in order to gain a better signal:noise ratio by reducing the thermal motion of the atoms. The gathered set of Bragg peaks can then indexed (using the CryAlisPro[29] software for the purposes of this thesis) and the space group symmetry of the crystal determined. One advantage of SCXRD over XRPD is the measuring of the intensities of each individual Bragg reflection, therefore the problem of peak overlap in XRPD is no longer an issue in SCXRD, and so reflection conditions and subsequent space group symmetries can be obtained more reliably.

SCXRD data collection and analysis was performed by Dr. Kirsten Christensen at the Chemistry Research Laboratory, University of Oxford. Data were collected on a Rigaku Oxford Diffraction Supernova A diffractometer using Mo radiation, with the sample cooled down to 150 K.

References

(1) Sivia, D. S. *Elementary Scattering Theory: For Xray And Neutron Users*; 2011.

(2) David, W. I. F.; Shankland, K.; McCusker, L. B.; Baerlocher, C. *Structure Determination from Powder Diffraction Data (International Union of Crystallography Monographs on Crystallography, 13)*; 2002.

(3) Hauptman, H. The Direct Methods of X-Ray Crystallography. *Science (80-.).* **1986**, *233* (4760), 178–183. https://doi.org/10.1126/science.233.4760.178.

(4) Oszlányi, G.; Süt̋o, A. Ab Initio Structure Solution by Charge Flipping. *Acta Crystallogr. Sect. A Found. Crystallogr.* **2004**, *60* (2), 134–141. https://doi.org/10.1107/S0108767303027569.

(5) Thompson, S. P.; Parker, J. E.; Potter, J.; Hill, T. P.; Birt, A.; Cobb, T. M.; Yuan, F.; Tang, C. C. Beamline I11 at Diamond: A New Instrument for High Resolution Powder Diffraction. *Rev. Sci. Instrum.* **2009**, *80* (7), 879. https://doi.org/10.1063/1.3167217.

(6) *https://www.diamond.ac.uk/Instruments/Crystallography/I11/layout/specs.html*.

(7) *https://www.diamond.ac.uk/Science/Machine/Components/diamondhouse.html*.

(8) Brown, G.; Halbach, K.; Harris, J.; Winick, H. Wiggler and Undulator Magnets - A Review. *Nucl. Instruments Methods Phys. Res.* **1983**, *208* (1–3), 65–77. https://doi.org/10.1016/0167-5087(83)91105-5.

(9) Rietveld, H. M. The Rietveld Method. *Physica Scripta*. IOP Publishing August 1, 2014, p 098002. https://doi.org/10.1088/0031-8949/89/9/098002.

(10) Chapon, L. C.; Manuel, P.; Radaelli, P. G.; Benson, C.; Perrott, L.; Ansell, S.; Rhodes, N. J.; Raspino, D.; Duxbury, D.; Spill, E.; Norris, J. Wish: The New Powder and Single Crystal Magnetic Diffractometer on the Second Target Station. *Neutron News*. Taylor & Francis Group April 29, 2011, pp 22–25. https://doi.org/10.1080/10448632.2011.569650.

(11) Suard, E.; Hewat, A. The Super-D2B Project at the ILL. *Neutron News* **2001**, *12* (4), 30–33. https://doi.org/10.1080/10448630108245006.

(12) Caglioti, G.; Paoletti, A.; Ricci, F. P. Choice of Collimators for a Crystal Spectrometer for Neutron Diffraction. *Nucl. Instruments* **1958**, *3* (4), 223–228. https://doi.org/10.1016/0369-643X(58)90029-X.

(13) Orench, I. P.; Clergeau, J. F.; Martínez, S.; Olmos, M.; Fabelo, O.; Campo, J. The New Powder Diffractometer D1B of the Institut Laue Langevin. In *Journal of Physics: Conference Series*; IOP Publishing, 2014; Vol. 549, p 012003. https://doi.org/10.1088/1742-6596/549/1/012003.

(14) *https://www.ill.eu/users/instruments/instruments-list/d1b/characteristics*.

(15) Coelho, A. A. TOPAS and TOPAS-Academic: An Optimization Program Integrating Computer Algebra and Crystallographic Objects Written in C++: An. *J. Appl. Crystallogr.* **2018**, *51* (1), 210–218. https://doi.org/10.1107/S1600576718000183.

(16) Campbell, B. J.; Stokes, H. T.; Tanner, D. E.; Hatch, D. M. ISODISPLACE: A Web-Based Tool for Exploring Structural Distortions. *J. Appl. Crystallogr.* **2006**, *39* (4), 607–614. https://doi.org/10.1107/S0021889806014075.

(17) Kleiner, R.; Koelle, D.; Ludwig, F.; Clarke, J. Superconducting Quantum Interference Devices: State of the Art and Applications. In *Proceedings of the IEEE*; Institute of Electrical and Electronics Engineers Inc., 2004; Vol. 92, pp 1534–1548.

https://doi.org/10.1109/JPROC.2004.833655.

(18) Fagaly, R. L. Superconducting Quantum Interference Device Instruments and Applications. In *Review of Scientific Instruments*; American Institute of PhysicsAIP, 2006; Vol. 77, p 101101. https://doi.org/10.1063/1.2354545.

(19) Zou, X.; Hovmöller, S.; Oleynikov, P. *Electron Crystallography: Electron Microscopy and Electron Diffraction: 16 (International Union of Crystallography Texts on Crystallography)*; 2011.

(20) Yano, J.; Yachandra, V. K. X-Ray Absorption Spectroscopy. *Photosynthesis Research*. Springer November 2009, pp 241–254. https://doi.org/10.1007/s11120-009-9473-8.

(21) Dent, A. J.; Cibin, G.; Ramos, S.; Smith, A. D.; Scott, S. M.; Varandas, L.; Pearson, M. R.; Krumpa, N. A.; Jones, C. P.; Robbins, P. E. B18: A Core XAS Spectroscopy Beamline for Diamond. In *Journal of Physics: Conference Series*; IOP Publishing, 2009; Vol. 190, p 012039. https://doi.org/10.1088/1742-6596/190/1/012039.

(22) Watts, J. F.; Wolstenholme, J. *An Introduction to Surface Analysis by XPS and AES*; 2019.

(23) Grosvenor, A. P.; Kobe, B. A.; Biesinger, M. C.; McIntyre, N. S. Investigation of Multiplet Splitting of Fe 2p XPS Spectra and Bonding in Iron Compounds. *Surf. Interface Anal.* **2004**, *36* (12), 1564–1574. https://doi.org/10.1002/sia.1984.

(24) Hummel, R. E. *Electronic Properties of Materials*; 2011.

(25) Rogers, D. W. *Einstein's Other Theory: The Planck-Bose-Einstein Theory of Heat Capacity*; 2005.

(26) Debye, P. Zur Theorie Der Spezifischen Wärmen. *Ann. Phys.* **1912**, *344* (14), 789–839. https://doi.org/10.1002/andp.19123441404.

(27) Frauenfelder, H. *The Mössbauer Effect*; 1962.

(28) Adetunji, J.; Dronsfield, A. The Beginnings of Mossbauer Spectroscopy. *Educ. Chem.* **2002**, *39* (4), 97–100.

(29) Agilent, CrysAlis PRO, Agilent Technologies Ltd, Yarnton, Oxfordshire, UK, 2014.

Chapter 3

3 Synthesis and Characterisation of $Ca_2FeO_2Fe_{1.6}OS_2$

3.1 Introduction

In 2016, Zhang *et al.*[1] first reported the $Ca_2Fe_{2.6}O_3S_2$ material. It adopts the structure shown in Figure 3.1, where it hosts Fe in two layers – an oxide-rich layer (Fe1) with distorted FeO_4S_2 octahedra and a sulfide-rich layer (Fe2) with FeO_2S_4 distorted octahedra. The presence of superstructure peaks in the XRPD pattern for this material was proposed to arise from Fe vacancy ordering in the Fe2 FeO_2S_4 layer, which reportedly refined to an occupancy of 0.800(6). A possible arrangement of these Fe vacancies was suggested but was not refined against any experimental data. 1D diffuse scattering was observed in single crystal x-ray diffraction data, proposed to arise due to stacking faults in the partially occupied Fe2 FeO_2S_4 layers, which hampered their attempt at structure solution. A clear transition in the magnetic susceptibility data suggested antiferromagnetic ordering below around 77 K. It was reported to be a narrow band gap Mott insulator of particular interest because of its very short Fe-Fe distances and it was proposed by Zhang *et al.*[1] as a potential pathway material towards novel Fe-based superconductors. This chapter will progress from this initial study of the $Ca_2Fe_{2.6}O_3S_2$ material by Zhang *et al.*[1] by investigating many further measurements which build on the limited data already reported.

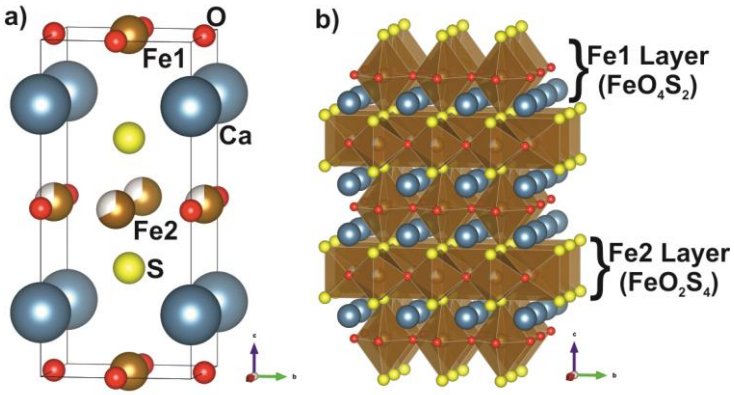


Figure 3.1: Crystal structure of $Ca_2FeO_2Fe_{1.6}OS_2$ depicting **a)** the unit cell and **b)** the alternating Fe1 and Fe2 layers. The Fe2 site is partially occupied.

3.2 Synthesis

A 3 g powder sample was made from stoichiometric amounts of CaO (Alfa Aesar 99.95 %), Fe (Alfa Aesar 99.998 %), FeO (Alfa Aesar 99.5 %) and S (Alfa Aesar 99.999 %) using traditional solid-state synthesis, heating the reagents at 900 °C for 24 h (1 °C/min ramping rate). The slow initial ramping rate was used to ensure the volatile sulfur reacted before reaching a high vapour pressure. Another 3 g batch was made by heating a mixture of the corresponding stoichiometry at 800 °C for 24 h (1 °C/min ramping rate) and then 900 °C for 24 h (10 °C/min ramping rate) with re-grinding and re-pelletising between the steps. This mixture was also further annealed at 800 °C for 80 h (10 °C/min ramping rate) to obtain single crystals.

3.3 Characterisation

3.3.1 Superstructure Determination

Deciphering the superstructure of $Ca_2FeO_2Fe_{1.6}OS_2$ was a difficult process and involved many failed attempts. The initial techniques used were transmission electron microscopy (TEM) and single crystal x-ray diffraction (SCXRD), with the idea being to assess reflection conditions from the resulting diffraction patterns in order to reveal possible space group symmetries.

The first attempt to decipher the symmetry of the supercell utilised transmission electron microscopy (TEM). Data were collected and analysed by Prof. Joke Hadermann and Dr. Maria Batuk. Diffraction patterns of a number of different zones (SAED) were collected at 300 K, as well as an electron diffraction tomography (EDT) series (see section 2.2.5.1 for an explanation of the techniques). These confirm that the supercell is indeed a $2\sqrt{2}a_{nuc} \times 2\sqrt{2}a_{nuc} \times 2c_{nuc}$ expansion of the nuclear unit cell, as claimed by Zhang *et al*.[1] The relationship between the basic unit cell and supercell is highlighted in Figure 3.2. From the reflection conditions derived, the space groups *Bmem* (space group 67) and *Bme*2/*B*2*em* (space group 39) are suggested. Structural models in these space groups give good fits to the XRPD data (an example refinement of a supercell in *Bmem* symmetry against XRPD data is given

in the Appendix A.1). However, these space groups give patterns of vacancies which seem unlikely to occur because the two formally negatively charged vacant sites are situated adjacent to one another. Examples of supercells in these symmetries are given in Figure 3.3. It should be noted that twinning is observed in the crystals measured, which can account for any violations of the reflection conditions derived.

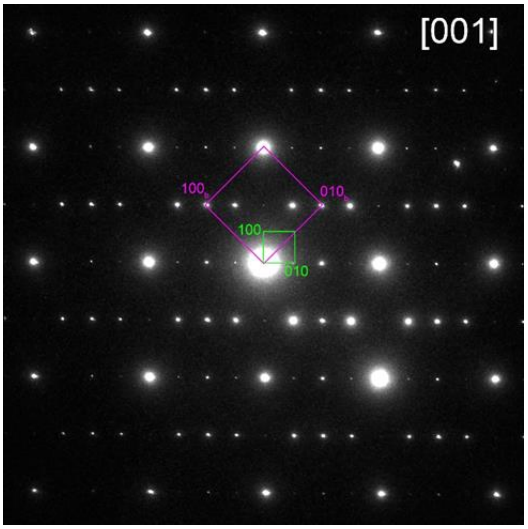


Figure 3.2: [001] zone of $Ca_2FeO_2Fe_{1.6}OS_2$ showing the relationship between the basic unit cell (pink) and supercell (green).

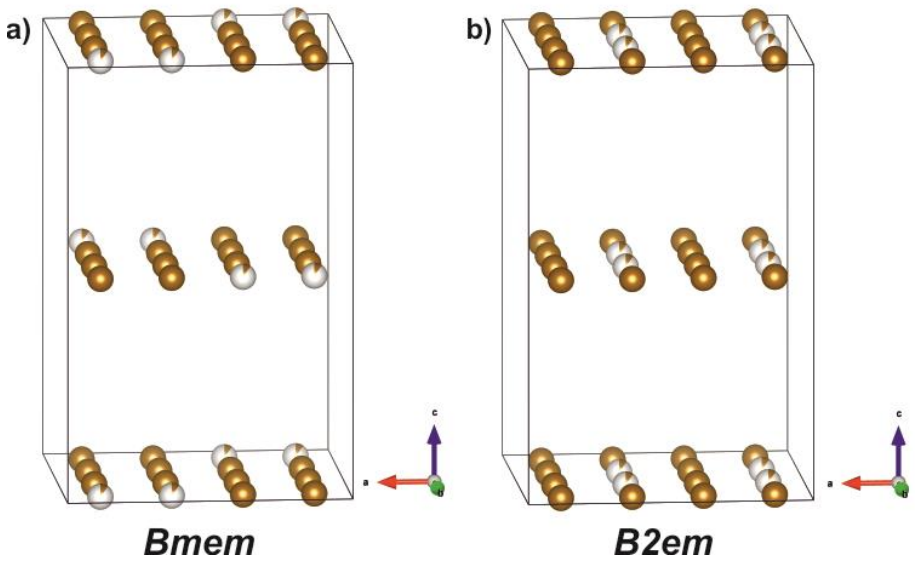


Figure 3.3: Example of the arrangement of Fe vacancies in the Fe2 layer when the symmetry imposed on the supercell is **a)** *Bmem* and **b)** *B2em*.

Some weak extra reflections, unable to be accounted for using a $2\sqrt{2}a_{nuc} \times 2\sqrt{2}a_{nuc} \times 2c_{nuc}$ expansion but able to be accounted for using a $2\sqrt{2}a_{nuc} \times 2\sqrt{2}a_{nuc} \times 4c_{nuc}$ expansion, only appear in the [112] zone (of the zones gathered in this study). This is illustrated in Figure 3.4. It is possible these are reflections from very nearby zones, as confirmed by looking at zones within a 4° tilt range to both sides. However, if these reflections are indeed from the [112] zone then this suggests the superstructure could be larger and perhaps more complex, which may also be a reason why the suggested space groups are unrealistic.

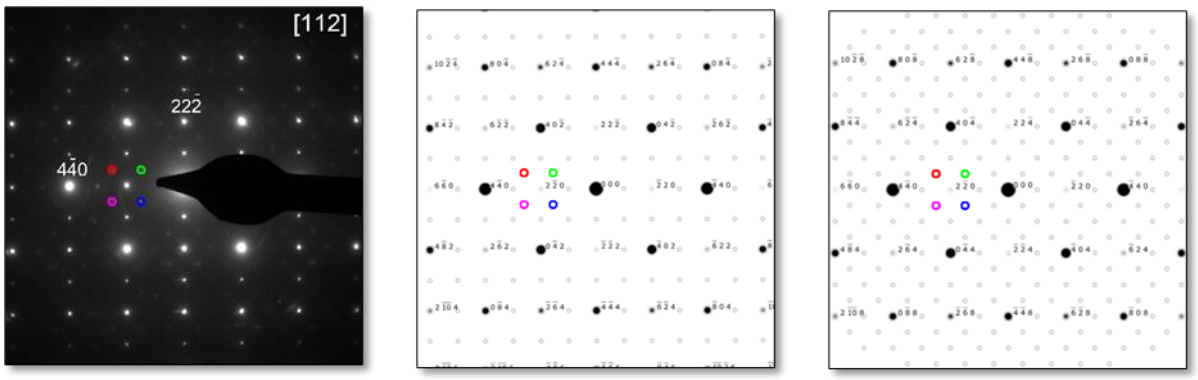


Figure 3.4: Experimental [112] zone of $Ca_2FeO_2Fe_{1.6}OS_2$ with the weak extra reflections highlighted by the small red, green, pink and blue circles (left), where the simulated patterns show the absence of these reflections for a $2\sqrt{2}a_{nuc} \times 2\sqrt{2}a_{nuc} \times 2c_{nuc}$ supercell (middle) and the presence of these reflections for a $2\sqrt{2}a_{nuc} \times 2\sqrt{2}a_{nuc} \times 4c_{nuc}$ supercell (right).

One of the annealed single crystals was taken and single crystal x-ray diffraction (SCXRD) data were gathered by Dr. Kirsten Christensen on an in-house diffractometer using Mo radiation at 150 K. The most likely space groups determined using these data are *Pnn*2 (space group 34) and *Pnnm* (space group 58). Examples of supercells in these symmetries are given in Figure 3.5. These vacancy ordering patterns do not fit the XRPD data well (an example refinement of a supercell in *Pnnm* symmetry against XRPD data is given in the Appendix A.2) and some ordering patterns, as is also the case for the ordering shown for the *B*2*em* space group in Figure 3.2, do not require a doubling of the unit cell and this further suggests they are incorrect. One interesting point is that there are no diffuse streaks in these patterns, as exemplified by the pattern shown in Figure 3.6, which are reported by Zhang *et al.*[1]

and is their reason for the determination of a space group being unsuccessful. Perhaps there are little or no stacking faults in these crystals, which is why no diffuse streaks are observed along the stacking direction (*c*-direction). However, twinning is again observed in the crystal that was measured and this adds further complications to the space group determination.

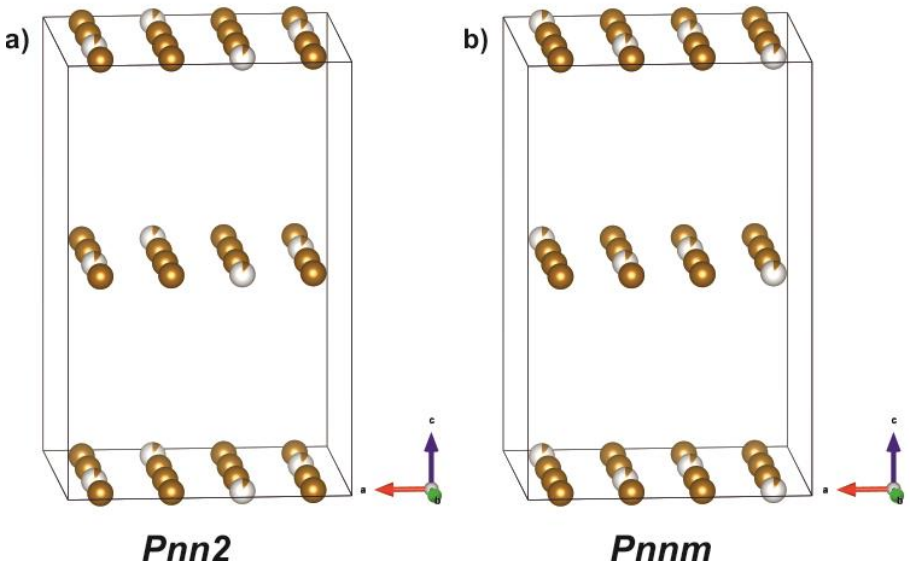


Figure 3.5: Example of the arrangement of Fe vacancies in the Fe2 layer when the symmetry imposed on the supercell is **a)** *Pnn*2 and **b)** *Pnnm*.

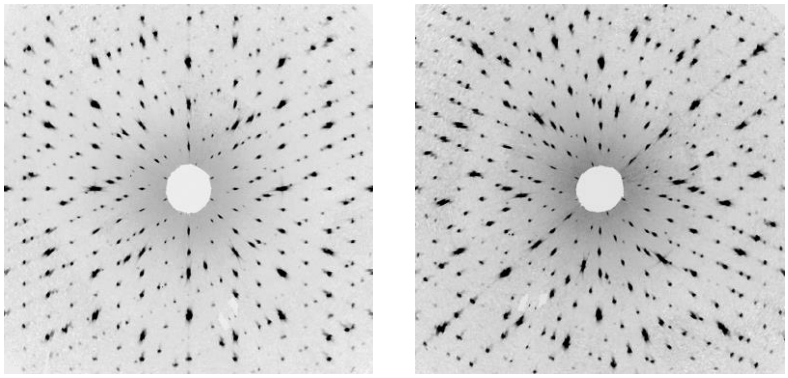


Figure 3.6: [h0l] zone (left) and [hhl] zone (right) of $Ca_2FeO_2Fe_{1.6}OS_2$ showing no obvious presence of diffuse streaks along the stacking direction (*c*-direction).

There is an obvious inconsistency between the TEM and SCXRD results which may suggest that the structure changes between 300 K and 150 K. This will be discussed later in the chapter.

Further approaches were taken to account for the ordering. Theoretically,[2] vacancies on a square-lattice favour ordering which positions the vacancies as far apart as possible and for the case where a site is 0.75 occupied (as would be relevant for $Ca_2FeO_2Fe_{1.5}OS_2$) the predicted ordering is that shown in Figure 3.7. This vacancy ordering pattern is correctly predicted for the $Sr_2MnO_2Cu_{1.5}S_2$ compound, which exhibits long-range Cu vacancy ordering below 240 K.[3] However, this arrangement gives a poor fit to the XRPD data and even though alternative arrangements arising from the relative shifting of one Fe2 layer to directly adjacent Fe2 layers results in fairly good fits to the XRPD data (an example refinement of a supercell in *P*1 symmetry, with this theoretical vacancy ordering pattern where adjacent layers are shifted by (0 ¼ 0) relative to one another, against XRPD data is given in the Appendix A.3) atoms tend to refine to positions which are unrealistically far from their starting sites.

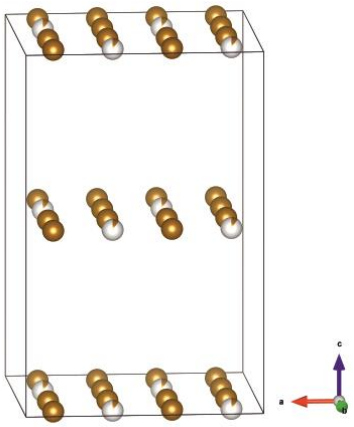


Figure 3.7: Theoretically[2] favoured arrangement of Fe vacancies in the Fe2 layer. Alternative supercells can be formed by moving the Fe vacancies in one Fe2 layer relative to the other as the theoretical ordering focusses only on ordering within the individual square-lattices.

A particular pattern of vacancies had been proposed by Zhang *et al*.[1] They had simulated a theoretical XRPD pattern from this particular ordering pattern and this matched the experimental XRPD data fairly well, although they did not take this idea further or perform a Rietveld refinement on this proposed model, so it is not entirely clear how they deduced this ordering scheme. In order to go beyond this work, a space group which can describe this ordering pattern has been deduced by evaluating the symmetry elements present in the supercell. The model refined from the XRPD data, to be detailed in section 3.3.2, is obtained.

3.3.2 Room Temperature XRPD

The crystal structure of $Ca_2FeO_2Fe_{1.6}OS_2$ was investigated at room temperature using synchrotron XRPD on beamline I11 at the Diamond Light Source. The high-resolution MAC detector was used to gather these data. All the Bragg reflections – both from the basic model and the superstructure – are accounted for. The best fit to the data, shown in Figure 3.8, is achieved using a structural model where there is long-range ordering of mostly vacant Fe sites in the Fe2 FeO_2S_4 layer accompanied by slight distortions of the fully occupied Fe sites in this Fe2 FeO_2S_4 layer within the *ab*-plane. In terms of the refinement of this model against the synchrotron XRPD data, the site occupancy factor of one of the four Fe positions in the Fe2 layer was allowed to freely refine (with the other three Fe sites in the Fe2 layer fixed as fully occupied) and the *x* and *y* coordinates for all four Fe positions in the Fe2 layer were allowed to freely refine. The model, refined from the synchrotron XRPD data in Figure 3.8, is illustrated in Figures 3.9 and 3.10.

The superstructure has *Aea*2 (space group 41) symmetry and is a $2\sqrt{2}a_{nuc} \times 2\sqrt{2}a_{nuc} \times 2c_{nuc}$ expansion of the nuclear unit cell. Alternatively, it could be described by *Aeam* (space group 64), which possesses the same systematic absences of Bragg reflections (an example refinement of a supercell in *Aeam* symmetry against XRPD data is given in the Appendix A.4). The structural models obtained by refinement of supercells with *Aea*2 and *Aeam* symmetry are almost identical (see Appendix A.5 for a comparison). The mostly vacant sites in the Fe2 FeO_2S_4 layers have an Fe occupancy of 0.091(3). A good fit to the synchrotron XRPD data can be achieved by this pattern of vacancies alone, but simultaneous refinement of one of the Fe site occupancies and Fe positions in the *x* and *y* directions results in a significantly improved fit. The displacement of the fully occupied Fe2 sites is towards the mostly vacant Fe2 sites, so it appears that the Fe atoms in these layers are relaxing towards the vacancies. It is important to note here that the supercell, although it has orthorhombic symmetry, maintains tetragonal dimensions as $a = b \neq c$ and refinement of the three lattice parameters with no constraints does not lead to a significant difference in the values of *a* and *b*. This situation also

results in the twinning which is observed in the TEM and SCXRD data and this is likely be a complicating factor in the analysis of the space group symmetry using those techniques, as previously alluded to. It is interesting to note that this vacancy ordering pattern can be reproduced by alternating the patterns found in the *Pnn*2 and *Pnnm* space groups suggested by SCXRD (shown in Figure 3.5) and it is the TEM results which suggest that face-centring should be present (i.e. the A-centring in *Aea*2).

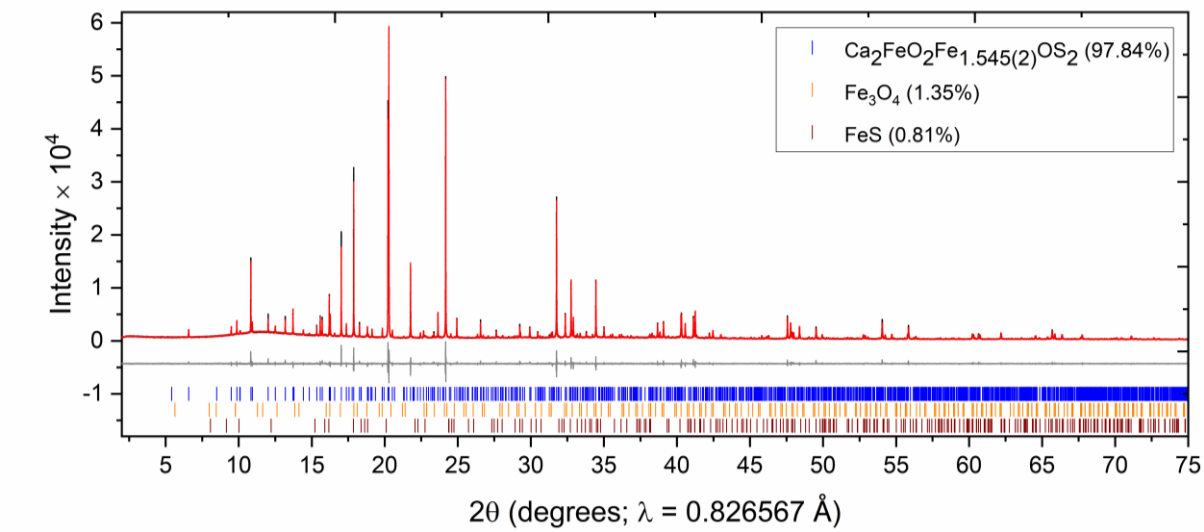


Figure 3.8: Preliminary refinement against the XRPD pattern of $Ca_2FeO_2Fe_{1.6}OS_2$ measured at 300 K on the MAC detector at I11 showing the observed (black), calculated (red) and difference (grey) curves. R_{wp}: 6.575%.

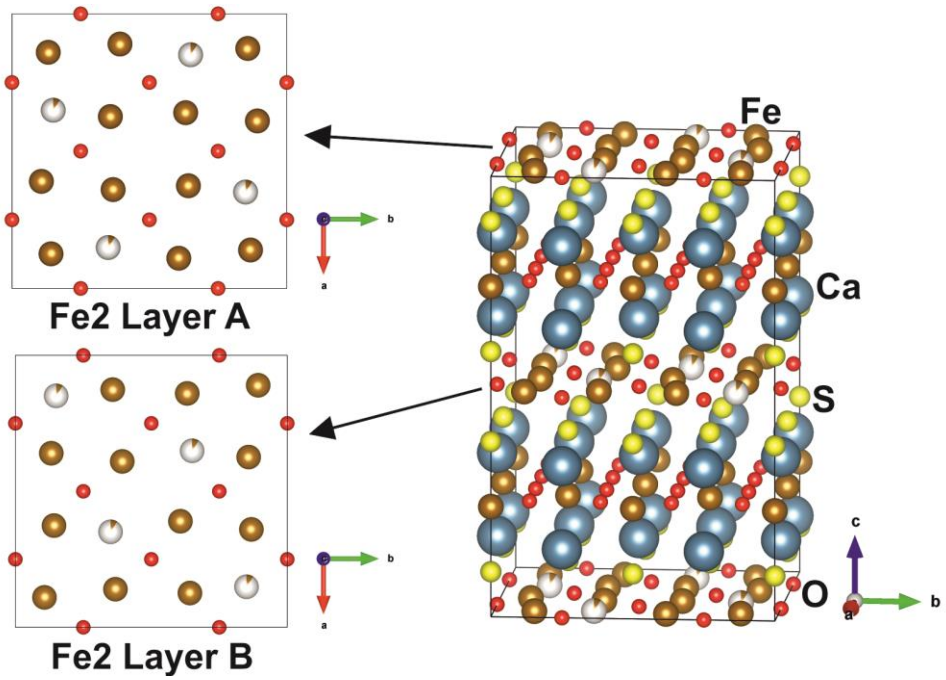


Figure 3.9: Structural model for the $Ca_2FeO_2Fe_{1.6}OS_2$ supercell, refined from the XRPD data given in Figure 3.8. The superstructure shown is a $2\sqrt{2}a_{nuc} \times 2\sqrt{2}a_{nuc} \times 2c_{nuc}$ expansion of the nuclear unit cell.

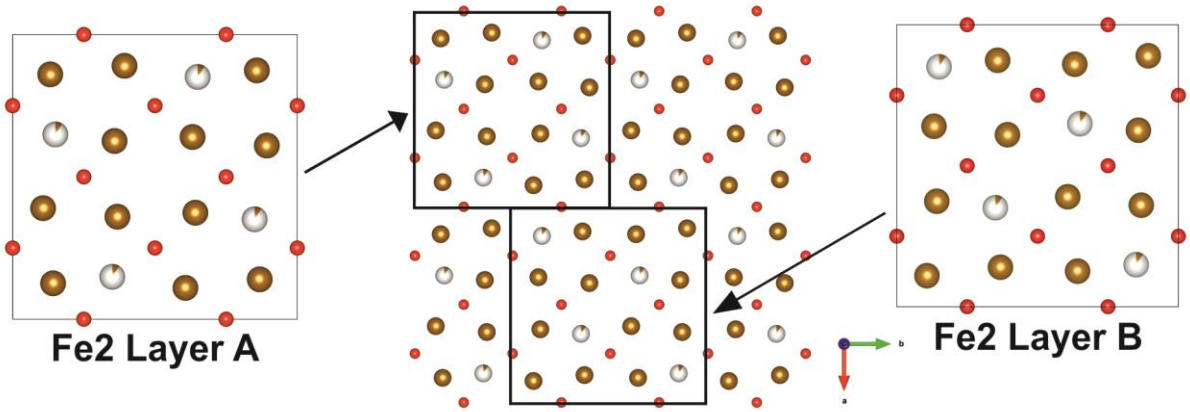


Figure 3.10: Here, one Fe2 layer has been expanded by $2a_{supercell} \times 2a_{supercell}$ to show that from this one Fe2 layer, the vacancy ordering pattern found in both Fe2 layers can be created (as highlighted by the black squares), but in the superstructure these two vacancy ordering patterns are related by (0, ½, ½) due to the A-centring (i.e. a translation of ½ in *b* relates the two black squares in the central diagram and a translation of ½ in *c* relates adjacent layers).

Figure 3.11 details the bond lengths of the FeO_4S_2 elongated octahedra in the Fe1 layer and the FeO_2S_4 compressed octahedra in the Fe2 layer. The FeO_4S_2 polyhedra are vertex-sharing, whereas the FeO_2S_4 polyhedra are face-sharing. There is also a sulfide-vertex shared between the FeO_4S_2 and FeO_2S_4 polyhedra, therefore the Fe1 and Fe2 layers are not separated, but instead are connected via an Fe-S-Fe pathway which is just over 5 Å in length.

The Fe1-Fe1 distance is 3.94648(1) Å and the shortest Fe2-Fe2 distance (considering fully occupied Fe2 sites only) is 2.93(4) Å. Zhang *et al.*[1] claim that the Fe-Fe distance plays an important role when materials lie close to the boundary between superconducting 'bad metals' and Mott- or Hund- insulators. Comparing Fe-based compounds from the literature, they show that by making the Fe-Fe distance shorter, one can push a Mott-insulator into the superconducting 'bad metal' regime. Their DFT calculations show that the vacancy-free $Ca_2FeO_2Fe_2OS_2$ is predicted to be metallic, which is likely to be a result of even shorter Fe2-Fe2 bonds from the lattice contraction when the Fe2 vacancies are completely filled.

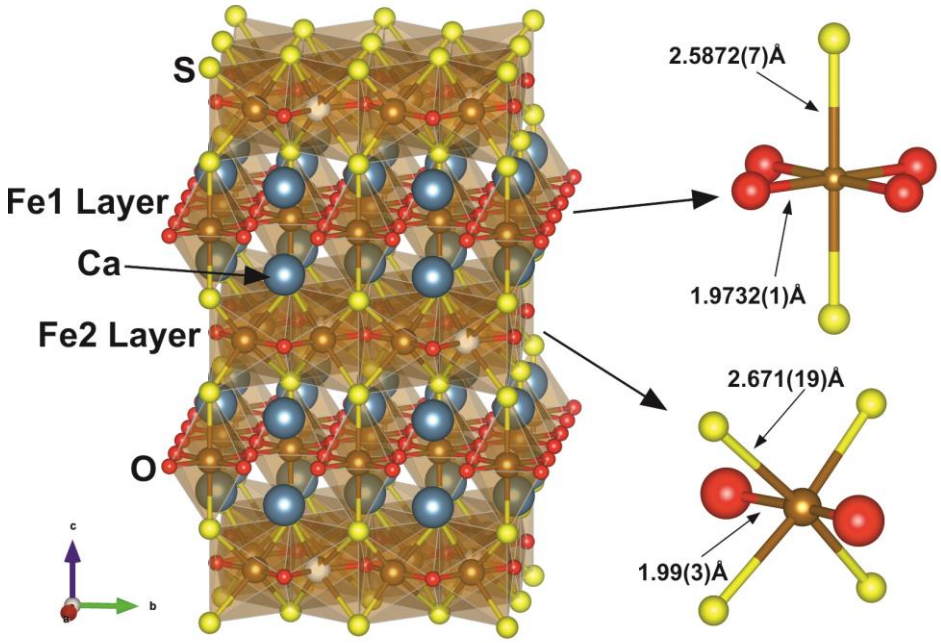


Figure 3.11: Structure of $Ca_2FeO_2Fe_{1.6}OS_2$. The FeO_4S_2 and FeO_2S_4 distorted octahedra are shown on the right-hand side. Ellipsoids with 99% displacement are given for these distorted octahedra using isotropic displacement parameters refined from room-temperature I11 XRPD data (detailed in Tables 3.1 and 3.2). Average bond lengths were calculated and displayed for the FeO_2S_4 polyhedra.

The preliminary refinement results are shown in detail in Table 3.1. Bond valence sums (BVS) for the various Fe sites were also performed, and the results of these are given in Table 3.2. The value of +2.85(1) for the Fe in the Fe1 FeO_4S_2 layer suggests that this layer hosts Fe^{3+} cations and the values for the Fe in the Fe2 FeO_2S_4 layer indicate the presence of Fe^{2+} as all four values are very close to +2. The BVS value of +2.11(13) for the almost vacant Fe2_1 site may be slightly unreliable due to the very low occupancy of this position, however it seems likely that this is also Fe^{2+}.

	$Ca_2FeO_2Fe_{1.6}OS_2$
Diffractometer	I11 (MAC)
Wavelength (Å)	0.826567
Temperature (K)	300
Space Group	*Aea*2
a (Å)	11.162320(10)$^+$
b (Å)	11.162320(10)$^+$
c (Å)	17.50705(3)
V (Å^3)	2181.333(5)

						$Ca_2FeO_2Fe_{1.6}OS_2$
Atom	Site	*x*	*y*	*z*	Occupancy	U_{iso} (Å^2)
Ca1_1	8*b*	0	0.25	0.34443(3)	1	0.00846(14)
Ca1_2	8*b*	0.25	0.5	0.34443(3)	1	0.00846(14)
Ca1_3	8*b*	0	0.25	0.15557(3)	1	0.00846(14)
Ca1_4	8*b*	0.25	0.5	0.15557(3)	1	0.00846(14)
Fe1_1	8*b*	0.75	0.25	0.25	1	0.00505(15)
Fe1_2	4*a*	0	0	0.75	1	0.00505(15)
Fe1_3	4*a*	0	0	0.25	1	0.00505(15)
Fe2_1	8*b*	0.851(3)	0.350(3)	0	0.091(3)	0.01203(19)
Fe2_2	8*b*	0.860(3)	0.868(3)	0	1	0.01203(19)
Fe2_3	8*b*	0.374(3)	0.358(3)	0	1	0.01203(19)
Fe2_4	8*b*	0.390(3)	0.893(3)	0	1	0.01203(19)
O1_1	8*b*	0.875	0.375	0.25	1	0.0111(5)
O1_2	8*b*	0.875	0.875	0.25	1	0.0111(5)
O1_3	8*b*	0.375	0.375	0.25	1	0.0111(5)
O1_4	8*b*	0.375	0.875	0.25	1	0.0111(5)
O2_1	8*b*	0	0.25	0	1	0.0216(9)
O2_2	8*b*	0.25	0.5	0	1	0.0216(9)
S1_1	8*b*	0.75	0.25	0.39778(4)	1	0.00749(15)
S1_2	4*a*	0	0	0.89778(4)	1	0.00749(15)
S1_3	4*a*	0	0	0.39778(4)	1	0.00749(15)
S1_4	4*a*	0	0	0.10222(4)	1	0.00749(15)
S1_5	4*a*	0	0	0.60222(4)	1	0.00749(15)
S1_6	8*b*	0.25	0.25	0.10222(4)	1	0.00749(15)

Table 3.1: Preliminary refinement results from the XRPD pattern collected at 300 K using the MAC detector at I11. In this model the atoms have not yet been given full freedom, but it defines the distribution of vacancies on the Fe2 sites along with the displacements of the Fe2 sites in the *x* and *y* directions. $^+$The *a* and *b* lattice parameters are refined using the same parameter, as when they are refined separately this gives insignificantly different values.

	Fe-O Distances (Å)	Fe-S Distances (Å)	Fe BVS
Fe2_1	2.00(3), 2.02(3)	2.392(15), 2.392(15), 2.962(18), 2.962(18)	+2.11(13)
Fe2_2	1.92(3), 2.04(3)	2.539(16), 2.539(16), 2.796(18), 2.796(18)	+2.01(13)
Fe2_3	1.85(3), 2.10(3)	2.564(17), 2.564(17), 2.774(18), 2.774(18)	+2.05(13)
Fe2_4	1.97(3), 2.01(3)	2.477(16), 2.477(16), 2.862(18), 2.862(18)	+2.03(13)

	Fe-O Distance (Å)	Fe-S Distance (Å)	Fe BVS
Fe1	1.9732(1)	2.5872(7)	+2.85(1)

Table 3.2: Fe bond valence sums (BVS) calculated using bond lengths refined from the XRPD pattern collected at 300 K using the MAC detector at I11. Values calculated assuming a +2 oxidation state for Fe2 and a +3 oxidation state for Fe1 and using reference values from *Brown and Altermatt*.[4]

The supercell can be formed by taking the basic cell with *P*4/*mmm* symmetry and expanding it. This results in atoms being located at specific positions. In order to keep the approach of the structure solution as simple as possible, in the preliminary refinement given in Figures 3.8-3.11 and Tables 3.1-3.2, only movements of the Fe in the Fe2 layer were refined as movement of these alone could account for the superstructure peaks. However, in *Aea*2 (space group 41) symmetry, all 8b sites can be refined in terms of their *x*, *y* and *z* coordinates as this is a general site. The final refinement shown in Figure 3.12, which was given the preliminary model as a starting point, is not a significant improvement and the refined positions given in Table 3.3 are not significantly different from their preliminary positions (displayed in Table 3.1).

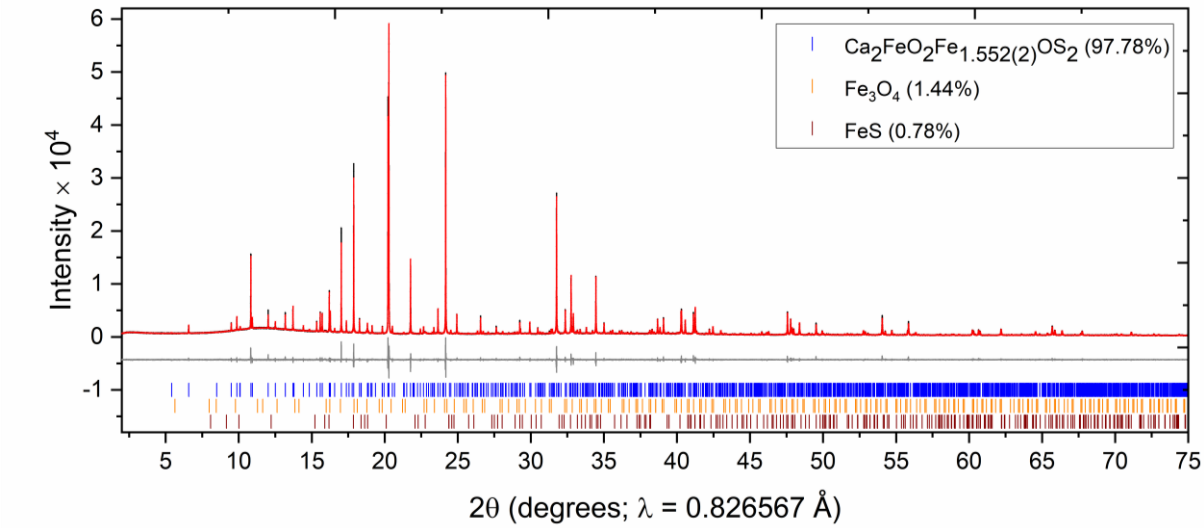


Figure 3.12: Final refinement against the XRPD pattern of $Ca_2FeO_2Fe_{1.6}OS_2$ measured at 300 K on the MAC detector at I11 showing the observed (black), calculated (red) and difference (grey) curves. R_{wp}: 6.314%.

	$Ca_2FeO_2Fe_{1.6}OS_2$
Diffractometer	I11 (MAC)
Wavelength (Å)	0.826567
Temperature (K)	300
Space Group	*Aea*2
a (Å)	11.162341(9)$^+$
b (Å)	11.162341(9)$^+$
c (Å)	17.50706(3)
V (Å^3)	2181.343(4)

						$Ca_2FeO_2Fe_{1.6}OS_2$
Atom	Site	*x*	*y*	*z*	Occupancy	U_{iso} (Å^2)
Ca1_1	8*b*	0.002(2)	0.247(2)	0.344(4)	1	0.00862(17)
Ca1_2	8*b*	0.252(2)	0.501(4)	0.344(4)	1	0.00862(17)
Ca1_3	8*b*	0.001(2)	0.252(2)	0.155(4)	1	0.00862(17)
Ca1_4	8*b*	0.248(2)	0.500(5)	0.155(4)	1	0.00862(17)
Fe1_1	8*b*	0.750(1)	0.249(1)	0.255(1)	1	0.00369(17)
Fe1_2	4*a*	0	0	0.754(1)	1	0.00369(17)
Fe1_3	4*a*	0	0	0.249(1)	1	0.00369(17)
Fe2_1	8*b*	0.861(5)	0.360(5)	0.997(5)	0.104(3)	0.01194(20)
Fe2_2	8*b*	0.858(1)	0.869(1)	0.001(1)	1	0.01194(20)
Fe2_3	8*b*	0.374(1)	0.358(1)	0.001(1)	1	0.01194(20)
Fe2_4	8*b*	0.392(1)	0.894(1)	0.999(1)	1	0.01194(20)
O1_1	8*b*	0.872(6)	0.377(4)	0.253(3)	1	0.0068(9)
O1_2	8*b*	0.875(6)	0.868(4)	0.248(3)	1	0.0068(9)
O1_3	8*b*	0.374(5)	0.389(3)	0.250(2)	1	0.0068(9)
O1_4	8*b*	0.378(5)	0.863(3)	0.252(2)	1	0.0068(9)
O2_1	8*b*	0.010(2)	0.244(2)	0.008(7)	1	0.0101(12)
O2_2	8*b*	0.254(3)	0.493(2)	0.008(6)	1	0.0101(12)
S1_1	8*b*	0.748(2)	0.251(5)	0.397(1)	1	0.00757(18)
S1_2	4*a*	0	0	0.900(2)	1	0.00757(18)
S1_3	4*a*	0	0	0.395(1)	1	0.00757(18)
S1_4	4*a*	0	0	0.100(2)	1	0.00757(18)
S1_5	4*a*	0	0	0.604(2)	1	0.00757(18)
S1_6	8*b*	0.251(2)	0.250(5)	0.102(1)	1	0.00757(18)

Table 3.3: Final refinement results from the XRPD pattern collected at 300 K using the MAC detector at I11. $^+$The *a* and *b* lattice parameters are refined using the same parameter, as when they are refined separately this gives insignificantly different values.

	Fe-O Distances (Å)	Fe-S Distances (Å)	Fe BVS
Fe2_1	2.10(6), 2.12(6)	2.45(7), 2.53(7), 2.84(6), 2.89(7)	+1.7(3)
Fe2_2	1.94(2), 1.94(3)	2.53(3), 2.55(3), 2.768(14), 2.786(17)	+2.1(2)
Fe2_3	1.91(2), 2.01(3)	2.55(3), 2.57(3), 2.743(15), 2.766(18)	+2.1(2)
Fe2_4	1.97(3), 2.00(3)	2.482(18), 2.496(16), 2.89(3), 2.90(3)	+2.0(2)

	Fe-O Distances (Å)	Fe-S Distances (Å)	Fe BVS
Fe1_1	1.90(5), 1.93(6), 1.97(6), 2.07(5)	2.495(10), 2.672(12)	+2.9(4)
Fe1_2	1.98(6), 1.98(6), 2.05(4), 2.05(4)	2.55(3), 2.63(2)	+2.6(3)
Fe1_3	1.87(5), 1.87(5), 2.03(6), 2.03(6)	2.554(17), 2.610(19)	+3.1(4)

Table 3.4: Fe bond valence sums (BVS) calculated using bond lengths refined from the XRPD pattern collected at 300 K using the MAC detector at I11. Values calculated assuming a +2 oxidation state for Fe2 and a +3 oxidation state for Fe1 and using reference values from *Brown and Altermatt*.[4]

Therefore, the final model detailed in Table 3.3 is one which gives a complete picture of the supercell, whereas the preliminary model detailed in Table 3.1 is useful for giving a simplified picture of the main origin of this complex supercell (i.e., the specific Fe-vacancy pattern coupled with the displacement of Fe and O in the *ab*-plane). As the supercell contains a vast number of atoms and crystallographic sites, it was often necessary to use the preliminary model in the refinement of diffraction data in order to reduce the number of parameters being refined. With too many parameters to refine, the TOPAS software[5] appeared to have difficulty performing the least-squares refinement and reaching the global minimum.

3.3.3 High Temperature NPD

In order to support the investigation into the crystal structure of $Ca_2FeO_2Fe_{1.6}OS_2$, high temperature NPD data were collected on the D2B instrument at the ILL, Grenoble. Data collected at 373 K were used for crystal structure analysis, where the material at this temperature is in the paramagnetic regime meaning there are no magnetic Bragg peaks contributing to the diffraction pattern. D2B has a high resolution at intermediate *d*-spacing values and a wide *d*-spacing coverage at λ = 1.594 Å, hence is useful in the determination of nuclear structures.

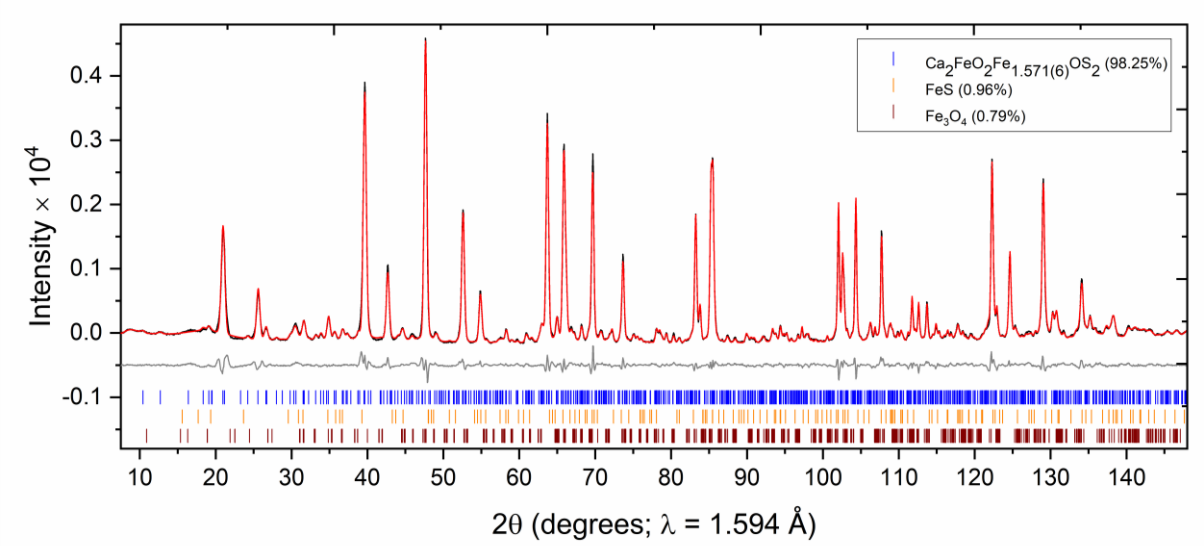


Figure 3.13: Preliminary refinement against the NPD pattern of $Ca_2FeO_2Fe_{1.6}OS_2$ measured at 373 K on the D2B instrument at the ILL showing the observed (black), calculated (red) and difference (grey) curves. R_{wp}: 4.158%.

Preliminary refinement of the model determined using the XRPD data was performed against this NPD data, as shown in Figure 3.13. The preliminary refinement results are shown in Table 3.5. When compared to the preliminary refinement results for the XRPD data (see Table 3.1), these preliminary refinement results for the NPD data agree well. Unlike in the XRPD preliminary refinement, the NPD preliminary refinement also allowed the oxygen anions in the Fe2 FeO_2S_4 layer to move freely in the *x* and *y* directions to determine whether these are significantly displaced as well as the Fe in this layer. Neutron scattering is better at determining oxygen positions than x-ray scattering, as explained in Chapter 2, but it must be said that in the case of this compound containing relatively light

accompanying elements (Ca, Fe, S) this is not as important an advantage as would be the case for materials containing heavy accompanying elements (e.g. 4*d*/5*d* transition metals or lanthanides). Comparing the XRPD and NPD final refinements (results detailed in Table 3.3 and Table 3.6 respectively), where the oxygens in the Fe2 FeO_2S_4 layer are allowed to freely refine in both cases, these oxide anions do not move away from their 'ideal' positions by a significant amount for either.

	$Ca_2FeO_2Fe_{1.6}OS_2$
Diffractometer	D2B (ILL)
Wavelength (Å)	1.594
Temperature (K)	373
Space Group	*Aea*2
a (Å)	11.17209(5)[+]
b (Å)	11.17209(5)[+]
c (Å)	17.5406(3)
V (Å^3)	2189.34(4)

						$Ca_2FeO_2Fe_{1.6}OS_2$
Atom	Site	*x*	*y*	*z*	Occupancy	U_{iso} (Å^2)
Ca1_1	8*b*	0	0.25	0.34420(14)	1	0.0062(6)
Ca1_2	8*b*	0.25	0.5	0.34420(14)	1	0.0062(6)
Ca1_3	8*b*	0	0.25	0.15580(14)	1	0.0062(6)
Ca1_4	8*b*	0.25	0.5	0.15580(14)	1	0.0062(6)
Fe1_1	8*b*	0.75	0.25	0.25	1	0.0014(4)
Fe1_2	4*a*	0	0	0.75	1	0.0014(4)
Fe1_3	4*a*	0	0	0.25	1	0.0014(4)
Fe2_1	8*b*	0.863(4)	0.363(4)	0	0.14(2)	0.0073(5)
Fe2_2	8*b*	0.854(4)	0.870(4)	0	1	0.0073(5)
Fe2_3	8*b*	0.371(4)	0.359(4)	0	1	0.0073(5)
Fe2_4	8*b*	0.394(4)	0.892(4)	0	1	0.0073(5)
O1_1	8*b*	0.875	0.375	0.25	1	0.0066(5)
O1_2	8*b*	0.875	0.875	0.25	1	0.0066(5)
O1_3	8*b*	0.375	0.375	0.25	1	0.0066(5)
O1_4	8*b*	0.375	0.875	0.25	1	0.0066(5)
O2_1	8*b*	0.0088(14)	0.2461(18)	0	1	0.0078(9)
O2_2	8*b*	0.2540(19)	0.4903(11)	0	1	0.0078(9)
S1_1	8*b*	0.75	0.25	0.3981(3)	1	0.0058(8)
S1_2	4*a*	0	0	0.8981(3)	1	0.0058(8)
S1_3	4*a*	0	0	0.3981(3)	1	0.0058(8)
S1_4	4*a*	0	0	0.1019(3)	1	0.0058(8)
S1_5	4*a*	0	0	0.6019(3)	1	0.0058(8)
S1_6	8*b*	0.25	0.25	0.1019(3)	1	0.0058(8)

Table 3.5: Preliminary refinement results from the NPD pattern collected at 373 K using the D2B instrument at the ILL. In this model the atoms have not yet been given full freedom, but it defines the distribution of vacancies on the Fe2 sites along with the displacements of the Fe2 and O2 sites in the *x* and *y* directions. [+]The *a* and *b* lattice parameters are refined using the same parameter, as when they are refined separately this gives insignificantly different values.

Full refinement of all 8b sites in terms of their *x*, *y* and *z* coordinates is shown in the final refinement depicted in Figure 3.14, with the resulting, final structure detailed in Table 3.6. Again, this is not a significant improvement on the preliminary refinement given in Figure 3.13 and Table 3.5, and once again the refined positions are not significantly different from the 'ideal' starting positions.

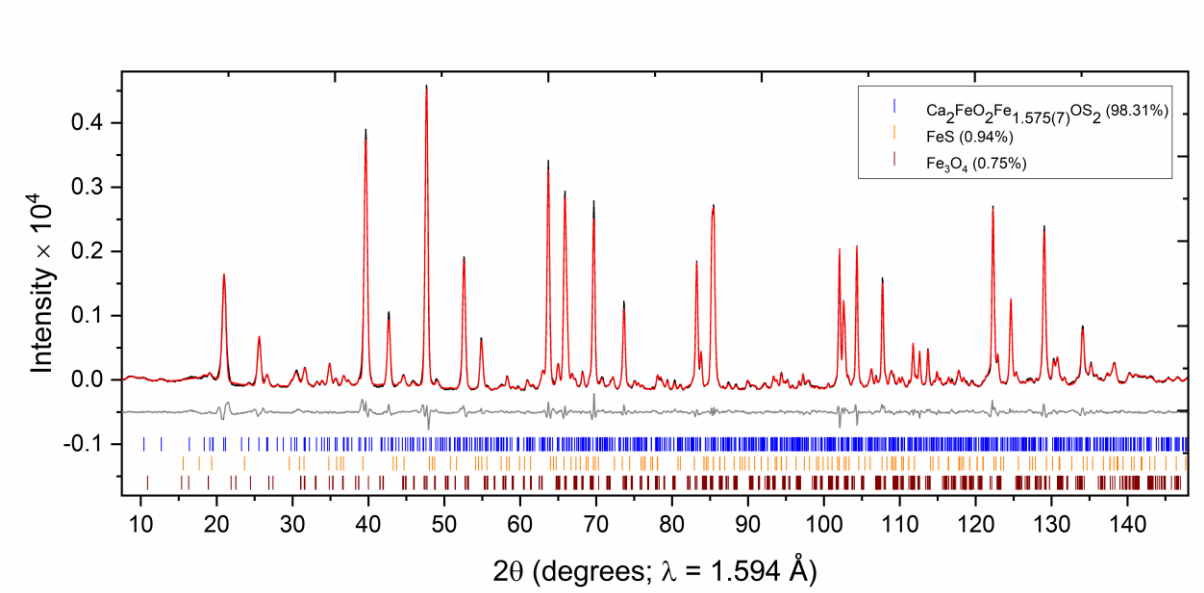


Figure 3.14: Final refinement against the NPD pattern of $Ca_2Fe_{2.6}O_3S_2$ measured at 373 K on the D2B instrument at the ILL showing the observed (black), calculated (red) and difference (grey) curves. R_{wp}: 3.900%.

	$Ca_2FeO_2Fe_{1.6}OS_2$
Diffractometer	D2B (ILL)
Wavelength (Å)	1.594
Temperature (K)	373
Space Group	*Aea*2
a (Å)	11.17279(5)[+]
b (Å)	11.17279(5)[+]
c (Å)	17.5419(3)
V (Å^3)	2189.78(4)

						$Ca_2FeO_2Fe_{1.6}OS_2$
Atom	Site	*x*	*y*	*z*	Occupancy	U_{iso} (Å^2)
Ca1_1	8*b*	0.998(5)	0.248(10)	0.344(8)	1	0.0064(9)
Ca1_2	8*b*	0.251(16)	0.498(7)	0.345(8)	1	0.0064(9)
Ca1_3	8*b*	0.997(5)	0.252(10)	0.155(7)	1	0.0064(9)
Ca1_4	8*b*	0.249(16)	0.499(7)	0.156(7)	1	0.0064(9)
Fe1_1	8*b*	0.747(4)	0.252(1)	0.253(2)	1	0.0016(6)
Fe1_2	4*a*	0	0	0.751(3)	1	0.0016(6)
Fe1_3	4*a*	0	0	0.249(3)	1	0.0016(6)
Fe2_1	8*b*	0.859(7)	0.358(6)	0.997(13)	0.149(13)	0.0075(5)
Fe2_2	8*b*	0.855(1)	0.870(2)	0.001(3)	1	0.0075(5)
Fe2_3	8*b*	0.371(2)	0.359(1)	0.999(3)	1	0.0075(5)
Fe2_4	8*b*	0.394(1)	0.892(1)	0.998(3)	1	0.0075(5)
O1_1	8*b*	0.874(10)	0.376(9)	0.252(4)	1	0.0063(6)
O1_2	8*b*	0.874(8)	0.878(8)	0.248(4)	1	0.0063(6)
O1_3	8*b*	0.378(8)	0.371(7)	0.251(3)	1	0.0063(6)
O1_4	8*b*	0.377(9)	0.873(9)	0.250(4)	1	0.0063(6)
O2_1	8*b*	0.009(2)	0.246(2)	0.997(8)	1	0.0068(12)
O2_2	8*b*	0.254(3)	0.490(2)	0.996(6)	1	0.0068(12)
S1_1	8*b*	0.747(7)	0.254(8)	0.398(4)	1	0.0051(13)
S1_2	4*a*	0	0	0.901(10)	1	0.0051(13)
S1_3	4*a*	0	0	0.397(8)	1	0.0051(13)
S1_4	4*a*	0	0	0.098(10)	1	0.0051(13)
S1_5	4*a*	0	0	0.603(8)	1	0.0051(13)
S1_6	8*b*	0.248(7)	0.247(8)	0.101(5)	1	0.0051(13)

Table 3.6: Final refinement results from the NPD pattern collected at 373 K using the D2B instrument at the ILL. [+]The *a* and *b* lattice parameters are refined using the same parameter, as when they are refined separately this gives insignificantly different values.

3.3.4 SQUID Magnetometry

The ZFC and FC curves shown in Figure 3.15a), measured in a field of 1000 Oe, both indicate the presence of what appears to be an antiferromagnetic ordering transition at around 70 K. This was reported by Zhang *et al*.[1] and assumed to be the only long-range magnetic ordering transition. This transition is even clearer in 5T-4T-3T measurement depicted in Figure 3.15b). Initially this measurement was performed to negate any ferromagnetic signals arising from any possible Fe_3O_4 impurity, however as further measurements (see Figures 3.16 and 3.17) show that the $Ca_2FeO_2Fe_{1.6}OS_2$ material appears to be weakly ferromagnetic itself, this now also negates the ferromagnetism of the main phase. Figure 3.15c) shows the weak ferromagnetism and small coercivity displayed by the compound at 5 K, which is shown in the magnetisation vs field plot in Figure 3.15d) to saturate just below 1 T at 300 K.

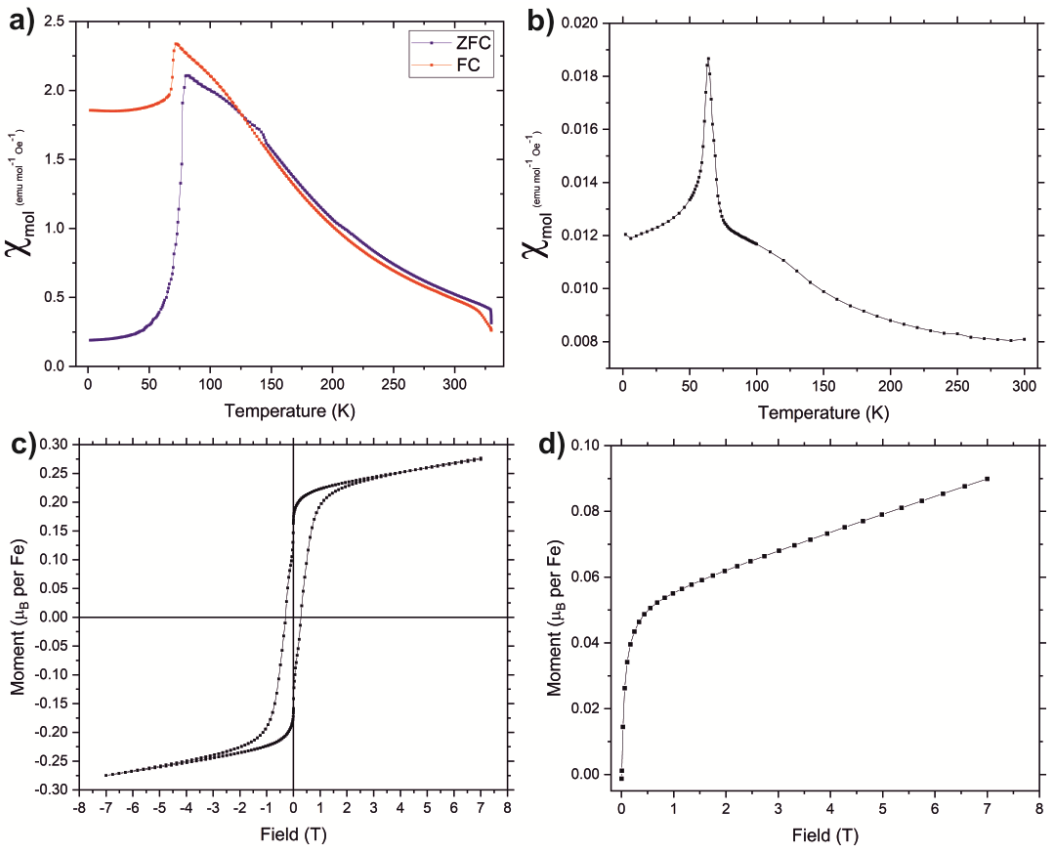


Figure 3.15: Magnetometry results for the $Ca_2FeO_2Fe_{1.6}OS_2$ compound showing data from **a)** the ZFC/FC measurements in a field of 1000 Oe **b)** the 5T-4T-3T susceptibility **c)** the 5 K magnetisation isotherm and **d)** the moment vs field at 300 K.

The hysteresis loop shown in Figure 3.15c) is of particular interest as it suggests a ferromagnetic (or ferrimagnetic) component to the magnetism. Further hysteresis loops were measured at different temperatures to explore this further, as shown in Figure 3.16. It can be seen that the onset of any significant coercivity is below 100 K and that upon warming from 100 K to 350 K the magnitude of the ferromagnetic moment drastically decreases. The 5 K curve exhibits multiple steps around the origin which indicate complex magnetic behaviour to be likely at these low temperatures.

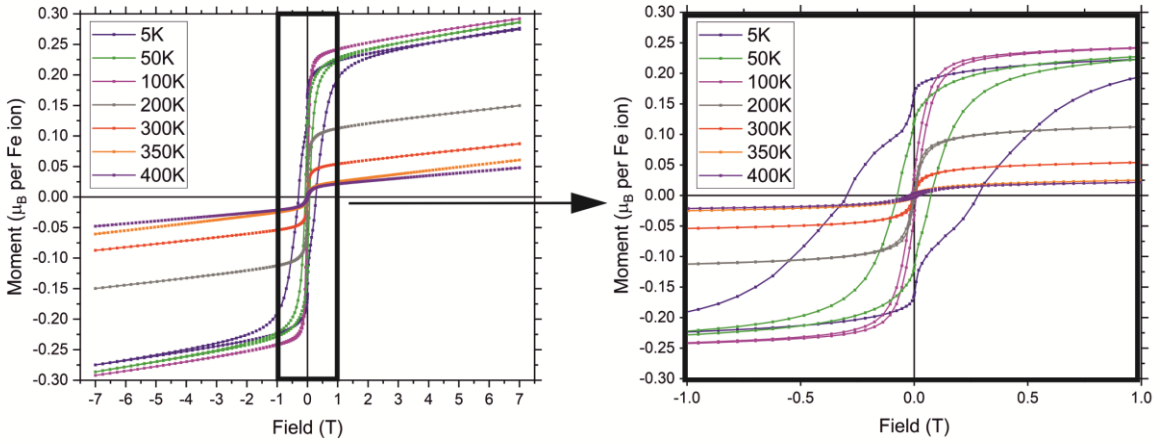


Figure 3.16: Variable temperature magnetisation isotherms for the $Ca_2FeO_2Fe_{1.6}OS_2$ compound. The graph on the right focusses on the data near the origin.

High temperature measurements were also carried out to investigate the magnetic behaviour of the sample. The ZFC and FC curves shown in Figure 3.17 (left) exhibit a sharp rise in magnetic susceptibility below 350 K indicating the presence of a magnetic transition which is likely ferromagnetic (or ferrimagnetic) in nature. The 400 K moment against field plot given in Figure 3.17 (right) suggests a ferromagnetic impurity forms a miniscule part of the sample, likely to be the Fe_3O_4 observed in the high resolution XRPD. 400 K was the temperature chosen for this measurement, as variable temperature NPD measurements (to be discussed in section 3.3.8) show that the sample is in the paramagnetic regime here.

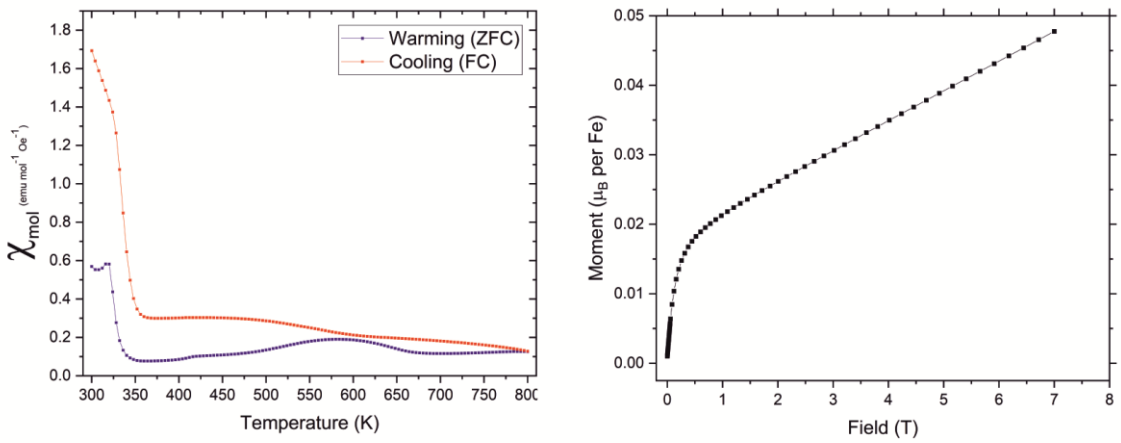


Figure 3.17: High temperature magnetometry results for the $Ca_2FeO_2Fe_{1.6}OS_2$ compound showing data from the ZFC/FC measurements in a field of 100 Oe (left) and the moment vs field at 400 K (right).

Figure 3.18 displays magnetic moment against field data collected after warming the sample up to 350 K (above the suspected high temperature ordering transition) then cooling to each temperature in zero-field. The ferrimagnetic moment increases upon going from 350 K to 300 K and then to 100 K. These data and those shown in Figure 3.16 show very similar responses of the magnetisation to applied field, therefore warming the sample up into the paramagnetic regime before measuring magnetisation with field has very little effect on the magnetic behaviour of the sample. At 5 K, the unusual steps in the magnetisation at very low applied magnetic field values, as seen in Figure 3.16, are seen more clearly in Figure 3.18 from around 0-0.3 T.

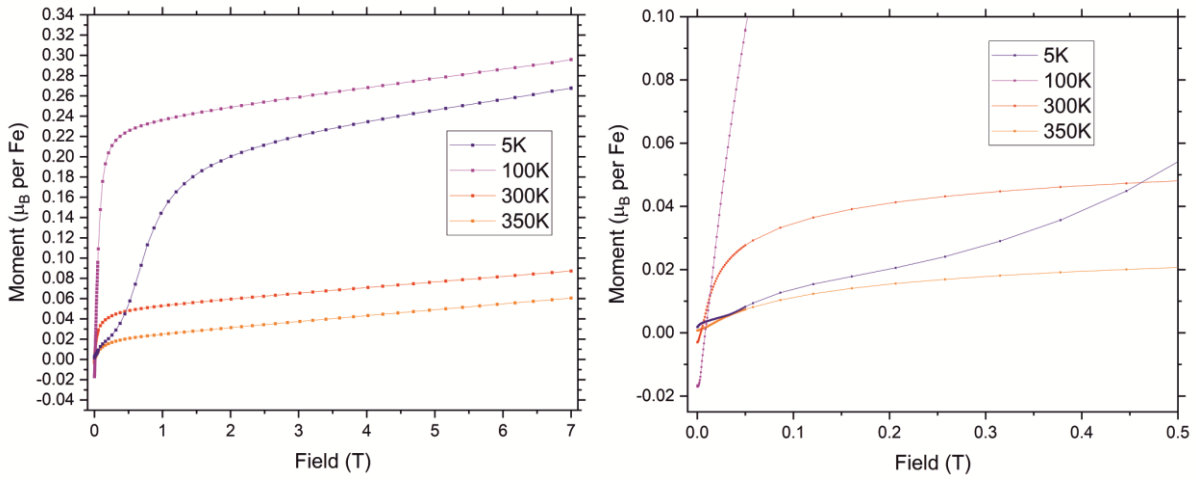


Figure 3.18: Variable temperature magnetisation isotherms for the $Ca_2FeO_2Fe_{1.6}OS_2$ compound. The graph on the right focusses on the data near the origin. Data at each temperature were collected after warming the sample to 350 K and cooling in zero-field.

3.3.5 XANES Measurements

The Fe oxidation states in $Ca_2FeO_2Fe_{1.6}OS_2$ were investigated at room temperature using synchrotron XANES experiments on beamline B18 at the Diamond Light Source. The spectrum is shown in Figure 3.19, along with those of the FeO and Fe_2O_3 standards that were used to compare the data against Fe^{2+} and Fe^{3+} respectively. The spectrum produced by the Fe K-edge in $Ca_2FeO_2Fe_{1.6}OS_2$ can be viewed as a combination of those characteristic of Fe^{2+} and Fe^{3+}, where the dominant K-edge is that of Fe^{2+} and the portion of the edge at higher energy is that of Fe^{3+}. The ratio of the edges which coincide with these Fe oxidation states is approximately 2:1 for Fe^{2+} and Fe^{3+} respectively, which agrees well with the assignment of Fe1 FeO_4S_2 as Fe^{3+} and Fe2 FeO_2S_4 as Fe^{2+}. Of course, some of the discrepancies will be due to the different coordination environments of the Fe in this oxysulfide compared to the oxides.

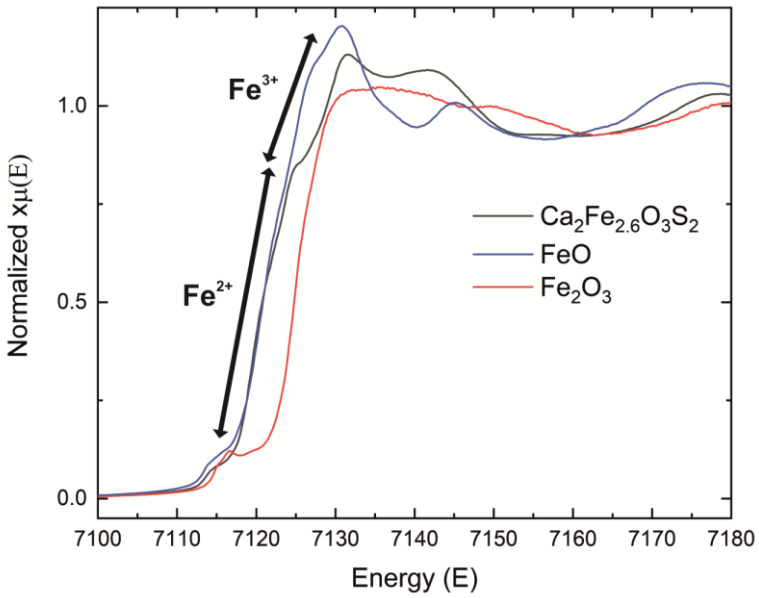


Figure 3.19: XANES K-edge for the $Ca_2FeO_2Fe_{1.6}OS_2$ compound and Fe^{2+}/Fe^{3+} standards.

3.3.6 XPS Measurements

XPS data were also collected on the $Ca_2FeO_2Fe_{1.6}OS_2$ sample by Prof. Robert Palgrave and his fitting of the Fe 2p peak is shown in Figure 3.20. A high spin Fe^{2+} model is used to fit the data here and this models most of the peak well. The blue arrows in Figure 3.20 highlight the areas of the spectrum that are not fitted by this model and suggest the presence of around 18% high spin Fe^{3+}, when taking the spectral intensity into account. Therefore, this experiment indicates that $Ca_2FeO_2Fe_{1.6}OS_2$ contains mostly Fe^{2+}, consistent with the XANES data in section 3.3.5. The calculated value of 82% Fe^{2+} may be inaccurate as here the fitting of a high spin Fe^{2+} model is performed assuming Fe^{2+} in a highly symmetric oxide environment, whereas in the case of $Ca_2FeO_2Fe_{1.6}OS_2$ it is in an FeO_2S_4 mixed-anion environment of lower symmetry.

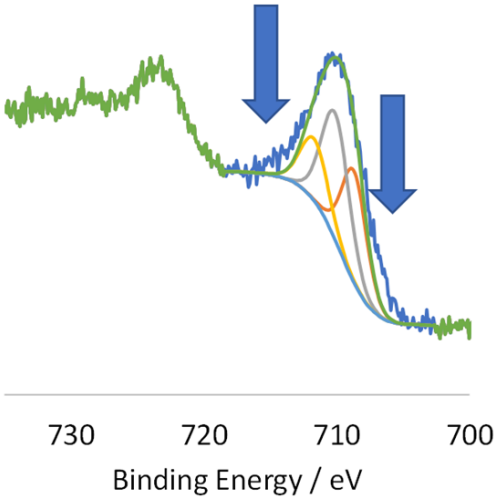


Figure 3.20: XPS spectrum of the $Ca_2FeO_2Fe_{1.6}OS_2$ compound showing the Fe 2p peak fitting. The blue arrows highlight areas of intensity not fit by the high spin Fe^{2+} model.

3.3.7 TEM-EDX

The imaging of a number of crystallites and mapping of the individual elements confirm that there is an even distribution of each type of ion throughout them. The average chemical formula determined by EDX analysis of multiple areas of multiple crystallites is $Ca_2Fe_{2.4(1)}O_{3.4(3)}S_{1.9(1)}$, which is in accordance with the presence of very small amounts of FeS and Fe_3O_4 impurities in the XRPD data (section 3.3.2) and agrees with refined values of Fe stoichiometry from the room temperature XRPD and NPD data, which are less than the targeted 2.6. An example of the study of one crystal is given in Figures 3.21 and 3.22.

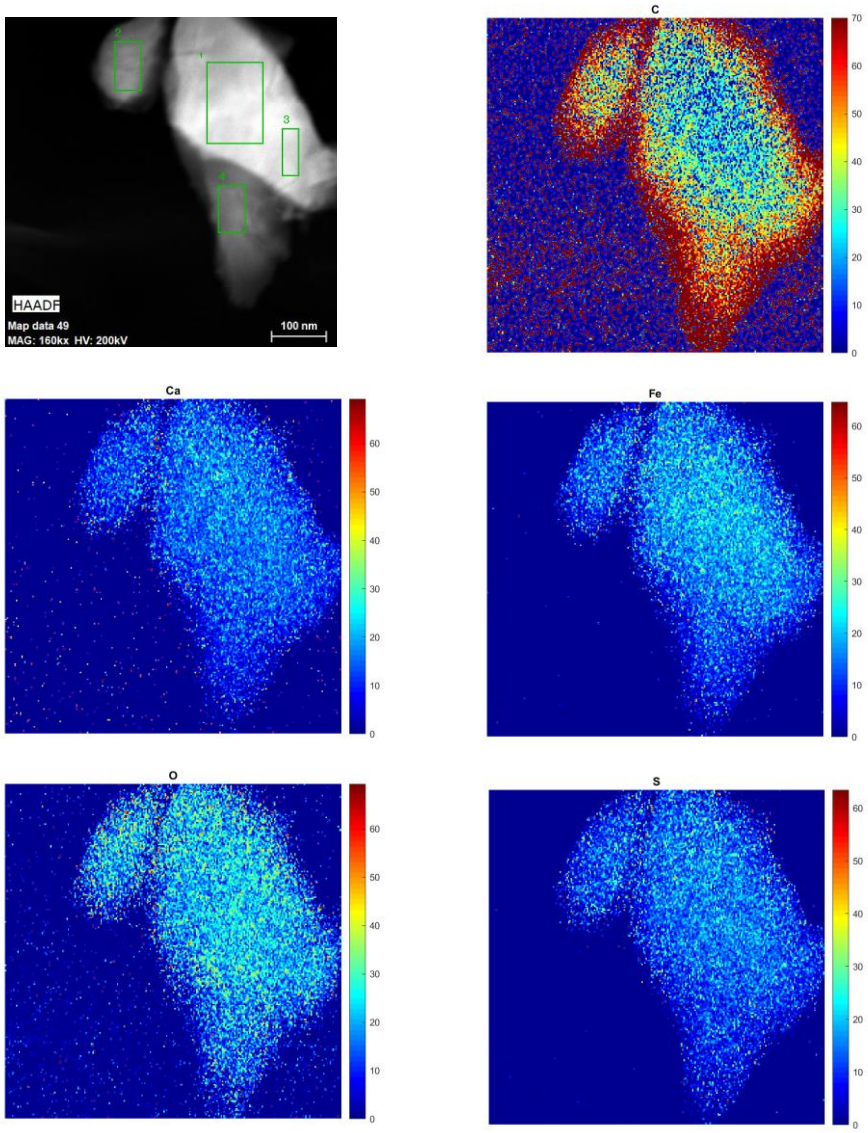
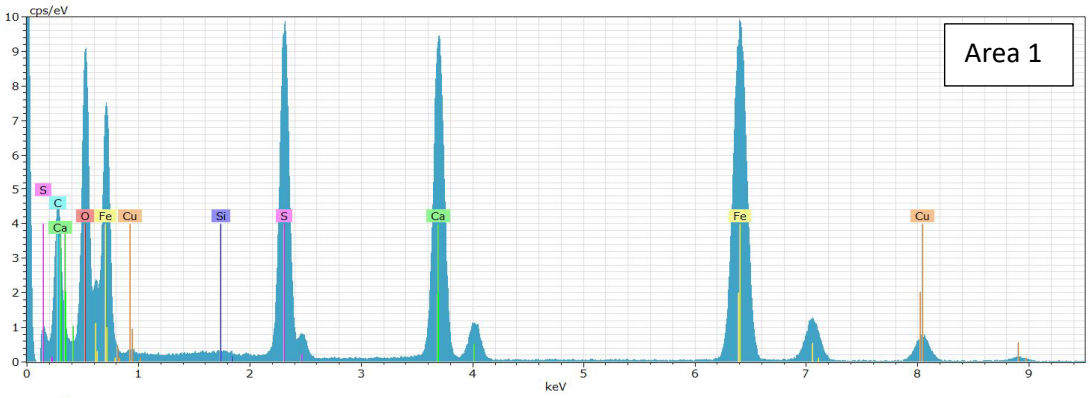
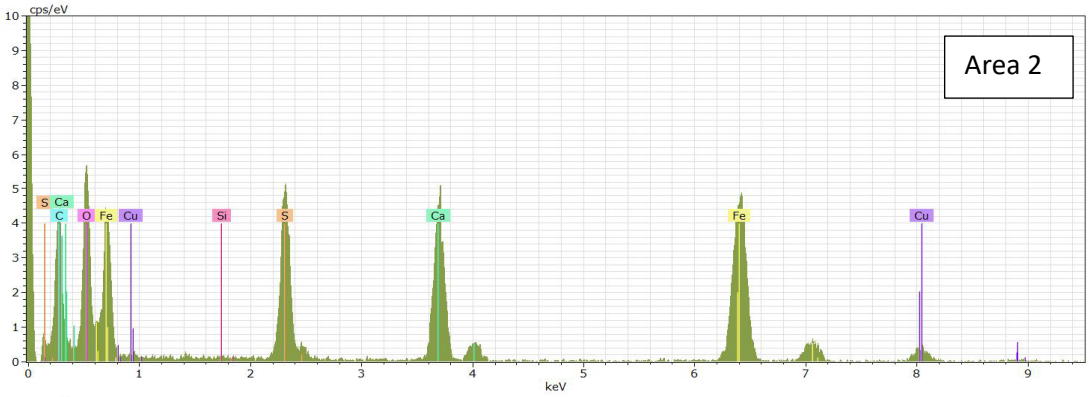
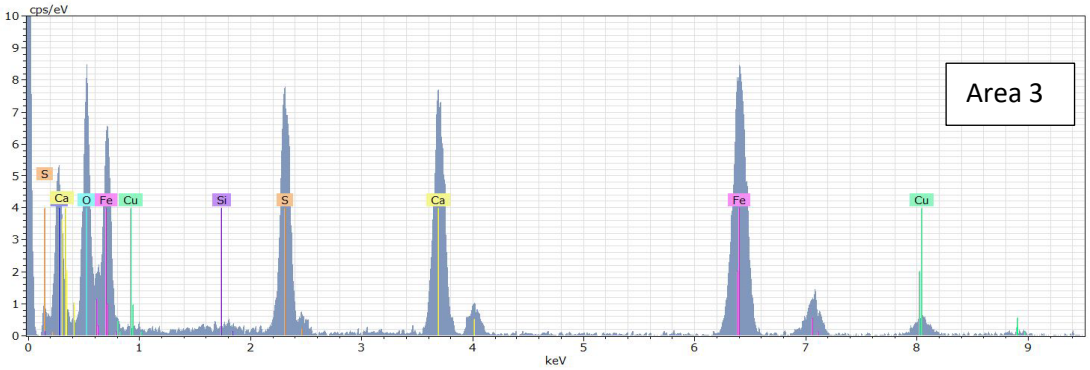
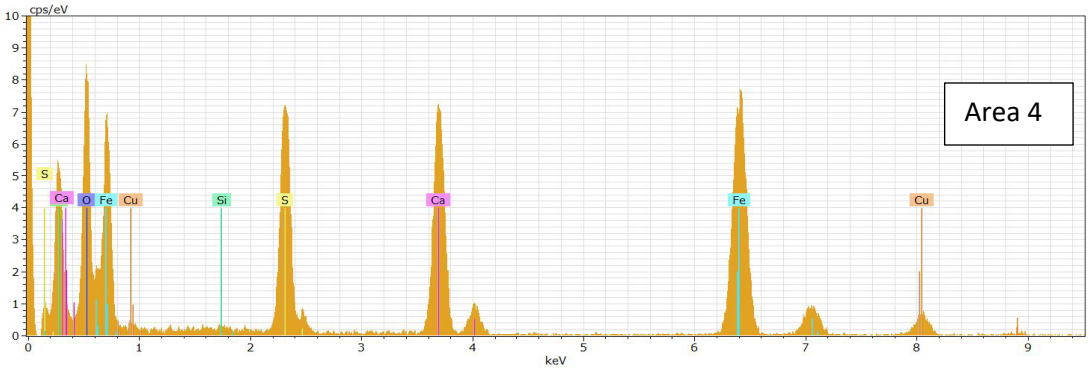


Figure 3.21: TEM-EDX imaging of a $Ca_2FeO_2Fe_{1.6}OS_2$ crystallite. The element mapping key is given in atomic % and the C arises due to the holey carbon grid that the sample is measured on.


cps/eV
Area 1
S
C
Ca
O
Fe
Cu
Si
S
Ca
Fe
Cu
keV


cps/eV
Area 2
S
Ca
C
O
Fe
Cu
Si
S
Ca
Fe
Cu
keV


cps/eV
Area 3
S
Ca
O
Fe
Cu
Si
S
Ca
Fe
Cu
keV


cps/eV
Area 4
S
Ca
O
Fe
Cu
Si
S
Ca
Fe
Cu
keV

Area	Ca (at %)	Fe (at %)	O (at %)	S (at %)	C (at %)	Cu (at %)	Si (at %)	Formula
1	15.603	17.839	21.435	14.849	28.381	1.594	0.299	$Ca_2Fe_{2.3}O_{2.7}S_{1.9}$
2	11.198	13.199	20.161	11.379	42.731	1.223	0.109	$Ca_2Fe_{2.4}O_{3.6}S_{2.0}$
3	13.404	16.332	19.815	12.733	36.005	1.345	0.366	$Ca_2Fe_{2.4}O_{3.0}S_{1.9}$
4	12.830	14.680	20.811	12.332	37.589	1.454	0.304	$Ca_2Fe_{2.3}O_{3.2}S_{1.9}$

Figure 3.22: TEM-EDX elemental analysis results for the areas 1-4 of the crystallite in Figure 3.21. Due to its low atomic mass, O content is only an estimate.

3.3.8 Variable Temperature NPD

Variable temperature NPD data were gathered on both the D1B and D2B instruments at the ILL. A comparison of the initial D2B data, as shown in Figure 3.23, shows the presence of two magnetic ordering transitions- one between 300 K and 373 K and another around 70 K, both of which are coincident with the transitions observed in the magnetometry discussed in section 3.3.4.

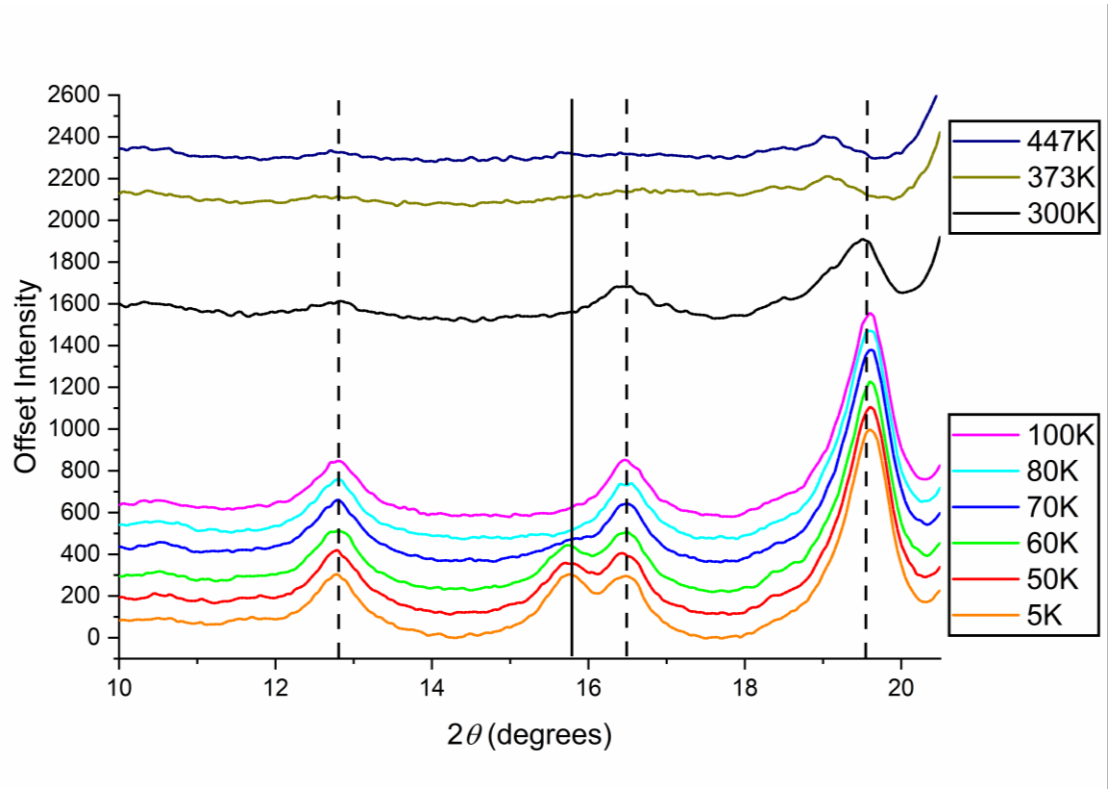


Figure 3.23: Variable temperature NPD data for $Ca_2FeO_2Fe_{1.6}OS_2$ measured on the D2B instrument at the ILL.

The approach taken to analyse these neutron powder diffraction data was one which made full use of the advantages of data collected using either D1B or D2B. The D2B data has good resolution at the *d*-spacings at which nuclear Bragg peaks arise and so these data were first used to obtain the nuclear structure. Due to its higher resolution in the long *d*-spacing regions, the D1B data were then used in the analysis of the long-range magnetic ordering, with the nuclear model fixed to that obtained using the D2B data at the corresponding temperature. The variables of the nuclear model were kept fixed to avoid too many parameters being refined simultaneously. Furthermore, as a number of Bragg peaks consist of both nuclear and magnetic intensity in the D1B data, and the *d*-spacing range

using λ = 2.52 Å on D1B is relatively limited, the nuclear model (from the wider *d*-spacing range on D2B) had to be kept fixed in order to obtain reliable magnetic models. The importance of D1B in the magnetic model analysis must be highlighted here as the 1.59 Å D2B data alone cannot provide a high enough resolution at long *d*-spacings or high enough *d*-spacing values (low angle) to reliably analyse possible magnetic models, with this partly being due to the large unit cell. A wavelength of 2.43 Å can be utilised on D2B in order to probe these longer *d*-spacings, however the resolution of this instrument is not optimised for these longer *d*-spacings, unlike the case for D1B. Instead, the highest resolution obtained on D2B is situated around $2\theta = 130°$ for the purposes of probing crystal structure. Comparison of the D1B and D2B resolutions is discussed in section 2.2.2.3.

It was noticed that at 100 K and lower temperatures, the room temperature nuclear model determined in sections 3.3.2 and 3.3.3 (at slightly higher temperatures) could not account for some intensities in the lower *d*-spacing region of the D2B data (i.e., outside the range of intense magnetic reflections). Even when all the atoms were allowed to refine with full freedom in the *Aea*2 space group, these intensities were not accounted for, as shown in Figure 3.24. As these discrepancies were not noticeable in low temperature XRPD data it was thought that they may arise due to displacement of the O atoms and as they could not be accounted for in *Aea*2 symmetry, it was thought a lowering of symmetry could be involved. Having tested different symmetries, it was found that by representing the unit cell using $P2_12_12$ (space group 18) symmetry [note- this is a subgroup of *Aeam*] and using the ISODISTORT[6] distortion mode approach, these small discrepancies could be accounted for via antiphase 'twisting' of the FeO_4 squares in the Fe1 layer. The refinement result from this is given in Figure 3.25 and the model shown in Figures 3.26 and 3.27. It is the antiphase nature of the twisting between layers that results in the loss of the A-centring. This is comparable to the 'twisting' of BO_6 octahedra in ABO_6 perovskites. The refined $P2_12_12$ model contains Fe in the Fe2 layer in a similar pattern to that refined using the *Aea*2 space group (shown in Figure 3.9), therefore it seems likely that the lowering in symmetry is only due to this 'twisting' of the O atoms in the Fe1 layer.

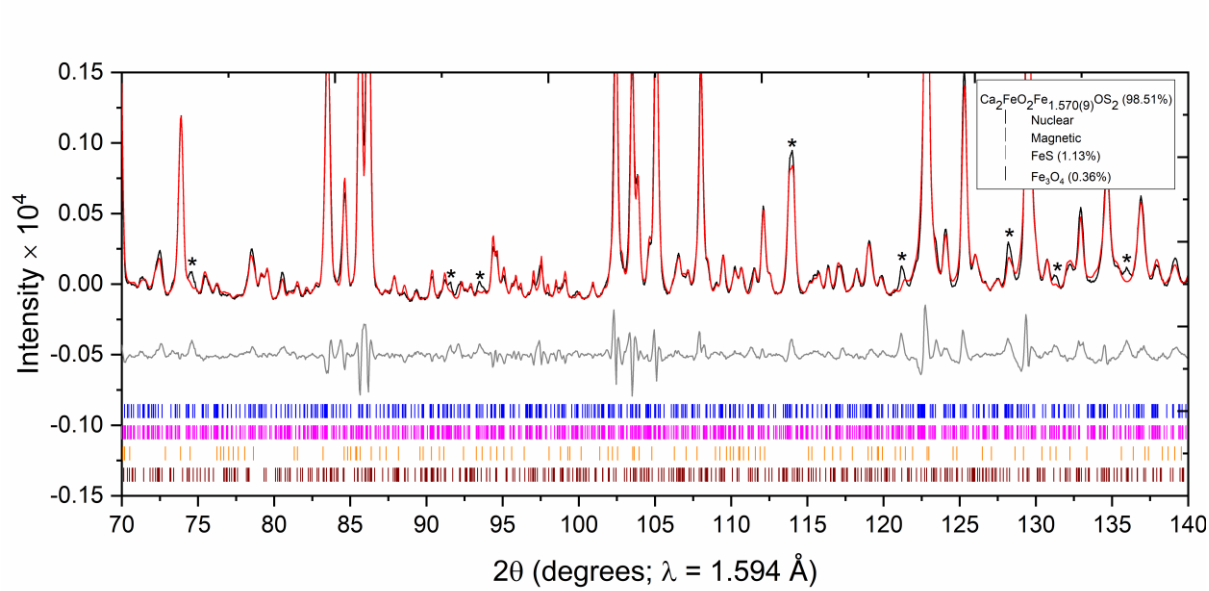


Figure 3.24: NPD pattern of $Ca_2FeO_2Fe_{1.6}OS_2$ measured at 5 K on the D2B instrument at the ILL showing the observed (black), calculated (red) and difference (grey) curves. The nuclear model being refined has *Aea*2 symmetry with all possible variables refining. The significant differences in intensity between the observed and calculated curves are highlighted by a *. R_{wp}: 6.174%.

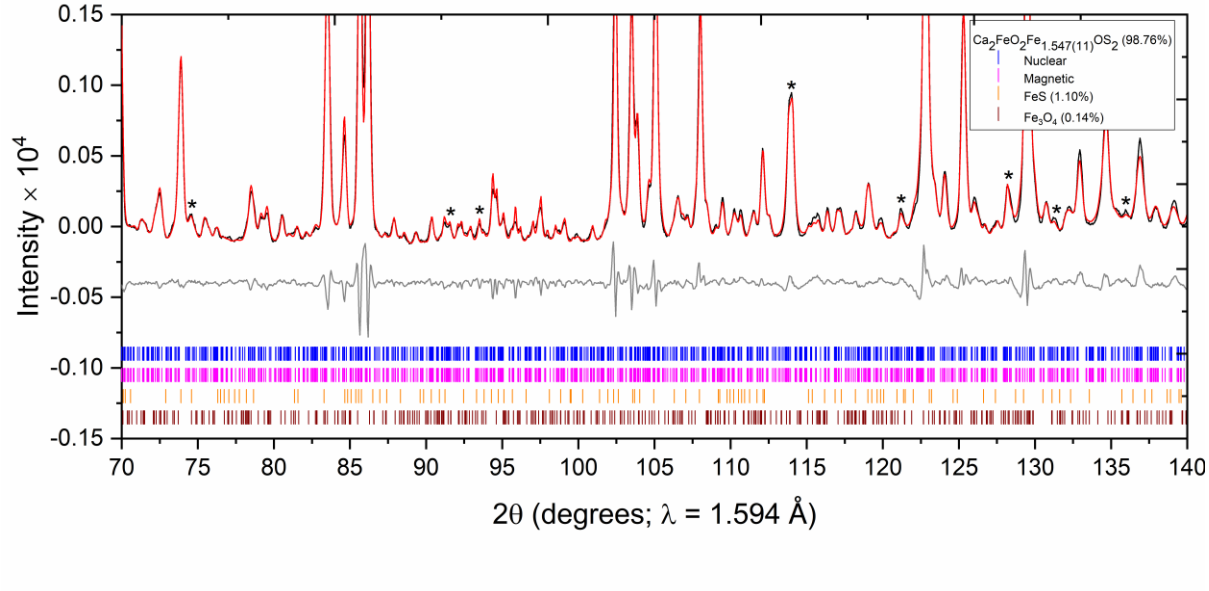


Figure 3.25: NPD pattern of $Ca_2FeO_2Fe_{1.6}OS_2$ measured at 5 K on the D2B instrument at the ILL showing the observed (black), calculated (red) and difference (grey) curves. The nuclear model being refined has $P2_12_12$ symmetry. The significant differences in intensity which have now been accounted for using this model are highlighted by a *. R_{wp}: 5.523%.

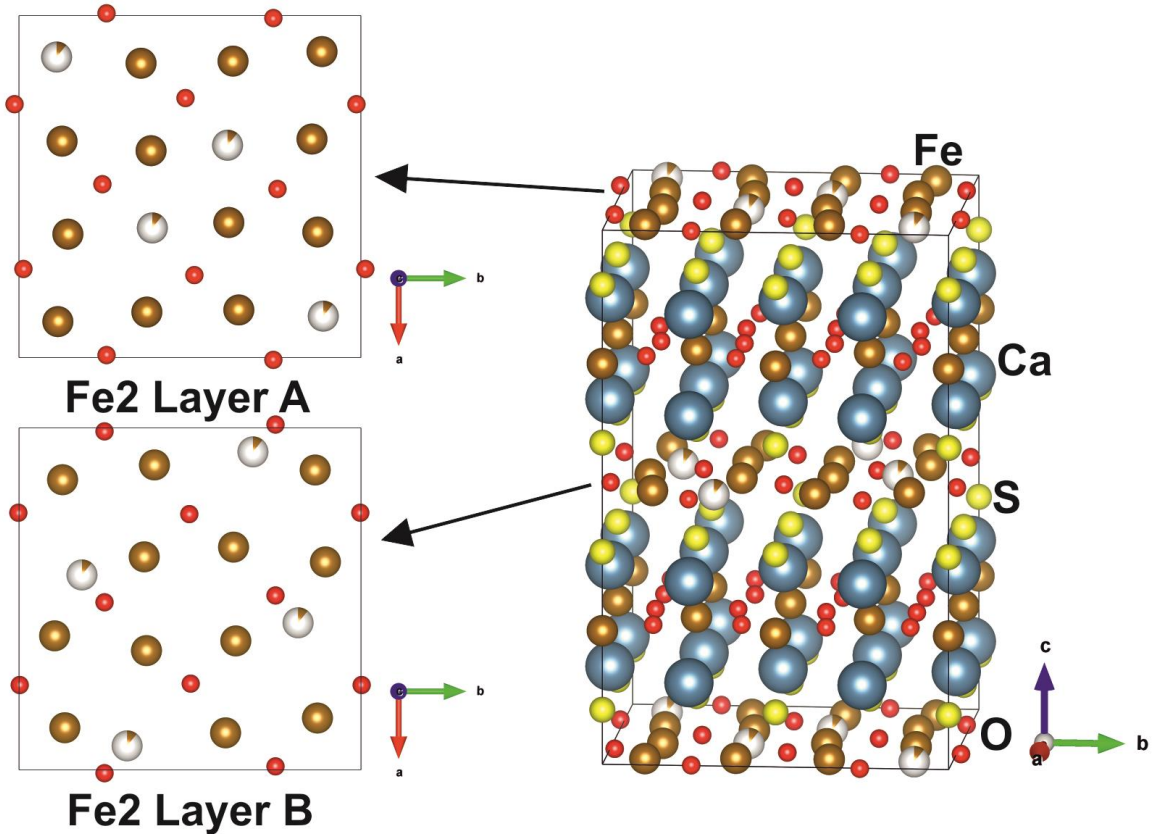


Figure 3.26: Structural model for the $Ca_2FeO_2Fe_{1.6}OS_2$ in the $P2_12_12$ space group, refined from the NPD data given in Figure 3.25.

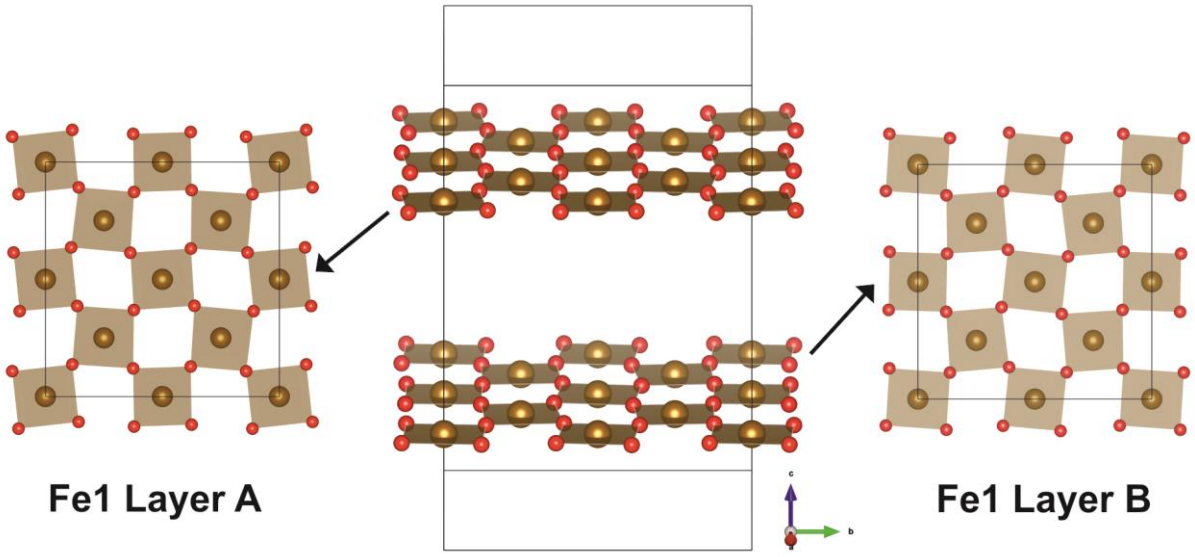


Figure 3.27: Diagram highlighting the antiphase 'twisting' of the FeO_4 in the Fe1 layer, refined from the NPD data given in Figure 3.25.

A useful starting point for deducing the magnetic ordering was the data at 100 K because at this temperature the magnetic Bragg reflections arising from the higher temperature transition (above 300 K) are high in intensity, but 100 K is a higher temperature than when the second transition occurs (around 70 K). The ISODISTORT[6] software was used obtain the various magnetic modes available to the supercell and refinement of possible magnetic models were performed using the TOPAS v6 software.[5] Different magnetic models were then tested in an attempt to account for the magnetic Bragg peaks.

In order to account for the existence and the intensity of all peaks, as the refinements in Figures 3.28 and 3.29 show, long-range magnetic ordering in both Fe layers needs to be present. The models for each Fe layer are depicted in Figure 3.30. As the nuclear supercell is the true representation of the structure and no further expansion of this cell is needed to account for the magnetic Bragg peaks which appear, all the magnetic models predicted for this material have *k*-vectors of $k = (0,0,0)$. In the Fe1 (FeO_4S_2) layer, there is checkerboard ordering of the moments in the *ab*-plane, such that each Fe-O-Fe superexchange pathway is antiferromagnetic. In the Fe2 (FeO_2S_4) layer, the moments are again ordered so that each Fe-O-Fe superexchange is antiferromagnetic, again with each Fe moment directed in the *ab*-plane.

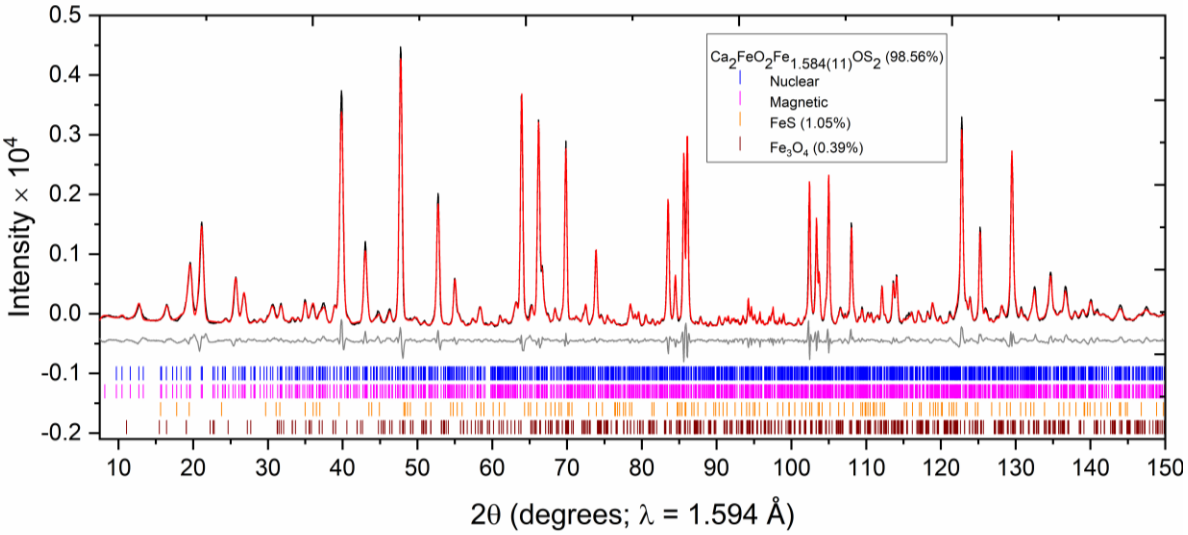


Figure 3.28: NPD pattern of $Ca_2FeO_2Fe_{1.6}OS_2$ measured at 100 K on the D2B instrument at the ILL showing the observed (black), calculated (red) and difference (grey) curves. R_{wp}: 5.296%.

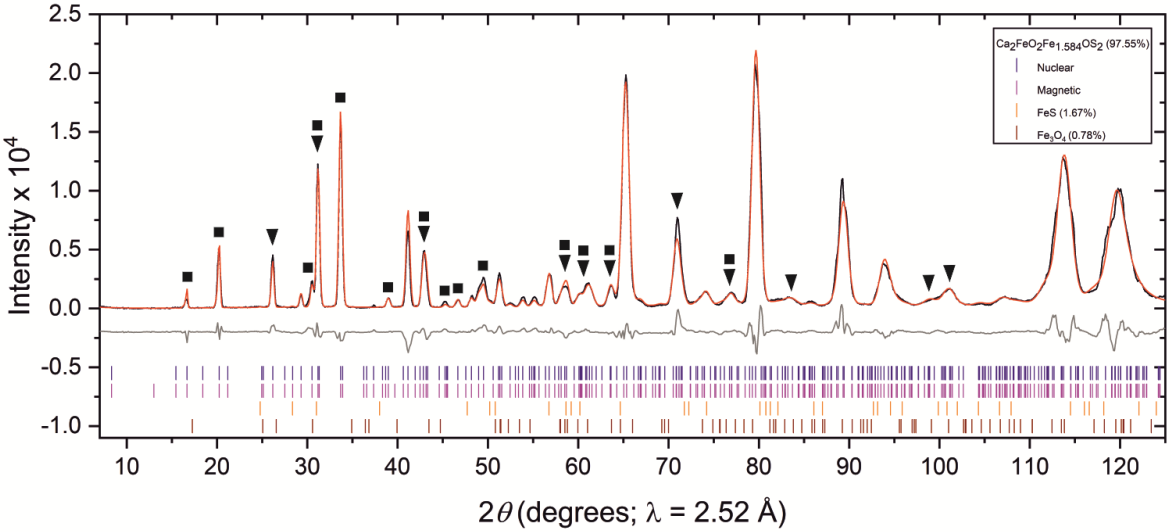


Figure 3.29: NPD pattern of $Ca_2FeO_2Fe_{1.6}OS_2$ measured at 100 K on the D1B instrument at the ILL showing the observed (black), calculated (red) and difference (grey) curves. R_{wp}: 8.363%. The magnetic ordering on the Fe1 sublattice gives rise to intensity on positions marked with a black triangle and the magnetic ordering on the Fe2 sublattice gives rise to intensity on positions marked with a black square.

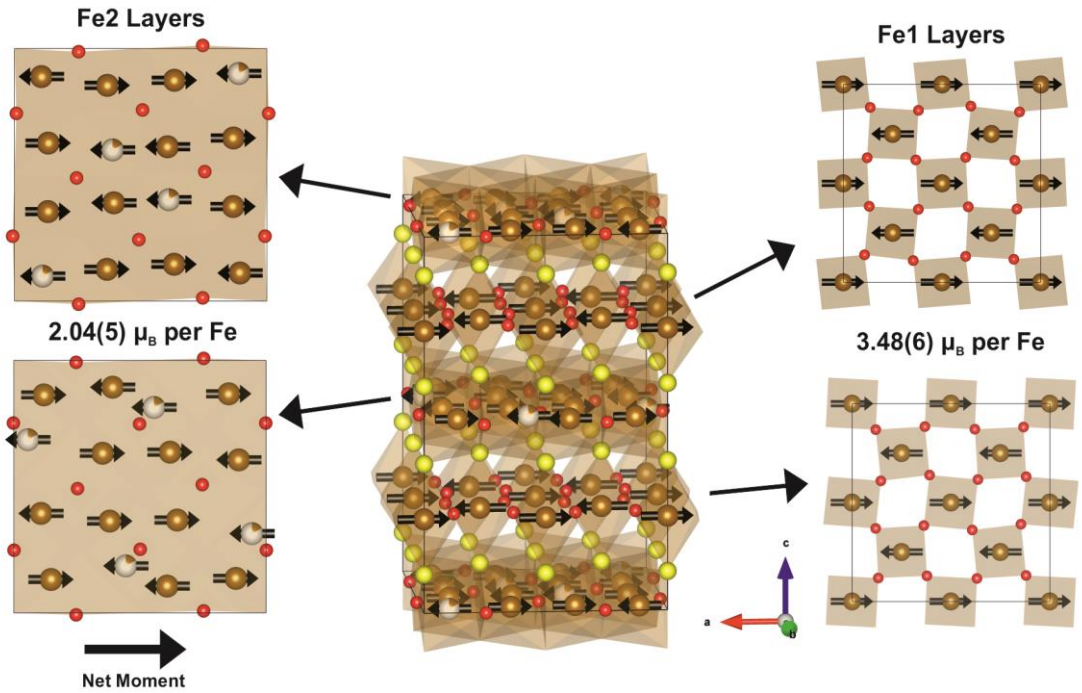


Figure 3.30: Magnetic model for $Ca_2FeO_2Fe_{1.6}OS_2$ at 100 K, refined using the NPD data collected on the D1B instrument at the ILL shown in Figure 3.29.

It is important to note that in the Fe2 layers, even though an equal number of Fe ions have moments directed to the left and to the right, there is an overall net moment as the almost vacant sites all have magnetic moments aligned in the same direction. This gives rise to ferrimagnetism and can explain the ferromagnetic behaviour seen in the hysteresis loops (Figure 3.16, section 3.3.4). The net moment per unit cell is approximately 16 μ_B which equates to 16/48 = $^1/_3$ μ_B per Fe. The magnetic moment in the 5 K hysteresis (Figure 3.16) appears to be saturating towards 0.3 μ_B per Fe, so this agrees well.

The data at 5 K were then analysed following the deduction of the 100 K magnetic model. Again, the nuclear model was refined using the D2B data at 5 K (Figure 3.31) and then this was fixed and the magnetic model was refined against the D1B data (Figure 3.32). Deducing a magnetic model which met the two criteria of fitting the NPD data well and making physical sense was non-trivial indeed. Here the most likely model that has been fit to the data to date is discussed, however the possibility of alternative models cannot be ruled out.

The new magnetic reflections, which appeared at around 70 K, can be accounted for by introducing canting of the moments in both layers. The moments in the Fe1 layer cant in the *c*-direction only, whereas the moments in the Fe2 layer cant in both the *c*-direction and the *a*-direction. In Figure 3.32, canting in the Fe1 layer contributes to peak intensities labelled with a black triangle and canting in the Fe2 layer contributes to peak intensities labelled with a black square. The resultant magnetic model is depicted in Figure 3.33.

It is important to note here that the 100 K magnetic model (shown in Figure 3.30) is a combination of three mGM4 modes (one on each of the Fe1 crystallographic sites) and four mGM3 modes (one on each of the Fe2 crystallographic sites). The magnetic model at 5 K (shown in Figure 3.33) also includes an additional mY1 and mY2 mode on each of the four Fe2 sites and either an additional mY1 or mY2 mode on each of the three Fe1 sites.

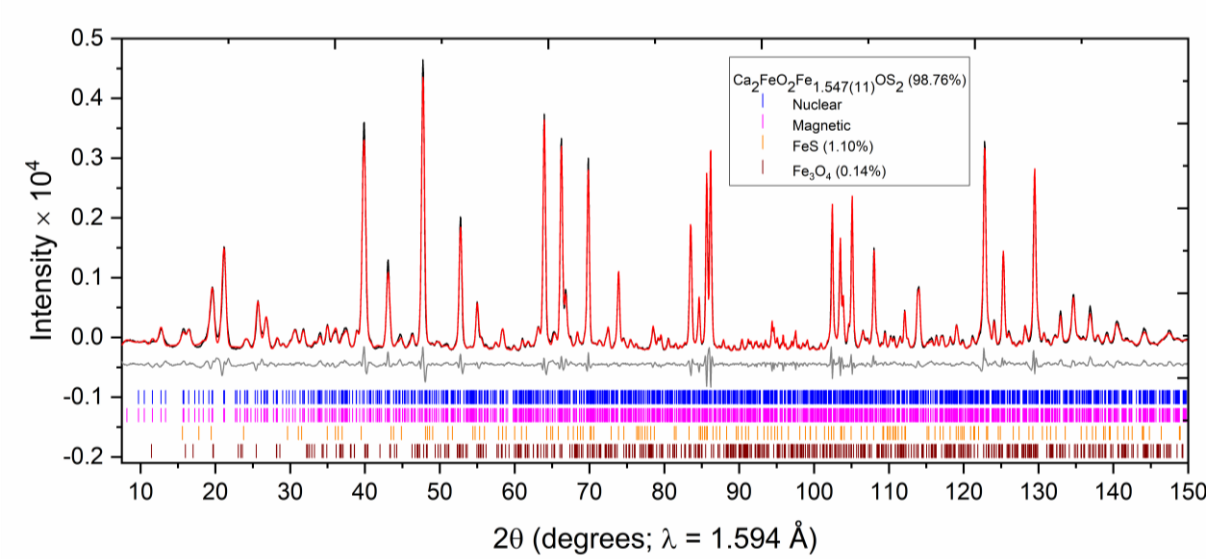


Figure 3.31: NPD pattern of $Ca_2FeO_2Fe_{1.6}OS_2$ measured at 5 K on the D2B instrument at the ILL showing the observed (black), calculated (red) and difference (grey) curves. R_{wp}: 5.523%.

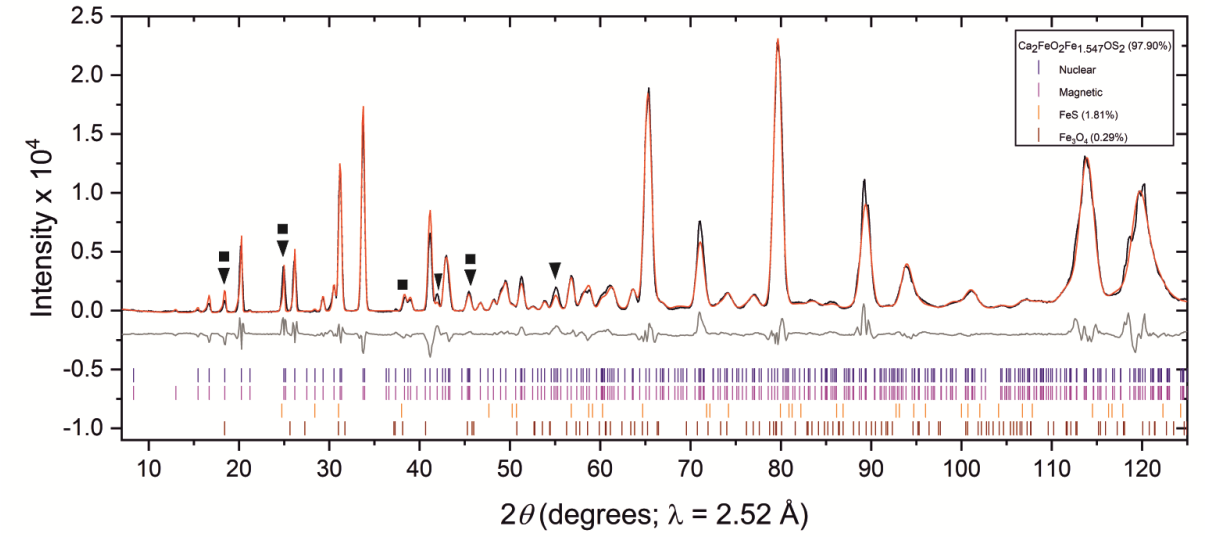


Figure 3.32: NPD pattern of $Ca_2FeO_2Fe_{1.6}OS_2$ measured at 5 K on the D1B instrument at the ILL showing the observed (black), calculated (red) and difference (grey) curves. R_{wp}: 9.375%. The additional magnetic ordering on the Fe1 sublattice gives rise to intensity on positions marked with a black triangle and the additional magnetic ordering on the Fe2 sublattice gives rise to intensity on positions marked with a black square.

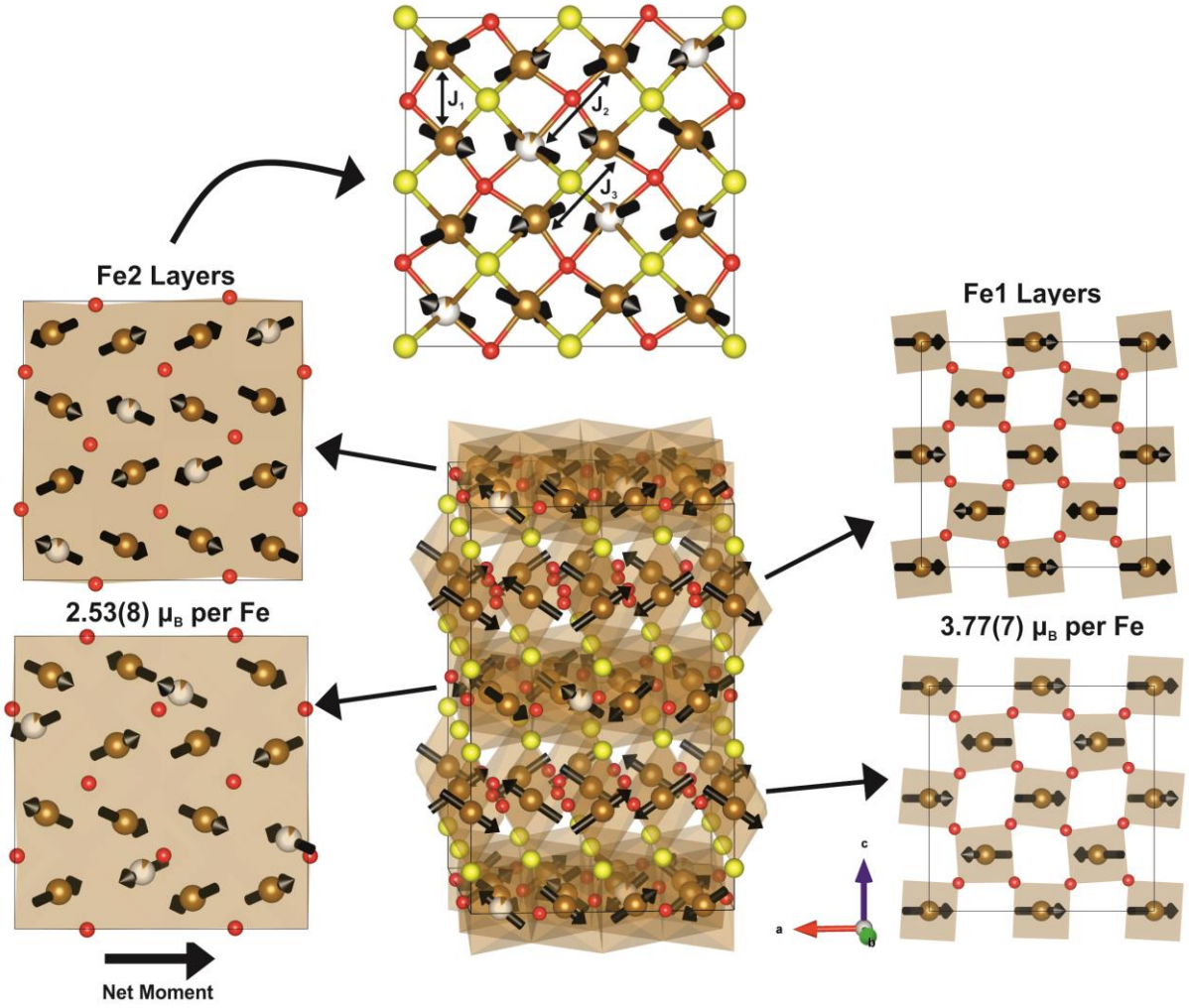


Figure 3.33: Magnetic model for $Ca_2FeO_2Fe_{1.6}OS_2$ at 5 K, refined using the NPD data collected on the D1B instrument at the ILL shown in Figure 3.32. The major magnetic interactions in the Fe2 layer- as considered for materials with analogous layers- are labelled J_1 (Fe-Fe direct exchange), J_2 (~180° Fe-O-Fe superexchange) and J_3 (~90° Fe-S-Fe superexchange).

The refined Fe1 moment of 3.77(7) μ_B suggests this is Fe^{3+} d^5 with the moment reduced from 5 μ_B due to covalency. The refined Fe2 moment of 2.53(8) μ_B suggests this is Fe^{2+} d^6 with the moment reduced from 4 μ_B due to both covalency and Fe2 vacancies in the layer disrupting the long-range order. The main competing magnetic interactions in the Fe2 layer are highlighted by Figure 3.33. These are described by Ni *et al*. for the $La_2O_2Mn_2OSe_2$ material[7] and are labelled here as J_1 (Fe2-Fe2 direct exchange), J_2 (~180° Fe2-O-Fe2 superexchange) and J_3 (~90° Fe2-S-Fe2 superexchange). Looking back at the 100 K model (Figure 3.30), the dominant interaction is likely to be the J_2 Fe2-O-Fe2 superexchange as every J_2 pathway contains antiferromagnetically coupled Fe^{2+} moments, as

expected for σ- and π-type exchanges between these high spin d^6-d^6 cations from Goodenough-Kanamori rules. The approximately 90° Fe2-S-Fe2 superexchange (J_3) would be predicted to be ferromagnetic and it can be seen from the 100 K model that this is the case for all these exchanges, so these are also likely to play a role in the observed magnetic ordering. The direct exchange interaction (J_1) between neighbouring Fe2 cations would involve interaction between d_{xz} and d_{yz} orbitals containing one electron, which would be predicted to be antiferromagnetic. As this is not always the case in Figure 3.30, these interactions are supposed to be superseded by the two superexchange interactions.

There is approximately an extra 0.35 μ_B of moment added to each Fe during this low temperature transition (upon cooling from 70 K to 5 K, see Figure 3.38). This extra moment may arise when itinerant electrons become localised on the Fe centres, which would be consistent with the metal to insulator transition observed in the resistivity data (see section 3.3.11). Intralayer interactions were first considered as a means to explain the canting pattern in the Fe1 layer, such as the Fe1-O-Fe1-O-Fe1 super-superexchange pathways (Figure 3.34). However, one would expect these 90° exchanges to involve ferromagnetic coupling of the spins rather than the antiferromagnetic interactions observed here and also these superexchange interactions are likely to already be acting at temperatures higher than 70 K. Therefore, the canting may instead be dictated by interlayer interactions between the Fe1 and Fe2 layers, which is discussed later in this section. The canting in the Fe2 layer may arise from direct exchange interactions between nearest neighbour Fe2 moments. When considering those nearest neighbour interactions that do not lie on an Fe2-O-Fe2 superexchange pathway- and so were presumed to not already be strongly interacting above 70 K (labelled $J_{A\text{-}C}$ in Figure 3.35)- each interaction now has an antiferromagnetic component in the *a*-direction, *b*-direction and/or *c*-direction. It seems likely that the moments in the Fe2 layer order in such a way to satisfy the criterion of all nearest neighbour spins coupling with some antiferromagnetic component (via direct exchange). The model also suggests possible interaction between the Fe1 and Fe2 layers, as ordering is

concurrent, and possible electron transfer between the Fe^{2+}/Fe^{3+} centres is unveiled by the structural signature which accompanies this transition, as discussed in section 3.3.9.

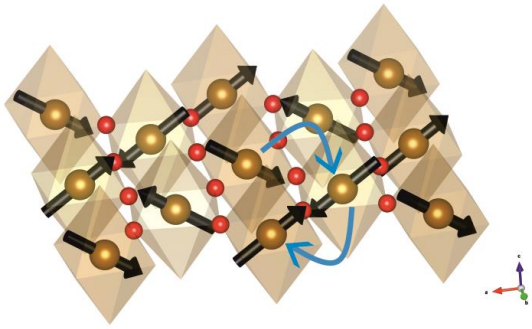


Figure 3.34: Magnetic ordering on the Fe1 sublattice. The blue arrows highlight the Fe1-O-Fe1-O-Fe1 super-superexchange pathway.

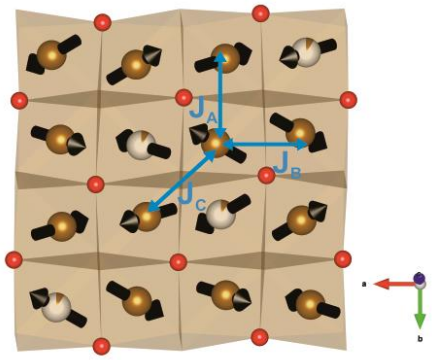


Figure 3.35: Magnetic ordering on the Fe2 sublattice. The Fe2-Fe2 nearest neighbour direct exchanges are given by the blue arrows labelled by J_{A-C}. These direct exchanges (denoted by J_1 in Figure 3.33) are predicted to favour antiferromagnetic interactions between the Fe2 centres.

There are therefore two transition temperatures in the $Ca_2FeO_2Fe_{1.6}OS_2$ material. One occurs at 330(10) K and is modelled as the onset of concurrent antiferromagnetic ordering in both Fe layers, as depicted in Figure 3.30. The other occurs at 69(2) K and is best modelled as a sudden concurrent increase in the magnitude of the Fe1 and Fe2 moments accompanied by canting of these moments, as illustrated in Figure 3.33. It is likely that the moments on the Fe1 layer interact with those on the Fe2 layer, as both sublattices are located on a *k*-vector of $k = (0,0,0)$ and undergo the two ordering transitions concurrently. The Fe1 and Fe2 centres are connected via approximately 130° Fe1-S-Fe2 superexchange pathways which presumably mediate this interaction. At all temperatures below 330(10) K (where all Fe are magnetically ordered) these pathways contain 24 antiferromagnetically

coupled Fe spins and 20 ferromagnetically coupled Fe spins per unit cell, with an example Fe1 centre shown in Figure 3.36. It should be noted here that participation of the mostly vacant Fe2 sites in the long-range magnetic ordering gives an insignificant change to the quality of the Rietveld fits, therefore these contributions have been treated as insignificant. As explained in Figures 3.36 and 3.37, these Fe1-S-Fe2 pathways would involve the $d_{x^2-y^2}$ and d_{z^2} orbitals of the Fe^{2+} (d^6) and Fe^{3+} (d^5) cations respectively, which results in neither antiferromagnetic or ferromagnetic coupling being favoured. Therefore, it seems unclear why the moments in both Fe layers cant in this manner, especially in the Fe1 layer where the canting arrangement is particularly challenging to explain. Further experiments, such as neutron powder diffraction in an applied magnetic field or neutron diffraction on single crystals, may give rise to an alternative magnetic model which can be better rationalised.

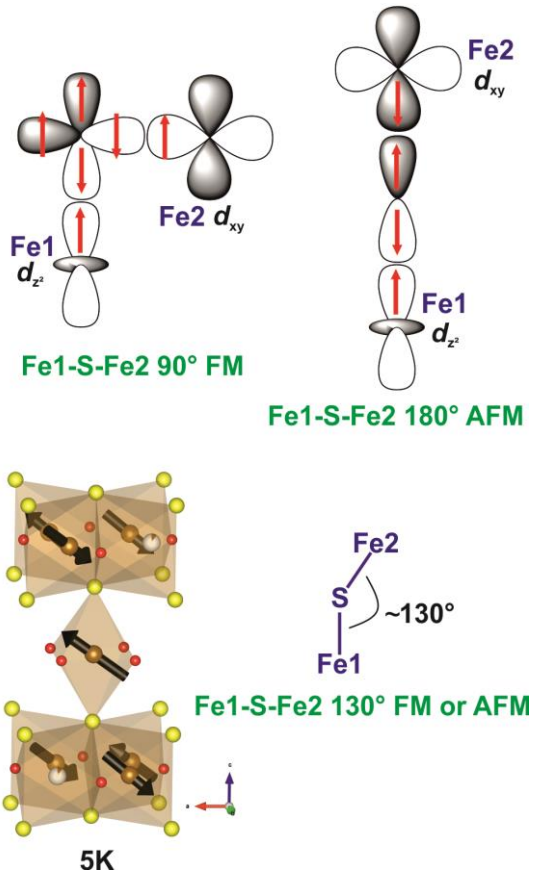


Figure 3.36: Diagrams explaining the expected ferromagnetic (FM) interaction and antiferromagnetic (AFM) interaction when the Fe1-S-Fe2 superexchange pathway has 90° geometry and 180° geometry respectively (top), where the actual case in the $Ca_2FeO_2Fe_{1.6}OS_2$ material is a geometry of ~130° for the Fe1-S-Fe2 pathway which presumably wouldn't favour FM or AFM coupling of the Fe spins (bottom). This only considers the σ interactions which are likely to be stronger than the π interactions present here too.

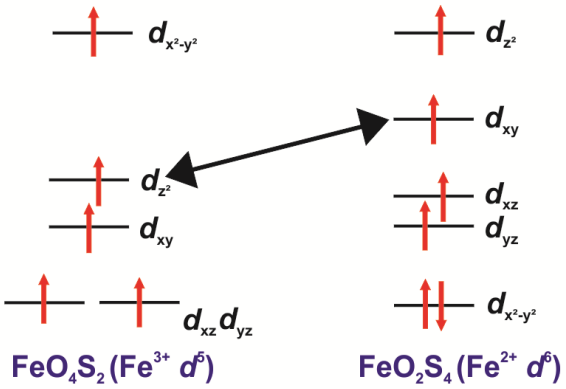


Figure 3.37: The Fe1-S-Fe2 superexchange pathways involve interaction of the Fe^{3+} d_{z^2} orbital and the Fe^{2+} d_{xy} orbital, both of which are occupied by a single electron.

The evolution of the Fe long-range ordered moments is plotted in Figure 3.38 and a plot of all the data collected on D1B are shown in Figure 3.39. The unusual linear increase of the Fe2 moment before 70 K reflects the linear increase in intensity of a selection of the magnetic Bragg peaks, for example the one which appears at 2θ = 20°. This is in contrast to the magnetic Bragg peak at 2θ = 26° which increases sharply in intensity initially then the rate of growth decreases. This gives rise to the different shapes of the curves for the Fe1 moment and the Fe2 moment (above 70 K). The $Eu(Fe_{0.86}Ir_{0.14})_2As_2$ material[8] is reported to exhibit magnetic Bragg peaks arising from the ferromagnetic ordering of the Eu^{2+} which also follow a very similar trend in integrated intensity to those observed here (in terms of the unusual increase in the magnitude of the Fe2 moments), however no comment is offered on the reason behind this unusual growth in intensity.

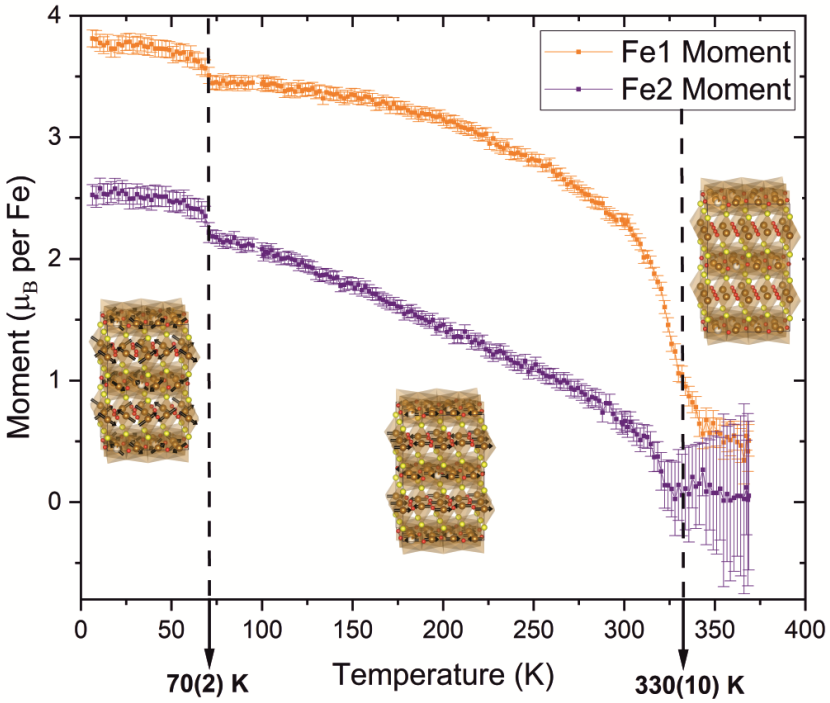


Figure 3.38: Magnetic moments on the Fe1 and Fe2 sites, refined from variable temperature NPD patterns of $Ca_2FeO_2Fe_{1.6}OS_2$ gathered on the D1B instrument at the ILL.

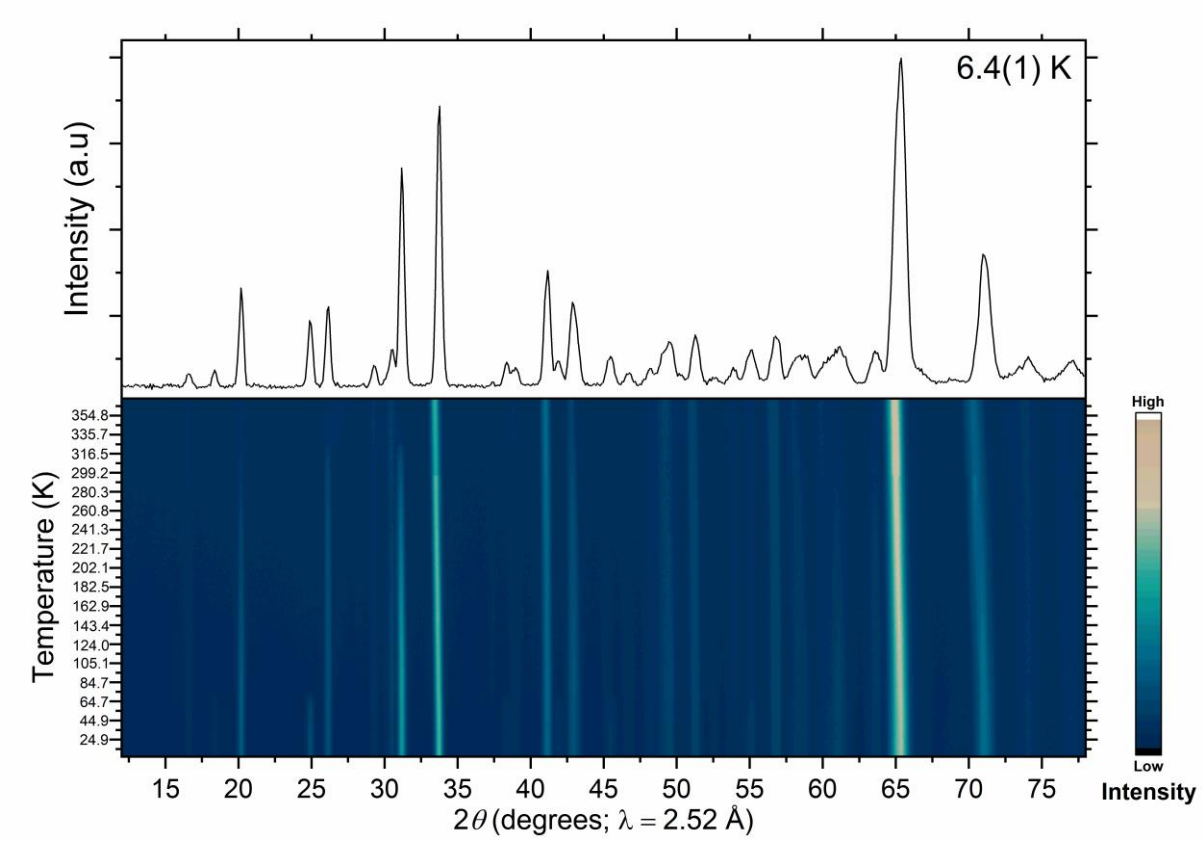


Figure 3.39: Plot of the NPD data collected for $Ca_2FeO_2Fe_{1.6}OS_2$ from 6 K to 369 K.

The variable temperature NPD data were also used to investigate any structural changes. Due to the low resolution in the *d*-spacing region where structural intensity appears in data from D1B, only the unit cell lattice parameters were refined. It can seen in the plot given in Figure 3.40 that there are changes to the linear decrease of the lattice parameters with decreasing temperature at around 333 K, 150 K and 70 K. The highest temperature coincides with the first long-range magnetic ordering transition and the lowest temperature with the second long-range magnetic ordering transition. The apparent increase in the *a* and *c* lattice parameters around 150 K is intriguing and Figure 3.41 shows that this is mainly a volume change with the *c*/*a* ratio approximately following the trend above and below this temperature. This change isn't present in the variable temperature XRPD data, as discussed in section 3.3.9, and so it is likely to be an artefact of the variable temperature NPD measurements.

The increasing *a* parameter below 70 K prompted further study using in-house variable temperature XRPD. This is described in section 3.3.9.

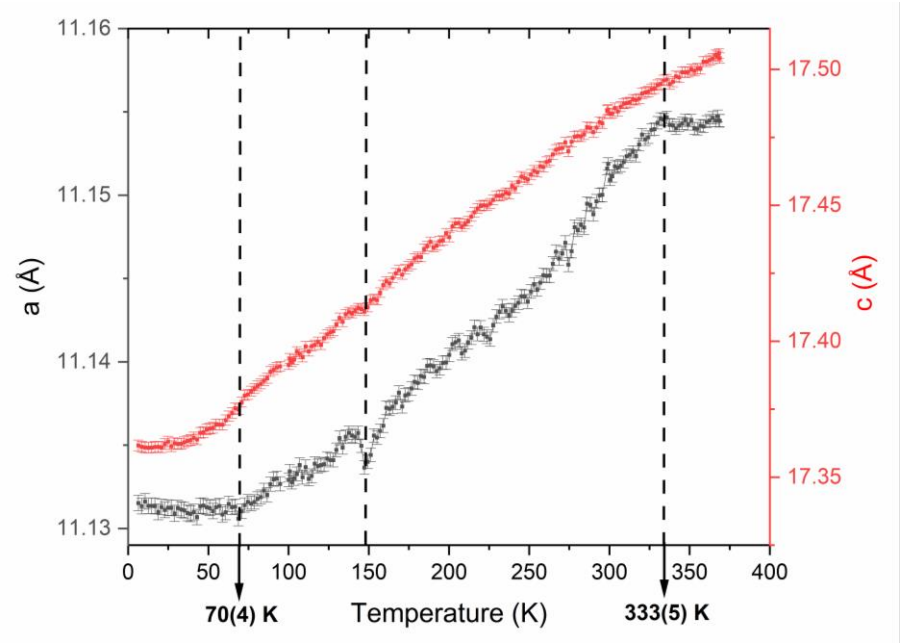


Figure 3.40: The *a* and *c* lattice parameters, refined from variable temperature NPD patterns of $Ca_2FeO_2Fe_{1.6}OS_2$ gathered on the D1B instrument at the ILL.

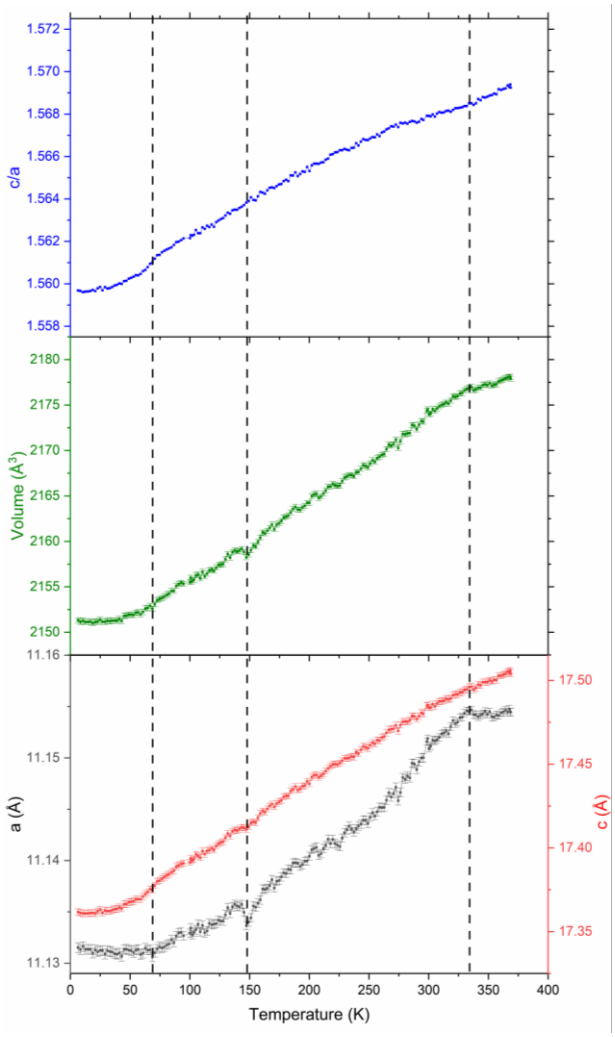


Figure 3.41: The *c*/*a* ratio (top), unit cell volume (middle) and lattice parameters (bottom), refined from variable temperature NPD patterns of $Ca_2FeO_2Fe_{1.6}OS_2$ gathered on the D1B instrument at the ILL.

3.3.9 Variable Temperature XRPD

Low temperature XRPD data were collected in-house in order to further probe the changes in the lattice parameters observed in the variable temperature NPD refinements (see section 3.3.8). It can be seen that as the temperature decreases below around 70 K, the *a* lattice parameter, which is an approximate proxy for the Fe-O bond lengths, begins to increase (Figure 3.42a)) while the *c* lattice parameter drops sharply (Figure 3.42b)). The significant decrease of *c* results in a similar decrease observed for the *c*/*a* ratio and the unit cell volume, as shown in Figure 3.42c) and 3.42d) respectively. There is evidently a structural signature of the low temperature magnetic ordering transition.

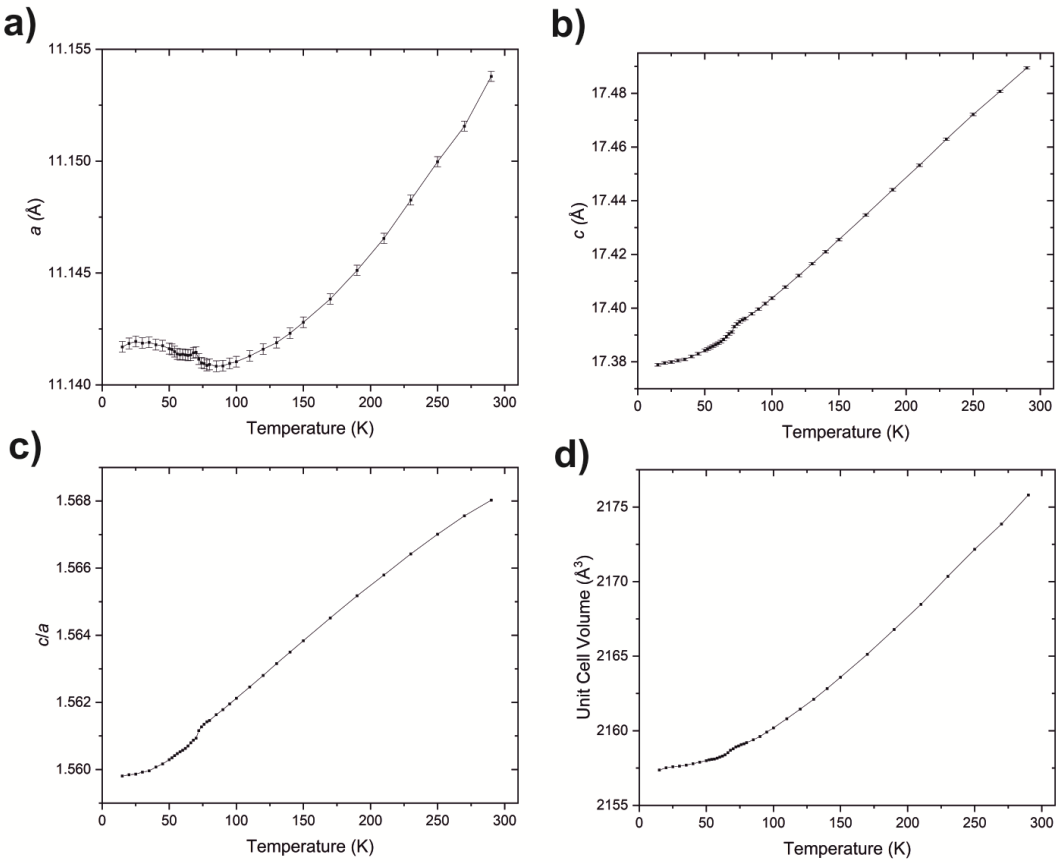


Figure 3.42: The variation with temperature of **a)** the *a* lattice parameter **b)** the *c* lattice parameter **c)** the *c*/*a* ratio and **d)** the unit cell volume, refined from variable temperature XRPD patterns of $Ca_2FeO_2Fe_{1.6}OS_2$ gathered on the Malvern Panalytical Empyrean Mo diffractometer with PheniX cryostage.

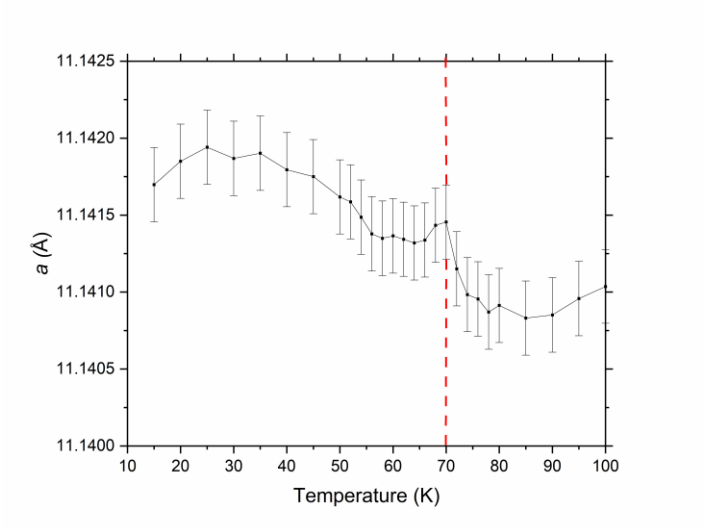


Figure 3.43: Low temperature region of Figure 3.42a).

The *a* lattice parameter behaves unusually in the low temperature region. Not only does it appear to increase upon cooling from around 85 K to 25 K, it also exhibits a sharp increase and then a drop centred around 70 K, as highlighted by the red dashed line in Figure 3.43.

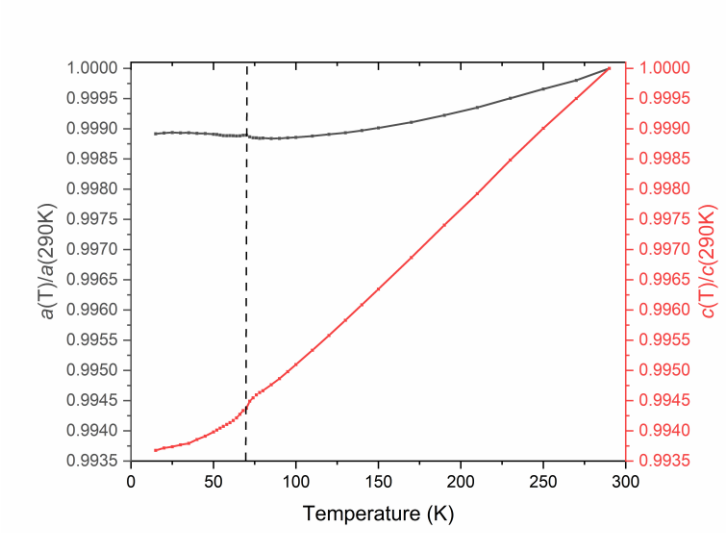


Figure 3.44: The *a* and *c* lattice parameters normalised against their value at 290 K.

Plots of the normalised lattice parameters given in Figure 3.44 show that, just before cooling to 70 K, the sharp rise in *a* is accompanied by the sharp drop in *c*. The volume change is dominated by the decrease in *c* because this drop in the normalised value is greater in magnitude than the increase in the normalised value of *a*.

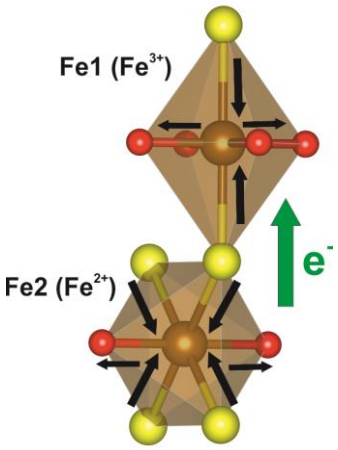


Figure 3.45: Schematic showing the small structural changes likely to occur in the Fe polyhedra (as depicted by the black arrows) observed upon cooling just before 70 K is reached. A possible driver for this transition would be a small amount of electron transfer indicated by the green arrow.

As *a* expands and *c* contracts, it can be predicted that in the distorted octahedra around Fe1 and Fe2 the Fe-O bonds increase in length and the Fe-S bonds decrease in length. This is illustrated in Figure 3.45 and could be caused by a small electron transfer from Fe2 Fe^{2+} d^6 to Fe1 Fe^{3+} d^5. As the predicted magnetic model appears to suggest that the Fe1 and Fe2 layers do not order independently and the pathway along Fe2-S-Fe1 is relatively short (~ 5 Å), electron transfer between the metal centres seems plausible. One may expect the magnitude of the Fe1 ordered moments to decrease ($d^5 \rightarrow d^6$) and Fe2 ordered moments to increase ($d^6 \rightarrow d^5$) during this redox process, however from the analysis of the NPD data shown in section 3.3.8 they both appear to increase as the ordering becomes stronger.

A variable temperature synchrotron XRPD experiment was performed at the ESRF (Grenoble, France) to obtain XRPD data of a higher resolution than the in-house data, with the hope that the Fe-S bond lengths of the FeO_4S_2 and FeO_2S_4 distorted octahedra could be extracted from refinement of the structural model against the data. Unfortunately, the bond distance errors are significant meaning no clear trend is observed (see Appendix A.6). Also, the changes in the lattice parameters appear at lower temperatures and this is likely to be an effect of sample heating from the intense x-ray beam (see Appendix A.7). The Fe-S bond lengths obtained from the variable temperature D2B NPD data have significant errors too (see Appendix A.8).

Therefore, further studies including high-resolution variable temperature NPD (e.g. using the HPRD instrument at ISIS Neutron and Muon Source) and variable temperature XANES experiments, could probe deeper into this low temperature structural change and help to deduce the likelihood of this electron transfer occurring. Another possibility is that this structural change is due to magnetostriction, as the second long-range magnetic ordering transition coincides with this change to the octahedral Fe environments (both of which occur around 70 K).

3.3.10 Heat Capacity

Heat capacity data measured by Dr. Dharmalingam Prabhakaran in Oxford Physics from room temperature down to 3 K exhibited a signal around 70 K, the origin of which is highly likely to be the magnetic transition at this temperature. Measurements in this temperature region were then taken with the sample under the influence of different applied magnetic fields. The signal from the antiferromagnetic ordering shifts to slightly lower temperatures and broadens, and appears to decrease in intensity as the field strength is increased until it is scarcely evident above the background lattice heat capacity at 10 T. These findings are shown in Figure 3.46.

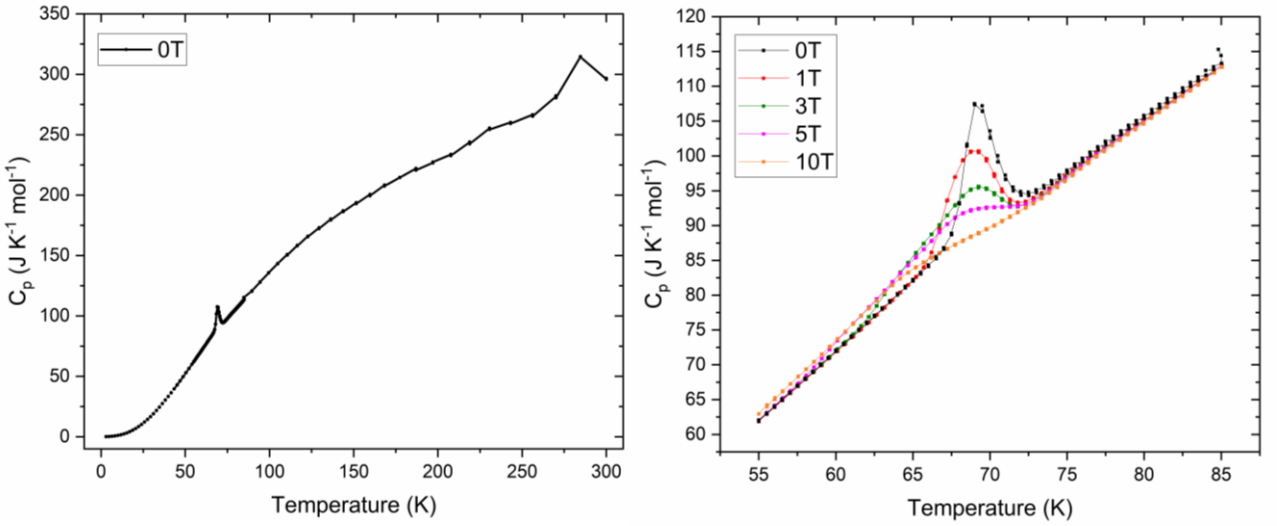


Figure 3.46: The specific heat capacity, C_p, of $Ca_2FeO_2Fe_{1.6}OS_2$ over the full temperature range with no applied field (left) and focussing on temperatures around the magnetic transition with different strengths of applied fields (right). Data above approximately 200 K should be ignored as these contain heat capacity changes from the grease and any adsorbed water.

Integration of a plot of $^{C_p}/_{T}$ $vs\ T$ under the magnetic peak is shown in Figure 3.47 and gives $\Delta S_{mag} = 0.58789\ JK^{-1}mol^{-1}$. As the expected maximum entropy change is equal to $Rln(2S+1)$, it follows that $S = 0.03663$ for this transition. This signifies that this long-range magnetic ordering transition involves approximately $^{1}/_{13}{}^{th}$ of an electron per Fe ion. However, a better approximation is perhaps performed by subtracting a linear baseline, as shown on the left of Figure 3.48. This gives the plot of $^{C_p}/_{T}$ $vs\ T$ shown on the right of Figure 3.48 and integration under this curve results in $\Delta S_{mag} =$

$1.69903\,JK^{-1}mol^{-1}$, which agrees fairly well with the value of $\Delta S_{mag} = 1.02\,JK^{-1}mol^{-1}$ reported by Zhang *et al*.[1] The value obtained here equates to $S = 0.11337$ (around $^1/_4$ of an electron) and could explain the extra 0.35 μ_B per Fe (or equivalently 0.35 e^- per Fe) which is predicted by the NPD data to arise during this transition (see section 3.3.8). These two different treatments exemplify the importance of subtracting a good estimation for the lattice contribution to C_p. For a more accurate determination of magnetic entropy, a non-magnetic analogous material should be measured to get a more accurate determination of the lattice contribution to C_p. This currently does not exist, but similar heat capacity studies have been done on structurally similar perovskite compounds.[9]

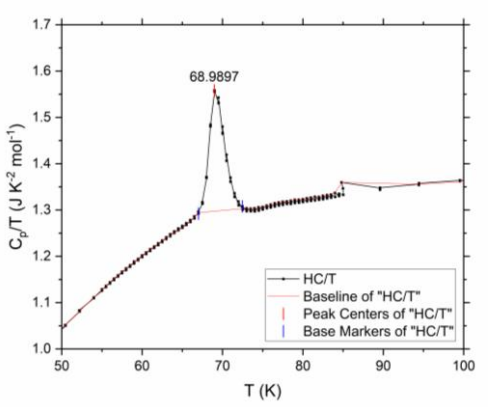


Figure 3.47: Integration of a plot of C_p/T vs T to calculate the area of the magnetic transition peak above the main curve, giving the entropy change for the magnetic transition.

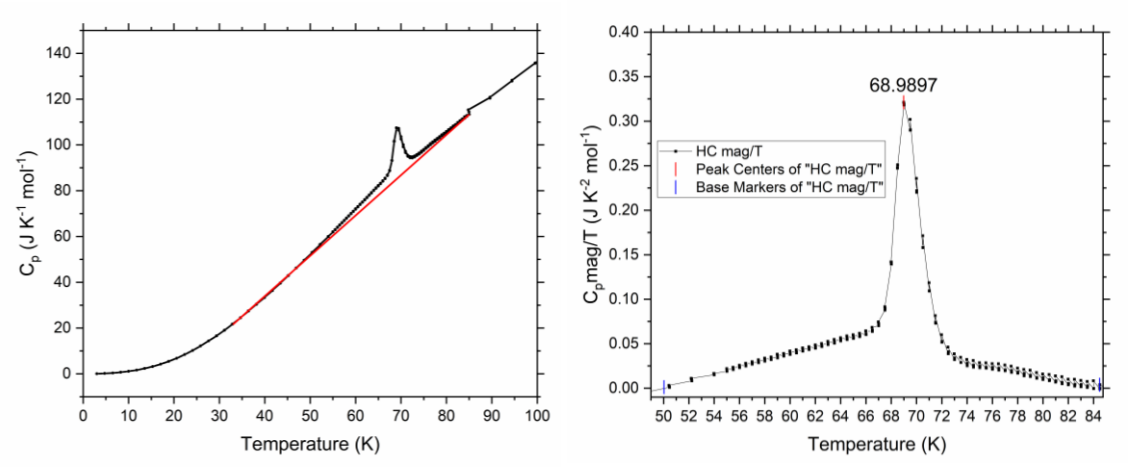


Figure 3.48: The baseline subtracted from C_p is shown by the linear red line (left) and the resulting integration of the plot of C_p/T vs T to calculate the area of the magnetic transition peak, giving the entropy change for the magnetic transition.

3.3.11 Resistivity

The change in resistivity of a sintered bar of $Ca_2FeO_2Fe_{1.6}OS_2$ with temperature is shown in Figure 3.49a). There is a sharp increase in the resistivity of the bar upon cooling below around 100 K and the material reaches its highest resistance around 80 K. The resistance of the bar was too high for the PPMS to measure below 80 K, therefore one would predict that the resistance of the bar at lower temperatures is very high. These data don't give any clear information about the 70 K transition itself except that they show that the resistivity is too large to measure below a temperature just above the transition. The plot given in Figure 3.49b) shows that the data over this whole temperature range can be fitted well as semiconducting behaviour, as the relationship shown is linear. An estimate for the band gap, E_a, is 0.090 eV and so the solid is a very small band gap semiconductor. This value agrees well with that of 0.073 eV found by Zhang *et al*.[1]

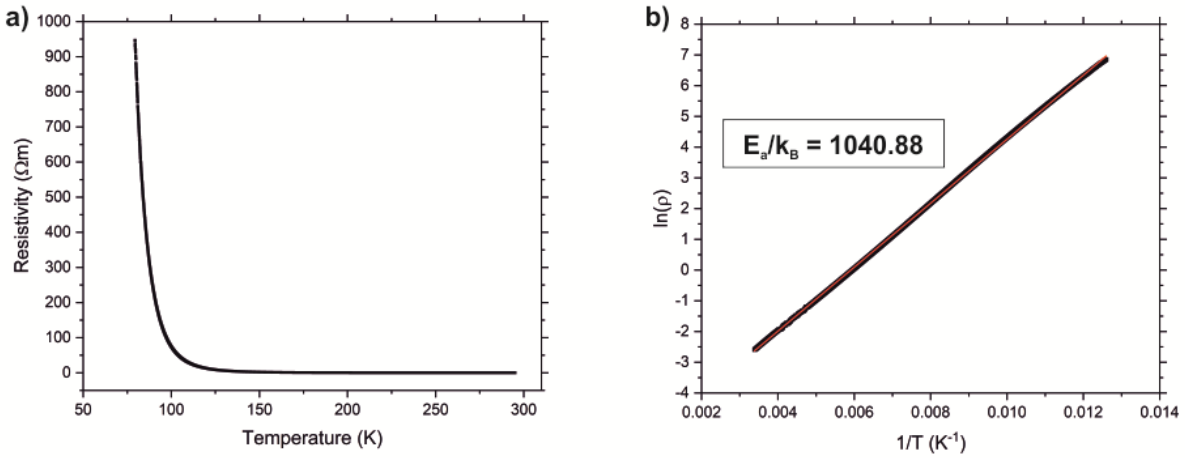


Figure 3.49: Plots showing **a)** the change in the resistivity of a sintered bar of $Ca_2FeO_2Fe_{1.6}OS_2$ and **b)** the resulting dependence of ln(ρ) with 1/T (black) and a linear fit to determine the gradient (red).

Data were collected upon cooling and then warming the sample, as illustrated in Figure 3.50. There is little hysteresis of the electrical behaviour of the sample, showing that the sharp rise in resistance is a reversible change. Resistivity data were collected by Dr Dharmalingam Prabhakaran in Oxford Physics.

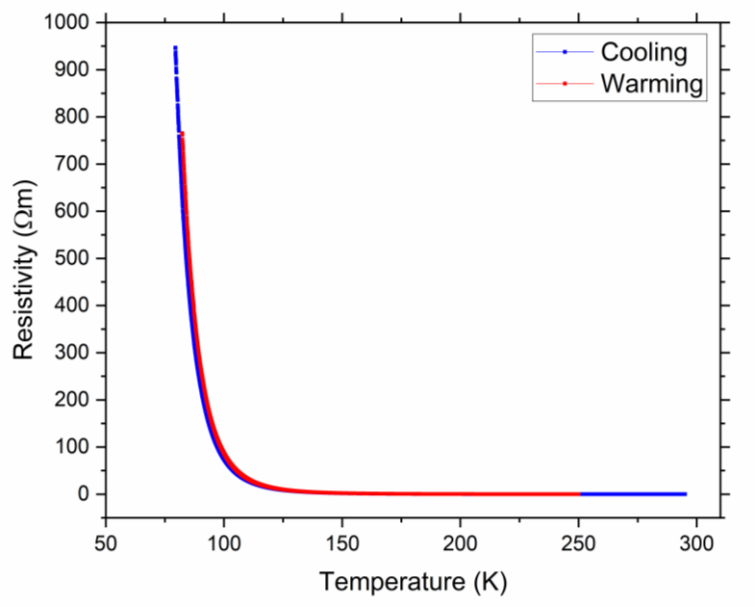


Figure 3.50: The change in the resistivity of $Ca_2FeO_2Fe_{1.6}OS_2$ upon cooling (blue) and then warming (red).

3.3.12 Mössbauer Spectroscopy

Figure 3.51 shows Mössbauer spectra at three temperatures- 300 K, 77 K and 10 K. At room temperature, the spectrum can be described as consisting of doublets and sextets. It is likely that the sextets arise from the Fe^{3+} in the Fe1 layer as at 300 K these are ordered to a fairly high degree (ordered moment at 300 K is around 2/3 of the saturated value at 5 K). The Fe^{2+} in the Fe2 layer may be producing the doublets as these are still only very weakly coupled at 300 K, as shown previously in Figure 3.38. As the material is cooled to 77 K and then 10 K, it can be seen that the intensity of the doublets diminishes and further sextets appear. The sextets also increase in quadrupole splitting, indicating the strength of the magnetic ordering increasing, as expected. The Mössbauer data were collected and analysed by Dr. Alex Scrimshire, Sheffield Hallam University.

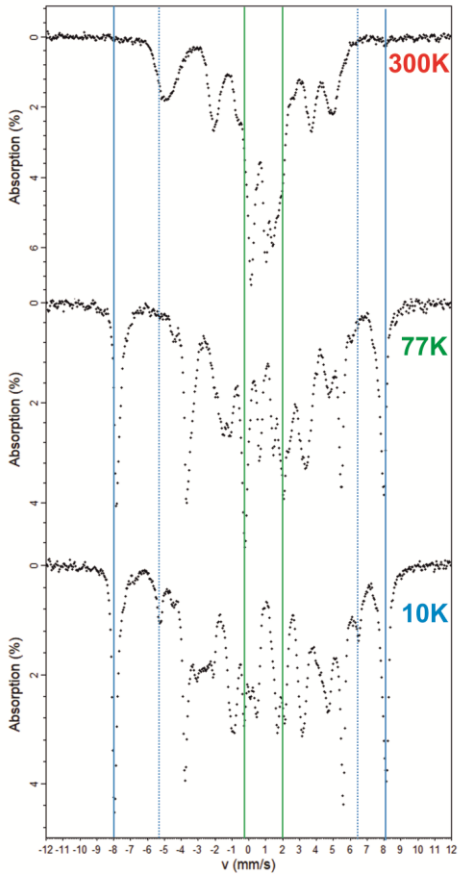


Figure 3.51: Variable temperature Mössbauer spectra of $Ca_2FeO_2Fe_{1.6}OS_2$. Highlighted are the outermost peaks at 10 K (blue solid lines), sextet peaks which visibly increase in quadrupole splitting upon going from 77 K to 10 K (blue dashed lines) and doublet peaks which visibly decrease in intensity upon going from 77 K to 10 K (green solid lines).

There appear to be some small differences between the spectra measured at 77 K and 10 K. The outermost peaks perhaps only shift to slightly greater values of velocity, *v*, as highlighted the blue solid lines in Figure 3.51, which indicate the final positions of these outermost peaks at 10 K and those at 77 K are very close to this. There also seems to visibly be a slight loss of intensity to central signals (green lines) and an increase in the quadrupole splitting of some sextets (blue dashed lines).

Looking at the fit for the 10 K data given in Figure 3.52 and Table 3.7, the doublet has a very low site population and all the Fe in the material is expected to be long-range ordered well above 10 K, so this site will be treated as insignificant. Sextets with a lower centre shift (CS) are assigned to high spin Fe^{3+} d^5 in the Fe1 layer and sextets with a higher centre shift (CS) are assigned to high spin Fe^{2+} d^6 in the Fe2 layer, as would usually be the case in ^{57}Fe Mössbauer. The exception to this is sextet 1, which could plausibly be explained by the presence of a small amount of low spin Fe^{2+} d^6 in the Fe2 layer. Fe1 site populations add up to 40(5)% and Fe2 site populations add up to 59(7)%, which agrees very well with the approximate ratio of 40:60 for the Fe1:Fe2 due to the stoichiometry.

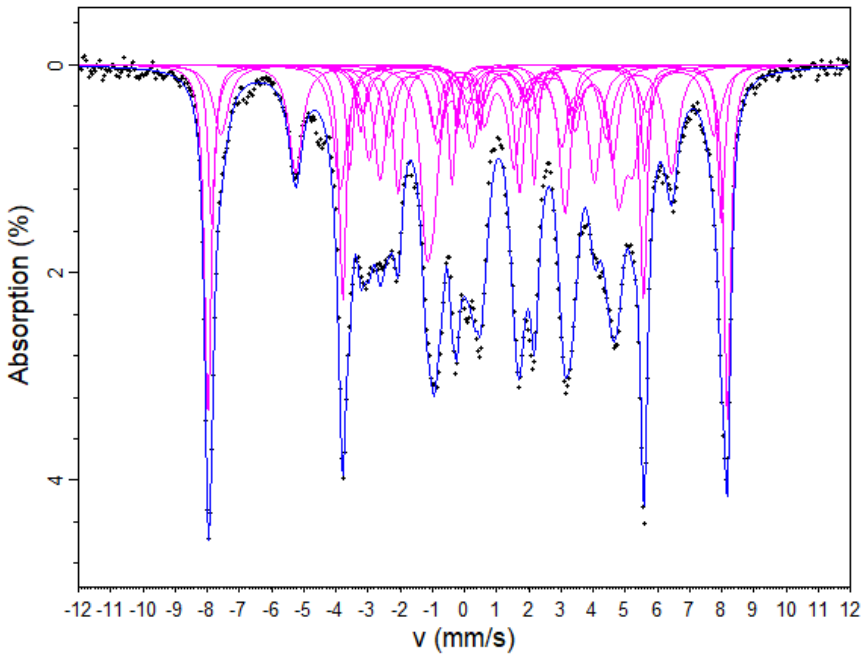


Figure 3.52: Fitting of the Mössbauer spectrum of $Ca_2FeO_2Fe_{1.6}OS_2$ at 10 K, showing the observed data (black points), calculated fit (blue line) and the contribution of each individual site (pink lines). Reduced χ^2: 3.05519.

Site	CS (mm/s)	Fe OS	Δ (mm/s)	Fe Layer	Site Population (%)
Doublet 1	0.133(13)	-	0.725(25)	-	1.41(25)
Sextet 1	-0.066(11)	+2	0.1035(100)	Fe2	7.81(67)
Sextet 2	0.4986(26)	+3	-0.3970(29)	Fe1	18.8(15)
Sextet 3	0.5426(54)	+3	-0.4772(64)	Fe1	8.4(22)
Sextet 4	0.632(10)	+3	0.3400(90)	Fe1	12.49(58)
Sextet 5	0.680(27)	+2	-0.578(25)	Fe2	8.1(17)
Sextet 6	0.818(12)	+2	-0.219(12)	Fe2	11.13(61)
Sextet 7	0.906(12)	+2	-0.188(14)	Fe2	10.5(14)
Sextet 8	1.040(18)	+2	-0.219(15)	Fe2	8.4(14)
Sextet 9	1.606(11)	+2	-1.1400(96)	Fe2	12.82(77)

Table 3.7: Fitting results for the Mössbauer spectrum of $Ca_2FeO_2Fe_{1.6}OS_2$ at 10 K (shown in Figure 3.50), including proposed Fe oxidation states (OS) and the Fe layer from which each site originates.

Now looking at the fit for the 77 K data given in Figure 3.53 and Table 3.8, the doublets have low site populations and all the Fe in the material is expected to be long-range ordered well above 77 K, so these sites will be treated as insignificant. Sextets 5-7 also have very low site populations and so will be treated as insignificant. Sextets with a lower centre shift (CS) are assigned to high spin Fe^{3+} d^5 in the Fe1 layer and sextets with a higher centre shift (CS) are assigned to high spin Fe^{2+} d^6 in the Fe2 layer, as would usually be the case in ^{57}Fe Mössbauer. Fe1 site populations add up to 35(5)% and Fe2 site populations add up to 46(3)%, which agrees fairly well with the approximate ratio of 40:60 for the Fe1:Fe2 due to the stoichiometry.

According to the crystal structure, there are three crystallographically unique Fe1 sites and three (fully occupied) crystallographically unique Fe2 sites. The 10 K fitting of the Mössbauer data contains three Fe1 sites and six Fe2 sites, whereas the 77 K data is fit using two Fe1 sites and two Fe2 sites. Therefore, the fitting of the Mössbauer spectra reflects the Fe1 sites well and, as all three sites are in very similar environments, perhaps the change from three sites at 10 K to two sites at 77 K is due to overlap between the sextets. The same reasoning of sextet overlap could be used to explain the two Fe2 sites at 77 K rather than the expected three from the crystal structure. It seems unusual that at 10 K there are six Fe2 sites used in the Mössbauer fitting, however this may be due to symmetry lowering of the crystal structure the 70 K transition, the nature of which needs probing further. It should be stressed that the fitting of Mössbauer data is a difficult task which can be achieved using multiple different

combinations of Fe sites, and that the assignments of the sites given here are done so in an attempt to rationalise these fittings performed by collaborator Dr. Alex Scrimshire.

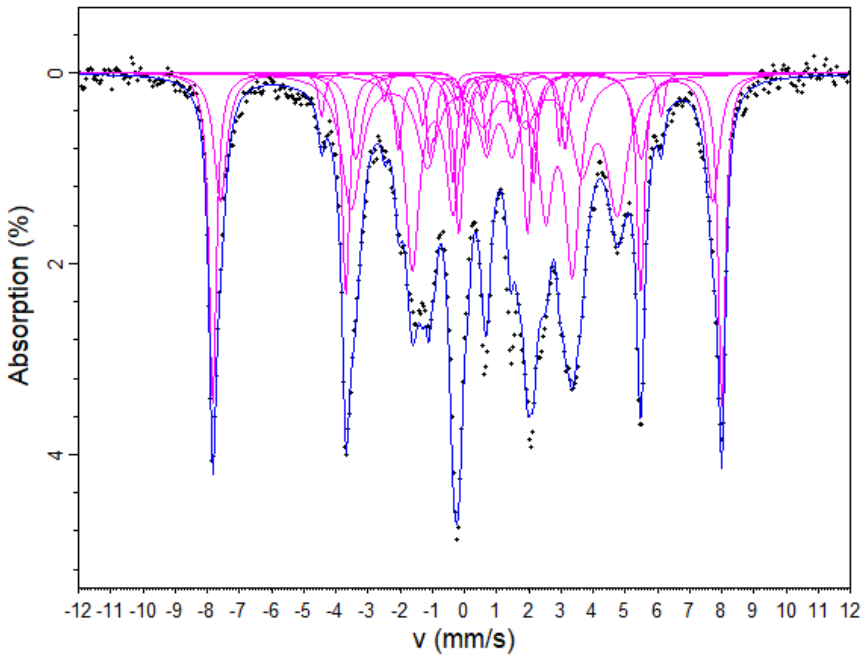


Figure 3.53: Fitting of the Mössbauer spectrum of $Ca_2FeO_2Fe_{1.6}OS_2$ at 77 K, showing the observed data (black points), calculated fit (blue line) and the contribution of each individual site (pink lines). Reduced χ^2: 2.31175.

Site	CS (mm/s)	Fe OS	Δ (mm/s)	Fe Layer	Site Population (%)
Doublet 1	0.408(17)	-	0.601(35)	-	1.99(29)
Doublet 2	0.896(10)	-	2.130(24)	-	6.19(48)
Sextet 1	0.4941(35)	+3	-0.4038(36)	Fe1	20.9(21)
Sextet 2	0.566(15)	+3	-0.495(15)	Fe1	14.1(26)
Sextet 3	0.937(23)	+2	-0.316(22)	Fe2	23.1(12)
Sextet 4	0.979(11)	+2	-0.1095(95)	Fe2	23.1(16)
Sextet 5	0.369(17)	-	0.169(18)	-	4.9(12)
Sextet 6	0.711(23)	-	0.131(23)	-	2.38(56)
Sextet 7	0.592(15)	-	0.337(13)	-	3.43(67)

Table 3.8: Fitting results for the Mössbauer spectrum of $Ca_2FeO_2Fe_{1.6}OS_2$ at 77 K (shown in Figure 3.51), including proposed Fe oxidation states (OS) and the Fe layer from which each site originates.

Unfortunately, the spectrum measured at 300 K (Figure 3.54) cannot be fit in a meaningful manner because of the presence of many features superimposed on each other. Therefore, as future work, the sample should be measured in the paramagnetic regime (i.e., above approximately 350 K), where only doublets would expected to be present and so the data would be able to be successfully fit.

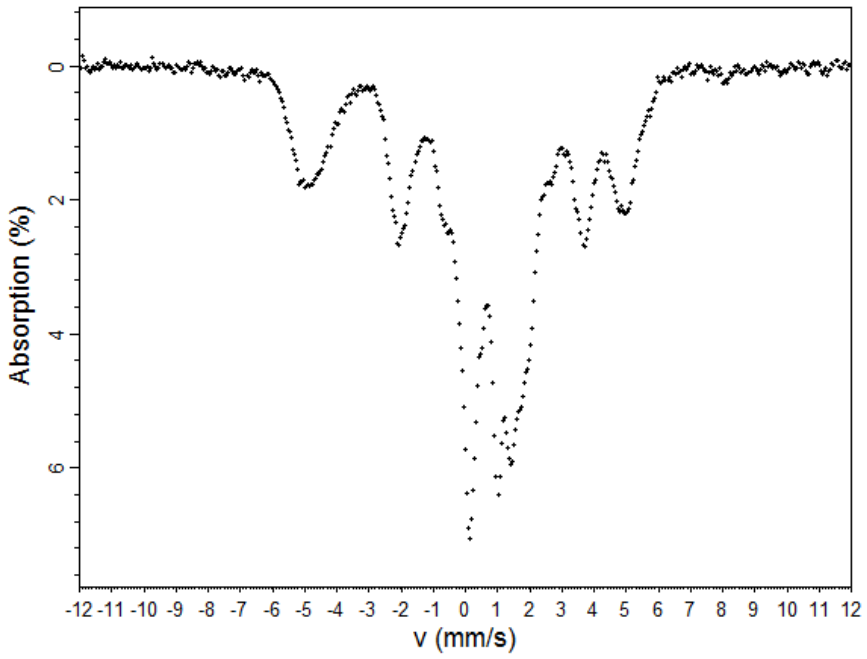


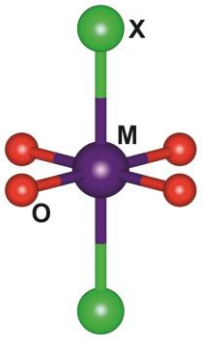
Figure 3.54: The Mössbauer spectrum of $Ca_2FeO_2Fe_{1.6}OS_2$ at 300 K.

3.4 Discussion

3.4.1 Crystal Structure

As previously mentioned, $Ca_2FeO_2Fe_{1.6}OS_2$ appears to be the only compound reported in the literature with this exact structure type prior to the work in this thesis (see Chapter 5 for analysis of the novel $Sr_2CrO_2Cr_2OAs_2$ material[10] which is indeed isostructural). There are also many examples of materials which contain either a layer analogous to the Fe1 layers $[FeO_2]^-$ (eg $Sr_2NiO_2Cu_2Se_2$[11]) or a layer analogous to fully occupied Fe2 layers $[Fe_{2-\delta}OS_2]^{(2+2\delta)-}$ (eg $Sr_2F_2Fe_2OS_2$[12]).

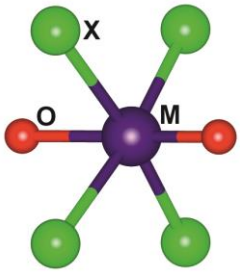
The type of layers present in the Fe1 layer are similar to those formed by other 3*d* transition metals in compounds such as those listed in Table 3.9. In these examples the 3*d* metal is in the +2 or +2.5 oxidation state, however in $Ca_2FeO_2Fe_{1.6}OS_2$ the data that has been presented in this thesis suggest that Fe^{3+} exists in these layers. It is likely that the shorter distances of the both the equatorial M-O and apical M-X bonds, partly arising from the presence of the small Ca^{2+} ion, stabilise the higher +3 oxidation state of the transition metal.



Compound	M-O Distances [x4] (Å)	M-X Distances [x2] (Å)	M BVS	M Formal OS
$Sr_2NiO_2Cu_2Se_2$	2.013235(4)	3.0843(3)	+1.671(1)	+2
$Sr_2CuO_2Cu_2Se_2$	1.99106(2)	3.1784(7)	+1.808(1)	+2
$Sr_2ZnO_2Cu_2Se_2$	2.03260(2)	3.0968(4)	+1.833(1)	+2
$Sr_2CoO_2Cl_2$	2.03126(2)	2.745(2)	+1.891(2)	+2
$Sr_2MnO_2Cu_{1.5}S_2$	2.0070(1)	2.915(1)	+2.531(2)	+2.5
$Ca_2FeO_2Fe_{1.6}OS_2$	1.9732(1)	2.5872(7)	+2.85(1)	+3

Table 3.9: Comparison of bond distances, bond valence sums (BVS) and formal metal oxidation states (OS) for $Sr_2NiO_2Cu_2Se_2$,[11] $Sr_2CuO_2Cu_2Se_2$,[13] $Sr_2ZnO_2Cu_2Se_2$,[14] $Sr_2CoO_2Cl_2$,[15] $Sr_2MnO_2Cu_{1.5}S_2$[16] and the Fe in the Fe1 layer of $Ca_2FeO_2Fe_{1.6}OS_2$.

The Fe2 layer type is present in a few existing materials and these are listed in Table 3.10. The 3*d* metal is in the +2 oxidation state in all cases where the non-oxide anion has a -2 formal charge (S^{2-} or Se^{2-}), including $Ca_2FeO_2Fe_{1.6}OS_2$ (see Table 3.11). For $BaTi_2OAs_2$, the non-oxide anion is As^{3-} and so in order to balance out the -3 charge the Ti must be in the +3 oxidation state. The Fe vacancies in the Fe2 layer in $Ca_2FeO_2Fe_{1.6}OS_2$ can be seen to arise due to the formal charge of the other layer in the material, $[Ca_2FeO_2]^{3+}$. The Fe2 layer type is the fully occupied $[Fe_2OS_2]^{2-}$ in the cases where the accompanying layer is instead formally divalent $[Sr_2F_2]^{2+}$ in $Sr_2F_2Fe_2OS_2$[12] or $[La_2O_2]^{2+}$ in $La_2O_2Fe_2OS_2$.[17]



Compound	M-O Distances [x2] (Å)	M-X Distances [x4] (Å)	M BVS	M Formal OS
$Sr_2F_2Fe_2OS_2$	2.020(1)	2.633(1)	+1.923(6)	+2
$La_2O_2Fe_2OS_2$	2.021	2.663	+1.84	+2
$La_2O_2Co_2OSe_2$	2.035(1)	2.688(1)	+1.983(6)	+2
$La_2O_2Mn_2OSe_2$	2.06970(2)	2.8061(10)	+2.014(3)	+2
$BaTi_2OAs_2$	2.022804	2.6908	+2.99	+3

Table 3.10: Comparison of bond distances, bond valence sums (BVS) and formal metal oxidation states (OS) for $Sr_2F_2Fe_2OS_2$,[12] $La_2O_2Fe_2OS_2$,[17] $La_2O_2Co_2OSe_2$,[18] $La_2O_2Mn_2OSe_2$[7] and $BaTi_2OAs_2$.[19]

	Fe-O Distances (Å)	Fe-S Distances (Å)	Fe BVS	Fe Formal OS
Fe2_1	2.00(3), 2.02(3)	2.392(15), 2.392(15), 2.962(18), 2.962(18)	+2.11(13)	+2
Fe2_2	1.92(3), 2.04(3)	2.539(16), 2.539(16), 2.796(18), 2.796(18)	+2.01(13)	+2
Fe2_3	1.85(3), 2.10(3)	2.564(17), 2.564(17), 2.774(18), 2.774(18)	+2.05(13)	+2
Fe2_4	1.97(3), 2.01(3)	2.477(16), 2.477(16), 2.862(18), 2.862(18)	+2.03(13)	+2

Table 3.11: Bond distances and bond valence sums (BVS) for the Fe in the Fe2 layer of $Ca_2FeO_2Fe_{1.6}OS_2$. This is a selection of the data reported earlier in Table 3.2.

3.4.2 Magnetic Structure

The Fe1 layers can be compared with other compounds containing infinite-layer MO_2 square-planar sheets. It is common for checkerboard ordering of the moments to occur here to enable all M-O-M superexchange pathways to exhibit antiferromagnetic coupling, as predicted by the Goodenough-Kanamori rules when considering transition metal ions with the same *d*-orbital electron count (e.g. d^5-d^5). Examples of checkerboard ordering of spins in MO_2 sheets include $Sr_2NiO_2Cu_2Se_2$ (canted spins),[11] $Sr_3Fe_2O_4Cl_2$ (spin along *c*-direction)[20] and $Sr_2CuO_2Cu_2Se_2$ (spins in *ab*-plane).[13]

The Fe2 layers and their composite FeO_2S_4 distorted octahedra exist in $La_2O_2Fe_2OS_2$. Free *et al*.[21] report that both $La_2O_2Fe_2OS_2$ and $La_2O_2Fe_2OSe_2$ adopt a frustrated arrangement of magnetic moments, with the moments oriented in the *ab*-plane, as depicted in image b) in Figure 3.55. The orientation of the moments is the same as in $Ca_2FeO_2Fe_{1.6}OS_2$, however the ordering is different. The saturated moment for $La_2O_2Fe_2OS_2$ and $La_2O_2Fe_2OSe_2$ are reported to be 2.60(3) μ_B and 2.69(4) μ_B respectively. The slightly lower saturated value of 2.53(8) μ_B in the case of $Ca_2FeO_2Fe_{1.6}OS_2$ is highly likely to be due to the presence of the vacancies, which decreases the strength of interaction between the Fe centres across the Fe2 layer, although it is important to emphasise that these saturated moments are all very similar in magnitude (especially when taking the uncertainties into account).

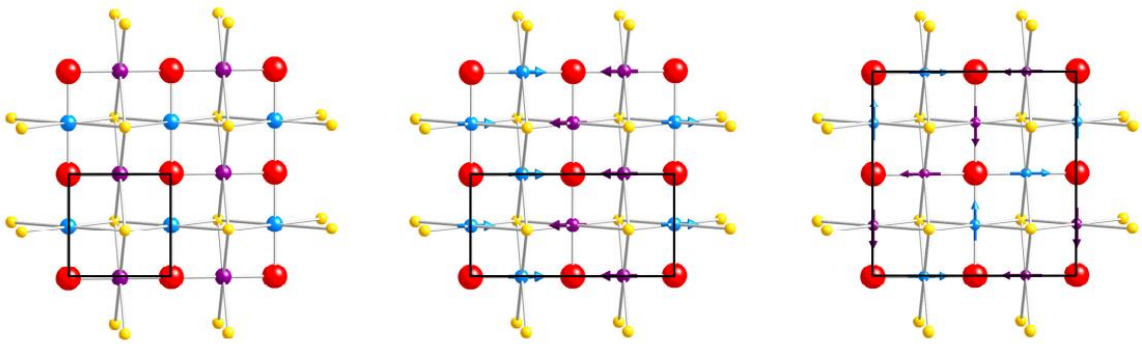


Figure 5.18 *Arrangement of the magnetic moments in (a) $La_2O_2Mn_2OSe_2$, (b) $La_2O_2Fe_2OSe_2$ and (c) $La_2O_2Co_2OSe_2$; M = blue/purple, O = red, Se = yellow; magnetic cells are outlined.*

Figure 3.55: Magnetic models for related compounds, as reported by Free *et al*.[21] This figure is taken from the PhD thesis of David G Free.[22] The spins could alternatively be directed perpendicular to the Co-O bonds in the $La_2O_2Co_2OSe_2$ case.[21]

A revised magnetic model is proposed by McCabe *et al*.[23] for $La_2O_2Fe_2OSe_2$ in which all Fe^{2+} moments point along the Fe-O bonds and which exhibits wholly antiferromagnetic Fe-O-Fe and ferromagnetic Fe-Se-Fe superexchanges. This results in less frustrated magnetic ordering, as all the superexchange interactions are satisfied and the direct exchange becomes negligible as moments are perpendicular.

Spin-orbit coupling arguments can be used to predict the most likely orientation of long-range ordered magnetic moments with respect to the principal *z*-axis, as detailed by Whangbo *et al*.[24] From the diagram in Figure 3.56, it can be seen that the change in magnetic quantum number between the HOMO and LUMO in the FeO_2S_4 environment (i.e. Fe2 sites) is given by $|\Delta L_z| = 1$, suggesting that the moments order perpendicular to the principal *z*-axis which is defined for an individual FeO_2S_4 unit to be directed along the Fe2-O bonds. The models which best fit the data at 100 K (Figure 3.30, section 3.3.8) and 5 K (Figure 3.33, section 3.3.8) show that the Fe2 moments are never directed along the Fe2-O bonds, so this agrees with the prediction to some degree. The Fe^{3+} d^5 ion is predicted to not have a preferred orientation because of the lack of an orbital moment. The $La_2O_2Fe_2OSe_2$ compound is reported by Free *et al*.[21] to contain Fe^{2+} moments ordered in the *ab*-plane, with half the moments directed along the Fe-O bonds (see Figure 3.55). This compound is therefore an example of one which violates the rules proposed by Whangbo *et al*.[24] as these Fe^{2+} moments would also be predicted to order perpendicular to the Fe-O bonds for the same reason as in the $Ca_2FeO_2Fe_{1.6}OS_2$ case.

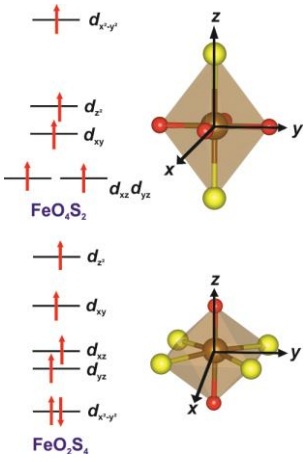


Figure 3.56: Ligand field splitting schemes for the FeO_4S_2 and FeO_2S_4 distorted octahedra. The *x*, *y* and *z* axes shown, which apply to these local coordinations, have been set so that the d_{z^2} orbital lies along the distorted axis of each octahedron. The ligand field splitting for the FeO_2S_4 case is described for analogous CoO_2Se_4 octahedra in $La_2O_2Co_2OSe_2$ by Wu *et al*.[25]

3.5 Conclusions

This study of $Ca_2FeO_2Fe_{1.6}OS_2$ has gone far beyond the initial findings from Zhang *et al*.[1]

The structure determination of $Ca_2FeO_2Fe_{1.6}OS_2$ proved challenging. The superstructure has been modelled using a $2\sqrt{2}a_{nuc} \times 2\sqrt{2}a_{nuc} \times 2c_{nuc}$ expansion of the nuclear unit cell in *Aea*2 symmetry (space group 41). Good fits against both synchrotron XRPD and high-resolution NPD data can be obtained through ordering of the vacancies in the Fe2 layer with accompanying distortion of the Fe and O atoms in the *ab*-plane. These distortions can be viewed as the Fe2 atoms in this layer shifting towards the vacant positions. Bond valence sums (BVS) suggest the Fe1 layer contains Fe^{3+} in the FeO_4S_2 distorted octahedra whereas the Fe2 layer most likely hosts Fe^{2+} in the FeO_2S_4 distorted octahedra. A subtle 'twisting' of the FeO_4 in the Fe1 layer accounts for new peaks appearing in the low *d*-spacing region of the NPD data from 300 K and below. It seems probable that this may occur with the onset of the magnetic ordering at 330(10) K and means that the *Aea*2 (space group 41) supercell model is superseded by a supercell model in $P2_12_12$ (space group 18).

There are two antiferromagnetic ordering transitions- one just above room temperature at 330(10) K and one at 70(2) K. The higher temperature ordering transition can be modelled as the onset of long-range magnetic ordering in both the Fe1 and Fe2 layers and has a *k*-vector of $k = (0,0,0)$ with respect to the supercell. A checkerboard ordering of the spins in the Fe1 layer arises due to antiferromagnetic interactions along the Fe-O-Fe superexchange pathways, where these same interactions result in the ordering observed in the Fe2 layer. At around 70 K, the magnetic Bragg peaks in the NPD data can be modelled with canting of the spins in both the Fe1 and Fe2 layers, again with a *k*-vector of $k = (0,0,0)$ with respect to the supercell. This increase in the Fe moments which accompanies this canting may be due to the localisation of itinerant electrons when the material undergoes a metal to insulator transition, as suggested by variable temperature resistivity measurements. At 5 K, the moments per Fe refine to 3.77(7) μ_B in the Fe1 layer and 2.53(8) μ_B in the Fe2 layer, suggesting these contain high spin Fe^{3+} d^5 and high spin Fe^{2+} d^6 respectively. The 70(2) K

transition has an accompanying structural change which sees simultaneous expansion of the *a* lattice parameter and contraction of the *c* lattice parameter. This may be due to some electron transfer from the Fe2 layer to the Fe1 layer.

The investigation of $Ca_2FeO_2Fe_{1.6}OS_2$ should be extended, as there are a number of intriguing avenues to explore. Successful growth of single crystals large enough for NPD measurements would shed further light on the long-range magnetic ordering in this system, especially the nature of the 70 K transition. The structural changes observed at temperatures close to this 70 K transition could be further investigated by a high-resolution NPD experiment on HRPD, which could also support the hypothesis of the subtle distortion of the FeO_4 squares in the Fe1 layer upon cooling. In addition, these data may also help in the investigation into the structural changes which are observed upon refinement of the structural model against high temperature XRPD data (see Figure 3.57). The unusual change in the *a* lattice parameter is coincident with the broad transitions in the high temperature magnetometry data, as illustrated in Figure 3.57.

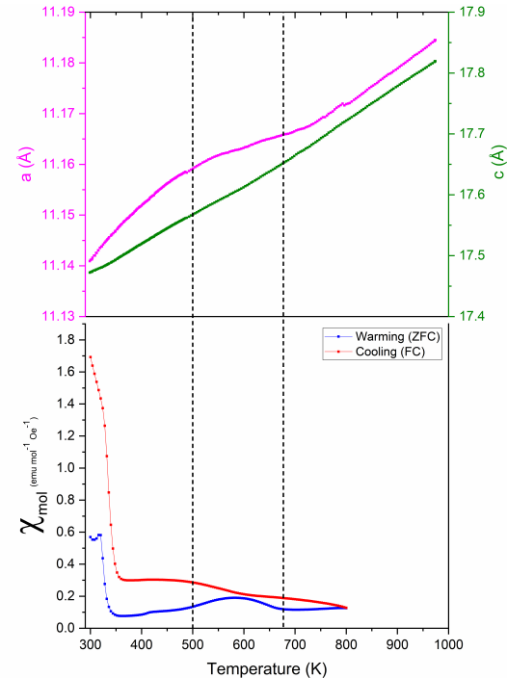


Figure 3.57: The *a* and *c* lattice parameters refined from variable temperature XRPD patterns of $Ca_2FeO_2Fe_{1.6}OS_2$ gathered at I11 (top) and the high temperature magnetometry results (bottom) for $Ca_2FeO_2Fe_{1.6}OS_2$ (as given earlier in Figure 3.17). There is an apparent transition between around 500 K and 680 K, suggested by the slower rate of change in the *a* lattice parameter with temperature and the broad transition in the ZFC curve of the magnetometry.

Another route to delve into is the multi-gram synthesis of $Ca_2FeO_2Fe_{1.6}OS_2$ without long-range Fe vacancy ordering which appears to form when the starting materials are ground together and then compressed under 7GPa, heated up to 900 °C in 10 minutes and then held under these conditions for 30 minutes. This synthesis was performed by Dr. Birgit Fuchs, University of Innsbruck. Figure 3.58 shows a comparison of the XRPD data for the standard pressure and high pressure (HP) syntheses, where there is an obvious disappearance of the superstructure peaks in the phase formed under 7GPa. NPD studies of this material would be of high interest. Thinking more broadly, the extent to which the Fe vacancy ordering can be controlled using different synthesis methods (eg quenching, slow cooling, annealing) should be investigated.

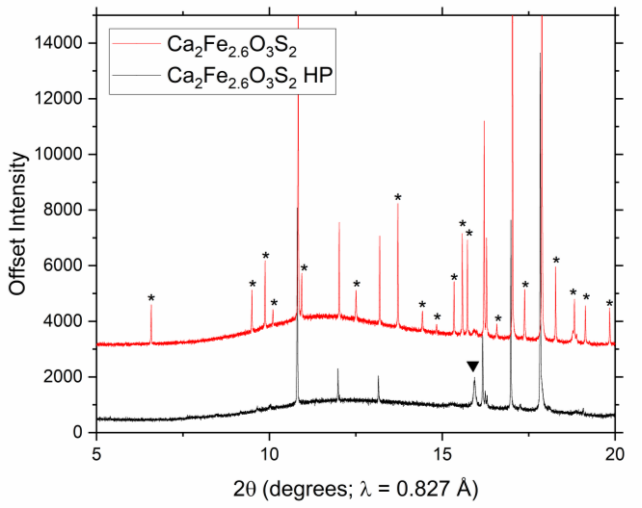


Figure 3.58: XRPD patterns of the $Ca_2Fe_{2.6}O_3S_2$ phases, synthesised under standard pressure (red) or high pressure (black), measured at 300 K on the MAC detector at I11. The Bragg reflections highlighted by a * denote superstructure peaks arising from Fe vacancy ordering. The black triangle denotes an FeS impurity peak in this 2θ range.

The isovalent substitution of ions is often a fruitful way of synthesising new materials, particularly solid solutions, which are commonly very similar to an existing material in terms of crystal structure but may differ in the physical properties exhibited. This idea is used by Zhang *et al*.[1] as they also report some members of the S/Se solid solution phases based on the $Ca_2FeO_2Fe_{1.6}OS_2$ compound. This will be explored in Chapter 4.

References

(1) Zhang, H.; Wu, X.; Li, D.; Jin, S.; Chen, X.; Zhang, T.; Lin, Z.; Shen, S.; Yuan, D.; Chen, X. $Ca_2O_3Fe_{2.6}S_2$: An Antiferromagnetic Mott Insulator at Proximity to Bad Metal. *J. Phys. Condens. Matter* **2016**, *28* (14), 145701. https://doi.org/10.1088/0953-8984/28/14/145701.

(2) González, S.; Perez-Mato, J. M.; Elcoro, L.; García, A. Superlattice Pseudouniform Orderings as Modulated Structures: Stripe and Checkerboard Arrangements. *Phys. Rev. B - Condens. Matter Mater. Phys.* **2011**, *84* (18), 184106. https://doi.org/10.1103/PhysRevB.84.184106.

(3) Adamson, P.; Hadermann, J.; Smura, C. F.; Rutt, O. J.; Hyett, G.; Free, D. G.; Clarke, S. J. Competing Magnetic Structures and the Evolution of Copper Ion/Vacancy Ordering with Composition in the Manganite Oxide Chalcogenides $Sr_2MnO_2Cu_{1.5}(S_{1-X}Se_x)_2$. *Chem. Mater.* **2012**, *24* (14), 2802–2816. https://doi.org/10.1021/cm301486v.

(4) Brown, I. D.; Altermatt, D. Bond-valence Parameters Obtained from a Systematic Analysis of the Inorganic Crystal Structure Database. *Acta Crystallogr. Sect. B* **1985**, *41* (4), 244–247. https://doi.org/10.1107/S0108768185002063.

(5) Coelho, A. A. TOPAS and TOPAS-Academic: An Optimization Program Integrating Computer Algebra and Crystallographic Objects Written in C++: An. *J. Appl. Crystallogr.* **2018**, *51* (1), 210–218. https://doi.org/10.1107/S1600576718000183.

(6) Campbell, B. J.; Stokes, H. T.; Tanner, D. E.; Hatch, D. M. ISODISPLACE: A Web-Based Tool for Exploring Structural Distortions. *J. Appl. Crystallogr.* **2006**, *39* (4), 607–614. https://doi.org/10.1107/S0021889806014075.

(7) Ni, N.; Climent-Pascual, E.; Jia, S.; Huang, Q.; Cava, R. J. Physical Properties and Magnetic Structure of the Layered Oxyselenide $La_2O_3Mn_2Se_2$. *Phys. Rev. B - Condens. Matter Mater. Phys.* **2010**, *82* (21). https://doi.org/10.1103/PhysRevB.82.214419.

(8) Anand, V. K.; Adroja, D. T.; Bhattacharyya, A.; Paramanik, U. B.; Manuel, P.; Hillier, A. D.; Khalyavin, D.; Hossain, Z. MsR and Neutron Diffraction Investigations on the Reentrant Ferromagnetic Superconductor $Eu(Fe_{0.86}Ir_{0.14})_2As_2$. *Phys. Rev. B - Condens. Matter Mater. Phys.* **2015**, *91* (9), 94427. https://doi.org/10.1103/PhysRevB.91.094427.

(9) Kumar, R.; Tomy, C. V.; Nagarajan, R.; Paulose, P. L.; Malik, S. K. Magnetization and Heat Capacity Studies of Double Perovskite Compounds Ba_2SmRuO_6 and Ba_2DyRuO_6. *Phys. B Condens. Matter* **2009**, *404* (16), 2369–2373. https://doi.org/10.1016/j.physb.2009.04.046.

(10) Sheath, B. C.; Xu, X.; Manuel, P.; Hadermann, J.; Batuk, M.; O'Sullivan, J.; Bonilla, R. S.; Clarke, S. J. Structures and Magnetic Ordering in Layered Cr Oxide Arsenides $Sr_2CrO_2Cr_2OAs_2$ and Sr_2CrO_3CrAs. *Inorg. Chem.* **2022**, *61* (31), 12373–12385. https://doi.org/10.1021/acs.inorgchem.2c01773.

(11) Smyth, R. D.; Blandy, J. N.; Yu, Z.; Liu, S.; Topping, C. V; Cassidy, S. J.; Smura, C. F.; Woodruff, D. N.; Manuel, P.; Bull, C. L.; Funnell, N. P.; Ridley, C. J.; McGrady, J. E.; Clarke, S. J. High- versus Low-Spin Ni^{2+} in Elongated Octahedral Environments: $Sr_2NiO_2Cu_2Se_2$, $Sr_2NiO_2Cu_2S_2$, and $Sr_2NiO_2Cu_2(Se_{1-X}S_X)_2$. *Chem. Mater.* **2022**, *16*, 15. https://doi.org/10.1021/acs.chemmater.2c02002.

(12) Kabbour, H.; Janod, E.; Corraze, B.; Danot, M.; Lee, C.; Whangbo, M. H.; Cario, L. Structure and Magnetic Properties of Oxychalcogenides $A_2F_2Fe_2OQ_2$ (A = Sr, Ba; Q = S, Se) with Fe_2O Square Planar Layers Representing an Antiferromagnetic Checkerboard Spin Lattice. *J. Am. Chem. Soc.* **2008**, *130* (26), 8261–8270. https://doi.org/10.1021/ja711139g.

(13) Blandy, J. N.; Liu, S.; Smura, C. F.; Cassidy, S. J.; Woodruff, D. N.; McGrady, J. E.; Clarke, S. J. Synthesis, Structure, and Properties of the Layered Oxide Chalcogenides $Sr_2CuO_2Cu_2S_2$ and $Sr_2CuO_2Cu_2Se_2$. *Inorg. Chem.* **2018**, *57* (24), 15379–15388. https://doi.org/10.1021/acs.inorgchem.8b02698.

(14) Broadley, S. MChem Thesis, University of Oxford, The Synthesis, Structures and Properties of Layered Oxychalcogenides, 2005.

(15) Knee, C. S.; Weller, M. T. Synthesis and Structure of Cobalt (II) Oxide Halides - $Sr_2CoO_2X_2$ (X=Cl, Br). *J. Solid State Chem.* **2002**, *168* (1), 1–4. https://doi.org/10.1006/jssc.2002.9682.

(16) Gál, Z. A.; Rutt, O. J.; Smura, C. F.; Overton, T. P.; Barrier, N.; Clarke, S. J.; Hadermann, J. Structural Chemistry and Metamagnetism of an Homologous Series of Layered Manganese Oxysulfides. *J. Am. Chem. Soc.* **2006**, *128* (26), 8530–8540. https://doi.org/10.1021/ja060892o.

(17) Zhu, J. X.; Yu, R.; Wang, H.; Zhao, L. L.; Jones, M. D.; Dai, J.; Abrahams, E.; Morosan, E.; Fang, M.; Si, Q. Band Narrowing and Mott Localization in Iron Oxychalcogenides $La_2O_2Fe_2O(Se,S)_2$. *Phys. Rev. Lett.* **2010**, *104* (21). https://doi.org/10.1103/PhysRevLett.104.216405.

(18) Wang, C.; Tan, M. Q.; Feng, C. M.; Ma, Z. F.; Jiang, S.; Xu, Z. A.; Cao, G. H.; Matsubayashi, K.; Uwatoko, Y. $La_2Co_2Se_2O_3$: A Quasi-Two-Dimensional Mott Insulator with Unusual Cobalt Spin State and Possible Orbital Ordering. *J. Am. Chem. Soc.* **2010**, *132* (20), 7069–7073. https://doi.org/10.1021/ja1001295.

(19) Wang, X. F.; Yan, Y. J.; Ying, J. J.; Li, Q. J.; Zhang, M.; Xu, N.; Chen, X. H. Structure and Physical Properties for a New Layered Pnictide-Oxide: $BaTi_2As_2O$. *J. Phys. Condens. Matter* **2010**, *22* (7). https://doi.org/10.1088/0953-8984/22/7/075702.

(20) Dixon, E.; Hayward, M. A. Suppression of Magnetic Order in $Sr_3Fe_2O_4Cl_2$ by Fe-Site Substitution by Cobalt. *Inorg. Chem.* **2011**, *50* (15), 7250–7256. https://doi.org/10.1021/ic200832n.

(21) Free, D. G.; Withers, N. D.; Hickey, P. J.; Evans, J. S. O. Synthesis, Structure and Properties of Several New Oxychalcogenide Materials with the General Formula $A_2O_2M_2OSe_2$ (A = La-Sm, M = Fe, Mn). *Chem. Mater.* **2011**, *23* (6), 1625–1635. https://doi.org/10.1021/cm1035453.

(22) Free, D. G. PhD Thesis, Durham University, Synthesis and Properties of New Oxychalcogenide Materials, 2011.

(23) McCabe, E. E.; Stock, C.; Rodriguez, E. E.; Wills, A. S.; Taylor, J. W.; Evans, J. S. O. Weak Spin Interactions in Mott Insulating $La_2O_2Fe_2OSe_2$. *Phys. Rev. B - Condens. Matter Mater. Phys.* **2014**, *89* (10), 100402. https://doi.org/10.1103/PhysRevB.89.100402.

(24) Whangbo, M. H.; Gordon, E. E.; Xiang, H.; Koo, H. J.; Lee, C. Prediction of Spin Orientations in Terms of HOMO-LUMO Interactions Using Spin-Orbit Coupling as Perturbation. *Acc. Chem. Res.* **2015**, *48* (12), 3080–3087. https://doi.org/10.1021/acs.accounts.5b00408.

(25) Wu, H. Electronic Structure, Spin State, and Magnetism of the Square-Lattice Mott Insulator $La_2Co_2Se_2O_3$ from First Principles. *Phys. Rev. B - Condens. Matter Mater. Phys.* **2010**, *82* (2). https://doi.org/10.1103/PhysRevB.82.020410.

Chapter 4

4 Synthesis and Characterisation of $Ca_2FeO_2Fe_{1.65}OS_{1.5}Se_{0.5}$, $Ca_2FeO_2Fe_{1.7}OSSe$ and $Ca_2FeO_2Fe_{1.75}OS_{0.5}Se_{1.5}$

4.1 Introduction

Zhang *et al.*[1] also reported the solid solution phases $Ca_2Fe_{2.6+\delta}O_3S_{2-x}Se_x$ (x = 0.0625, 0.125, 0.25, 0.5, 0.75, 1; $0 < \delta \leq 0.07$) which are isostructural to the $Ca_2Fe_{2.6}O_3S_2$ compound studied in Chapter 3. There is the expected linear increase in the *a* and *c* lattice parameters as the Se content increases and the low temperature resistivity data show an almost identical trend to the all-sulfide phase. As S is substituted for Se, they find suppression of the long-range Fe vacancy ordering from the loss of the superstructure peaks in the XRPD data and also suppression of the 77 K transition present in the magnetometry data.

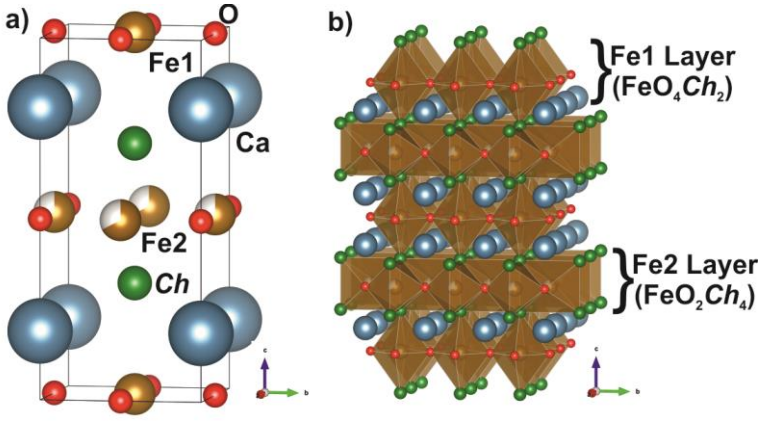


Figure 4.1: Crystal structure of $Ca_2FeO_2Fe_{1.6+\delta}OCh_2$ (*Ch* = S, Se) depicting **a)** the unit cell and **b)** the alternating Fe1 and Fe2 layers.

4.2 Synthesis

3 g powder samples were made from stoichiometric amounts of CaO (Alfa Aesar 99.95 %), Fe (Alfa Aesar 99.998 %), FeO (Alfa Aesar 99.5 %), S (Alfa Aesar 99.999 %) and Se (Alfa Aesar 99.999 %) using traditional solid-state synthesis, heating the reagents at 800 °C for 24 h (1 °C/min ramping rate). A second heating cycle of 800 °C for 24 h (1 °C/min ramping rate) was used for the $Ca_2FeO_2Fe_{1.75}OS_{0.5}Se_{1.5}$ mixture, with re-grinding and re-pelletising, however the phase purity did not change significantly with this additional heating step.

It was found that increasing the stoichiometry of Fe in the synthesis as the proportion of Se in the target material increased resulted in a higher purity of the target phase. This is exemplified in Figure 4.2 for the case where the target phase contains a 1:1 ratio of S:Se. A stoichiometry of $Ca_2FeO_2Fe_{1.6}OSSe$ was initially attempted, as this is the same stoichiometry as the all-sulfide phase. However, a major CaS impurity was present and it was thought that this was forming due to a lack of Fe in the starting mixture. The $Ca_2FeO_2Fe_{1.67}OSSe$ stoichiometry was then targeted as this was the stoichiometry reported by Zhang *et al*.[1] It can be seen in Figure 4.2 that this greatly decreased the amount of CaS in the sample and then the $Ca_2FeO_2Fe_{1.7}OSSe$ stoichiometry appeared to be phase pure.

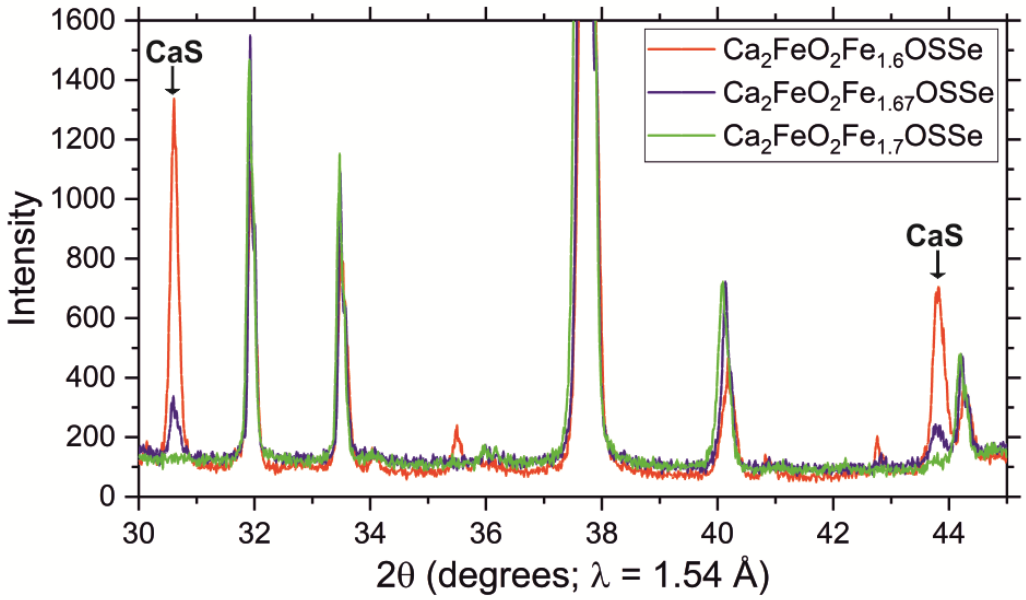


Figure 4.2: XRPD patterns of $Ca_2FeO_2Fe_{1.6}OSSe$, $Ca_2FeO_2Fe_{1.67}OSSe$ and $Ca_2FeO_2Fe_{1.7}OSSe$ measured at 300 K on the Bruker D8 Eco in-house diffractometer. The XRPD patterns were all collected after the starting mixtures had been heated at 800 °C for 24 h (1 °C/min ramping rate).

4.3 Characterisation

4.3.1 Room Temperature XRPD

Room temperature XRPD data on the three phases were collected on beamline I11 at the Diamond Light Source. The high-resolution MAC detector was used to gather these data. The Bragg reflections can be accounted for without the adoption of a supercell for all the solid solution phases, unlike for $Ca_2FeO_2Fe_{1.6}OS_2$, as there are no superstructure peaks visible in the diffraction data. Refinements of the structural models against the data are given in Figures 4.3-4.5 and the results in Tables 4.1-4.3.

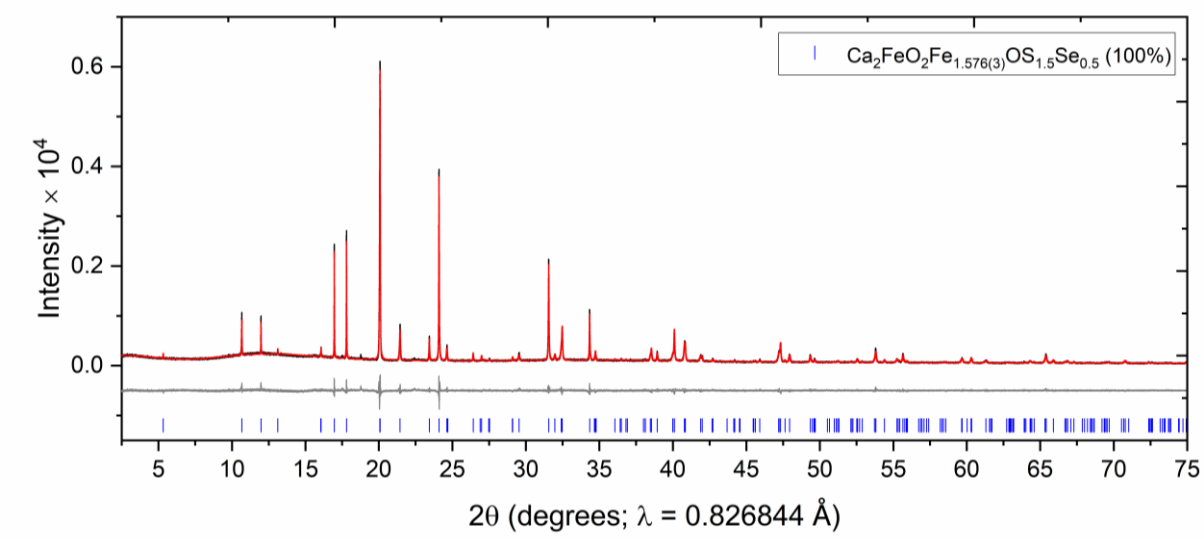


Figure 4.3: XRPD pattern of $Ca_2FeO_2Fe_{1.65}OS_{1.5}Se_{0.5}$ measured at 300 K on the MAC detector at I11 showing the observed (black), calculated (red) and difference (grey) curves. R_{wp}: 7.630%.

	$Ca_2Fe_{2.65}O_3S_{1.5}Se_{0.5}$
Diffractometer	I11 (MAC)
Wavelength (Å)	0.826844
Temperature (K)	300
Space Group	*P4/mmm*
a (Å)	3.96053(3)
c (Å)	8.88767(6)
V (Å^3)	139.410(2)

								$Ca_2Fe_{2.65}O_3S_{1.5}Se_{0.5}$
Atom	Site	*x*	*y*	*z*	Occupancy	U_{11} (Å^2)	U_{22} (Å^2)	U_{33} (Å^2)
Ca	2*h*	0.5	0.5	0.18323(9)	1	0.0184(3)	$=U_{11}$	0.0242(7)
Fe1	1*a*	0	0	0	1	0.0130(3)	$=U_{11}$	0.0247(6)
Fe2	2*e*	0.5	0	0.5	0.7882(15)	0.0501(5)	$=U_{11}$	0.0170(6)
O1	2*f*	0.5	0	0	1	0.0291(8)	$=U_{11}$	$=U_{11}$
O2	1*d*	0.5	0.5	0.5	1	0.0221(12)	$=U_{11}$	$=U_{11}$
S	2*g*	0	0	0.2982(5)	0.759(3)	0.0372(16)	$=U_{11}$	0.036(3)
Se	2*g*	0	0	0.2969(4)	0.241(3)	0.0004(8)	$=U_{11}$	0.0003(14)

Table 4.1: Refinement results from the XRPD pattern collected at 300 K using the MAC detector at I11.

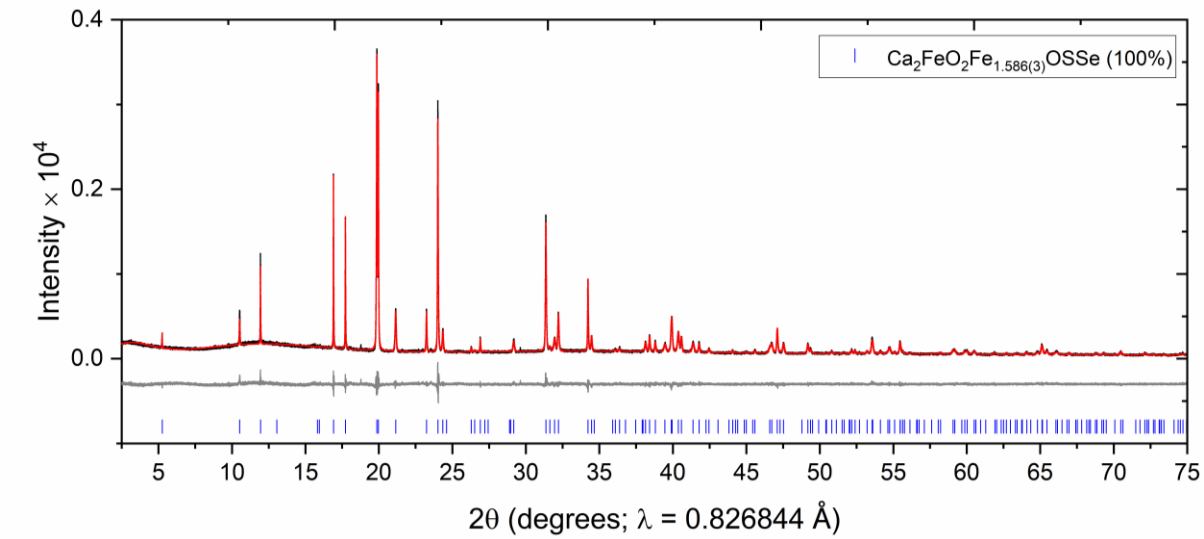


Figure 4.4: XRPD pattern of $Ca_2FeO_2Fe_{1.7}OSSe$ measured at 300 K on the MAC detector at I11 showing the observed (black), calculated (red) and difference (grey) curves. R_{wp}: 7.816%.

	$Ca_2Fe_{2.7}O_3SSe$
Diffractometer	I11 (MAC)
Wavelength (Å)	0.826844
Temperature (K)	300
Space Group	*P4/mmm*
a (Å)	3.97308(3)
c (Å)	9.00977(7)
V (Å^3)	142.222(2)

								$Ca_2Fe_{2.7}O_3SSe$
Atom	Site	*x*	*y*	*z*	Occupancy	U_{11} (Å^2)	U_{22} (Å^2)	U_{33} (Å^2)
Ca	2*h*	0.5	0.5	0.18098(10)	1	0.0226(3)	$=U_{11}$	0.0345(7)
Fe1	1*a*	0	0	0	1	0.0164(3)	$=U_{11}$	0.0254(6)
Fe2	2*e*	0.5	0	0.5	0.7931(15)	0.0496(5)	$=U_{11}$	0.0224(6)
O1	2*f*	0.5	0	0	1	0.0268(8)	$=U_{11}$	$=U_{11}$
O2	1*d*	0.5	0.5	0.5	1	0.0495(19)	$=U_{11}$	$=U_{11}$
S	2*g*	0	0	0.2976(8)	0.484(4)	0.097(5)	$=U_{11}$	0.085(6)
Se	2*g*	0	0	0.2981(2)	0.516(4)	0.0097(3)	$=U_{11}$	0.0119(5)

Table 4.2: Refinement results from the XRPD pattern collected at 300 K using the MAC detector at I11.

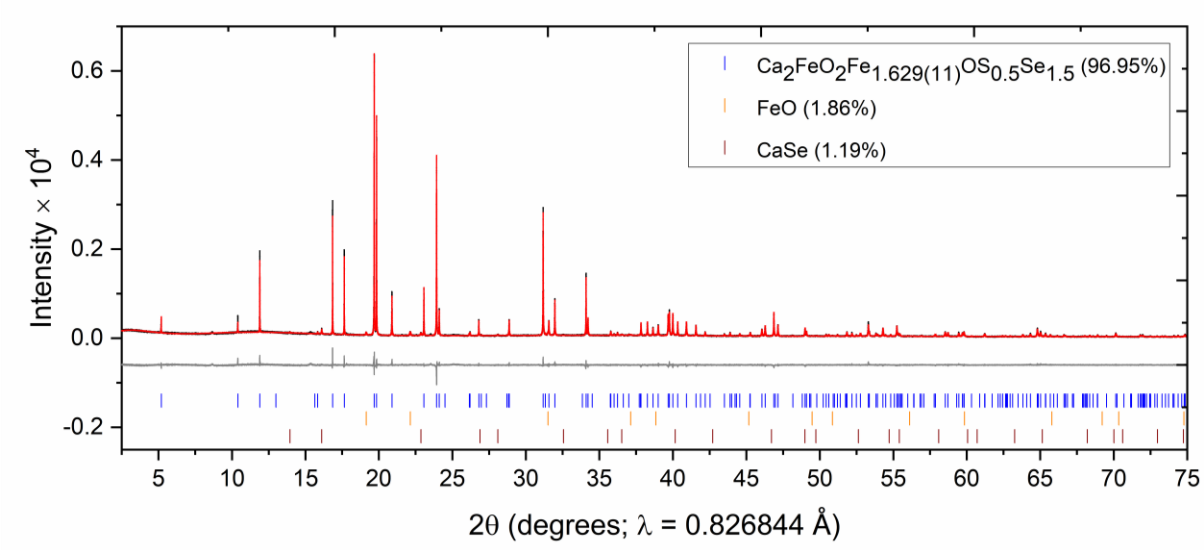


Figure 4.5: XRPD pattern of $Ca_2FeO_2Fe_{1.75}OS_{0.5}Se_{1.5}$ measured at 300 K on the MAC detector at I11 showing the observed (black), calculated (red) and difference (grey) curves. R_{wp}: 8.909%.

	$Ca_2Fe_{2.75}O_3S_{0.5}Se_{1.5}$
Diffractometer	I11 (MAC)
Wavelength (Å)	0.826844
Temperature (K)	300
Space Group	*P4/mmm*
a (Å)	3.987923(7)
c (Å)	9.11813(3)
V (Å^3)	145.010(1)

								$Ca_2Fe_{2.75}O_3S_{0.5}Se_{1.5}$
Atom	Site	*x*	*y*	*z*	Occupancy	U_{11} (Å^2)	U_{22} (Å^2)	U_{33} (Å^2)
Ca	2*h*	0.5	0.5	0.17839(10)	1	0.0223(3)	$=U_{11}$	0.0344(7)
Fe1	1*a*	0	0	0	1	0.0169(3)	$=U_{11}$	0.0231(5)
Fe2	2*e*	0.5	0	0.5	0.8147(18)	0.0439(4)	$=U_{11}$	0.0209(5)
O1	2*f*	0.5	0	0	1	0.0287(7)	$=U_{11}$	$=U_{11}$
O2	1*d*	0.5	0.5	0.5	1	0.0591(20)	$=U_{11}$	$=U_{11}$
S	2*g*	0	0	0.2911(17)	0.231(6)	0.21(3)	$=U_{11}$	0.083(14)
Se	2*g*	0	0	0.2985(1)	0.769(6)	0.0177(3)	$=U_{11}$	0.0160(4)

Table 4.3: Refinement results from the XRPD pattern collected at 300 K using the MAC detector at I11.

Comparing the four compounds of this series, Table 4.4 and Figure 4.6 show that the Fe2 cations always have a BVS around +2, whereas the Fe1 BVS steadily decreases from +2.85(1) to +2.70(2) as more Se is incorporated into the structure. Therefore, it is possible that the Fe1 cations are being reduced upon the Fe occupancy of the Fe2 layer increasing, as illustrated in Figure 4.7, where the trends for this across the series is approximately linear for both the reduction in the Fe1 BVS and the increase in Fe stoichiometry. The higher proportion of Se in the S:Se ratio results in more reducing Se^{2-}

around the Fe centres, which could also contribute to this decrease in BVS, however one would expect this to also reduce the BVS of the Fe2 sites, which is not the case. In fact, as the Fe2 sites (FeO_2Ch_4) have a higher proportion of chalcogen in the coordination environment compared to the Fe1 sites (FeO_4Ch_2), one might expect the Fe2 cations to be reduced more than the Fe1 sites. Therefore, it seems likely that the reduction of the Fe1 sites is almost entirely due to the inclusion of more Fe on the Fe2 sites.

Compound		Fe-O Distance (Å)	Fe-S Distance (Å)	Fe-Se Distance (Å)	Fe BVS
$Ca_2FeO_2Fe_{1.65}OS_{1.5}Se_{0.5}$	Fe1	1.9803(1)	2.650(5)	2.639(4)	+2.77(1)
	Fe2	1.9803(1)	2.672(3)	2.680(3)	+2.02(1)
$Ca_2FeO_2Fe_{1.7}OSSe$	Fe1	1.9865(1)	2.681(7)	2.6860(14)	+2.73(1)
	Fe2	1.9865(1)	2.697(5)	2.6935(10)	+2.06(2)
$Ca_2FeO_2Fe_{1.75}OS_{0.5}Se_{1.5}$	Fe1	1.9940(1)	2.654(16)	2.7217(9)	+2.70(2)
	Fe2	1.9940(1)	2.758(11)	2.7114(6)	+2.07(4)

Table 4.4: Fe bond valence sums (BVS) calculated using bond lengths refined from the XRPD pattern collected at 300 K using the MAC detector at I11. Values calculated using reference values from *Liu and Thorp*,[2] *Brown and Altermatt*[3] and *Brese and O'Keeffe*,[3] where literature bond lengths used were Fe^{2+}-S 2.12 Å, Fe^{3+}-S 2.15 Å and Fe-Se 2.28 Å. A weighted average, determined by the S:Se ratio, of the Fe-*Ch* bonds was used to compare to the same weighted average of the literature Fe-S and Fe-Se bonds.

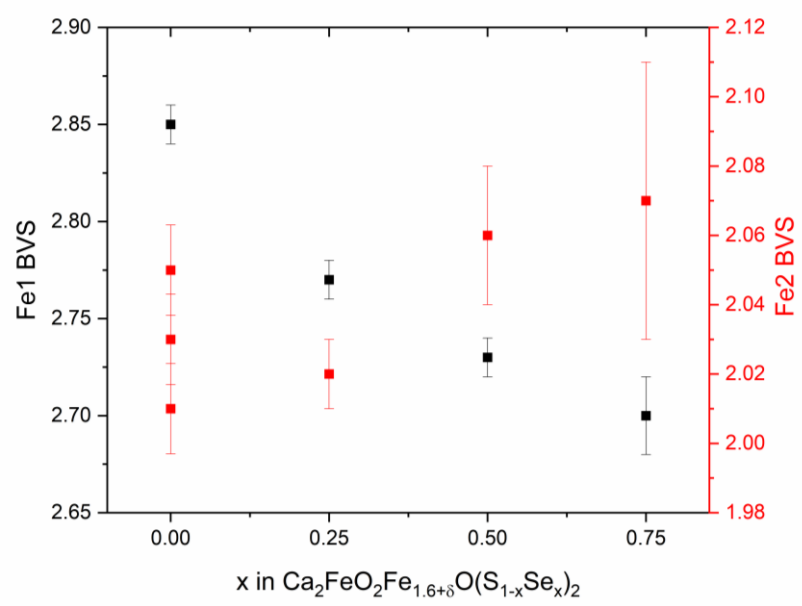


Figure 4.6: Comparison of the Fe bond valence sums (BVS) in each Fe layer for the $Ca_2FeO_2Fe_{1.6+\delta}OCh_2$ (*Ch* = S, Se) compounds. The data presented for the Fe2 sites in $Ca_2FeO_2Fe_{1.6}OS_2$ are the three fully occupied sites.

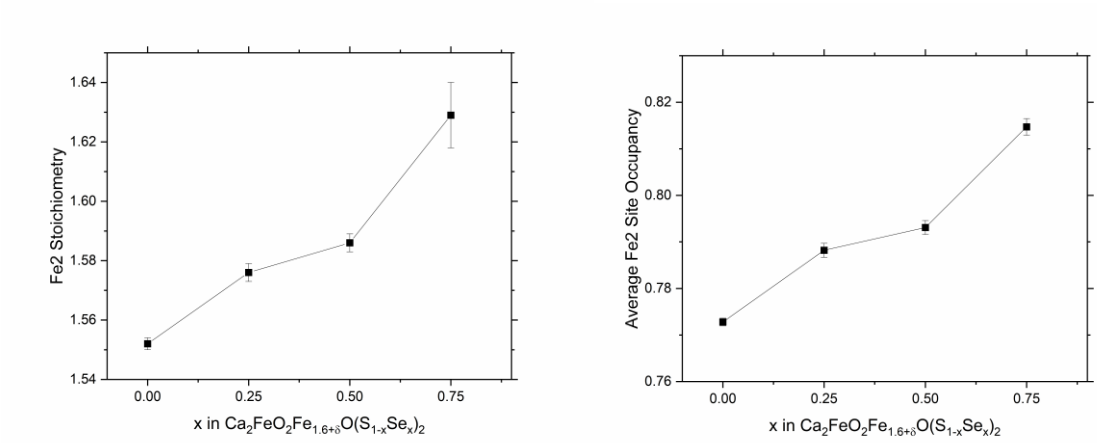


Figure 4.7: Comparison of Fe2 stoichiometries (left) and corresponding average Fe2 site occupancies (right) for the $Ca_2FeO_2Fe_{1.6+\delta}OCh_2$ (*Ch* = S, Se) compounds, refined from room-temperature XRPD data.

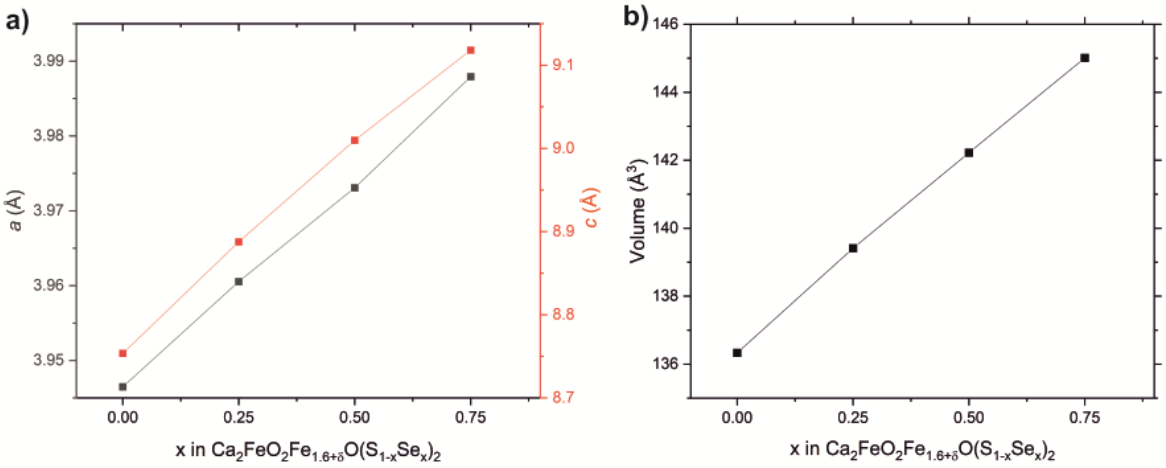


Figure 4.8: Comparison of the **a)** lattice parameters and **b)** volume for the basic unit cell of the $Ca_2FeO_2Fe_{1.6+\delta}OCh_2$ (*Ch* = S, Se) compounds, refined from room-temperature XRPD data.

Figure 4.8 illustrates the expected linear trend in the *a* and *c* lattice parameters and the unit cell volume across this series as the proportion of Se included is changed linearly. The fact that the unit cell expands as more Se is incorporated could explain the reason behind the higher occupancies of the Fe2 sites. When the unit cell expands, the Fe to anion distances increase and so in order to compensate for this, more Fe is included in the Fe2 layer which supply extra electrons to the system, thus overall reducing the Fe in the system. The decrease in the BVS values will of course also be due to this increase in the Fe to anion bond lengths when more Se is included, however one might expect both the Fe1 and Fe2 to become under-bonded whereas here only the Fe1 BVS value appears to decrease.

4.3.2 Room Temperature NPD

In order to support the investigation into these crystal structures, room temperature NPD data were collected on the D2B instrument at the ILL. D2B has a high resolution at intermediate *d*-spacing values and measures out to short d-spacings of around 0.8 Å, hence is useful in the determination of nuclear structures (see section 2.2.2.2). Refinements of the structural models against the data are given in Figures 4.9-4.11 and the results in Tables 4.5-4.7.

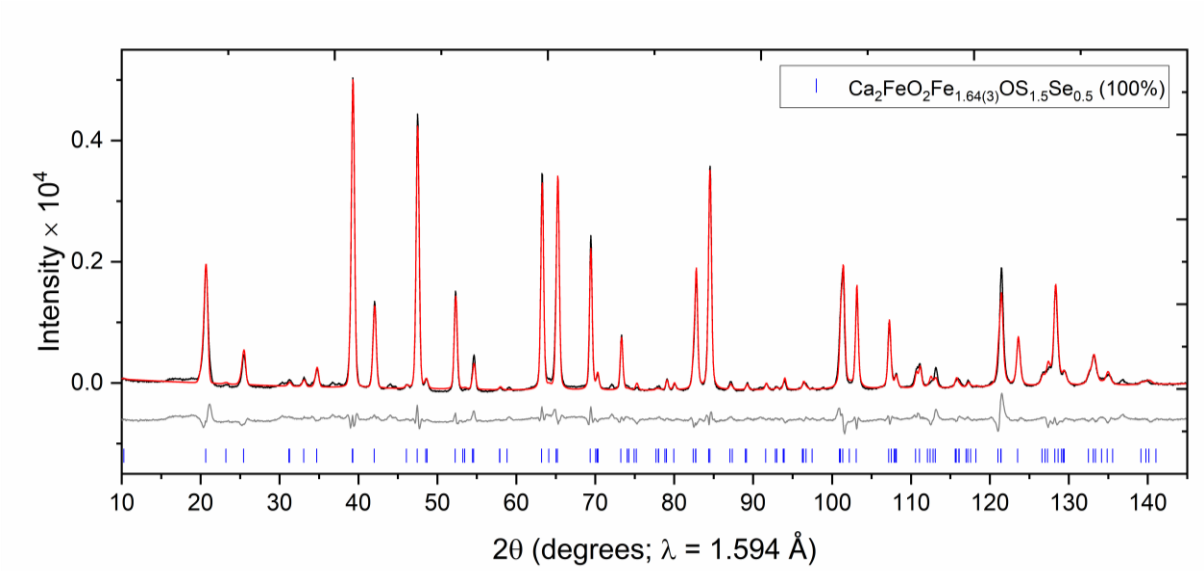


Figure 4.9: NPD pattern of $Ca_2FeO_2Fe_{1.65}OS_{1.5}Se_{0.5}$ measured at 300 K on the D2B instrument at the ILL showing the observed (black), calculated (red) and difference (grey) curves. R_{wp}: 6.315%.

	$Ca_2Fe_{2.65}O_3S_{1.5}Se_{0.5}$
Diffractometer	D2B (ILL)
Wavelength (Å)	1.594
Temperature (K)	300
Space Group	*P*4/*mmm*
a (Å)	3.96157(5)
c (Å)	8.8943(3)
V (Å^3)	139.587(5)

						$Ca_2Fe_{2.65}O_3S_{1.5}Se_{0.5}$
Atom	Site	*x*	*y*	*z*	Occupancy	U_{iso} (Å^2)
Ca	2*h*	0.5	0.5	0.1833(5)	1	0.0070(11)
Fe1	1*a*	0	0	0	1	0.0002(7)
Fe2	2*e*	0.5	0	0.5	0.822(12)	0.0298(11)
O1	2*f*	0.5	0	0	1	0.0128(8)
O2	1*d*	0.5	0.5	0.5	1	0.0099(12)
S	2*g*	0	0	0.2964(6)$^+$	0.770(14)	0.0014(13)$^+$
Se	2*g*	0	0	0.2964(6)$^+$	0.230(14)	0.0014(13)$^+$

Table 4.5: Refinement results from the NPD pattern collected at 300 K using the D2B instrument at the ILL (shown in Figure 4.9). $^+$These values were refined using the same parameter.

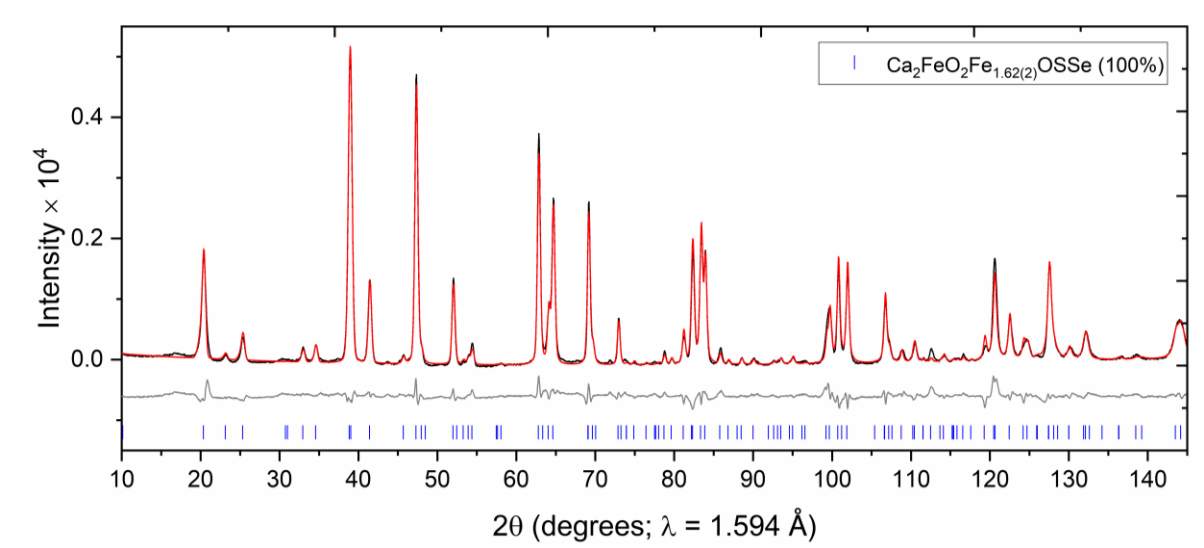


Figure 4.10: NPD pattern of $Ca_2FeO_2Fe_{1.7}OSSe$ measured at 300 K on the D2B instrument at the ILL showing the observed (black), calculated (red) and difference (grey) curves. R_{wp}: 5.890%.

	$Ca_2Fe_{2.7}O_3SSe$
Diffractometer	D2B (ILL)
Wavelength (Å)	1.594
Temperature (K)	300
Space Group	*P*4/*mmm*
a (Å)	3.97488(5)
c (Å)	9.0179(3)
V (Å^3)	142.480(6)

						$Ca_2Fe_{2.7}O_3SSe$
Atom	Site	*x*	*y*	*z*	Occupancy	U_{iso} (Å^2)
Ca	2*h*	0.5	0.5	0.1801(5)	1	0.0086(11)
Fe1	1*a*	0	0	0	1	0.0055(8)
Fe2	2*e*	0.5	0	0.5	0.809(11)	0.0235(9)
O1	2*f*	0.5	0	0	1	0.0127(7)
O2	1*d*	0.5	0.5	0.5	1	0.0189(17)
S	2*g*	0	0	0.2981(4)$^+$	0.525(14)	0.0019(9)$^+$
Se	2*g*	0	0	0.2981(4)$^+$	0.475(14)	0.0019(9)$^+$

Table 4.6: Refinement results from the NPD pattern collected at 300 K using the D2B instrument at the ILL (shown in Figure 4.10). $^+$These values were refined using the same parameter.

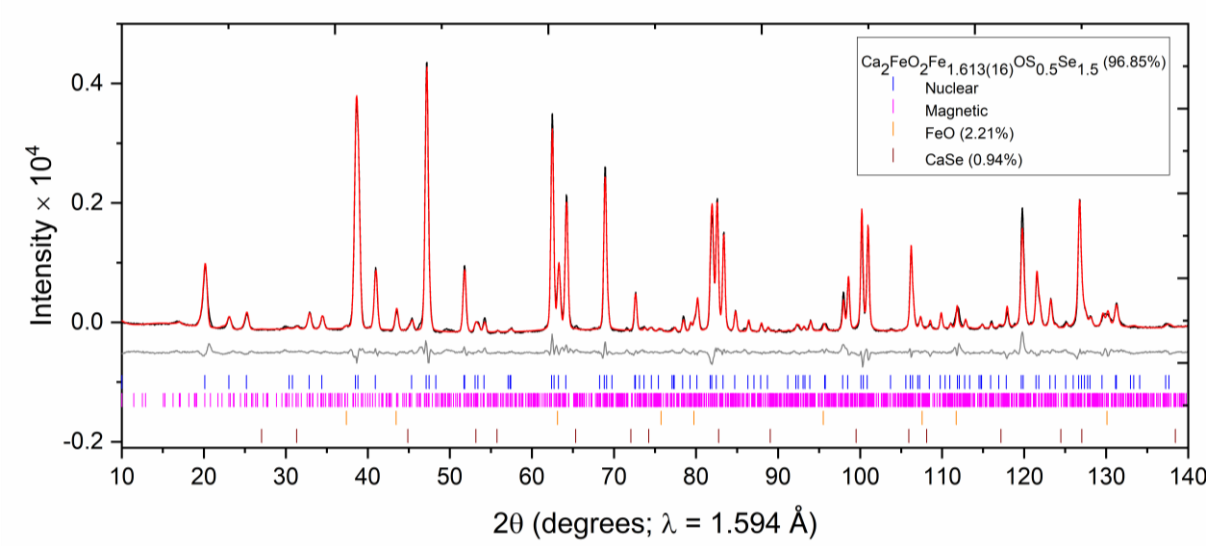


Figure 4.11: NPD pattern of $Ca_2FeO_2Fe_{1.75}OS_{0.5}Se_{1.5}$ measured at 300 K on the D2B instrument at the ILL showing the observed (black), calculated (red) and difference (grey) curves. R_{wp}: 4.846%.

	$Ca_2Fe_{2.75}O_3S_{0.5}Se_{1.5}$
Diffractometer	D2B (ILL)
Wavelength (Å)	1.594
Temperature (K)	300
Space Group	*P*4/*mmm*
a (Å)	3.98878(4)
c (Å)	9.1214(2)
V (Å^3)	145.124(4)

						$Ca_2Fe_{2.75}O_3S_{0.5}Se_{1.5}$
Atom	Site	*x*	*y*	*z*	Occupancy	U_{iso} (Å^2)
Ca	2*h*	0.5	0.5	0.1767(4)	1	0.0089(8)
Fe1	1*a*	0	0	0	1	0.0049(6)
Fe2	2*e*	0.5	0	0.5	0.807(8)	0.0170(5)
O1	2*f*	0.5	0	0	1	0.0155(5)
O2	1*d*	0.5	0.5	0.5	1	0.0238(13)
S	2*g*	0	0	0.2980(3)$^+$	0.260(12)	0.0052(6)$^+$
Se	2*g*	0	0	0.2980(3)$^+$	0.740(12)	0.0052(6)$^+$

Table 4.7: Refinement results from the NPD pattern collected at 300 K using the D2B instrument at the ILL (shown in Figure 4.11). $^+$These values were refined using the same parameter.

It can be seen from these refinements and those from the XRPD data given in section 3.4.1 that the refined S and Se occupancies all agree very well with the targeted stoichiometries. One difference between these refinements is that the trend in the Fe stoichiometry is no longer suggested by these NPD refinement results. The process of fitting a model to the diffraction data and obtaining the refined Fe2 occupancy values always has some ambiguity as there are many factors which contribute to the intensity of a Bragg peak other than the Fe2 site occupancy (eg site occupancies of other atoms, positions of atoms within the unit cell, atomic displacement parameters). The Fe2 site occupancy will heavily correlate with the atomic displacement parameter for this site and so the Fe2 U_{iso} values will greatly affect the refined Fe2 occupancies. As the trend in Fe2 stoichiometry shown by the XRPD refinements is further supported by the lack of presence of any significant impurity phases in the products even when more Fe is introduced to the starting mixtures with increasing Se content, it seems likely that this trend reflects the actual Fe2 occupancies in these compounds. One point to also note here is that the uncertainties from all these refinements are usually an underestimate of the true uncertainty and so future work could include using techniques such as single crystal x-ray diffraction (if crystals can be obtained) to quantify the ratio of the constituent elements in the crystallites more accurately.

4.3.3 SQUID Magnetometry

A comparison of the magnetic susceptibilities with varying temperature is illustrated in Figure 4.12. It is clear that the 70 K magnetic transition appears to be suppressed upon addition of Se. Further magnetometry results for the solid solution compounds are shown in Figures 4.13-4.15, each including a 5T-4T-3T susceptibility measurement where the signals arising from any magnetic impurities (eg Fe, FeO) are subtracted from the measured data (as explained in section 2.2.4.1).

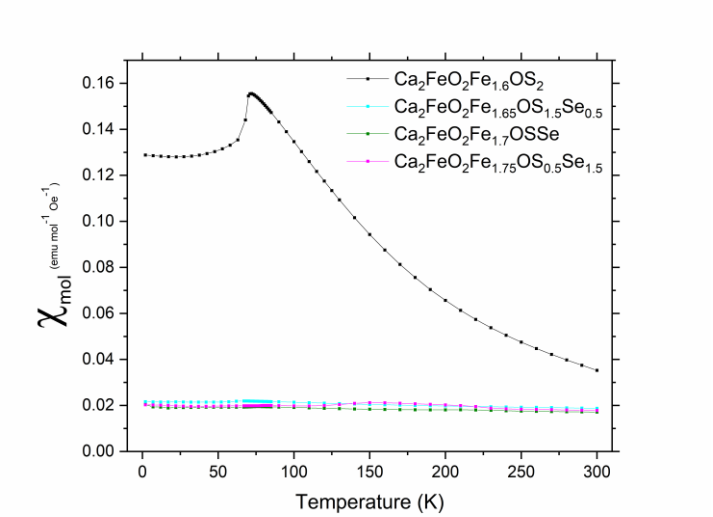


Figure 4.12: Comparison of the FC magnetic susceptibility against temperature for the $Ca_2FeO_2Fe_{1.6+\delta}OCh_2$ (*Ch* = S, Se) compounds, measured in a field of 3 T.

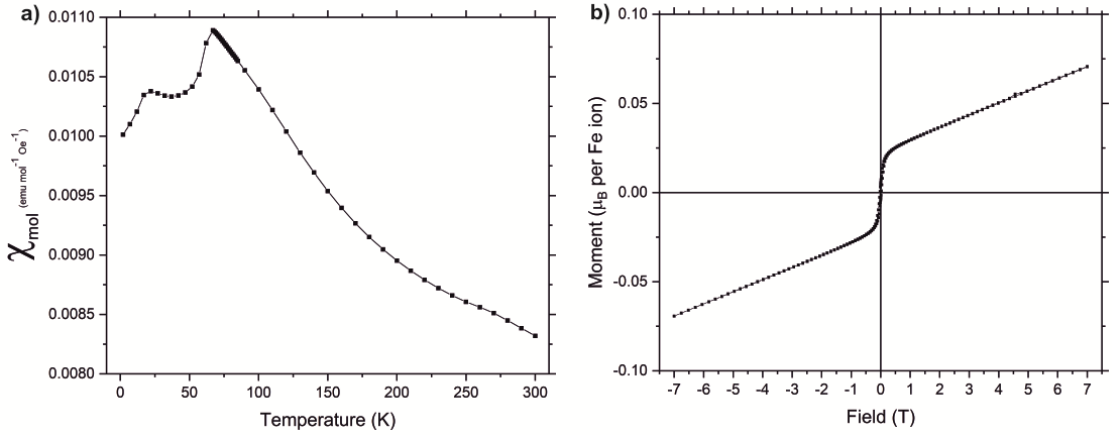


Figure 4.13: Magnetometry results for the $Ca_2FeO_2Fe_{1.65}OS_{1.5}Se_{0.5}$ compound showing data from **a)** the 5T-4T-3T susceptibility and **b)** the 5 K magnetisation isotherm.

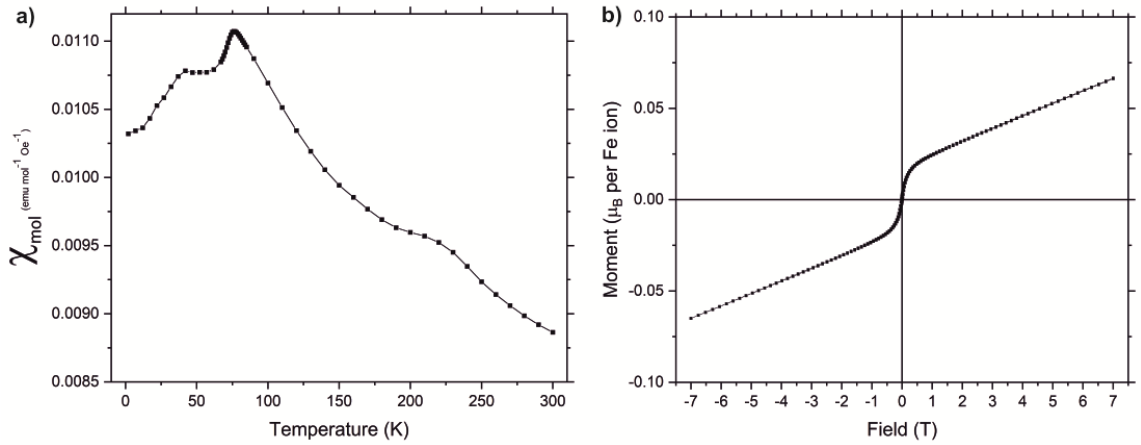


Figure 4.14: Magnetometry results for the $Ca_2FeO_2Fe_{1.7}OSSe$ compound showing data from **a)** the 5T-4T-3T susceptibility and **b)** the 5 K magnetisation isotherm.

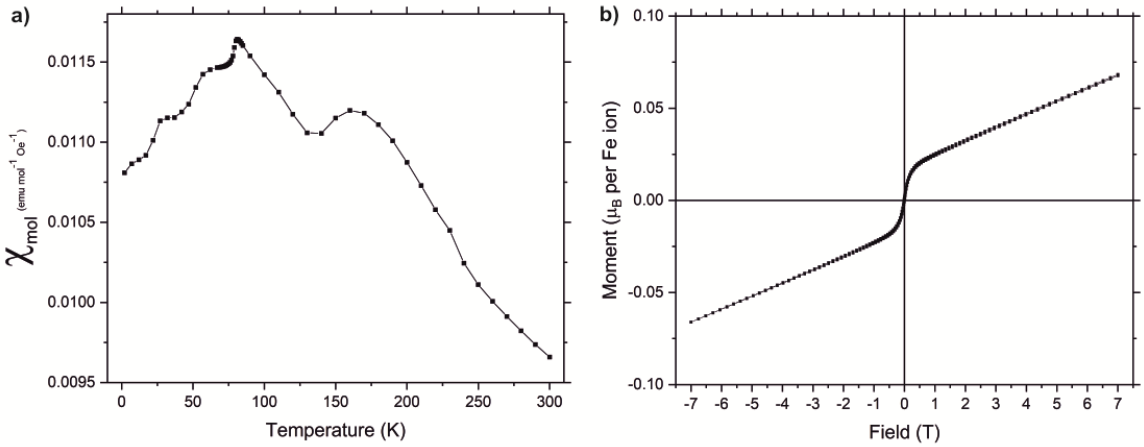


Figure 4.15: Magnetometry results for the $Ca_2FeO_2Fe_{1.75}OS_{0.5}Se_{1.5}$ compound showing data from **a)** the 5T-4T-3T susceptibility and **b)** the 5 K magnetisation isotherm.

All three materials exhibit an antiferromagnetic ordering transition at around 70 K, as previously seen in the case of the $Ca_2FeO_2Fe_{1.6}OS_2$ material. As more Se is introduced into the structure, in place of S, the emergence of a second, broader signal at higher temperatures is apparent. This is most pronounced in the $Ca_2FeO_2Fe_{1.75}OS_{0.5}Se_{1.5}$ compound and is centred around 160 K. Unlike for $Ca_2FeO_2Fe_{1.6}OS_2$, there is no coercive field in the 5 K hysteresis loops and these isotherms also suggest that the materials lose the ferromagnetic component upon incorporation of Se into the structure, as illustrated by Figure 4.16. The loss of the ferromagnetic behaviour arises in the solid solution compounds because there is loss of long-range Fe vacancy ordering in the Fe2 layer, which in turn results in the loss of the ferrimagnetic arrangement of the moments, as described in Chapter 3.

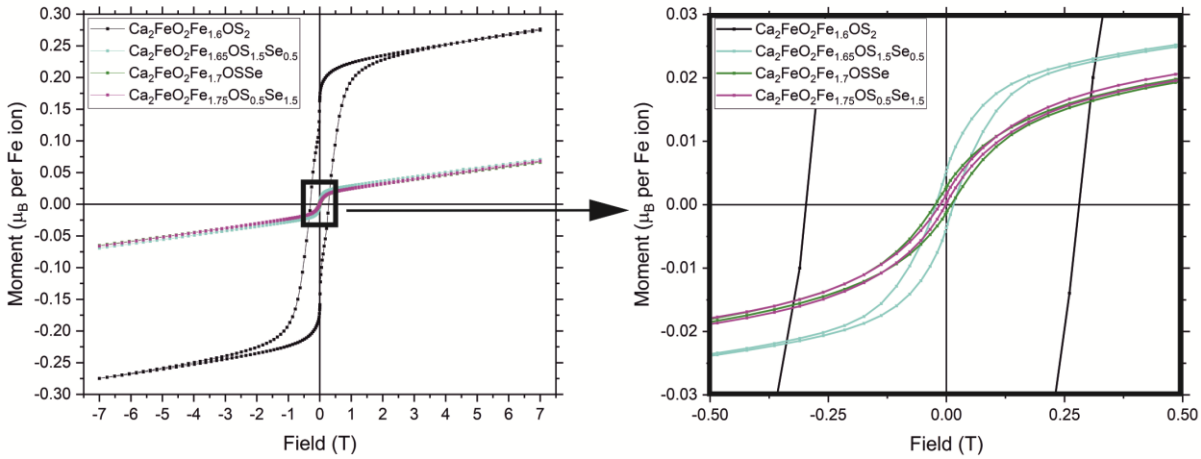


Figure 4.16: 5 K magnetisation isotherms for the $Ca_2FeO_2Fe_{1.6+\delta}OCh_2$ (*Ch* = S, Se) compounds. The graph on the right focusses on the data near the origin.

4.3.4 XANES Measurements

The Fe oxidation states in the three phases were investigated at room temperature using synchrotron XANES experiments on beamline I18 at the Diamond Light Source. The spectra are shown in Figures 4.17 and 4.18, along with $Ca_2FeO_2Fe_{1.6}OS_2$ for comparison and the FeS, FeO and Fe_2O_3 standards.

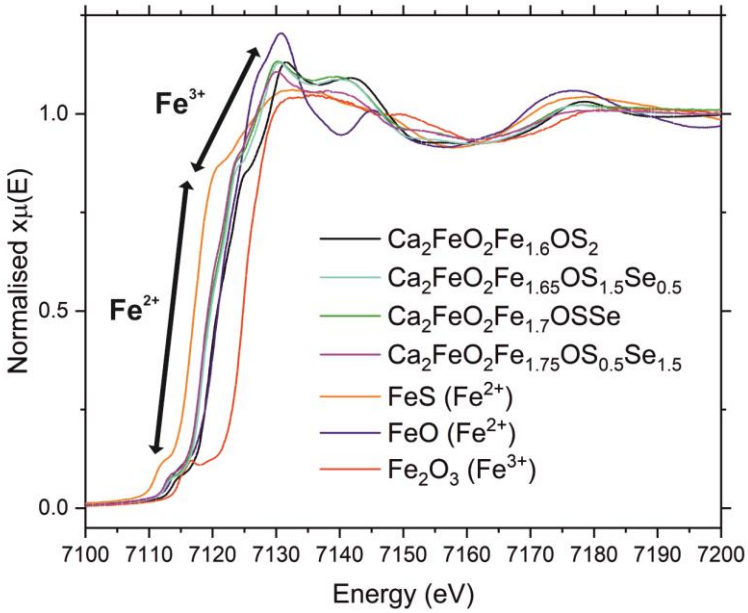


Figure 4.17: XANES K-edge for the $Ca_2FeO_2Fe_{1.6+\delta}OCh_2$ (*Ch* = S, Se) compounds and Fe^{2+}/Fe^{3+} standards.

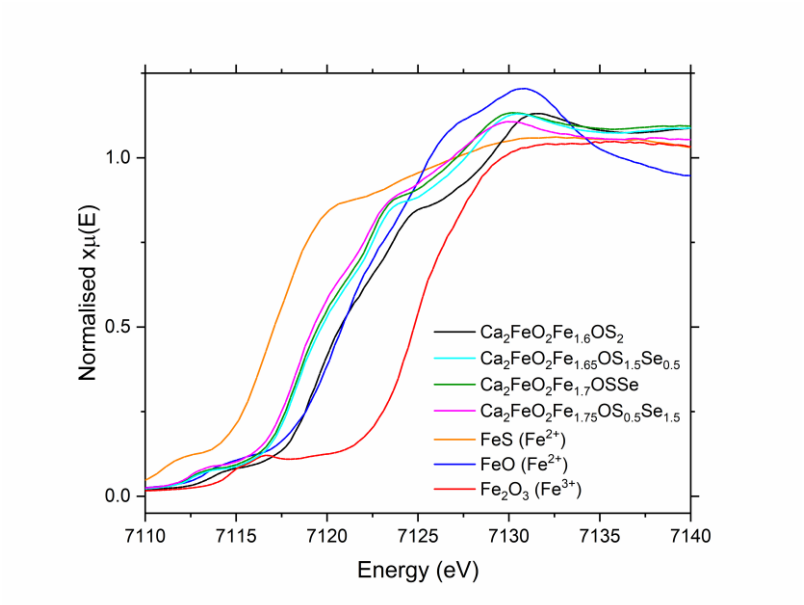


Figure 4.18: Closer view of the XANES K-edges shown in Figure 4.17.

The K-edges are almost identical for all three of the solid solution phases, however the slight decrease in energy of the K-edges as more Se is introduced is likely to be due to the more reducing nature of Se^{2-} compared to S^{2-}. The K-edges are interpreted as being comprised of a first edge at lower energy (Fe^{2+}) and a second edge at higher energy (Fe^{3+}). In Chapter 3, this edge was discussed for $Ca_2FeO_2Fe_{1.6}OS_2$ and the ratio of the edges was approximately 2:1 for Fe^{2+}:Fe^{3+}. It can be seen in Figure 4.18 that as more Se is incorporated, the first edge becomes longer relative to the second edge, suggesting that the Fe^{2+}:Fe^{3+} ratio is tending towards more Fe^{2+}. This is consistent with the increase in the Fe2 site occupancy by Fe^{2+} cations, as alluded to by the BVS in section 4.3.1, which results in a greater proportion of Fe^{2+} than Fe^{3+}. The K-edges for the solid solution phases fall between those for FeS and FeO, consistent with the Fe^{3+} and Fe^{2+} being present in a mixed-anion environment (i.e., the FeO_4Ch_2 and FeO_2Ch_4 environments present in these materials).

It should be noted that assignment of a specific edge to a specific oxidation state is not straightforward as the Fe K-edge position is affected by other factors such as the Fe coordination environment, of which there are two that exist in this structure. The assignments made here do however agree well with BVS calculations (section 4.3.1) and localised magnetic moments deduced from NPD refinements (section 4.3.5). The significant difference between the $Ca_2FeO_2Fe_{1.6}OS_2$ K-edges and the K-edges of the solid solution phases, which is greater than the differences between the K-edges of the three solid solution phases, is likely due to the significant changes to the Fe coordination environments when the long-range vacancy ordering is lost.

4.3.5 Variable Temperature NPD

Variable temperature NPD data were gathered on the D2B instrument at the ILL. Due to time constraints, only room temperature and 5 K data sets were collected for $Ca_2FeO_2Fe_{1.65}OS_{1.5}Se_{0.5}$ and $Ca_2FeO_2Fe_{1.7}OSSe$. Data at more temperatures were obtained for $Ca_2FeO_2Fe_{1.75}OS_{0.5}Se_{1.5}$ in order to investigate the broad signal in the magnetometry data.

4.3.5.1 $Ca_2FeO_2Fe_{1.65}OS_{1.5}Se_{0.5}$

The nuclear model was fixed to that refined from the 300 K D2B data, with only lattice parameters and the *z*-coordinates of calcium and the chalcogenides allowed to refine. The magnetic Bragg peaks can be accounted for by introducing the mM5+ magnetic mode with $k = (1/2, 1/2, 0)$ on the Fe1 site and a combination of the mX1- and mX2- magnetic modes with $k = (0, 1/2, 0)$ on the Fe2 site. The contribution of the ordering on the Fe1 and Fe2 sites to the magnetic Bragg peaks is depicted in Figure 4.19 and the model is illustrated in Figure 4.20.

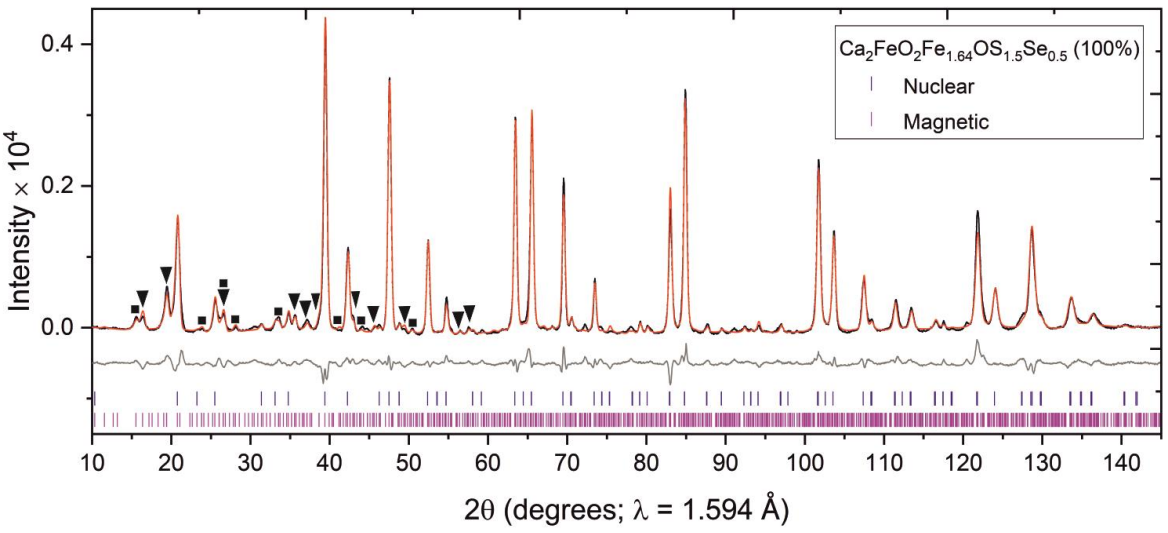


Figure 4.19: NPD pattern of $Ca_2FeO_2Fe_{1.65}OS_{1.5}Se_{0.5}$ measured at 5 K on the D2B instrument at the ILL showing the observed (black), calculated (red) and difference (grey) curves. R_{wp}: 6.181%. The magnetic ordering on the Fe1 sublattice gives rise to intensity on positions marked with a black triangle and the magnetic ordering on the Fe2 sublattice gives rise to intensity on positions marked with a black square.

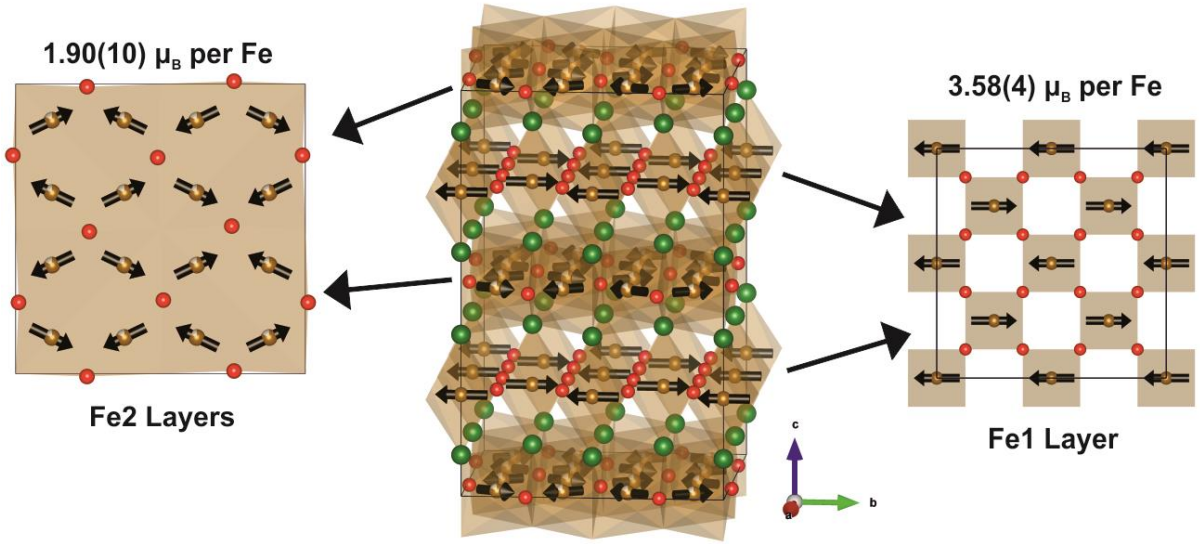


Figure 4.20: Magnetic model for $Ca_2FeO_2Fe_{1.65}OS_{1.5}Se_{0.5}$ at 5 K, refined using the NPD data collected on the D2B instrument at the ILL shown in Figure 4.19.

4.3.5.2 $Ca_2FeO_2Fe_{1.7}OSSe$

The nuclear model was fixed to that refined from the 300 K D2B data, with only lattice parameters and the *z*-coordinates of calcium and the chalcogenides allowed to refine. The magnetic Bragg peaks can be accounted for by introducing the mM5+ magnetic mode with $k = (^1/_2, ^1/_2, 0)$ on the Fe1 site and a combination of the mX1- and mX2- magnetic modes with $k = (0, ^1/_2, 0)$ on the Fe2 site. The contribution of the ordering on the Fe1 and Fe2 sites to the magnetic Bragg peaks is depicted in Figure 4.21 and the model is illustrated in Figure 4.22.

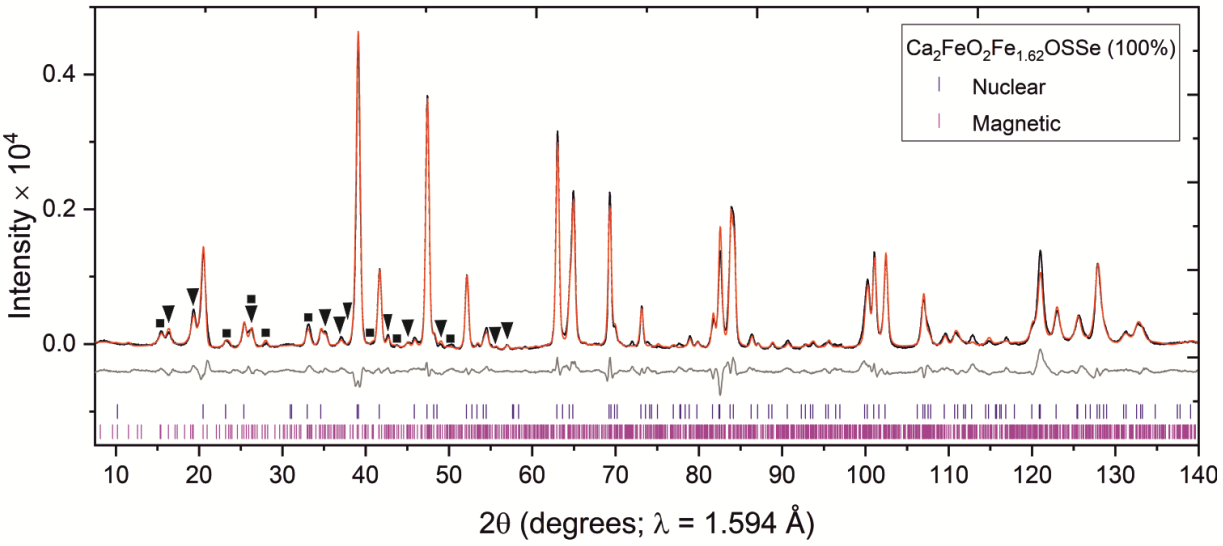


Figure 4.21: NPD pattern of $Ca_2FeO_2Fe_{1.7}OSSe$ measured at 5 K on the D2B instrument at the ILL showing the observed (black), calculated (red) and difference (grey) curves. R_{wp}: 6.244%. The magnetic ordering on the Fe1 sublattice gives rise to intensity on positions marked with a black triangle and the magnetic ordering on the Fe2 sublattice gives rise to intensity on positions marked with a black square.

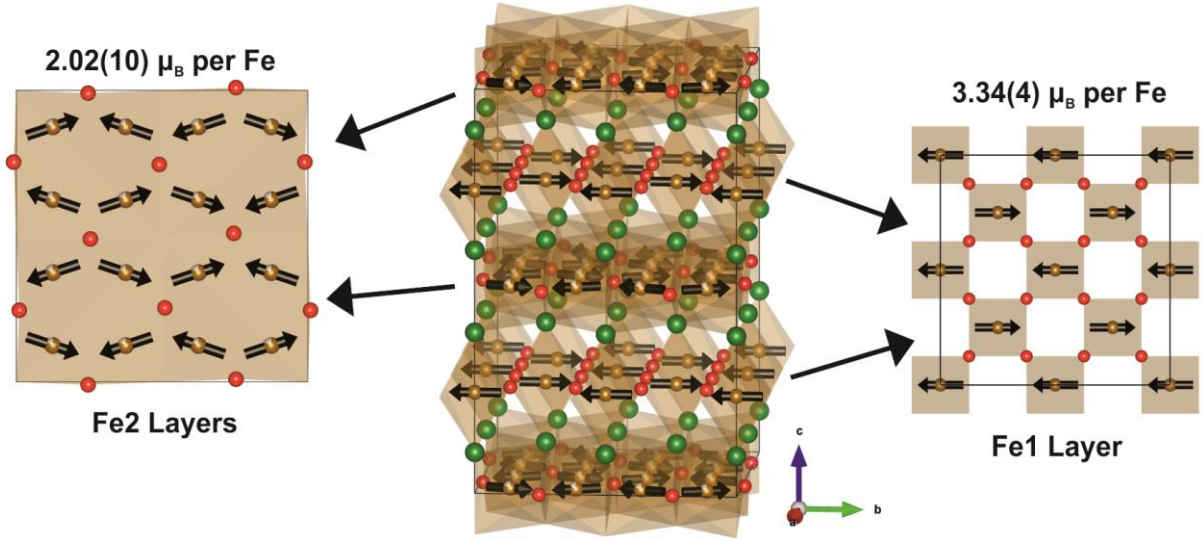


Figure 4.22: Magnetic model for $Ca_2FeO_2Fe_{1.7}OSSe$ at 5 K, refined using the NPD data collected on the D2B instrument at the ILL shown in Figure 4.21.

4.3.5.3 $Ca_2FeO_2Fe_{1.75}OS_{0.5}Se_{1.5}$

Refinement against the 5 K data was performed by fixing the Fe2 occupancy and chalcogenide ratio as refined at room temperature. The resulting fit to the experimental data is shown in Figure 4.23. As well as the small amounts of CaSe and FeO impurities, the relatively low intensity magnetic peak (highlighted by the green square at around $2\theta = 36°$ with *d*-spacing of 2.588 Å) can be accounted for as the highest intensity magnetic Bragg peak of FeO. In order to account for all the magnetic peaks, long-range ordering of the Fe moments in both the Fe1 and Fe2 layers were again modelled, where the best fit to the data is illustrated by the model in Figure 4.24. The magnetic Bragg peaks can be accounted for by introducing the mM5+ and mA2+ magnetic modes, which have $k = (1/2, 1/2, 0)$ and $k = (1/2, 1/2, 1/2)$ respectively, on the Fe1 site and a combination of the mX1- and mX2- magnetic modes with $k = (0, 1/2, 0)$ on the Fe2 site.

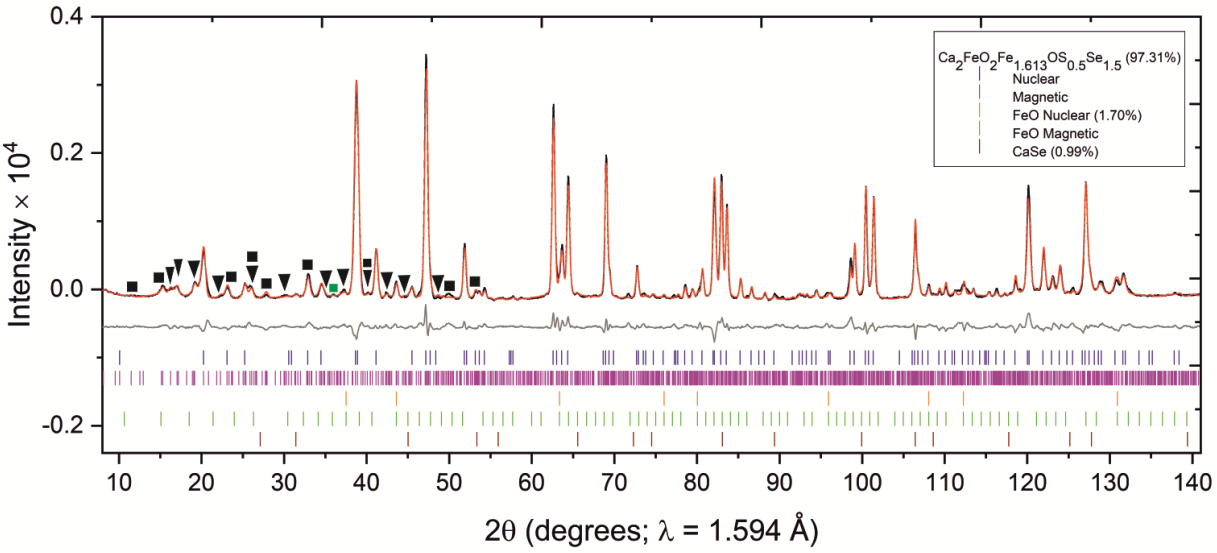


Figure 4.23: NPD pattern of $Ca_2FeO_2Fe_{1.75}OS_{0.5}Se_{1.5}$ measured at 5 K on the D2B instrument at the ILL showing the observed (black), calculated (red) and difference (grey) curves. R_{wp}: 5.733%. The magnetic ordering on the Fe1 sublattice gives rise to intensity on positions marked with a black triangle and the magnetic ordering on the Fe2 sublattice gives rise to intensity on positions marked with a black square. The magnetic ordering in the FeO impurity gives rise to the peak marked with a green square.

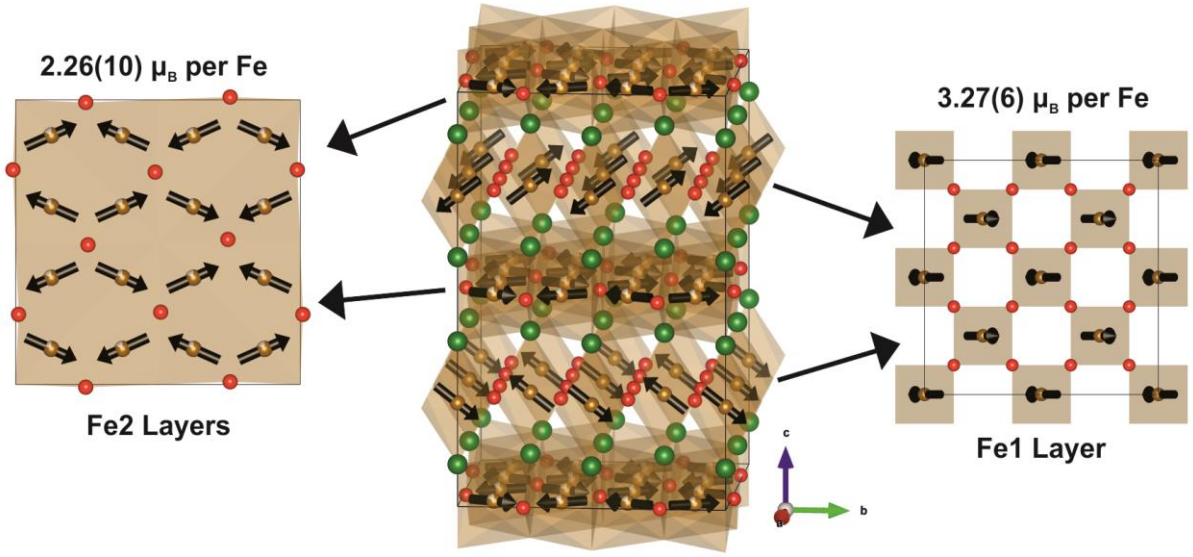


Figure 4.24: Magnetic model for $Ca_2FeO_2Fe_{1.75}OS_{0.5}Se_{1.5}$ at 5 K, refined using the NPD data collected on the D2B instrument at the ILL shown in Figure 4.23.

The ordering in each layer is much like that we have seen for $Ca_2FeO_2Fe_{1.65}OS_{1.5}Se_{0.5}$ and $Ca_2FeO_2Fe_{1.7}OSSe$, although in the case of $Ca_2FeO_2Fe_{1.75}OS_{0.5}Se_{1.5}$ the moments in adjacent Fe1 layers are antiferromagnetically coupled and all the Fe1 spins are also canted towards the *c*-axis. This antiferromagnetic alignment of spins in adjacent Fe1 layers potentially suggests there are stronger interactions between these layers in the case of $Ca_2FeO_2Fe_{1.75}OS_{0.5}Se_{1.5}$. Figure 4.25 highlights two potential super-superexchange pathways over which the spins in adjacent Fe1 layers could interact. There is the Fe-*Ch*…*Ch*-Fe pathway shown by the pink lines and the Fe-*Ch*-Fe-*Ch*-Fe pathway shown by the blue lines. It seems likely that the Fe-*Ch*…*Ch*-Fe super-superexchange is the stronger of the two interactions due to the 180° geometry (allowing for maximum orbital overlap) and the overall shorter distance of the pathway. It is also likely that these interactions are only strong enough to result in moments in adjacent Fe1 layers coupling antiferromagnetically for the case with the highest proportion of Se (ie $Ca_2FeO_2Fe_{1.75}OS_{0.5}Se_{1.5}$) because of the fact that the Se^{2-} 4*p* orbitals are more radially distributed than the S^{2-} 3*p* orbitals, which allows for greater orbital overlap with the Fe 3*d* orbitals involved in the Fe-*Ch*…*Ch*-Fe pathway.

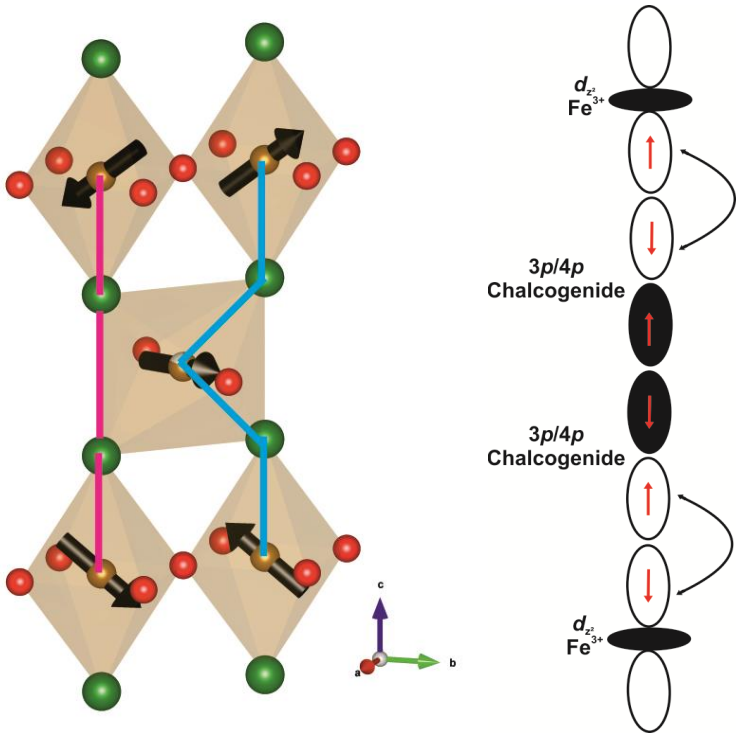


Figure 4.25: Possible super-superexchange pathways over which Fe spins on adjacent Fe1 sublattices could interact. The pink lines highlight the Fe-*Ch*…*Ch*-Fe pathway and the blue lines highlight the Fe-*Ch*-Fe-*Ch*-Fe pathway. The orbital interactions along the Fe-*Ch*…*Ch*-Fe pathway are shown on the right hand side.

This Fe-*Ch*…*Ch*-Fe super-superexchange is predicted to be an antiferromagnetic exchange, as displayed on the right hand side of Figure 4.25. In the $Cu_2UO_2(PO_4)_2$ compound, calculations by Koo and Whangbo[4] predict that the interchain Cu-O…O-Cu super-superexchange pathways are much stronger than the intrachain superexchange interactions and that these Cu-O…O-Cu couplings are predicted to be strongly antiferromagnetic. This supports the idea that the Fe in adjacent Fe1 layers interact antiferromagnetically via the Fe-*Ch*…*Ch*-Fe super-superexchange shown in Figure 4.25. However, it should be noted that in the $Cu_2UO_2(PO_4)_2$ example the Cu-O…O-Cu pathway contains Cu-O-Cu angles of around 130° and so is not completely analogous to the Fe-*Ch*…*Ch*-Fe pathway. It could be the case that interactions between spins in the Fe2 layers with spins in the Fe1 layers via the Fe2-*Ch*-Fe1 superexchanges (which act along the blue line in Figure 4.25) are responsible for the canting of the moments in the Fe1 layers, however further neutron scattering experiments- preferably on single crystals- are needed to explore the evolution of the moments with temperature and to improve on the existing magnetic model. An upcoming D1B experiment will be carried out by another

student with the aim of obtaining NPD data with higher resolution at longer *d*-spacings and collecting data over a large temperature range (5 K to 350 K) in small temperature intervals (approximately every 2 K) for all three of the solid solution phases in this chapter. Calculations of the magnitude of competing magnetic coupling interactions in each of the solid solution phases would also be possible further work.

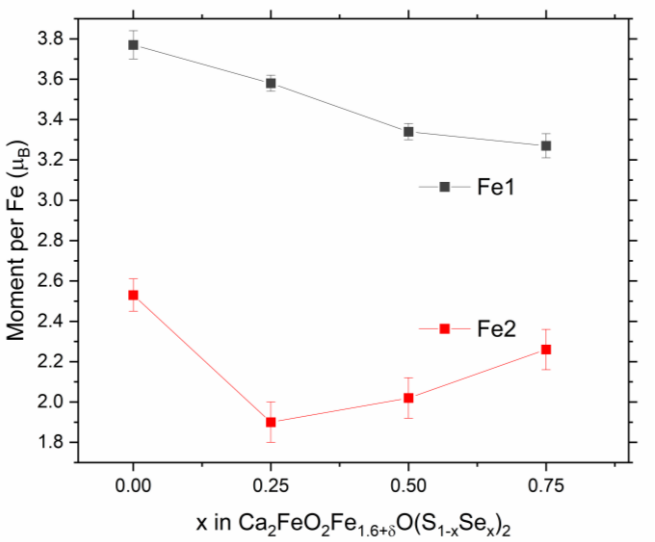


Figure 4.26: Comparison of the long-range ordered magnetic moments in the Fe1 and Fe2 layers for the $Ca_2FeO_2Fe_{1.6+\delta}OCh_2$ (*Ch* = S, Se) compounds, refined from 5 K NPD data. The moment values per Fe given on the *y*-axis for Fe2 are the moment per occupied Fe2 site, as these values have taken the partial occupancies of these sites into account.

The variation in saturated moment with composition is given in Figure 4.26. The steady decrease in the Fe1 moment agrees well with the conclusion drawn from the BVS (section 4.3.1) and XANES (section 4.3.4), which suggests the inclusion of more Fe^{2+} in the Fe2 layer reduces the Fe^{3+} in the Fe1 layer slightly. The initial drop in the Fe2 moment may be caused by the loss of the long-range ordering of the Fe vacancies in this layer, as this results in more disorder within this layer and so the magnitude of the long-range ordered moment naturally decreases. Then, as the Fe2 vacancies become filled, the superexchange interactions become stronger as a network throughout the whole layer, resulting in a greater long-range ordered moment going from $Ca_2FeO_2Fe_{1.65}OS_{1.5}Se_{0.5}$ to $Ca_2FeO_2Fe_{1.7}OSSe$ to $Ca_2FeO_2Fe_{1.75}OS_{0.5}Se_{1.5}$.

Variable temperature NPD data, as depicted in Figure 4.27, were collected for the $Ca_2FeO_2Fe_{1.75}OS_{0.5}Se_{1.5}$ compound in order to investigate the magnetic evolution on the two Fe sublattices, especially focussing on the broad feature seen in the magnetometry data centred around 160 K (see section 4.3.3). It is especially interesting to see that between 100 K and 162 K there is a simultaneous increase in the magnetic peaks labelled with a blue square and decrease in the magnetic peaks labelled with a blue star. The magnetic Bragg peaks in this temperature region can be fitted using a combination of the Fe1 mM2+ mode (with moments directed along the *c*-axis) and the Fe1 mA5+ mode (with moments directed in the *ab*-plane).

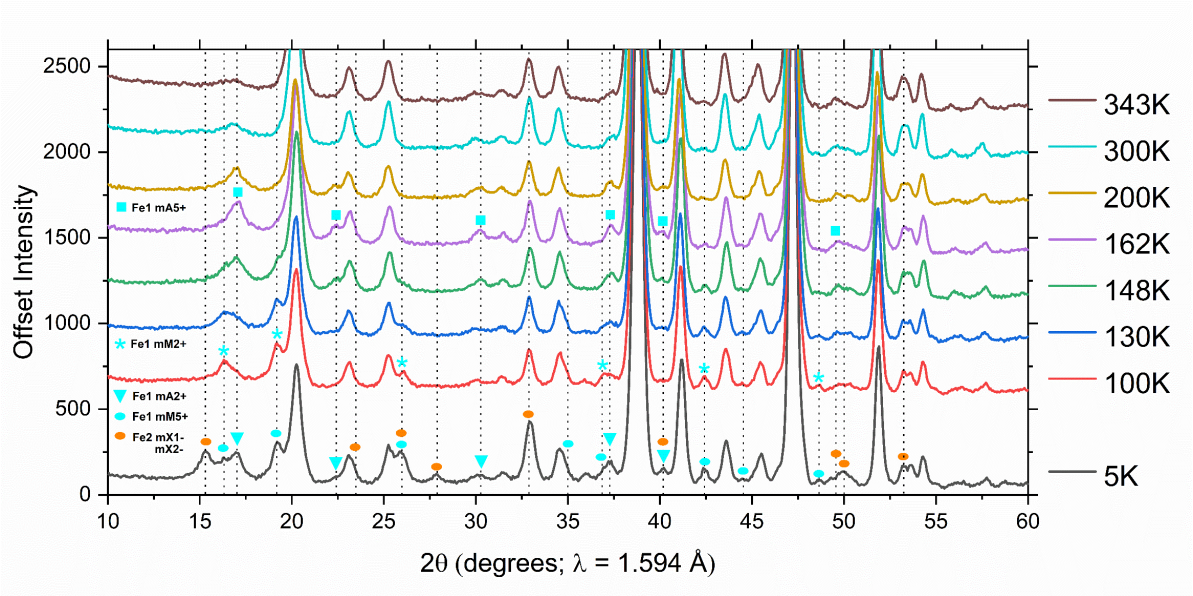


Figure 4.27: NPD patterns for $Ca_2FeO_2Fe_{1.75}OS_{0.5}Se_{1.5}$ at different temperatures measured on the D2B instrument at the ILL showing the evolution of the magnetic peaks. Magnetic Bragg peaks are labelled with the magnetic modes which contribute to their intensity.

Figures 4.28-4.34 show the refinements of the nuclear and magnetic models against NPD data collected at temperatures from 100 K to 343 K. The key changes to the ordering of the Fe moments with temperature are depicted in Figure 4.35 and changes in the moment magnitudes and orientations are given in Figure 4.36.

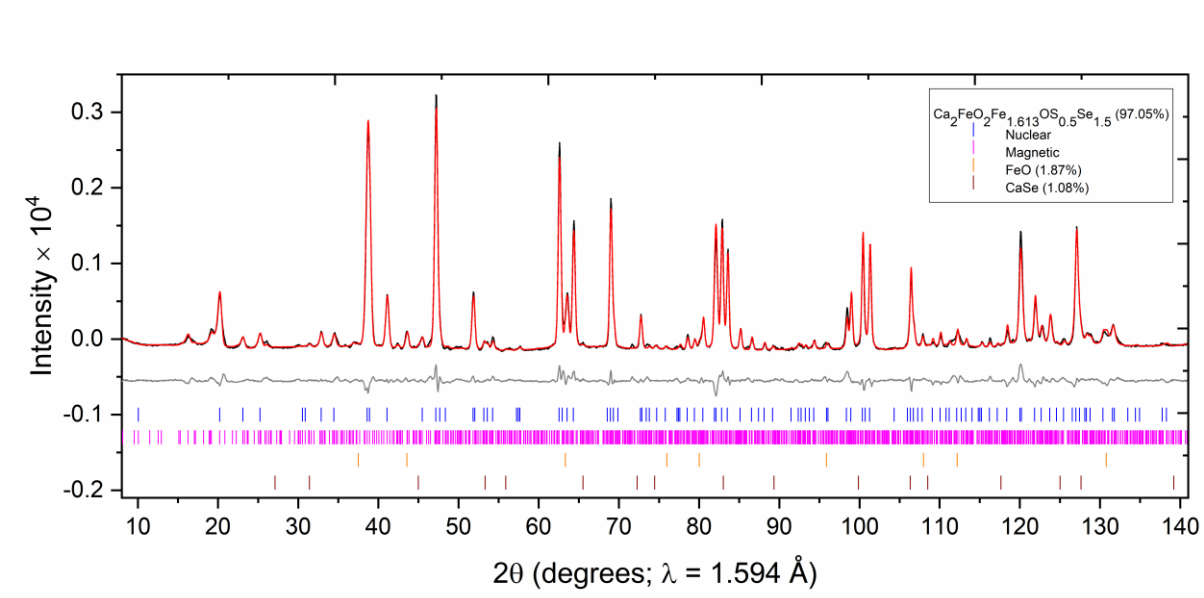


Figure 4.28: NPD pattern of $Ca_2FeO_2Fe_{1.75}OS_{0.5}Se_{1.5}$ measured at 100 K on the D2B instrument at the ILL showing the observed (black), calculated (red) and difference (grey) curves. R_{wp}: 5.330%.

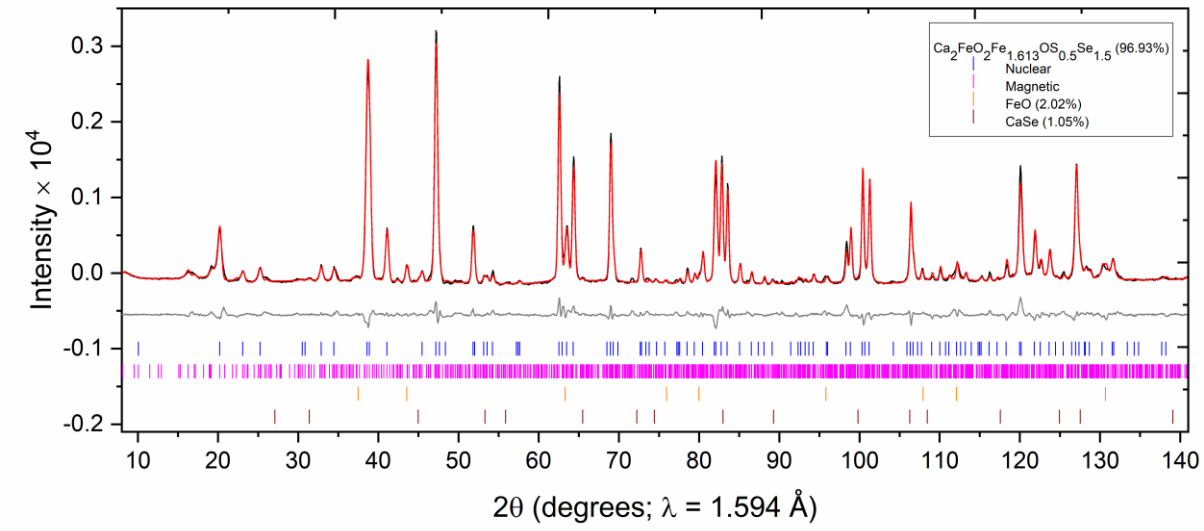


Figure 4.29: NPD pattern of $Ca_2FeO_2Fe_{1.75}OS_{0.5}Se_{1.5}$ measured at 130 K on the D2B instrument at the ILL showing the observed (black), calculated (red) and difference (grey) curves. R_{wp}: 5.126%.

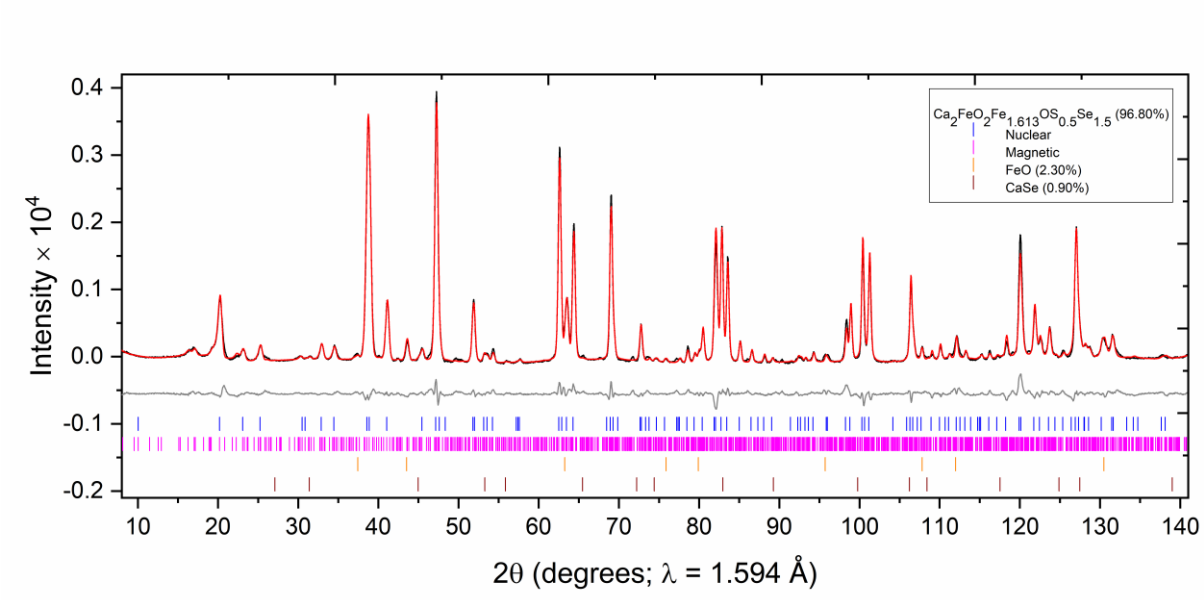


Figure 4.30: NPD pattern of $Ca_2FeO_2Fe_{1.75}OS_{0.5}Se_{1.5}$ measured at 148 K on the D2B instrument at the ILL showing the observed (black), calculated (red) and difference (grey) curves. R_{wp}: 4.981%.

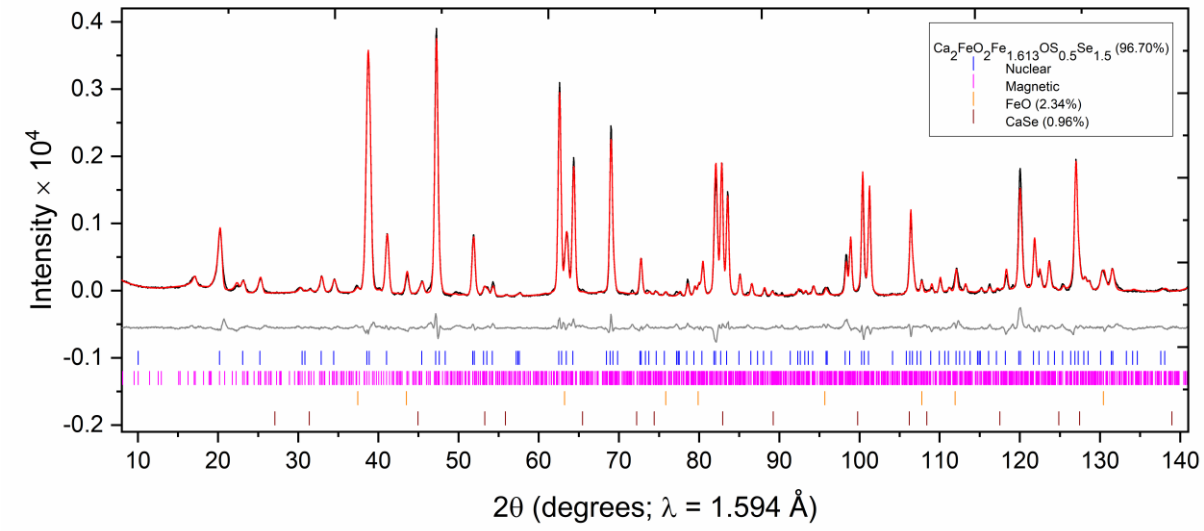


Figure 4.31: NPD pattern of $Ca_2FeO_2Fe_{1.75}OS_{0.5}Se_{1.5}$ measured at 162 K on the D2B instrument at the ILL showing the observed (black), calculated (red) and difference (grey) curves. R_{wp}: 4.759%.

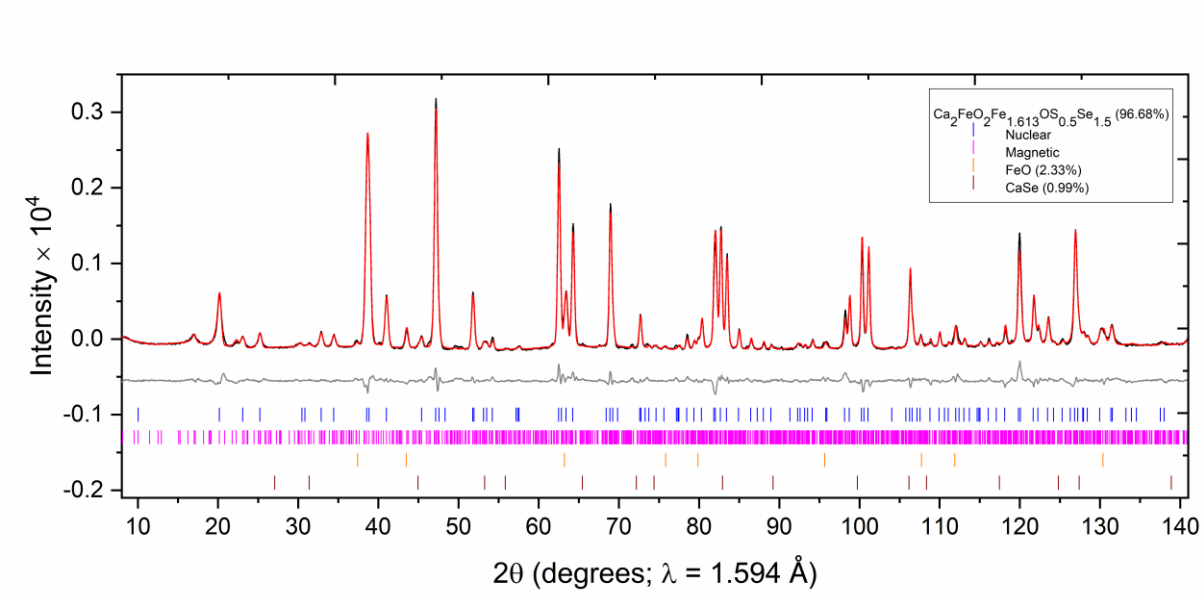


Figure 4.32: NPD pattern of $Ca_2FeO_2Fe_{1.75}OS_{0.5}Se_{1.5}$ measured at 200 K on the D2B instrument at the ILL showing the observed (black), calculated (red) and difference (grey) curves. R_{wp}: 4.888%.

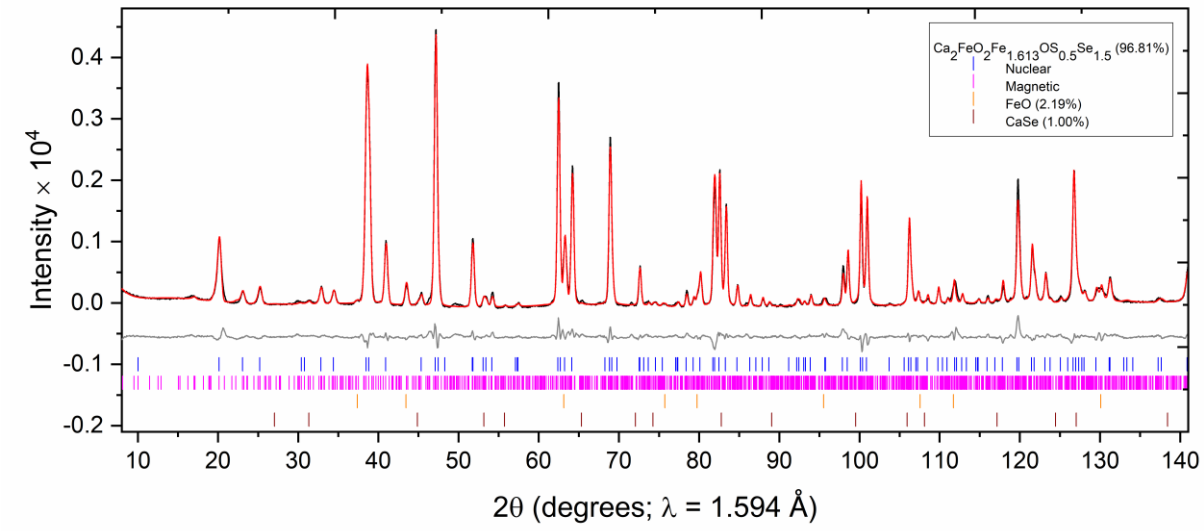


Figure 4.33: NPD pattern of $Ca_2FeO_2Fe_{1.75}OS_{0.5}Se_{1.5}$ measured at 300 K on the D2B instrument at the ILL showing the observed (black), calculated (red) and difference (grey) curves. R_{wp}: 4.853%.

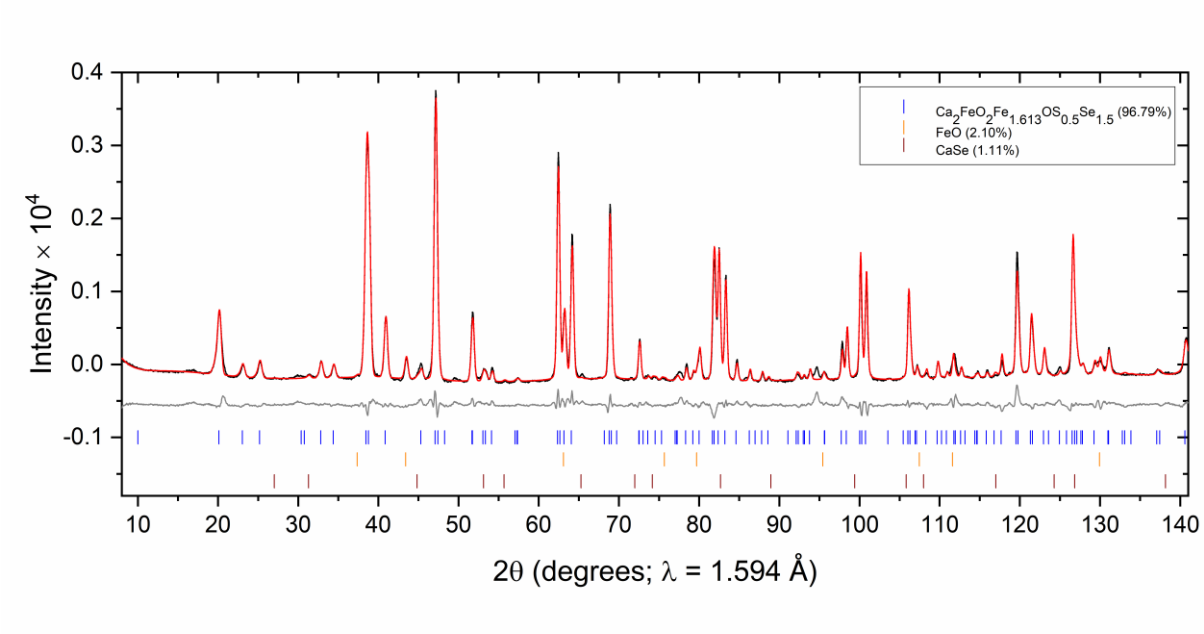


Figure 4.34: NPD pattern of $Ca_2FeO_2Fe_{1.75}OS_{0.5}Se_{1.5}$ measured at 343 K on the D2B instrument at the ILL showing the observed (black), calculated (red) and difference (grey) curves. R_{wp}: 4.838%.

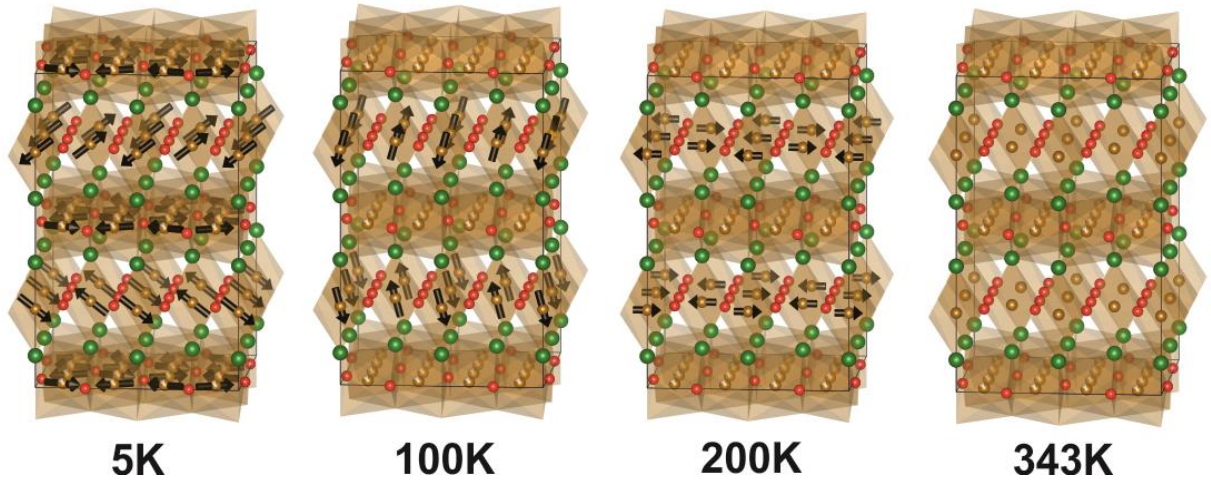


Figure 4.35: Models for the long-range magnetic ordering in $Ca_2FeO_2Fe_{1.75}OS_{0.5}Se_{1.5}$ at key temperatures, illustrating the spin-reorientations of the moments in the Fe1 layer between 5 K and 200 K.

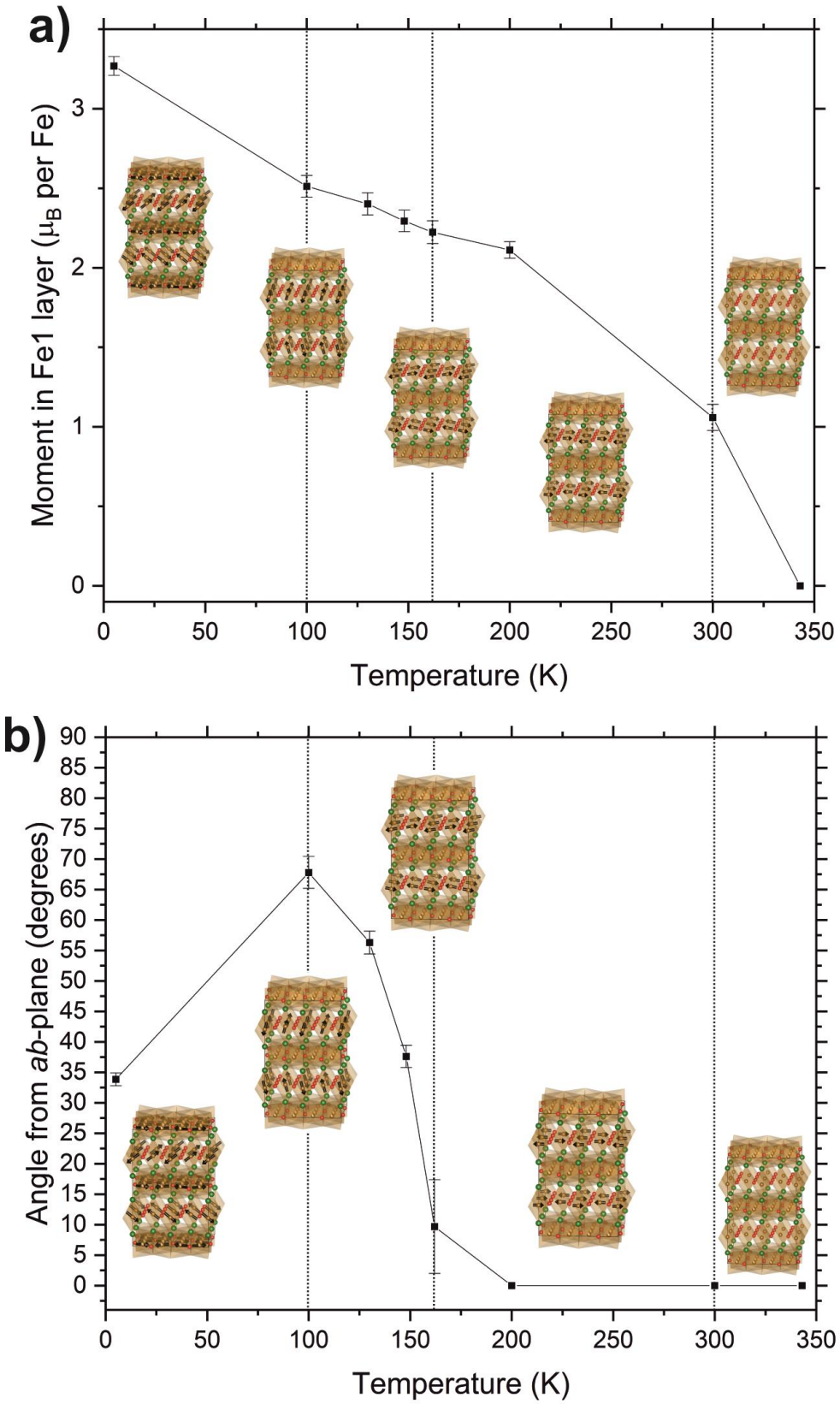


Figure 4.36: The change in **a)** the magnitude of the Fe1 moment and **b)** the angle of the Fe1 moment from the *ab*-plane, for the $Ca_2FeO_2Fe_{1.75}OS_{0.5}Se_{1.5}$ material, refined from the variable temperature D2B data given in Figure 4.23 and Figures 4.28-4.34.

The moments in the Fe1 layer appear to undergo two spin-reorientations. The first coincides with the loss of the long-range ordered moments in the Fe2 layer between 5 K and 100 K and the second occurs between 100 K and 200 K. When the moments in the Fe2 layers cease to order, the moments in the Fe1 layers reorient towards the *c*-axis. This is perhaps a result of the loss of the Fe1-*Ch*-Fe2 superexchange interactions (depicted by the blue pathway in Figure 4.37) when the long-range ordering in the Fe2 layer no longer exists. It is usually the case that magnetic moments on different *k*-vector sublattices don't interact with each other, however if there is local ordering of the Fe2 vacancies (as discussed in section 4.3.6) then the solid solution phases are more comparable to the $Ca_2FeO_2Fe_{1.6}OS_2$ case where, due to the adoption of a supercell, magnetic ordering on both layers can be described as being on a *k*-vector of $k = (0\ 0\ 0)$ and therefore all moments can interact. As discussed in section 3.3.8, this approximately 130° Fe1-*Ch*-Fe2 superexchange is unlikely to heavily favour an antiferromagnetic or ferromagnetic coupling, however the loss of long-range ordering of the Fe2 moments does seem to have some degree of influence on the orientation of the Fe1 moments.

Upon warming the material these Fe1 moments then reorient into the *ab*-plane, before eventually losing long-range order between 300 K and 343 K. This spin-reorientation at higher temperatures is again difficult to rationalise. It could potentially be driven by the antiferromagnetic Fe-*Ch*…*Ch*-Fe superexchange interactions which mediate interactions of Fe1 spins in adjacent Fe1 layers (as depicted earlier in Figure 4.25). Alternatively it is perhaps the case that there is short-range ordering of the Fe2 spins at 100 K, just before these moments undergo the long-range ordering transition, but this short-range order doesn't exist at higher temperatures, and so the approximately 130° Fe1-*Ch*-Fe2 superexchange interactions only begin to play a role in the Fe1 moment orientation at around 100 K.

This switching of C-type ordering at 100 K to G-type ordering at 200 K is also seen in the $Sr_2Mn_{2.23}Cr_{0.77}As_2O_2$ compound, which exhibits C-type ordering at lower temperatures and G-type ordering at higher temperatures in the $[M_2As_2]^{2-}$ (M = Mn/Cr mixture) layers, as reported by Lawrence *et al*.[5]

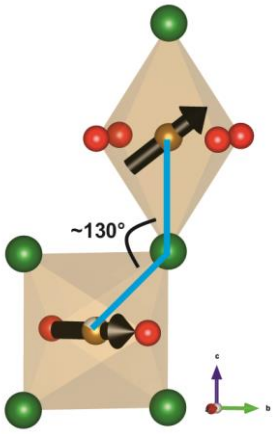


Figure 4.37: The Fe1-*Ch*-Fe2 superexchange pathway, as highlighted by the blue lines.

As mentioned earlier, these variable temperature magnetic models for $Ca_2FeO_2Fe_{1.75}OS_{0.5}Se_{1.5}$ will be investigated further in an upcoming variable temperature D1B experiment by another student. With the higher resolution data at longer *d*-spacings, it may be possible that these models are adapted with the help of these diffraction data, especially at 5 K where it is difficult to disentangle the three apparent magnetic Bragg peaks at around 2θ = 15-17.5° (see Figure 4.23) and the relative contributions of the magnetic modes to them. These data may also reveal whether any incommensurately modulated magnetic Bragg peaks are present, the existence of which could also help to explain the spin-reorientations, as in the $Sr_2CrO_2Cr_2As_2$ material.[6] A temperature scan from 5 K to just above 300 K in approximately 2 K steps will be performed (similar to the data collected for $Ca_2FeO_2Fe_{1.6}OS_2$ in section 3.3.8) and this should give an improved idea of the Fe1 and Fe2 moment evolutions with temperature, in terms of both magnitude and orientation. Experiments which probe local magnetic structure, such as neutron scattering experiments performed on single crystals, could shed light on whether short-range ordering of the Fe2 moments exists before the long-range ordering in this layer.

4.3.6 Mössbauer Spectroscopy

Room temperature ^{57}Fe Mössbauer spectra were collected and analysed by Dr. Alex Scrimshire at Sheffield Hallam University in order to probe the Fe oxidation states, Fe coordination environments and long-range magnetic ordering of the Fe moments in these solid solution compounds.

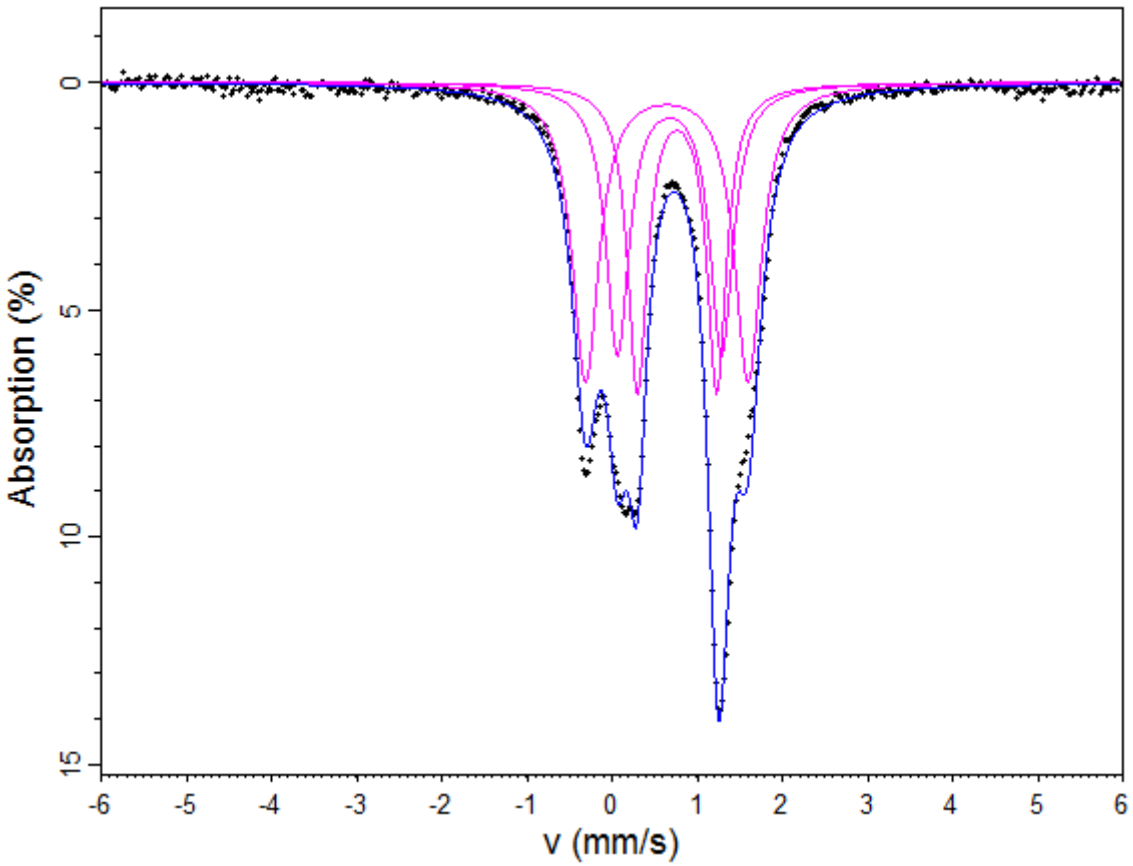


Figure 4.38: Fitting of the Mössbauer spectrum of $Ca_2FeO_2Fe_{1.65}OS_{1.5}Se_{0.5}$ at 300 K, showing the observed data (black points), calculated fit (blue line) and the contribution of each individual site (pink lines). Reduced χ^2: 2.94633.

The data at 300 K for $Ca_2FeO_2Fe_{1.65}OS_{1.5}Se_{0.5}$ in Figure 4.38 can be fit by three doublets. There are no sextets present which means there is no long-range magnetic ordering at 300 K, as also suggested by the NPD data (section 4.3.5.1). The doublet with the lowest centre shift, CS = 0.6440(20) mm/s, can be assigned to the Fe^{3+} in the Fe1 layer and the other two doublets assigned to the Fe^{2+} in the Fe2 layer, giving approximately a 60:40 ratio of Fe^{2+}:Fe^{3+}.

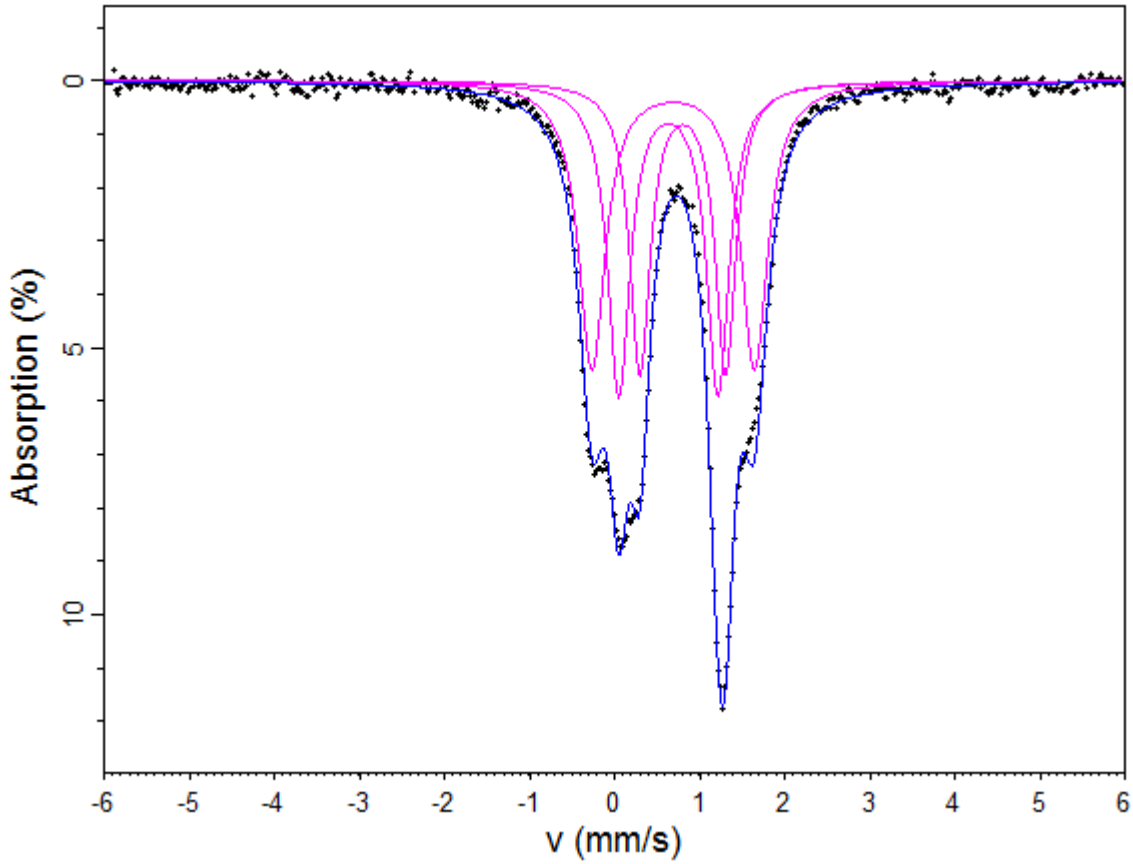


Figure 4.39: Fitting of the Mössbauer spectrum of $Ca_2FeO_2Fe_{1.7}OSSe$ at 300 K, showing the observed data (black points), calculated fit (blue line) and the contribution of each individual site (pink lines). Reduced χ^2: 1.62628.

The data for $Ca_2FeO_2Fe_{1.7}OSSe$ in Figure 4.39 can be fit by three doublets. There are no sextets present which means there is no long-range magnetic ordering at 300 K, as also suggested by the NPD data (section 4.3.5.2). The doublet with the lowest centre shift, CS = 0.6341(43) mm/s, can be assigned to the Fe^{3+} in the Fe1 layer and the other two doublets assigned to the Fe^{2+} in the Fe2 layer, giving approximately a 65:35 ratio of Fe^{2+}:Fe^{3+}.

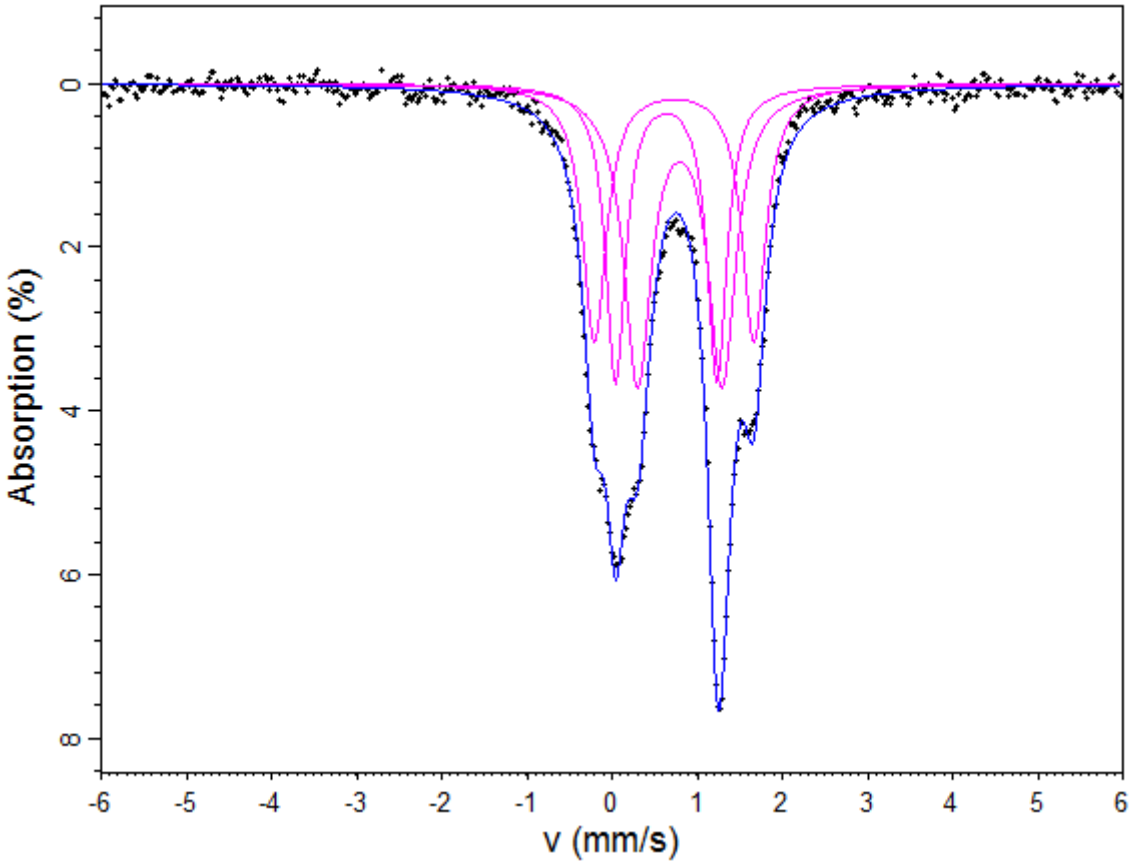


Figure 4.40: Fitting of the Mössbauer spectrum of $Ca_2FeO_2Fe_{1.75}OS_{0.5}Se_{1.5}$ at 300 K, showing the observed data (black points), calculated fit (blue line) and the contribution of each individual site (pink lines). Reduced χ^2: 0.94519.

The data for $Ca_2FeO_2Fe_{1.75}OS_{0.5}Se_{1.5}$ in Figure 4.40 can be fit by three doublets. There are no sextets present which means there is no long-range magnetic ordering at 300 K, as also suggested by the NPD data (section 4.3.5.3). The doublet with the lowest centre shift, CS = 0.6384(58) mm/s, can be assigned to the Fe^{3+} in the Fe1 layer and the other two doublets assigned to the Fe^{2+} in the Fe2 layer, giving approximately a 70:30 ratio of Fe^{2+}:Fe^{3+}.

Table 4.8 shows that as more Se is introduced the proportion of Fe^{2+} increases, as expected due to the stoichiometry of Fe in the material increasing and resulting in more Fe^{2+} on the Fe2 site and possible concurrent reduction of the Fe^{3+} on the Fe1 site (as discussed in sections 4.3.1, 4.3.4 and 4.3.5.3). Table 4.8 also details the fitting results of the Mössbauer spectra shown in Figures 4.38-4.40.

Compound	Fe^{2+}: Fe^{3+} Ratio	Fe^{2+}/ Fe^{3+}	Fe^{2+}/ Fe^{3+} (Expected from formula)
$Ca_2FeO_2Fe_{1.65}OS_{1.5}Se_{0.5}$	60(6):40(2)	1.5(3)	1.65
$Ca_2FeO_2Fe_{1.7}OSSe$	66(4):34(2)	1.9(3)	1.7
$Ca_2FeO_2Fe_{1.75}OS_{0.5}Se_{1.5}$	71(5):29(3)	2.5(5)	1.75

					$Ca_2FeO_2Fe_{1.65}OS_{1.5}Se_{0.5}$
Site	CS (mm/s)	Fe OS	Δ (mm/s)	Fe Layer	Site Population (%)
Doublet 1	0.7647(43)	+2	0.9312(67)	Fe2	29.4(24)
Doublet 2	0.6440(20)	+3	1.9087(70)	Fe1	39.7(15)
Doublet 3	0.6761(37)	+2	1.223(11)	Fe2	30.9(36)

					$Ca_2FeO_2Fe_{1.7}OSSe$
Site	CS (mm/s)	Fe OS	Δ (mm/s)	Fe Layer	Site Population (%)
Doublet 1	0.8037(40)	+2	1.0074(69)	Fe2	28.8(19)
Doublet 2	0.6904(26)	+2	1.8113(79)	Fe2	37.4(13)
Doublet 3	0.6341(43)	+3	1.1650(80)	Fe1	33.9(20)

					$Ca_2FeO_2Fe_{1.75}OS_{0.5}Se_{1.5}$
Site	CS (mm/s)	Fe OS	Δ (mm/s)	Fe Layer	Site Population (%)
Doublet 1	0.7974(83)	+2	0.991(14)	Fe2	40.4(31)
Doublet 2	0.7313(36)	+2	1.872(11)	Fe2	30.6(17)
Doublet 3	0.6384(58)	+3	1.191(11)	Fe1	29.0(28)

Table 4.8: Comparison of the Fe^{2+}:Fe^{3+} (or equivalently Fe2:Fe1) ratios, derived from the fitting of Mössbauer spectra measured at 300 K (top) and the fitting results for the Mössbauer spectra measured at 300 K for the solid solution phases (bottom), as shown in Figures 4.38-4.40. The fitting results include proposed Fe oxidation states (OS) and the Fe layer from which each site originates.

It is perhaps unexpected that there are 3 Fe sites needed to fit these Mössbauer spectra, where there are only 2 unique Fe environments in the crystal structure- FeO_4Ch_2 in the Fe1 layer and FeO_2Ch_4 in the Fe2 layer. This result may be hinting that there is some local ordering on the Fe2 sites, as it is these sites which have been fitted using two doublets. The presence of local order on the Fe2 sites may support the apparent Fe1-S-Fe2 interactions between adjacent Fe1 and Fe2 layers, as discussed in section 4.3.5.

4.4 Discussion

4.4.1 Crystal Structure

The solid solution phases adopt the same structure as the $Ca_2FeO_2Fe_{1.6}OS_2$ material, but without long-range ordering of the Fe vacancies in the Fe2 layer and without long-range ordering of sulfide and selenide ions on the chalcogenide positions. The possibility of local ordering of the Fe vacancies and/or chalcogenide anions cannot be ruled out, however the positions of the chalcogenide anions relative to the oxide anions is fixed due to the structure. This results in the FeO_4Ch_2 and FeO_2Ch_4 distorted octahedra having trans-geometry, even though cis-ordering of more-similar anions around octahedra is commonly more energetically favourable than trans-ordering,[7] as exhibited by compounds such as $SrMO_2N$ (M = Nb, Ta).[8] Any local ordering of the chalcogenide anions could however show cis-geometry or trans-geometry. Further experiments would need to be performed to explore the possibility of local ordering, such as x-ray pair distribution function (PDF) measurements.

Comparisons between the solid solution phases and also with the all-sulfide phase have been made in section 4.3.1. A summary of the BVS values is presented in Table 4.9. Even though the absolute value of the BVS should be used with caution, these data all support the assignment of Fe^{3+} on the Fe1 site and Fe^{2+} on the Fe2 site. It seems likely that as more selenide anions are incorporated along with reduction in the number of Fe2 vacancies and the increase in the Fe content, the Fe on the Fe1 site become more reduced. As the composition moves towards the fully stoichiometric $Ca_2FeO_2Fe_2OCh_2$, the Fe on the Fe1 site would be predicted to tend towards Fe^{2+} in order to charge balance the system.

Compound		Fe BVS	Fe Formal OS
$Ca_2FeO_2Fe_{1.6}OS_2$	Fe1	+2.85(1)	+3
	Fe2	+2.01(13), +2.03(13), +2.05(13), +2.11(13)	+2
$Ca_2FeO_2Fe_{1.65}OS_{1.5}Se_{0.5}$	Fe1	+2.77(1)	+3
	Fe2	+2.02(1)	+2
$Ca_2FeO_2Fe_{1.7}OSSe$	Fe1	+2.73(1)	+3
	Fe2	+2.06(2)	+2
$Ca_2FeO_2Fe_{1.75}OS_{0.5}Se_{1.5}$	Fe1	+2.70(2)	+3
	Fe2	+2.07(4)	+2

Table 4.9: Comparison of Fe bond valence sums (BVS) and formal Fe oxidation states (OS).

4.4.2 Magnetic Structure

The Fe1 layers of all three solid solution phases exhibit checkerboard ordering of the moments to ensure all Fe-O-Fe superexchange pathways are antiferromagnetically coupled, as predicted by the Goodenough-Kanamori rules. Even when the suspected reduction of these Fe^{3+} ions towards Fe^{2+} is taken into account, as more Se is incorporated into the structure, coupling between Fe^{3+} and Fe^{2+} cations would still be predicted to be antiferromagnetic as the two $d_{x^2-y^2}$ orbitals both remain occupied by one electron. At 5 K, $Ca_2FeO_2Fe_{1.65}OS_{1.5}Se_{0.5}$ and $Ca_2FeO_2Fe_{1.7}OSSe$ contain Fe1 moments oriented in the *ab*-plane, however $Ca_2FeO_2Fe_{1.75}OS_{0.5}Se_{1.5}$ contains Fe1 moments which are canted towards the *c*-axis, as in the model proposed for $Ca_2FeO_2Fe_{1.6}OS_2$. The nature of the canting differs from that in $Ca_2FeO_2Fe_{1.6}OS_2$, as full antiferromagnetic order along all Fe-O-Fe superexchange pathways is maintained in the case of $Ca_2FeO_2Fe_{1.75}OS_{0.5}Se_{1.5}$ (see Figure 4.41 for a comparison), where this difference may be due to the presence or absence of canting of the long-range ordered moment in the Fe2 layer accompanying the canting in the Fe1 layer.

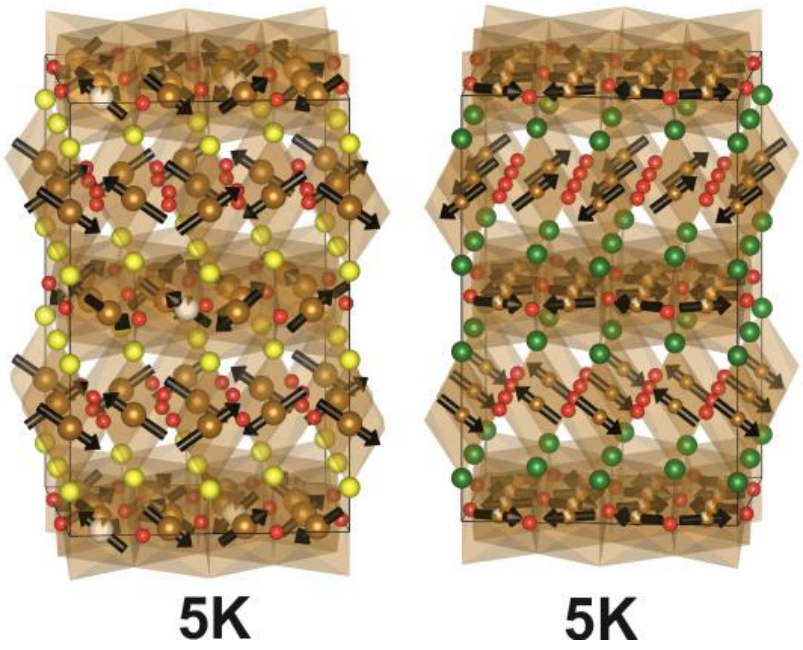


Figure 4.41: Comparison of the magnetic ordering models at 5 K for $Ca_2FeO_2Fe_{1.6}OS_2$ (left) and $Ca_2FeO_2Fe_{1.75}OS_{0.5}Se_{1.5}$ (right).

The Fe2 layers order similarly for the $Ca_2FeO_2Fe_{1.65}OS_{1.5}Se_{0.5}$, $Ca_2FeO_2Fe_{1.7}OSSe$ and $Ca_2FeO_2Fe_{1.75}OS_{0.5}Se_{1.5}$ compounds and the ordering pattern is the same as that seen in the Fe2 layers of $Ca_2FeO_2Fe_{1.6}OS_2$ (at 100 K), thus an explanation for the relative arrangement of the spins in these layers has already been provided in section 3.3.8. As expected all Fe-O-Fe superexchange pathways are antiferromagnetic however, compared to the Fe2 moments in $Ca_2FeO_2Fe_{1.6}OS_2$, the Fe2 moments in the solid solution phases are directed further away from the crystallographic axes and more towards the directions of the Fe-O bonds.

Returning to the spin-orbit coupling arguments of Whangbo *et al*.[9] the Fe^{3+} in the Fe1 layer are predicted to have no preferred orientation due to the lack of an orbital moment and the Fe^{2+} in the Fe2 layer are predicted to order perpendicular to the principal *z*-axis which is directed along the Fe2-O bonds (as the change in magnetic quantum number between the HOMO and LUMO in the FeO_2Ch_4 environment is given by $|\Delta L_z| = 1$). The orbital splitting diagrams given in Figure 4.42 are used in this spin-orbit coupling analysis. The Fe2 moments are never ordered completely parallel to the Fe2-O bond and so, like the $Ca_2FeO_2Fe_{1.6}OS_2$ case, the magnetic models proposed for the three solid solution phases agree with this prediction to some degree.

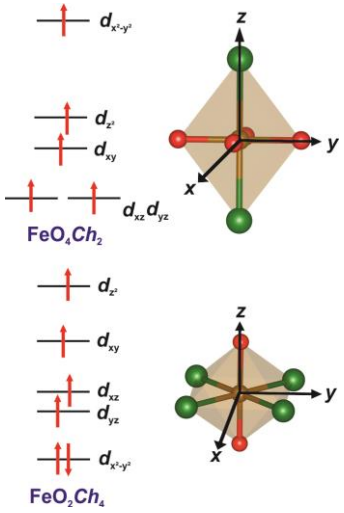


Figure 4.42: Ligand field splitting schemes for the FeO_4Ch_2 and FeO_2Ch_4 distorted octahedra. The *x*, *y* and *z* axes shown, which apply to these local coordinations, have been set so that the d_{Z^2} orbital lies along the distorted axis of each octahedra. The ligand field splitting for the FeO_2Ch_4 case is described for analogous CoO_2Se_4 octahedra in $La_2O_2Co_2OSe_2$ by Wu *et al*.[10]

4.5 Conclusions

This study has progressed the work initially reported by Zhang *et al*.[1]

Unlike the $Ca_2FeO_2Fe_{1.6}OS_2$ phase explored in Chapter 3, the $Ca_2FeO_2Fe_{1.65}OS_{1.5}Se_{0.5}$, $Ca_2FeO_2Fe_{1.7}OSSe$ and $Ca_2FeO_2Fe_{1.75}OS_{0.5}Se_{1.5}$ materials show no evidence for long-range structural ordering of the Fe vacancies in the Fe2 layer as superstructure peaks in the high-resolution XRPD data are no longer present. As the proportion of the larger Se^{2-} anion included in the structure increases, more Fe is incorporated into the Fe2 layer (suggested by the synthesis stoichiometries and XRPD refinement results), resulting in fewer Fe vacancies and a slight reduction of the Fe^{3+} in the Fe1 layer.

The low temperature magnetic models predicted for the three solid solution compounds are all comparable. A checkerboard ordering of the moments in the Fe1 layer ensures that all the 180° Fe-O-Fe superexchange pathways possess antiferromagnetic ordering with values of 3.58(4), 3.34(4) and 3.27(6) μ_B per Fe for $Ca_2FeO_2Fe_{1.65}OS_{1.5}Se_{0.5}$, $Ca_2FeO_2Fe_{1.7}OSSe$ and $Ca_2FeO_2Fe_{1.75}OS_{0.5}Se_{1.5}$ respectively. The decrease in these values is likely to be due to the decreasing vacancy concentration in the Fe2 layers as more Se^{2-} is incorporated, which results in the slight reduction in the Fe^{3+} centres in this layer. The nature of the ordering of the moments in the Fe2 layer also results in all the 180° Fe-O-Fe superexchange pathways possessing antiferromagnetic ordering with values of 1.90(10), 2.20(10) and 2.26(10) μ_B per Fe ion present for $Ca_2FeO_2Fe_{1.65}OS_{1.5}Se_{0.5}$, $Ca_2FeO_2Fe_{1.7}OSSe$ and $Ca_2FeO_2Fe_{1.75}OS_{0.5}Se_{1.5}$ respectively. The increase in these values is likely to be due to the decreasing vacancy concentration in the Fe2 layers as more Se^{2-} is incorporated, which results in stronger long-range interactions between the metal centres throughout the layers. The values of the refined moments in the Fe1 and Fe2 layers suggest these contain high spin Fe^{3+} d^5 and high spin Fe^{2+} d^6 respectively. The $Ca_2FeO_2Fe_{1.75}OS_{0.5}Se_{1.5}$ material exhibits spin-reorientations of the moments on the Fe1 sublattice, both between 5 K and 100 K upon loss of the long-range ordered moments in the Fe2 layer and then between 100 K and 200 K, with the moments oriented in the *ab*-plane before losing long-range order between 300 K and 343 K.

Further NPD measurements on D1B were due to be performed before the completion of this thesis, however these have been rescheduled due to a reactor shutdown, and will be investigated by another student. It is hoped that these measurements will help deduce the nature of any magnetic transition around 70 K for $Ca_2FeO_2Fe_{1.65}OS_{1.5}Se_{0.5}$ and $Ca_2FeO_2Fe_{1.7}OSSe$, as well as supporting the proposed magnetic models for all three solid solution phases upon analysis of the high-resolution magnetic Bragg peaks in the long *d*-spacing region. Other follow-up experiments could include those used to investigate any short-range ordering of the Fe vacancies and/or chalcogenide anions. X-ray pair distribution function (PDF) analysis, High-Resolution Transmission Electron Microscopy (HRTEM) imaging and experiments performed on single crystals could all be used to explore the possibility of local order.

References

(1) Zhang, H.; Wu, X.; Li, D.; Jin, S.; Chen, X.; Zhang, T.; Lin, Z.; Shen, S.; Yuan, D.; Chen, X. $Ca_2O_3Fe_{2.6}S_2$: An Antiferromagnetic Mott Insulator at Proximity to Bad Metal. *J. Phys. Condens. Matter* **2016**, *28* (14), 145701. https://doi.org/10.1088/0953-8984/28/14/145701.

(2) Thorp, H. H. Bond Valence Sum Analysis of Metal-Ligand Bond Lengths in Metalloenzymes and Model Complexes. *Inorg. Chem.* **1992**, *31* (9), 1585–1588. https://doi.org/10.1021/ic00035a012.

(3) Brown, I. D.; Altermatt, D. Bond-valence Parameters Obtained from a Systematic Analysis of the Inorganic Crystal Structure Database. *Acta Crystallogr. Sect. B* **1985**, *41* (4), 244–247. https://doi.org/10.1107/S0108768185002063.

(4) Koo, H. J.; Dai, D.; Whangbo, M. H. Importance of Supersuperexchange Interactions in Determining the Dimensionality of Magnetic Properties. Determination of Strongly Interacting Spin Exchange Paths in $A_2Cu(PO_4)_2$ (A = Ba, Sr), $ACuP_2O_7$ (Ba, Ca, Sr, Pb), $CaCuGe_2O_6$ and $Cu_2UO_2(PO_4)_2$ on the Basis of Qualitative Spin Dimer Analysis. *Inorg. Chem.* **2005**, *44* (12), 4359–4365. https://doi.org/10.1021/ic050159i.

(5) Lawrence, G. B.; Wildman, E. J.; Stenning, G. B. G.; Ritter, C.; Fauth, F.; McLaughlin, A. C. Electronic and Magnetic Properties of Cation Ordered $Sr_2Mn_{2.23}Cr_{0.77}As_2O_2$. *Inorg. Chem.* **2020**, *59* (11), 7553–7560. https://doi.org/10.1021/acs.inorgchem.0c00447.

(6) Xu, X.; Jones, M. A.; Cassidy, S. J.; Manuel, P.; Orlandi, F.; Batuk, M.; Hadermann, J.; Clarke, S. J. Magnetic Ordering in the Layered Cr(II) Oxide Arsenides $Sr_2CrO_2Cr_2As_2$ and $Ba_2CrO_2Cr_2As_2$. *Inorg. Chem.* **2020**, *59* (21), 15898–15912. https://doi.org/10.1021/acs.inorgchem.0c02415.

(7) Pilania, G.; Ghosh, A.; Hartman, S. T.; Mishra, R.; Stanek, C. R.; Uberuaga, B. P. Anion Order in Oxysulfide Perovskites: Origins and Implications. *npj Comput. Mater.* **2020**, *6* (1), 1–11. https://doi.org/10.1038/s41524-020-0338-1.

(8) Yang, M.; Oró-Solée, J.; Rodgers, J. A.; Jorge, A. B.; Fuertes, A.; Attfield, J. P. Anion Order in Perovskite Oxynitrides. *Nat. Chem.* **2011**, *3* (1), 47–52. https://doi.org/10.1038/nchem.908.

(9) Whangbo, M. H.; Gordon, E. E.; Xiang, H.; Koo, H. J.; Lee, C. Prediction of Spin Orientations in Terms of HOMO-LUMO Interactions Using Spin-Orbit Coupling as Perturbation. *Acc. Chem. Res.* **2015**, *48* (12), 3080–3087. https://doi.org/10.1021/acs.accounts.5b00408.

(10) Wu, H. Electronic Structure, Spin State, and Magnetism of the Square-Lattice Mott Insulator $La_2Co_2Se_2O_3$ from First Principles. *Phys. Rev. B - Condens. Matter Mater. Phys.* **2010**, *82* (2). https://doi.org/10.1103/PhysRevB.82.020410.

Chapter 5

5 Synthesis and Characterisation of $Sr_2CrO_2Cr_2OAs_2$

5.1 Introduction

Recent work in our group, published by Xu *et al*. in 2020,[1] revealed the presence of stacking faults in the high resolution transmission electron microscopy (TEM) measurements performed on $Sr_2CrO_2Cr_2As_2$, as highlighted by Figure 5.1. These stacking faults were presumed to arise from the oxidation of some $[Cr_2As_2]^{2-}$ layers containing Cr^{2+} to $[Cr_2OAs_2]^{2-}$ layers containing Cr^{3+}. This led us to target $Sr_2CrO_2Cr_2OAs_2$ which is the fully oxidised analogue of $Sr_2CrO_2Cr_2As_2$ where all $[Cr_2As_2]^{2-}$ layers have been oxidised, accompanied by a relative shift of (½, ½, 0) in the *ab*-plane of neighbouring $[Sr_2CrO_2]^{2+}$ blocks as shown in Figure 5.2. The structure of $Sr_2CrO_2Cr_2OAs_2$ is analogous to that reported for the cation-defective $Ca_2FeO_2Fe_{1.6}OS_2$ material studied in Chapter 3, and the $[Cr_2OAs_2]^{2-}$ blocks are the exact anti-type of the $[Sr_2CrO_2]^{2+}$ (i.e. $[O_2CrSr_2]^{2+}$) blocks. The work reported in this chapter has been published in *Inorganic Chemistry*.[2]

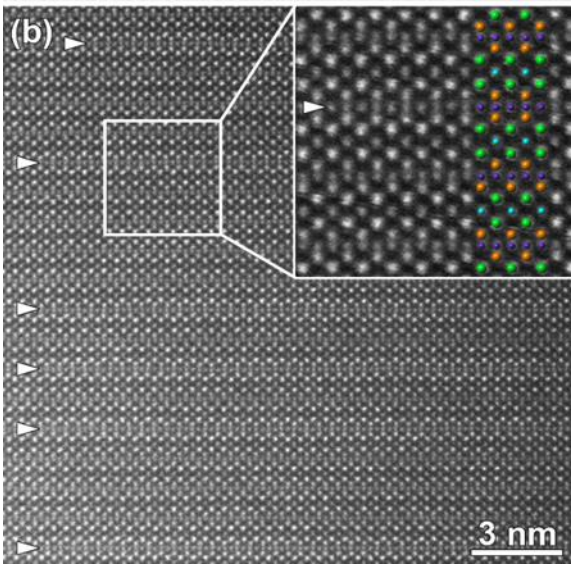


Figure 5.1: TEM image of $Sr_2CrO_2Cr_2As_2$, where the white arrows highlight the presence of oxygen-rich stacking faults. This figure is taken from the publication by Xu *et al*.[1]

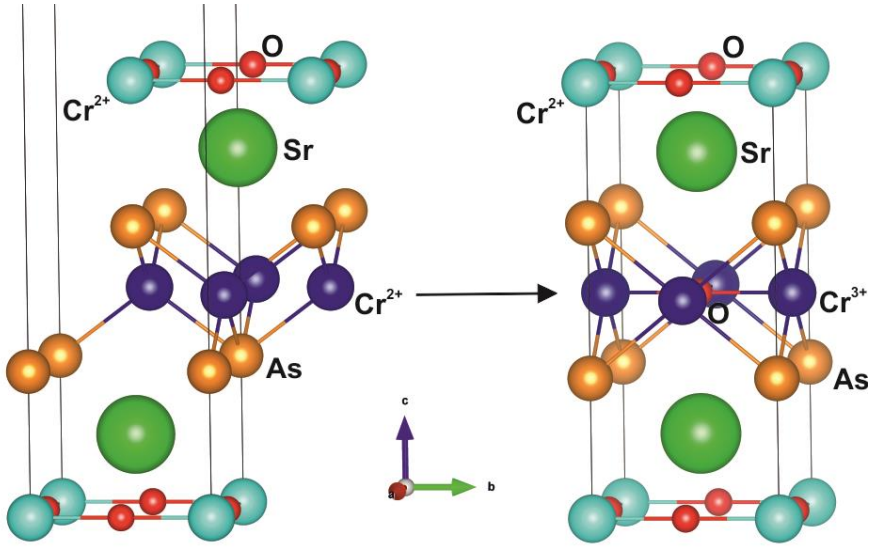


Figure 5.2: The crystal structures of $Sr_2CrO_2Cr_2As_2$ (left) and $Sr_2CrO_2Cr_2OAs_2$ (right). The structure of $Sr_2CrO_2Cr_2OAs_2$ may formally be derived from oxidation of the $[Cr_2As_2]^{2-}$ layers in $Sr_2CrO_2Cr_2As_2$ and relative shifts of the $[Sr_2CrO_2]^{2+}$ slabs.

5.2 Synthesis

A 1 g powder sample was made from SrO, Cr_2O_3 (Alfa Aesar, 99.6 %), Cr (Alfa Aesar, 99.95 %) and As (Alfa Aesar, 99 %) in the ratio of 6:0.85:7.3:6. This mixture targeted a stoichiometry of $Sr_2Cr_3O_{2.85}As_2$ and the 5 % oxygen deficiency was employed as it increased the phase purity of the sample, as proposed by Jiang *et al.*[3] in their synthesis of $Sr_2CrO_2Cr_2As_2$. SrO had been previously prepared via thermal decomposition of $SrCO_3$ (Alfa Aesar 99.994 %) by heating it at 830 °C for 16 hours and then 1100 °C for 4 hours, all under dynamic vacuum. Cr_2O_3 was also pre-dried in a furnace before use. Traditional solid-state synthesis was used, with the reagents heated at 800 °C for 2 h (1 °C min^{-1} ramping rate) then 1200 °C for 8 h (10 °C min^{-1} ramping rate) then 1200 °C for 2 h (10 °C min^{-1} ramping rate), with grinding and re-pelletising between the two 1200 °C heating steps and quenching in ice water from both 1200 °C heating steps. The 800 °C heating step with slow ramping rate was used to ensure that the As reacted before reaching a high vapour pressure. It should be stressed that this phase was difficult to obtain with high purity and numerous attempts using a range of starting materials and heating profiles were attempted before the sample studied in this thesis was finally synthesised.

5.3 Characterisation

5.3.1 Room Temperature XRPD

Room temperature XRPD data were collected on beamline I11 at the Diamond Light Source. The high-resolution MAC detector was used to gather these data. Refinement of a model against these data is given in Figure 5.3 and Table 5.1. Even though an oxygen deficiency was used in the starting mixture, there is no evidence in this refinement that the final phase is oxygen deficient. It is plausible that additional O arises due to reaction with the silica tubes, however the impurities present are also consistent with a stoichiometric target phase given the slight off-stoichiometry of the reaction mixture. Each site occupancy factor was allowed to freely refine in the early stages of the refinement, but there was no significant deviation from the ideal value of 1 by any atom, so these values were then fixed.

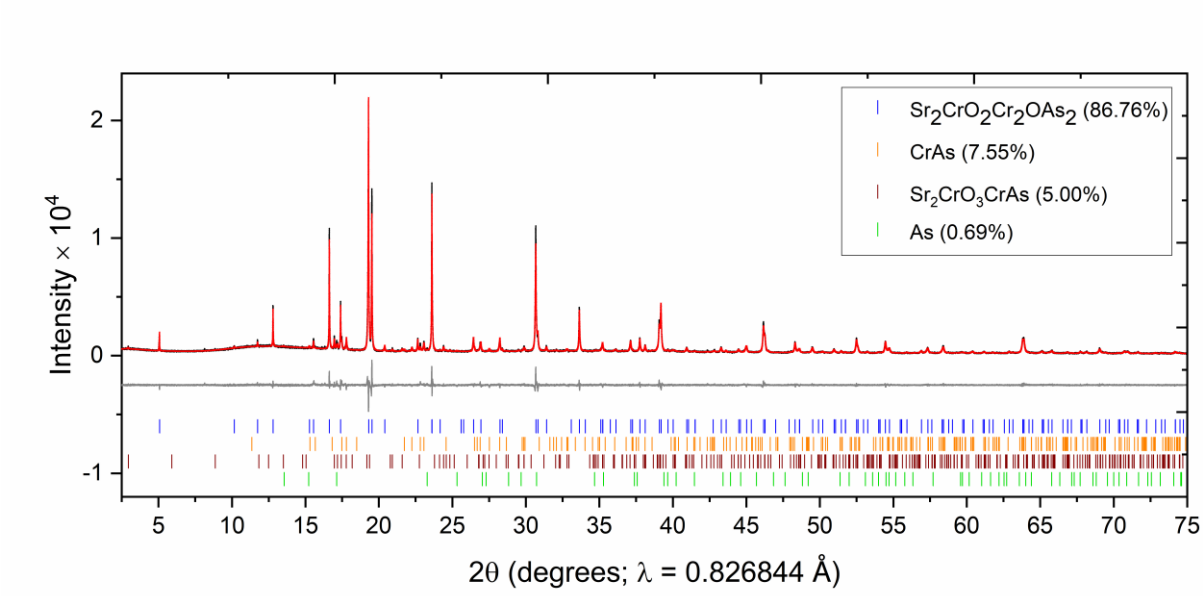


Figure 5.3: XRPD pattern of $Sr_2CrO_2Cr_2OAs_2$ measured at 300 K on the MAC detector at I11 showing the observed (black), calculated (red) and difference (grey) curves. R_{wp}: 7.679%.

	$Sr_2CrO_2Cr_2OAs_2$
Diffractometer	I11 (MAC)
Wavelength (Å)	0.826844
Temperature (K)	300
Space Group	*P*4/*mmm*
a (Å)	4.040319(16)
c (Å)	9.33140(7)
V (Å^3)	152.327(2)

								$Sr_2CrO_2Cr_2OAs_2$
Atom	Site	*x*	*y*	*z*	Occupancy	U_{11} (Å^2)	U_{22} (Å^2)	U_{33} (Å^2)
Sr	2*h*	0.5	0.5	0.17664(8)	1	0.0024(2)	=U_{11}	0.0114(6)
Cr1	1*a*	0	0	0	1	0.0000(4)	=U_{11}	0.0171(9)
Cr2	2*e*	0.5	0	0.5	1	0.0002(3)	=U_{11}	0.0134(6)
O1	2*f*	0.5	0	0	1	0.0063(8)$^+$	=U_{11}	=U_{11}
O2	1*d*	0.5	0.5	0.5	1	0.0063(8)$^+$	=U_{11}	=U_{11}
As	2*g*	0	0	0.32192(8)	1	0.0000(3)	=U_{11}	0.0125(7)

Table 5.1: Refinement results from the XRPD pattern collected at 300 K using the MAC detector at I11. $^+$These oxygen displacement parameters were fixed at the same value and they were refined isotropically.

5.3.2 Room Temperature NPD

Room temperature NPD data were collected on the WISH instrument at ISIS. Refinement against these data is given in Figure 5.4 and Table 5.2. Again, there is no evidence in this refinement that the final phase is oxygen deficient and each site occupancy factor was allowed to freely refine in the early stages of the refinement, but there was no significant deviation from the ideal value of 1 by any atom so these values were then fixed. While lattice parameters are determined with more precision from the XRPD data, the better ability of NPD to locate light atoms (as discussed in section 2.2.2) means that the NPD refinement is a more reliable confirmation that the O site is fully occupied. It is clearly evident in Figure 5.4 that magnetic scattering exists at room temperature for this compound.

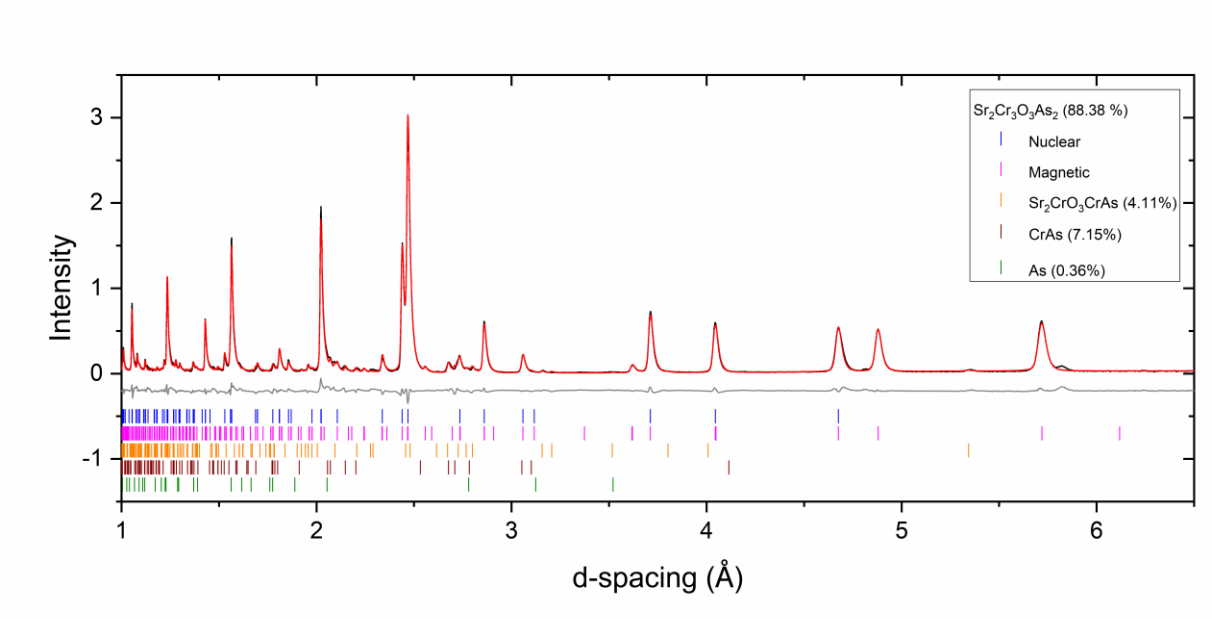


Figure 5.4: NPD pattern of $Sr_2CrO_2Cr_2OAs_2$ (combination of banks 3 and 8 with average $2\theta = 90°$) measured at 300 K on the WISH instrument at ISIS showing the observed (black), calculated (red) and difference (grey) curves. R_{wp}: 5.722%.

	$Sr_2CrO_2Cr_2OAs_2$
Diffractometer	WISH (ISIS)
Wavelength (Å)	white beam TOF
Temperature (K)	300
Space Group	*P*4/*mmm*
a (Å)	4.04490(7)
c (Å)	9.35284(18)
V (Å^3)	153.024(6)

								$Sr_2CrO_2Cr_2OAs_2$
Atom	Site	*x*	*y*	*z*	Occupancy	U_{11} (Å^2)	U_{22} (Å^2)	U_{33} (Å^2)
Sr	2*h*	0.5	0.5	0.1838(2)	1	0.0084(7)	$=U_{11}$	$=U_{11}$
Cr1	1*a*	0	0	0	1	0.032(3)	$=U_{11}$	$=U_{11}$
Cr2	2*e*	0.5	0	0.5	1	0.0073(12)	$=U_{11}$	$=U_{11}$
O1	2*f*	0.5	0	0	1	0.0167(9)	$=U_{11}$	$=U_{11}$
O2	1*d*	0.5	0.5	0.5	1	0.0088(13)	$=U_{11}$	$=U_{11}$
As	2*g*	0	0	0.3286(3)	1	0.0116(8)	$=U_{11}$	$=U_{11}$

Table 5.2: Refinement results from the NPD pattern collected at 300 K using the WISH instrument at ISIS. Refinement of the data was performed using isotropic displacement parameters for all atoms.

The structure of $Sr_2CrO_2Cr_2OAs_2$ is depicted in Figure 5.5, along with bond lengths for the vertex-sharing CrO_4As_2 and face-sharing CrO_2As_4 distorted octahedra which make up the Cr1 and Cr2 layers respectively. Due to the arrangement of the atoms in the structure and the connectivity of the two distorted Cr octahedra, the Cr1-O and Cr2-O bond lengths are inherently identical and equal to *a*/2. The BVS calculations given in Table 5.3 heavily suggest Cr^{2+} on the Cr1 site and Cr^{3+} on the Cr2 site, as one might expect when charge balancing the chemical formula.

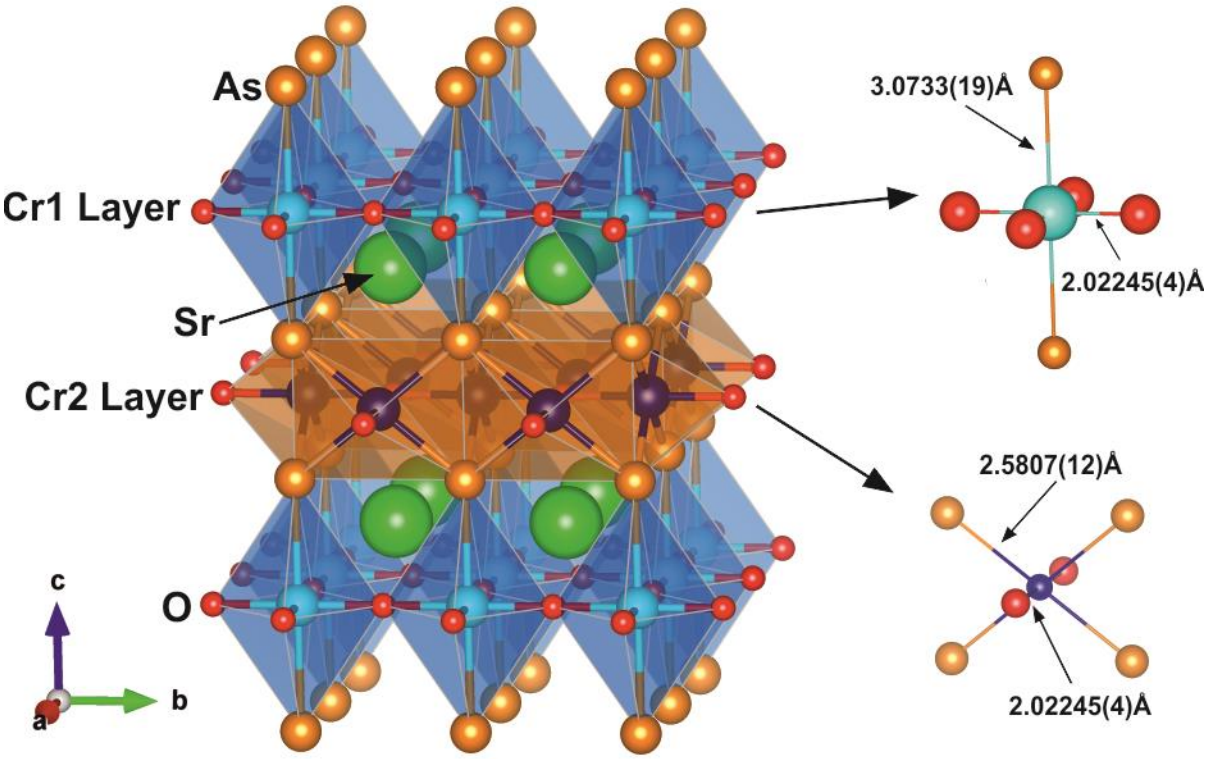


Figure 5.5: The structure of $Sr_2CrO_2Cr_2OAs_2$. The CrO_4As_2 and CrO_2As_4 distorted octahedra are shown by the blue and orange polyhedra respectively. 99% displacement ellipsoids are given (right) using isotropic displacement parameters refined from room temperature WISH NPD data (detailed in Table 5.2).

	Cr-O Distances (Å)	Cr-As Distances (Å)	Cr BVS
Cr1	2.02245(4) [x4]	3.0733(19) [x2]	+2.09(1)
Cr2	2.02245(4) [x2]	2.5807(12) [x4]	+2.98(1)

Table 5.3: Cr bond valence sums (BVS) calculated using bond lengths refined from the NPD pattern collected at 300 K using the WISH instrument at ISIS. Values calculated assuming a +2 oxidation state for Cr1 and a +3 oxidation state for Cr2 for the Cr-O bond lengths from *Brese and O'Keeffe*[4]. The same literature value for a Cr-As bond length, from *Brese and O'Keeffe*,[4] was used for both Cr sites.

5.3.3 SQUID Magnetometry

The results of high temperature magnetometry measurements are shown in Figure 5.6. There appears to be a broad magnetic transition between 400 K and 500 K, the origin of which is contemplated in section 5.3.5. The low temperature ZFC and FC curves given in Figure 5.7a) are likely to be dominated by the CrAs impurity, which orders just below 300 K (at around 248 K[5] or 280 K[6] - there is some dispute) and the 5 K hysteresis loop in Figure 5.7b) shows little hysteresis and a low sample moment, as is typical of antiferromagnets. The discrepancy in the room temperature magnetic susceptibility values of the low and high temperature measurements is likely to be due to the different sample environments used in the two measurements. It should also be noted that these measurements do not cover a Curie-Weiss region for this material.

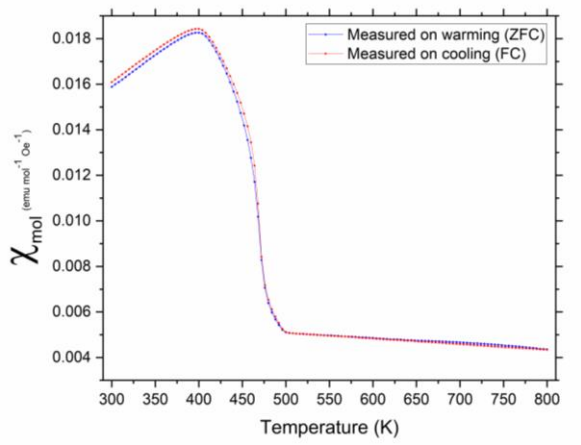


Figure 5.6: High temperature Zero Field Cooled (ZFC) and Field Cooled (FC) curves for $Sr_2CrO_2Cr_2OAs_2$ measured in a field of 100 Oe.

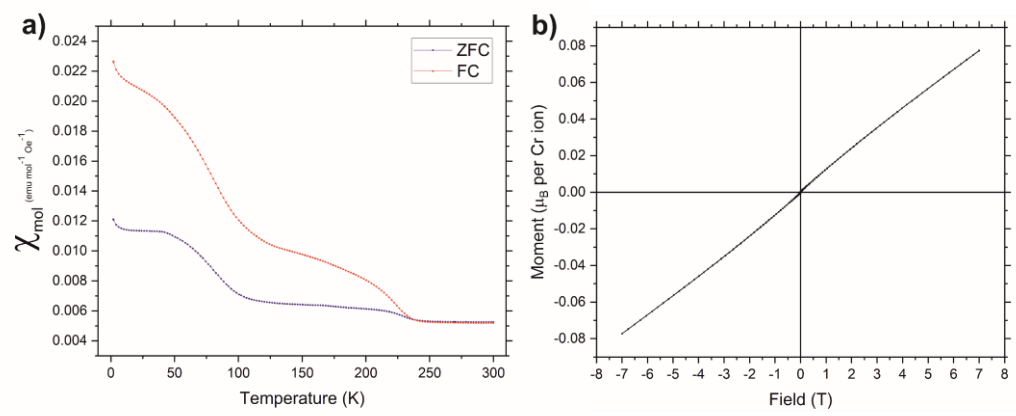


Figure 5.7: Magnetometry results for $Sr_2CrO_2Cr_2OAs_2$ showing **a)** low temperature Zero Field Cooled (ZFC) and Field Cooled (FC) curves measured in a field of 100 Oe and **b)** the magnetisation isotherm measured at 5 K.

5.3.4 Variable Temperature NPD

Variable temperature NPD data were gathered on the WISH instrument at ISIS. The data collected on the $Sr_2CrO_2Cr_2OAs_2$ sample at 10 K (displayed in Figure 5.8) show a series of reflections where the intensities and *d*-spacings cannot not be accounted for from scattering due to the nuclear model alone. These additional peaks only occur at long *d*-spacings which is indicative of a magnetic origin. These peaks decrease in intensity as the sample is warmed (evident in Figure 5.9) and can be explained by scattering from arrays of long-range ordered magnetic moments. The reflections labelled by black triangles in Figure 5.8 are positioned on top of nuclear peaks and are therefore accounted for by the $k = (0\ 0\ 0)$ propagation vector. In contrast, the *k*-vector of the peaks denoted by a black square is $k = (^1/_2\ ^1/_2\ 0)$ and these imply that the cell of the magnetic structure is a $2a_{nuc} \times 2a_{nuc} \times c_{nuc}$ expansion of the nuclear unit cell, and that the two Cr sublattices order independently with different propagation vectors. A number of much less intense magnetic Bragg reflections are highlighted by a * and disappear on warming between 200 K and 300 K. These can be attributed to the magnetic structure of the CrAs side phase, evident in the XRPD pattern, which has a Néel temperature of approximately 300 K. The magnetic ordering transitions of $Sr_2CrO_2Cr_2OAs_2$ are not detected in the high temperature magnetometry data (discussed in section 5.3.3).

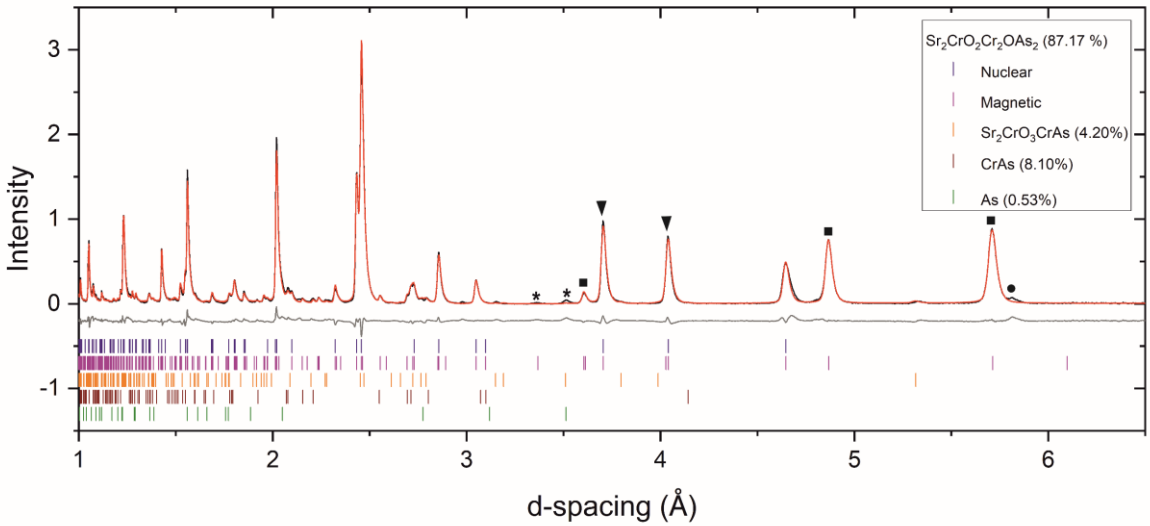


Figure 5.8: NPD pattern of $Sr_2CrO_2Cr_2OAs_2$ (combination of banks 3 and 8 with average $2\theta = 90°$) measured at 10 K on the WISH instrument at ISIS showing the observed (black), calculated (red) and difference (grey) curves. The black triangles and black squares denote reflections with $k = (0\ 0\ 0)$ and $k = (^1/_2\ ^1/_2\ 0)$ respectively. The * give examples of peaks which disappear before 300 K and are due to magnetic order in CrAs. The black circle highlights an unidentified impurity peak, which is presumably nuclear (not magnetic) in origin as it does not change intensity with varying temperature. R_{wp}: 5.751%.

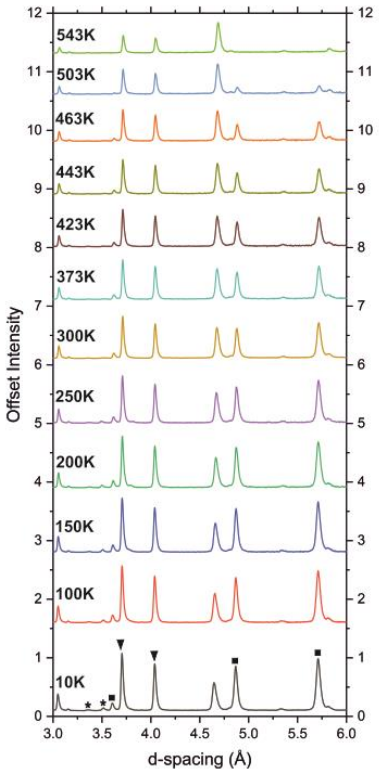


Figure 5.9: NPD patterns of $Sr_2CrO_2Cr_2OAs_2$ (combination of banks 3 and 8 with average 2θ = 90°) at different temperatures measured on the WISH instrument at ISIS showing the evolution of the magnetic peaks. Magnetic Bragg peaks labelled with a black square disappear between 503 K and 543 K, whereas those labelled by a black triangle are still present at 543 K. Those highlighted by a * can be explained as the magnetic Bragg peaks of CrAs (T_N ~ 300 K).

The ISODISTORT package[7] was used to deduce the magnetic modes available to this system and the most suitable model is one which contains the mM3+ A2(a,0) mode in the Cr1 layer and the mGM4+ B1(a,0) mode in the Cr2 layer, as depicted in Figure 5.10. The resulting model has all the Cr moments aligned along the *c*-axis in antiferromagnetic arrangements, which is consistent with the absence of any intensity on reflections indexed perpendicular to the *c*-axis (i.e. (00l) reflections), as explained in section 2.2.2. Nearest neighbours in the Cr1 sublattice (CrO_2 layers) are coupled antiferromagnetically, as is expected for σ- and π-type superexchange interactions between high spin d^4-d^4 ions in co-aligned elongated octahedral coordination mediated by the 2*p* orbitals of the O^{2-} anion.

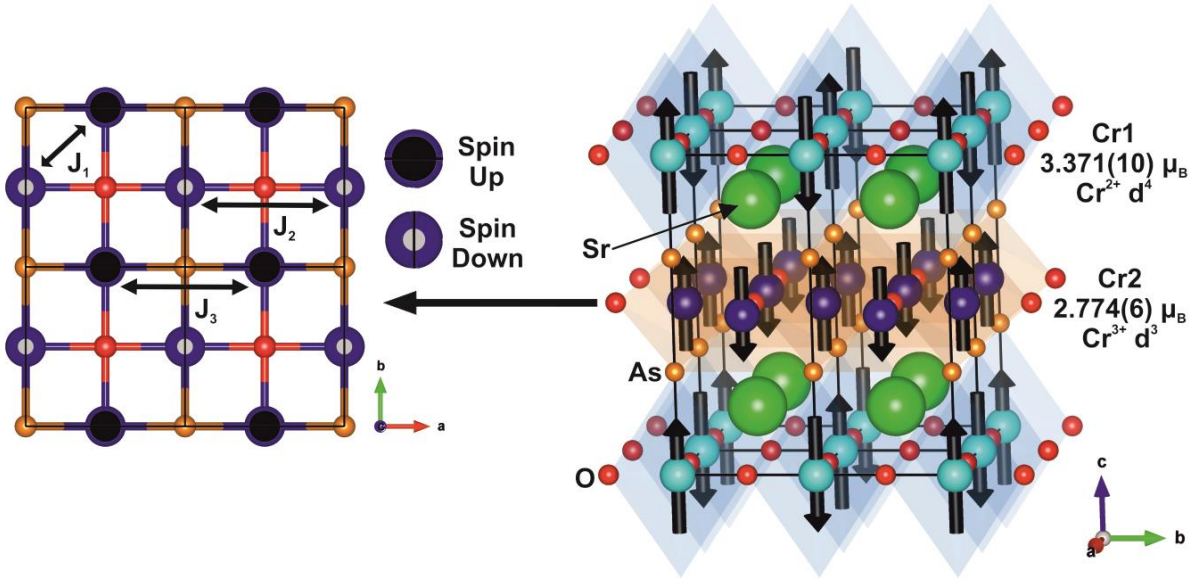


Figure 5.10: Model for the magnetic order on the Cr1 oxide-rich sublattice and Cr2 arsenide-rich sublattice of $Sr_2CrO_2Cr_2OAs_2$ at 10 K. The major magnetic interactions in the Cr2 layer- as considered for materials with analogous layers- are labelled J_1 (Cr-Cr direct exchange), J_2 (180° Cr-O-Cr superexchange) and J_3 (~100° Cr-As-Cr superexchange).

The model for the Cr2 sublattice (Cr_2OAs_2 layers) in $Sr_2CrO_2Cr_2OAs_2$ also has antiferromagnetic coupling of nearest neighbour Cr^{3+} moments. The main competing magnetic interactions are highlighted by Figure 5.10 (as previously described by Ni *et al.*[8]): the direct exchange between nearest neighbour Cr^{3+} centres (J_1); the 180° superexchange mediated by O^{2-} (J_2) and the approximately 100° superexchange mediated by As^{3-} (J_3). It seems that this system is dominated by the direct exchange interaction (J_1) between the d_{xz} and d_{yz} orbitals of neighbouring Cr centres, which is antiferromagnetic in nature. This interaction acts between all the Cr^{3+} ions which are nearest neighbours, forming a checkerboard pattern of Cr^{3+} spins aligned along the *c*-axis and alternating in their relative directions. The model suggests that this direct exchange is the strongest coupling mechanism, superseding the superexchange interactions. The linear superexchange (J_2) involving empty d_{z^2} orbitals is predicted to be an antiferromagnetic interaction by application of the Goodenough-Kanamori rules, however here the moments are ferromagnetically aligned along that pathway. The other superexchange interaction (J_3) involving empty d_{xy} orbitals is predicted to be ferromagnetic in nature and the moments connected by this interaction are indeed aligned

ferromagnetically. Therefore this interaction could play a role in the ordering of the Cr^{3+} moments, however this interaction would be predicted to be weak due to the fact that there are no electrons occupying these d_{xy} orbitals.

The significantly larger refined long-range ordered moment per Cr ion in the Cr1 layer of 3.371(10) μ_B compared to the 2.774(6) μ_B per Cr in the Cr2 layer are consistent with the assignment of these as Cr^{2+} d^4 and Cr^{3+} d^3 cations respectively, with the ordered moments reduced below the maximum expected spin-only values of 4 μ_B and 3 μ_B respectively by covalency. The observed antiferromagnetism, the bond valence sums (see section 5.3.2) and the sizes of the ordered moments are consistent with a lack of mixed valency on the Cr1 and Cr2 sites. Figure 5.11 displays the refined value of the Cr moment in each layer in $Sr_2CrO_2Cr_2OAs_2$ as the temperature is increased. Upon warming the sample, it is the Cr1 (Cr^{2+}) moments which lose long-range order first and have the lower T_N of 530(10) K, with the T_N of the Cr2 (Cr^{3+}) moments predicted to be approximately 600 K based on the evolution of the moment with temperature. It was not possible to measure the neutron diffraction pattern to higher temperatures due to time limitations during the remote experiment period.

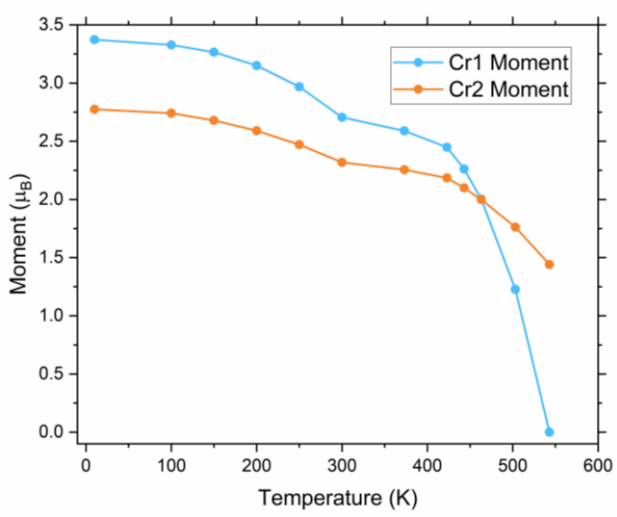


Figure 5.11: Value of the Cr1 and Cr2 moments (per Cr ion) in $Sr_2CrO_2Cr_2OAs_2$ refined from NPD data collected at different temperatures on the WISH instrument at ISIS. The error on each value of the moment is smaller than the width of the corresponding data point. The apparent dip in the value of the moments at 300 K is likely to be an artefact of the different instrument environments upon changing from low temperature data collection to high temperature data collection on the WISH instrument. This is supported by the lattice parameter values, refined from NPD data, which behave slightly differently above and below 300 K (see Appendix A.9).

5.3.5 Variable Temperature XRPD

Variable temperature XRPD data were collected on beamline I11 at Diamond Light Source. Upon initial analysis, it was noticeable that the lattice parameters did not decrease in a linear fashion as the sample was cooled from 600 K to 300 K. Instead, below 400 K, the rate by which the lattice parameters diminish increases for lattice parameter *a* but decreases for lattice parameter *c* perpendicular to the layers (Figure 5.12(a)). However, the decrease in unit cell volume adopts a linear trend (Figure 5.12(b)). We note that this deviation is extremely subtle and only readily evident because the data were collected with high resolution in temperature (and not, for example, in 10-20 degree intervals). The possibility that this is an experimental artefact was considered, however the agreement factors for the sequential refinements do not show this same trend or any other anomalies. This observation prompted further investigation into changes in bond lengths and bond valence sums (BVS). The trends shown by these values in the region from 500 K down to 400 K differ from the trends exhibited in the 600-500 K and 400-300 K regions. As the temperature is decreased, the Cr1 octahedra (CrO_4As_2) become marginally less distorted (Figure 5.12(e)) and the Cr2 octahedra (CrO_2As_4) become marginally more distorted (Figure 5.12(g)). In tandem with this structural change to the Cr polyhedra, the BVS values for Cr1 increase faster and those for Cr2 essentially remain constant (Figure 5.12(h)). This suggests that the Cr^{3+} ions in the Cr2 layers may be being reduced by the Cr^{2+} in the Cr1 layers to a very small degree (of the order of 0.02 e^- according to the trends in the BVS). The high temperature magnetometry data in Figure 5.12(i) supports the idea that the driving force behind this structural change is likely to be electronic in origin as it shows a transition in the magnetic susceptibility of $Sr_2CrO_2Cr_2OAs_2$ between 500 K and 400 K (i.e., exactly in the region of the structural change), which cannot be accounted for by the magnetic ordering of the Cr2 and Cr1 layers as these have higher Néel temperatures of ~600 K and 530(10) K respectively – i.e. the subtle structural change occurs below the temperature of magnetic long range ordering on both sublattices, and is so small that we would not expect to observe any modulation of the ordered moments. The origin of the structural distortion could alternatively be magnetostriction, which is a change to the unit cell dimensions caused by the

change in magnetic state, as the structural distortion of $Sr_2CrO_2Cr_2OAs_2$ occurs at temperatures when the Cr1 and Cr2 ordered moments are starting to near their saturated values. Examples of antiferromagnets which exhibit magnetostriction include $TbNi_2B_2C$[9] and $CoCl_2$.[10] We also cannot completely rule out that the transition in the magnetometry is due to an impurity (although the small $Sr_2CrO_2Cr_2As_2$ impurity observed does not have transitions in this range), but this would not account for the structural observation. The structural distortion and proposed electronic transition are illustrated in Figure 5.13.

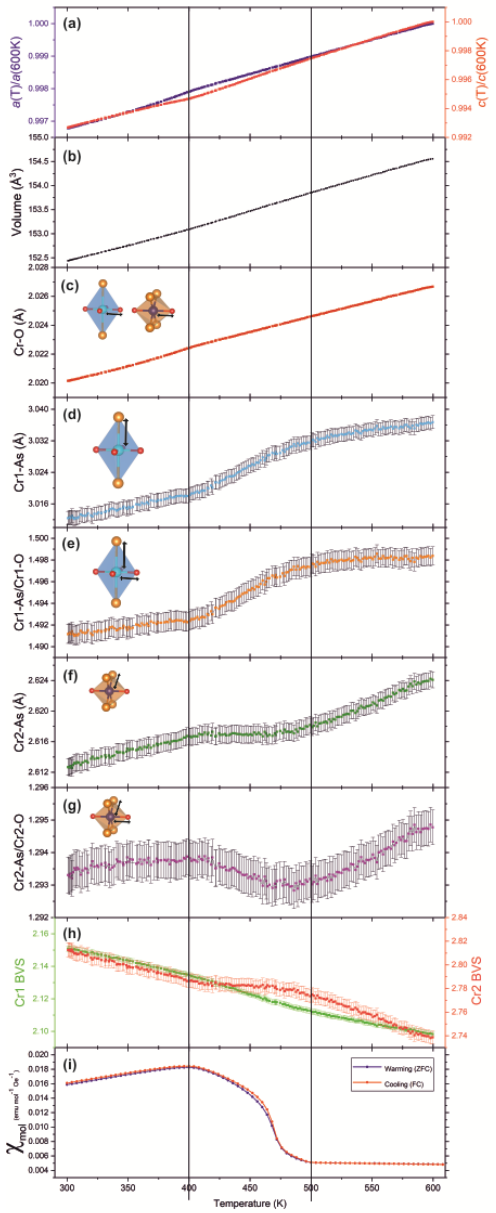


Figure 5.12: Refinement results of the variable temperature XRPD data of $Sr_2CrO_2Cr_2OAs_2$ showing changes in **(a)** lattice parameters *a* and *c* normalised against their value at 600 K; **(b)** unit cell volume; **(c)** Cr-O distances [identical for Cr1-O and Cr2-O]; **(d)** Cr1-As distance; **(e)** Cr1-As/Cr1-O bond length ratio; **(f)** Cr2-As distance; **(g)** Cr2-As/Cr2-O bond length ratio and **(h)** Cr1 and Cr2 bond valence sum (BVS) [calculated using bond length data provided by *Brese and O'Keefe*[4] and where the literature Cr-As bond length used was that for Cr^{II}-As in both cases as a known Cr^{III}-As bond length was not found]. High temperature Zero Field Cooled (ZFC) and Field Cooled (FC) curves, measured in a field of 100 Oe, are given in **(i)**.

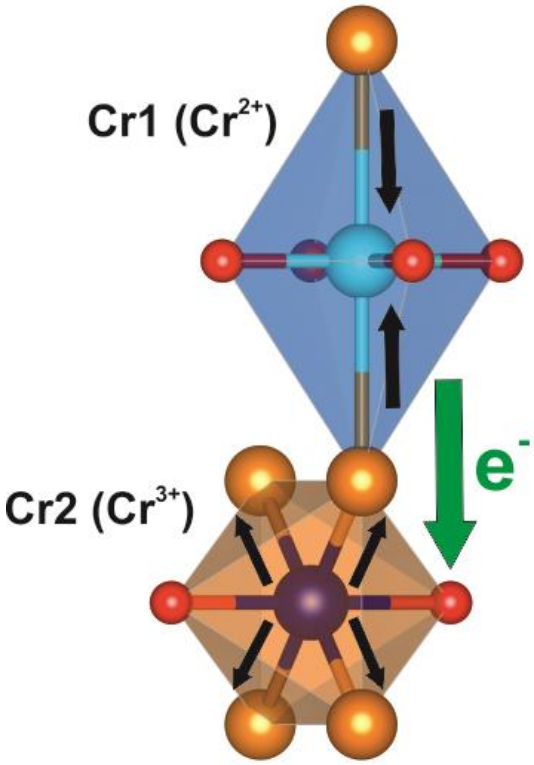


Figure 5.13: The subtle electronic transition proposed to drive the structural change observed in the Cr polyhedra (as depicted by the black arrows) between 500 K and 400 K as $Sr_2CrO_2Cr_2OAs_2$ is cooled. It should be emphasised that the structural changes observed using the high-resolution synchrotron data are consistent with a minuscule amount of electron transfer of this type (approx. 0.02 e^-).

5.3.6 High Temperature Resistance Measurements

High temperature resistance experiments were attempted in the high temperature range specifically to qualitatively test whether there was any observable electronic anomaly. These measurements were performed by John O'Sullivan in the Oxford Materials Science Department using the 4-point probe technique (as described in section 2.2.8). The data suggest metallic behaviour for this compound, due to the low resistance values and increase of resistance with increasing temperature, but did not show any transition in the 400-500 K region (Figure 5.14). The most likely explanations for the lack of an obvious transition are the relatively low sensitivity of the experimental setup and the extremely subtle nature of the structural change observed in the material. It is possible that the impurities in the sample also affected these measurements. We propose that further measurements of the structure, magnetism, and transport properties on single crystal samples, perhaps backed up by computation to suggest whether the proposed internal redox process is plausible, would be required to shed further light on this subtle structural change.

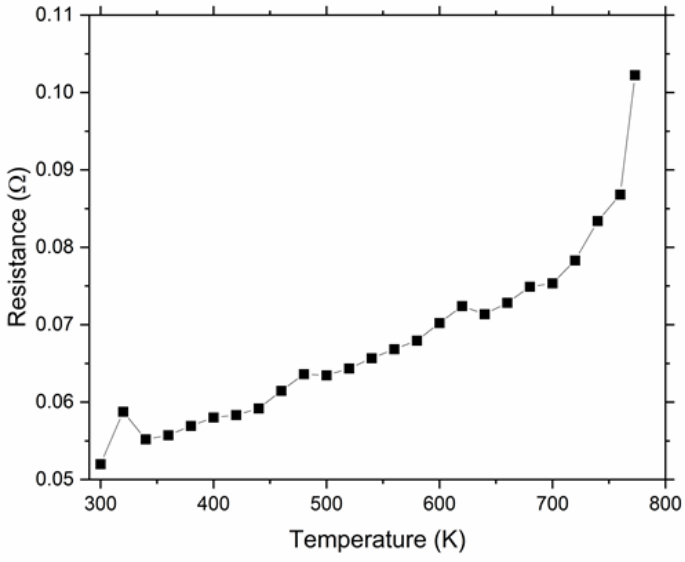


Figure 5.14: Resistance vs temperature curve for a sintered bar of the $Sr_2CrO_2Cr_2OAs_2$ material. There is no significant change in resistance between 400 K and 500 K.

5.4 Discussion

5.4.1 Crystal Structure

$Sr_2CrO_2Cr_2OAs_2$ adopts the lesser-explored structure type formally derived by oxygen insertion from that of $Sr_2CrO_2Cr_2As_2$, the structure of which was first reported for $A_2MnO_2Mn_2B_2$ (A = Sr, Ba; B = As, Sb, Bi) by Brechtel *et al*.[11] Comparisons can be made by focusing on each type of layer in the structure. Xu *et al*.[1] previously reported that the Cr-O distance within the CrO_2 square-planar sheets of $Sr_2CrO_2Cr_2As_2$ refined to a value of 2.00400(1) Å (= half the basal lattice parameter) and in the case of $Sr_2CrO_2Cr_2OAs_2$ we find a similar value of 2.0202(1) Å for this Cr1-O distance. The formal oxidation of the Cr_2As_2 layer to Cr_2OAs_2 therefore seems to leave these CrO_2 sheets unaffected, as would be expected due to the largely unchanged Cr1 environment. $Sr_2CrO_2Cr_2OAs_2$ is the first reported example of Cr_2OAs_2 layers, however some iron oxychalcogenides have been discovered with analogous Fe_2OCh_2 (Ch = S, Se) environments, such as $A_2F_2Fe_2OQ_2$ (A = Sr, Ba; Q = S, Se)[12] and $La_2O_2Fe_2OCh_2$ (Ch = S, Se).[13,14,15] Further examples where layers of this type host alternative 3*d* transition metals include the Mn_2OSe_2 environments in $A_2O_2Mn_2OSe_2$ (A = La, Ce, Pr),[8,2] the Co_2OSe_2 environments in $La_2O_2Co_2OSe_2$[2,16] and the Ti_2OAs_2 environments in $Ba_2Ti_2OAs_2Cr_2As_2$,[17] $BaTi_2OAs_2$[18] and $Ba_2Ti_2OAs_2Fe_2As_2$.[19]

All these compounds containing M_2OX_2 layers follow the rule that when X is a chalcogenide anion the transition metal is M^{2+} but when X is a pnictide anion the transition metal is M^{3+}. This presumably arises due to the need to charge balance the layer so that it always carries a charge of -2 (e.g., $[Mn_2OSe_2]^{2-}$ hosts Mn^{2+} and $[Ti_2OAs_2]^{2-}$ hosts Ti^{3+}). Interestingly, the $Ca_2FeO_2Fe_{1.6}OS_2$ compound studied in Chapter 3 has +2 and +3 3*d* transition metal cations situated in the opposite layers compared to the $Sr_2CrO_2Cr_2OAs_2$ compound. It may be the case that it is energetically favourable for the Cr^{2+} d^4 cation to sit in the CrO_4As_2 environment so that the electrons are situated in lower-lying orbitals (as illustrated in Figure 5.15) which leaves the Cr^{3+} d^3 cation, which has no significant preference based on electronic stabilisation, to sit in the CrO_2As_4 environment. However, Fe^{3+} d^5 may

prefer the FeO_4S_2 coordination and Fe^{2+} the FeO_2S_4 coordination due to hard-soft acid-base arguments and the lack of any significant preference based on electronic stabilisation (also shown in Figure 5.15, where the differences in electronic occupancy for Fe^{2+} or Fe^{3+} are in the most non-bonding orbitals). The term 'hard-soft acid-base arguments' in this case refers to the preference for the more charge-dense, 'hard' Fe^{3+} cation to be positioned on the more oxide-rich site, as O^{2-} is less polarisable and so a 'harder' anion than S^{2-}. The driving force behind this preference is the formation of stronger bonds in the crystal structure. To summarise, perhaps the oxidation state site preferences in $Sr_2CrO_2Cr_2OAs_2$ are electronically driven whereas in $Ca_2FeO_2Fe_{1.6}OS_2$ the preferences are driven by the formation of stronger bonds (hard-soft acid-base theory).

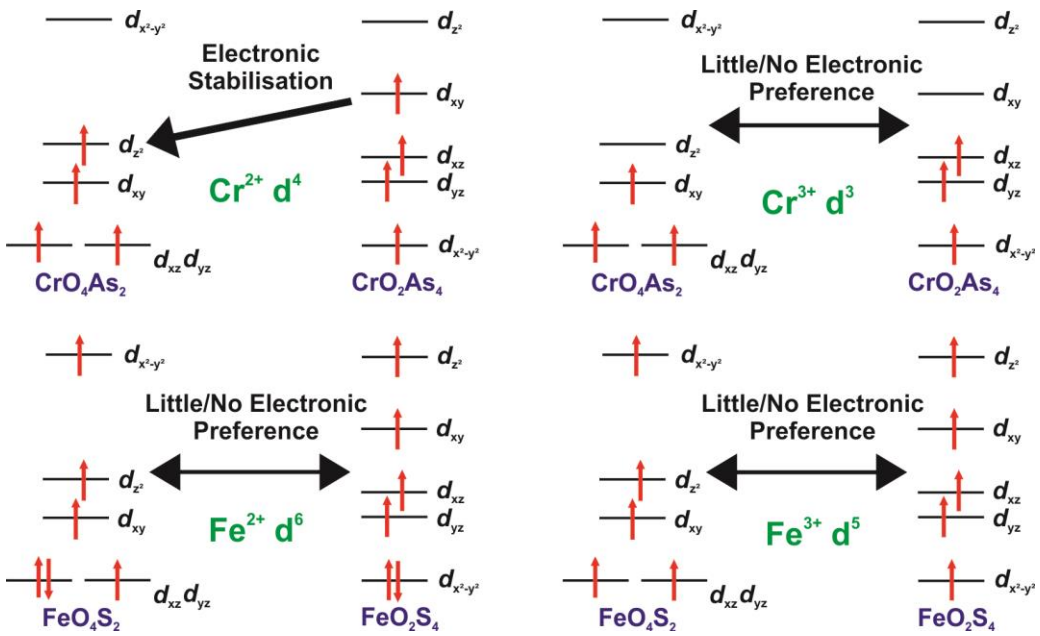


Figure 5.15: Comparison of the electron configurations for the Cr^{2+}/ Cr^{3+} cations in either a CrO_4As_2 or CrO_2As_4 coordination environment and the Fe^{2+}/ Fe^{3+} cations in either a FeO_4S_2 or FeO_2S_4 coordination environment.

5.4.2 Magnetic Structure

The Cr1 layers contain the checkerboard ordering of Cr moments which is very common for infinite-layer MO_2 square-planar sheets. Not only has this already been observed in the analogous layers of the $Ca_2FeO_2Fe_{1.6}OS_2$ compound studied in Chapter 3 and the isostructural solid solution phases explored in Chapter 4, but there are also many examples of this ordering in the literature, such as $Sr_2CoO_2Ag_2Se_2$.[20] The Cr1 (Cr^{2+}) moment is similar in direction and magnitude to the Cr^{2+} moment in the analogous layers in both $Ba_2CrO_2Cr_2As_2$ and $Sr_2CrO_2Cr_2As_2$[1,21] where the CrO_2 layers are also antiferromagnetically ordered in this checkerboard arrangement.

In terms of the Cr2 layers, Stock and McCabe[22] summarise a number of long-range magnetic ordering schemes reported for layered materials comprising M_2OSe_2 (*M* = transition metal) blocks. One observation of interest is that the magnetic structure for the Cr2 sublattice in the Cr_2OAs_2 layers of $Sr_2CrO_2Cr_2OAs_2$ is similar to that described for $La_2O_2Mn_2OSe_2$,[8,2] containing Mn_2OSe_2 layers similar to the Cr_2OAs_2 layers considered here, where the d^5 moments for Mn^{2+} ions are also directed perpendicular to the layers and order in a similar checkerboard manner. The magnetic structure of $La_2O_2Mn_2OSe_2$ was proposed to be a consequence of the antiferromagnetic nearest neighbour direct exchange interactions being dominant and frustrating the J_2 and J_3 superexchange interactions resulting in ferromagnetic alignment of the moments along the perpendicular -Mn-O-Mn-O-Mn- chains.

Whangbo *et al*.[23] describe a method by which the spin direction in a magnetically ordered system can be related to the ligand field of the magnetic ion using spin-orbit coupling arguments, and the cases for $Sr_2CrO_2Cr_2OAs_2$ are given in Figure 5.16. In the CrO_4As_2 elongated octahedra (Cr1), the change in the magnetic quantum number between the HOMO and LUMO is given by $|\Delta L_z| = 0$, predicting that the moments order parallel to the principal axis (along the crystallographic *c*-direction, perpendicular to the layers). As for the CrO_2As_4 environments (Cr2), this change in the magnetic quantum number between the HOMO and LUMO is given by $|\Delta L_z| = 1$, therefore predicting that the moments order

perpendicular to the principal axis which is defined in Figure 5.16 as parallel to the Cr2-O bonds and thus the moments are permitted to lie parallel to the crystallographic *c*-axis and thus perpendicular to the layers, as observed, or alternatively they could lie perpendicular to the Cr2-O bonds but in the *ab*-plane (i.e., along the crystallographic *b*-axis which is also perpendicular to Cr2-O). It seems that the predictions proposed by Whangbo *et al*.[23] cannot distinguish the two cases which both satisfy the condition of moments directed 'perpendicular to *z*'. It is reported that $La_2O_2Fe_2OSe_2$[14] and $La_2O_2Co_2OSe_2$[2,16] have transition metal moments oriented in the *ab*-plane, whereas $La_2O_2Mn_2OSe_2$[8,2] contains moments directed along the *c*-axis. The FeO_2Se_4 and CoO_2Se_4 coordination environments have $|\Delta L_z| = 1$ and $|\Delta L_z| = 0$ respectively. Therefore, the Fe compound is predicted to contain moments perpendicular to *z* and the Co compound moments parallel to *z* (where *z* is parallel to the O-*M*-O direction of the MO_2Se_4 octahedron as defined in Figure 5.16). This agrees with the models determined by experiment because moments perpendicular and parallel to z can both lie in the crystallographic *ab*-plane. The Mn^{2+} d^5 ion is predicted to have little spin direction preference. Overall, the transition metal moments in these M_2OQ_2 (*M* = transition metal; *Q* = chalcogen or pnictogen) layers lie perpendicular to the crystallographic *ab*-plane for Cr^{3+} (d^3) and Mn^{2+} (d^5) and lie within the *ab*-plane for Fe^{2+} (d^6) and Co^{2+} (d^7).

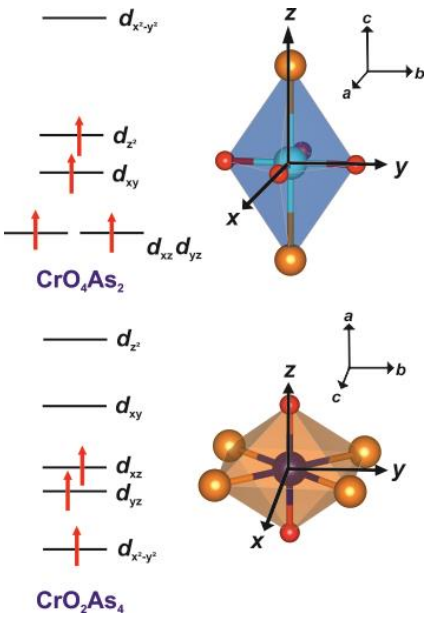


Figure 5.16: Ligand field splitting schemes for the CrO_4As_2 and CrO_2As_4 distorted octahedra. The *x*, *y* and *z* axes shown, which apply to these local coordinations, correspond to the *a*, *b* and *c* crystallographic axes respectively for the CrO_4As_2 case and the *c*, *b* and *a* crystallographic axes respectively for the CrO_2As_4 case. The ligand field splitting for the CrO_2As_4 case is as described for analogous CoO_2Se_4 distended octahedra in $La_2O_2Co_2OSe_2$ by Wu *et al.*[24]

5.5 Conclusions

This study has investigated the structure and long-range magnetic ordering of the newly synthesised $Sr_2CrO_2Cr_2OAs_2$ phase.

The compound crystallises in the *P*4/*mmm* space group and the structure consists of two distinct Cr coordination environments- CrO_4As_2 in the Cr1 layer and CrO_2As_4 in the Cr2 layer. Cr^{2+} and Cr^{3+} are present in the Cr1 and Cr2 layers respectively. A subtle structural distortion occurs between 400 K and 500 K, accompanied by an anomaly in the magnetic susceptibility data, which would be consistent with a very small degree of electron transfer from the Cr^{2+} to the Cr^{3+}, corroborated by changes seen in the bond lengths and bond valence sums of the distorted Cr octahedra. A further investigation would be necessary to confirm this, possibly with single crystals of the pure material, although the extent of it is minuscule.

$Sr_2CrO_2Cr_2OAs_2$ exhibits long-range antiferromagnetic ordering on both Cr sublattices. Just above 600 K the Cr2 (Cr^{3+} d^3) moments order parallel to the *c*-axis in a manner which results in all nearest neighbour Cr spins aligning antiferromagnetically. It is likely that the ordering in this Cr2 layer is dictated by direct exchange interactions via the d_{xz} and d_{yz} orbitals of neighbouring Cr^{3+} cations. At 530(10) K the Cr1 (Cr^{2+} d^4) moments also order parallel to the *c*-axis where all 180° Cr-O-Cr superexchange pathways contain antiferromagnetic Cr spins, as expected for all the 180° superexchange interactions between equally occupied orbitals according to Goodenough-Kanamori rules. In this material the Jahn-Teller axis is perpendicular to the Cr1 layer resulting in antiferromagnetic ordering, whereas in Rb_2CrCl_4[25] the Jahn-Teller axis is in-plane with respect to the layers and the orbitals order in a manner which results in ferromagnetic ordering (as explained in section 1.5.2).

The refined long-range ordered moment per Cr ion in the Cr1 layer is 3.371(10) μ_B compared to the 2.774(6) μ_B per Cr in the Cr2 layer, which are consistent with the assignment of these as Cr^{2+} d^4 and Cr^{3+} d^3 cations respectively. The ordering temperature of 530(10) K for the Cr^{2+} moments is

significantly higher than the ordering temperature of 330(5) K for the Cr^{2+} moments in the CrO_2 layers of $Sr_2CrO_2Cr_2As_2$.[1] This is presumably because the adjacent Cr1 layers are able to couple in $Sr_2CrO_2Cr_2OAs_2$ but cannot couple in $Sr_2CrO_2Cr_2As_2$ because in this case the CrO_2 layers are related by body-centring.

References

(1) Xu, X.; Jones, M. A.; Cassidy, S. J.; Manuel, P.; Orlandi, F.; Batuk, M.; Hadermann, J.; Clarke, S. J. Magnetic Ordering in the Layered Cr(II) Oxide Arsenides $Sr_2CrO_2Cr_2As_2$ and $Ba_2CrO_2Cr_2As_2$. *Inorg. Chem.* **2020**, *59* (21), 15898–15912. https://doi.org/10.1021/acs.inorgchem.0c02415.

(2) Free, D. G.; Withers, N. D.; Hickey, P. J.; Evans, J. S. O. Synthesis, Structure and Properties of Several New Oxychalcogenide Materials with the General Formula $A_2O_2M_2OSe_2$ (A = La-Sm, M = Fe, Mn). *Chem. Mater.* **2011**, *23* (6), 1625–1635. https://doi.org/10.1021/cm1035453.

(3) Jiang, H.; Bao, J. K.; Zhai, H. F.; Tang, Z. T.; Sun, Y. L.; Liu, Y.; Wang, Z. C.; Bai, H.; Xu, Z. A.; Cao, G. H. Physical Properties and Electronic Structure of $Sr_2Cr_3As_2O_2$ Containing CrO_2 and Cr_2As_2 Square-Planar Lattices. *Phys. Rev. B - Condens. Matter Mater. Phys.* **2015**, *92* (20), 205107. https://doi.org/10.1103/PhysRevB.92.205107.

(4) Brese, N. E.; O'Keeffe, M. Bond-valence Parameters for Solids. *Acta Crystallogr. Sect. B* **1991**, *47* (2), 192–197. https://doi.org/10.1107/S0108768190011041.

(5) Boller, H.; Kallel, A. First Order Crystallographic and Magnetic Phase Transition in CrAs. *Solid State Commun.* **1971**, *9* (19), 1699–1706. https://doi.org/10.1016/0038-1098(71)90344-9.

(6) Watanabe, H.; Kazama, N.; Yamaguchi, Y.; Ohashi, M. Magnetic Structure of CrAs and Mn-Substituted CrAs. *J. Appl. Phys.* **1969**, *40* (3), 1128–1129. https://doi.org/10.1063/1.1657559.

(7) Campbell, B. J.; Stokes, H. T.; Tanner, D. E.; Hatch, D. M. ISODISPLACE: A Web-Based Tool for Exploring Structural Distortions. *J. Appl. Crystallogr.* **2006**, *39* (4), 607–614. https://doi.org/10.1107/S0021889806014075.

(8) Ni, N.; Climent-Pascual, E.; Jia, S.; Huang, Q.; Cava, R. J. Physical Properties and Magnetic Structure of the Layered Oxyselenide $La_2O_3Mn_2Se_2$. *Phys. Rev. B - Condens. Matter Mater. Phys.* **2010**, *82* (21). https://doi.org/10.1103/PhysRevB.82.214419.

(9) Song, C.; Islam, Z.; Lottermoser, L.; Goldman, A. I.; Canfield, P. C.; Detlefs, C. Magnetostriction-Induced Tetragonal-to-Orthorhombic Phase Transition in $TbNi_2B_2C$. *Phys. Rev. B - Condens. Matter Mater. Phys.* **1999**, *60* (9), 6223–6225. https://doi.org/10.1103/PhysRevB.60.6223.

(10) Kalita, V. M.; Lozenko, A. F.; Ryabchenko, S. M. Analysis of the Temperature-Field Dependence of the Magnetostriction in the Antiferromagnetic Phase of the Easy-Plane Antiferromagnet $CoCl_2$. *Low Temp. Phys.* **2000**, *26* (7), 489–493. https://doi.org/10.1063/1.1306404.

(11) Brechtel, E.; Cordier, G.; Schäfer, H. On Oxidpnictides: Preparation and Crystal Structure of $A_2Mn_3B_2O_2$ with A = Sr, Ba and B = As, Sb, Bi. *Zeitschrift fur Naturforsch. - Sect. B J. Chem. Sci.* **1979**, *34* (6), 777–780. https://doi.org/10.1515/znb-1979-0603.

(12) Kabbour, H.; Janod, E.; Corraze, B.; Danot, M.; Lee, C.; Whangbo, M. H.; Cario, L. Structure and Magnetic Properties of Oxychalcogenides $A_2F_2Fe_2OQ_2$ (A = Sr, Ba; Q = S, Se) with Fe_2O Square Planar Layers Representing an Antiferromagnetic Checkerboard Spin Lattice. *J. Am. Chem. Soc.* **2008**, *130* (26), 8261–8270. https://doi.org/10.1021/ja711139g.

(13) Zhu, J. X.; Yu, R.; Wang, H.; Zhao, L. L.; Jones, M. D.; Dai, J.; Abrahams, E.; Morosan, E.; Fang, M.; Si, Q. Band Narrowing and Mott Localization in Iron Oxychalcogenides $La_2O_2Fe_2O(Se,S)_2$. *Phys. Rev. Lett.* **2010**, *104* (21). https://doi.org/10.1103/PhysRevLett.104.216405.

(14) Free, D. G.; Evans, J. S. O. Low-Temperature Nuclear and Magnetic Structures of $La_2O_2Fe_2OSe_2$

from x-Ray and Neutron Diffraction Measurements. *Phys. Rev. B - Condens. Matter Mater. Phys.* **2010**, *81* (21). https://doi.org/10.1103/PhysRevB.81.214433.

(15) Oogarah, R. K.; Suard, E.; McCabe, E. E. Magnetic Order and Phase Transition in the Iron Oxysulfide $La_2O_2Fe_2OS_2$. *J. Magn. Magn. Mater.* **2018**, *446*, 101–107. https://doi.org/10.1016/j.jmmm.2017.09.024.

(16) Fuwa, Y.; Endo, T.; Wakeshima, M.; Hinatsu, Y.; Ohoyama, K. Orthogonal Spin Arrangement in Quasi-Two-Dimensional $La_2Co_2O_3Se_2$. *J. Am. Chem. Soc.* **2010**, *132* (51), 18020–18022. https://doi.org/10.1021/ja109007g.

(17) Ablimit, A.; Sun, Y. L.; Jiang, H.; Bao, J. K.; Zhai, H. F.; Tang, Z. T.; Liu, Y.; Wang, Z. C.; Feng, C. M.; Cao, G. H. Synthesis, Crystal Structure and Physical Properties of a New Oxypnictide $Ba_2Ti_2Cr_2As_4O$ Containing $[Ti_2As_2O]^{2-}$ and $[Cr_2As_2]^{2-}$ layers. *J. Alloys Compd.* **2017**, *694*, 1149–1153. https://doi.org/10.1016/j.jallcom.2016.10.152.

(18) Wang, X. F.; Yan, Y. J.; Ying, J. J.; Li, Q. J.; Zhang, M.; Xu, N.; Chen, X. H. Structure and Physical Properties for a New Layered Pnictide-Oxide: $BaTi_2As_2O$. *J. Phys. Condens. Matter* **2010**, *22* (7). https://doi.org/10.1088/0953-8984/22/7/075702.

(19) Sun, Y. L.; Jiang, H.; Zhai, H. F.; Bao, J. K.; Jiao, W. H.; Tao, Q.; Shen, C. Y.; Zeng, Y. W.; Xu, Z. A.; Cao, G. H. Ba 2Ti 2Fe 2As 4O: A New Superconductor Containing Fe_2As_2 Layers and Ti_2O Sheets. *J. Am. Chem. Soc.* **2012**, *134* (31), 12893–12896. https://doi.org/10.1021/ja304315e.

(20) Herkelrath, S. J. C.; Blandy, J. N.; Clarke, S. J. Magnetic Ordering in the Layered Oxyselenides $Sr_2CoO_2Ag_2Se_2$ and $Ba_2CoO_2Ag_2Se_2$. *J. Solid State Chem.* **2018**, *264*, 119–123. https://doi.org/10.1016/j.jssc.2018.05.018.

(21) Liu, J.; Wang, J.; Sheng, J.; Ye, F.; Taddei, K. M.; Fernandez-Baca, J. A.; Luo, W.; Sun, G. A.; Wang, Z. C.; Jiang, H.; Cao, G. H.; Bao, W. Neutron Diffraction Study on Magnetic Structures and Transitions in $Sr_2Cr_3As_2O_2$. *Phys. Rev. B* **2018**, *98* (13), 134416. https://doi.org/10.1103/PhysRevB.98.134416.

(22) Stock, C.; McCabe, E. E. The Magnetic and Electronic Properties of Oxyselenides - Influence of Transition Metal Ions and Lanthanides. *Journal of Physics Condensed Matter*. 2016. https://doi.org/10.1088/0953-8984/28/45/453001.

(23) Whangbo, M. H.; Gordon, E. E.; Xiang, H.; Koo, H. J.; Lee, C. Prediction of Spin Orientations in Terms of HOMO-LUMO Interactions Using Spin-Orbit Coupling as Perturbation. *Acc. Chem. Res.* **2015**, *48* (12), 3080–3087. https://doi.org/10.1021/acs.accounts.5b00408.

(24) Wu, H. Electronic Structure, Spin State, and Magnetism of the Square-Lattice Mott Insulator $La_2Co_2Se_2O_3$ from First Principles. *Phys. Rev. B - Condens. Matter Mater. Phys.* **2010**, *82* (2). https://doi.org/10.1103/PhysRevB.82.020410.

(25) Day, P.; Hutchings, M. T.; Janke, E.; Walker, P. J. Co-Operative Jahn-Teller Ordering in the Crystal Structure of Rb_2CrCl_4: A Two-Dimensional Easy-Plane Ionic Ferromagnet. *J. Chem. Soc. Chem. Commun.* **1979**, No. 16, 711–713. https://doi.org/10.1039/C39790000711.

Chapter 6

6 Structure and Magnetism of Ba_2FeSbS_5 and Ba_2FeBiS_5

6.1 Introduction

Geng *et al.* first reported the structure and properties of Ba_2FeSbS_5 and Ba_2FeBiS_5 in 2011.[1] These quaternary sulfides are isostructural, with both crystallising in the *Pnma* space group, and they also adopt the same structure type as a high-pressure phase of Ba_3FeS_5.[2] They are semiconductors with experimental band gaps of 0.95 eV and 1.28 eV for Ba_2FeSbS_5 and Ba_2FeBiS_5 respectively. From first-principles DFT calculations, it is thought these band gaps involve charge transfer from the S 3*p* valence band to the Fe 3*d* conduction band. Clear antiferromagnetic transitions with Néel temperatures of 13 K (Ba_2FeSbS_5) and 35 K (Ba_2FeBiS_5) were observed in the magnetometry data, which encouraged further exploration of the long-range magnetic ordering using powder neutron diffraction.

6.2 Synthesis

3 g samples of Ba_2FeSbS_5 and Ba_2FeBiS_5 were synthesised from BaS (Aldrich 99.9 %), Fe (Alfa Aesar 99.998 %), Sb (Alfa Aesar 99.999 %) / Bi (Aldrich 99.999 %) and S (Alfa Aesar 99.999 %) in the ratio of 2:1:1:3. The reagents were thoroughly ground together using an agate pestle and mortar until the mixtures appeared homogeneous. The powders were then pressed into pellets, placed in alumina crucibles and sealed inside evacuated silica tubes. During the tube sealing process, the lower part of the tube – where the crucibles were residing – was submerged in liquid nitrogen to prevent the evaporation of sulfur. The Ba_2FeSbS_5 mixture was heated at 400 °C for 24 h (0.1 °C/min ramping rate) then 700 °C for 24 h (0.5 °C/min ramping rate) and the Ba_2FeBiS_5 mixture was heated at 400 °C for 24 h (0.1 °C/min ramping rate) then 750 °C for 24 h (0.5 °C/min ramping rate). The 400 °C heating step and slow ramping rates ensured that the sulfur reacted before reaching a high vapour pressure.

6.3 Characterisation

6.3.1 Room Temperature XRPD

Room temperature XRPD data were collected on beamline I11 at the Diamond Light Source. The high-resolution MAC detector was used to gather these data. Refinements of a structural model against the data are depicted in Figures 6.1 and 6.2. The data do not indicate the presence of any side phases or stoichiometry away from the target formulae.

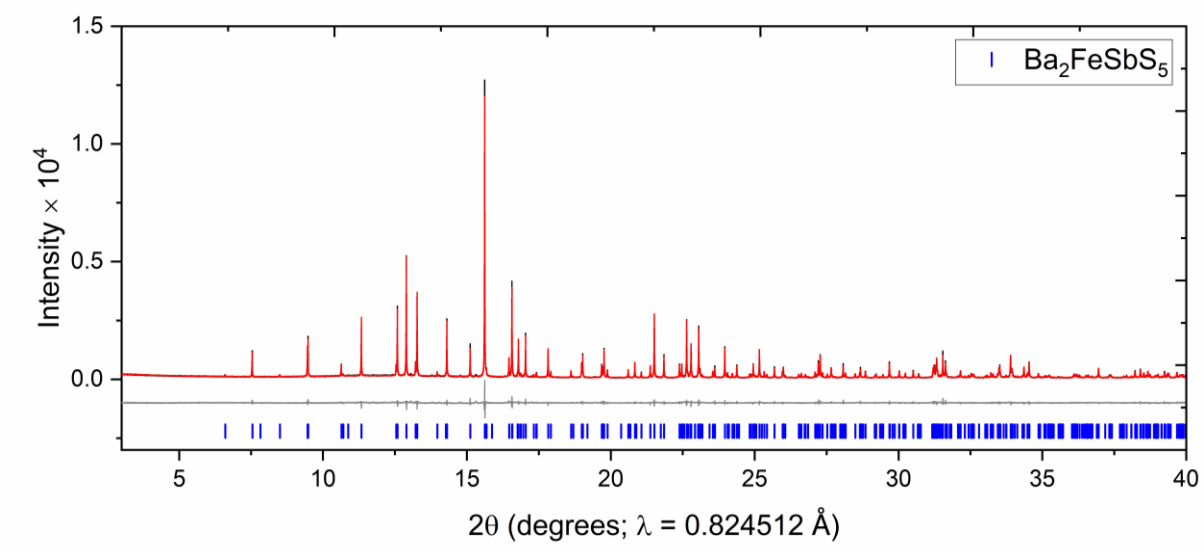


Figure 6.1: XRPD pattern of Ba_2FeSbS_5 measured at 300 K on the MAC detector at I11 showing the observed (black), calculated (red) and difference (grey) curves. R_{wp}: 7.733%.

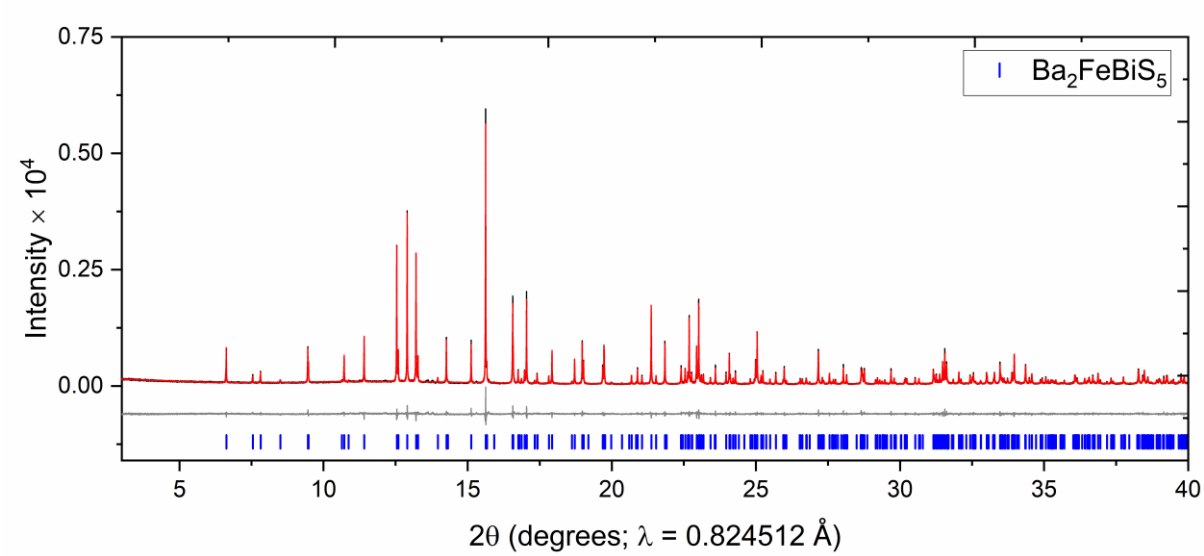


Figure 6.2: XRPD pattern of Ba_2FeBiS_5 measured at 300 K on the MAC detector at I11 showing the observed (black), calculated (red) and difference (grey) curves. R_{wp}: 8.401%.

These materials crystallise in the orthorhombic *Pnma* space group (structure given in Figure 6.3a)) and can be viewed as consisting of infinite $[FeMS_5]^{4-}$ (M = Sb, Bi) chains (see Figure 6.3b)), where Fe^{3+} is tetrahedrally coordinated by sulfide anions and a distorted octahedral arrangement of sulfide anions surrounds M^{3+}. Figure 6.4 depicts these two polyhedra. The edge-sharing MS_6 polyhedra form the backbone of these chains and the FeS_4 tetrahedra share one of their edges with one of the edges of an MS_6 polyhedron. The FeS_4 tetrahedra are arranged on alternating sides of the MS_6 polyhedral chains, and this allows adjacent Sb/Bi stereoactive lone pairs, most likely positioned between the two M-$S1^b$ bonds, to be situated on opposite sides of the backbone.

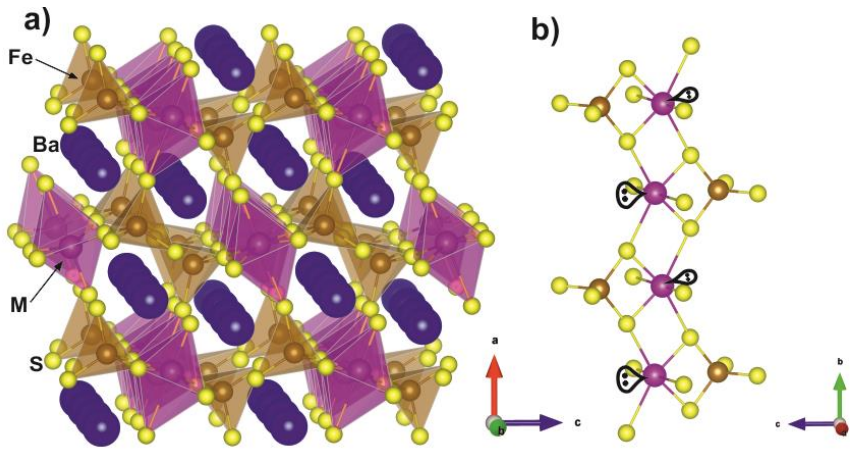


Figure 6.3: The structure of Ba_2FeMS_5 (M = Sb, Bi) **a)** with the FeS_4 (brown) and MS_6 (purple) polyhedra highlighted and **b)** showing only the infinite $[FeMS_5]^{4-}$ (M = Sb, Bi) 1D chains which run through the structure, with the most likely position of the stereoactive lone pair illustrated.

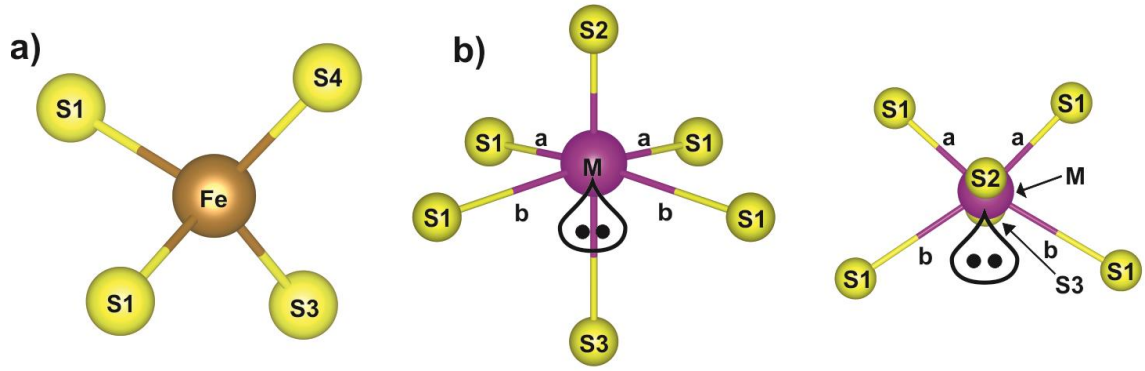


Figure 6.4: Labelled diagrams for **a)** the FeS_4 tetrahedra and **b)** the MS_6 (M = Sb, Bi) distorted octahedra, with the most likely position of the stereoactive lone pair indicated between the two M-$S1^b$ bonds. Bond distances are given in Table 6.1.

	Ba_2FeSbS_5	Ba_2FeBiS_5
Diffractometer	I11 (MAC)	I11 (MAC)
Wavelength (Å)	0.824512	0.824512
Temperature (K)	300	300
Space Group	*Pnma*	*Pnma*
a (Å)	12.08609(3)	12.09610(3)
b (Å)	8.83426(2)	8.89281(2)
c (Å)	8.89114(2)	8.82437(2)
V (Å^3)	949.321(3)	949.224(3)

					Ba_2FeSbS_5
Atom	Site	*x*	*y*	*z*	U_{iso} (Å^2)
Ba	8*d*	0.32277(6)	0.00774(9)	0.37767(6)	0.0160(3)
Sb	4*c*	0.02265(9)	0.25	0.51819(13)	0.0134(4)
Fe	4*c*	0.09434(18)	0.25	0.1705(3)	0.0066(7)
S1	8*d*	0.0527(3)	0.0501(3)	0.3236(3)	0.0154(11)
S2	4*c*	0.2099(4)	0.25	0.6157(5)	0.0118(15)
S3	4*c*	0.2737(4)	0.25	0.1173(5)	0.0184(16)
S4	4*c*	0.4936(4)	0.25	0.5347(5)	0.0181(14)

					Ba_2FeBiS_5
Atom	Site	*x*	*y*	*z*	U_{iso} (Å^2)
Ba	8*d*	0.32224(7)	0.00985(10)	0.38338(9)	0.0042(4)
Bi	4*c*	0.01744(7)	0.25	0.53310(8)	0.0044(4)
Fe	4*c*	0.0942(3)	0.25	0.1715(3)	0.0000(9)
S1	8*d*	0.0551(3)	0.0457(4)	0.3199(4)	0.0028(12)
S2	4*c*	0.2159(4)	0.25	0.6245(6)	0.0027(17)
S3	4*c*	0.2760(4)	0.25	0.1177(6)	0.0017(16)
S4	4*c*	0.4963(4)	0.25	0.5345(5)	0.0050(14)

Bond Type	Distance (Å) {Ba_2FeSbS_5}	Distance (Å) {Ba_2FeBiS_5}
Fe-S1 [2]	2.286(3)	2.289(4)
Fe-S3 [1]	2.219(5)	2.250(6)
Fe-S4 [1]	2.193(5)	2.170(6)
M-S1^a [2]	2.499(3)	2.655(4)
M-S1^b [2]	3.136(3)	3.061(4)
M-S2 [1]	2.424(4)	2.532(5)
M-S3 [1]	3.241(4)	3.209(5)
Fe BVS	+3.10(4)	+3.08(5)
M BVS	+3.46(5)	+3.41(5)

Table 6.1: Refinement results from XRPD patterns collected at 300 K using the MAC detector at I11. The numbers in the square brackets give the multiplicity of each type of bond and the labelling of the S atoms is the system adopted by Geng *et al*.[1] The coordination environments are shown in Figure 6.4. Bond valence sum (BVS) values calculated using reference values from *Brown and Altermatt*.[3]

Table 6.1 details the refinement results, along with the bond valence sums (BVS) of the Fe and M (M = Sb, Bi) ions. The unit cell volumes are almost identical due to the fact that the longer *a*-axis is largely unchanged upon going from the Sb to the Bi analogue and the shorter *b*-axis and *c*-axis are also very similar in magnitude. This can be attested to the similar ionic radii of Sb^{3+} and Bi^{3+} due to the lanthanide and relativistic contractions and the minimal change in structure between the two samples. The stereoactive ns^2 lone pair is likely to be directed between the M-$S1^b$ bonds, in the space where no atoms reside. It is this lone pair that gives the M cation the unusual distorted octahedral coordination environment via a 2nd order Jahn-Teller distortion involving n*s*/n*p* mixing mediated by the anion valence orbitals.[4]

The Fe BVS value is very close to +3 for both compounds, which is the expected formal oxidation state of Fe in these systems based on the formulae. The fact that these values are comparable reflects the similar Fe-S bond lengths and arrangement of the S^{2-} anions around the Fe centres in the FeS_4 tetrahedra for two materials. With the much longer M-$S1^b$ and M-S3 included, so that the coordination number of M is six, the calculated BVS values for M are slightly larger than +3 (but without these distances included the M cation has a coordination number of three and the BVS values are +3.01(3) (M= Sb) and +2.70(4) (M= Bi)).

6.3.2 SQUID Magnetometry

Magnetometry measurements on the two compounds are shown in Figures 6.5a) and 6.6a) for Ba_2FeSbS_5 and Ba_2FeBiS_5 respectively. As previously discovered,[1] both show antiferromagnetic transitions – Ba_2FeSbS_5 at 12-14 K and Ba_2FeBiS_5 at 34-36 K. The 5 K magnetisation isotherms in Figures 6.5b) and 6.6b) are very similar as both are symmetric with respect to the origin and show an increase in gradient at higher fields. This increase could plausibly indicate a field-induced moment re-orientation at much higher fields.

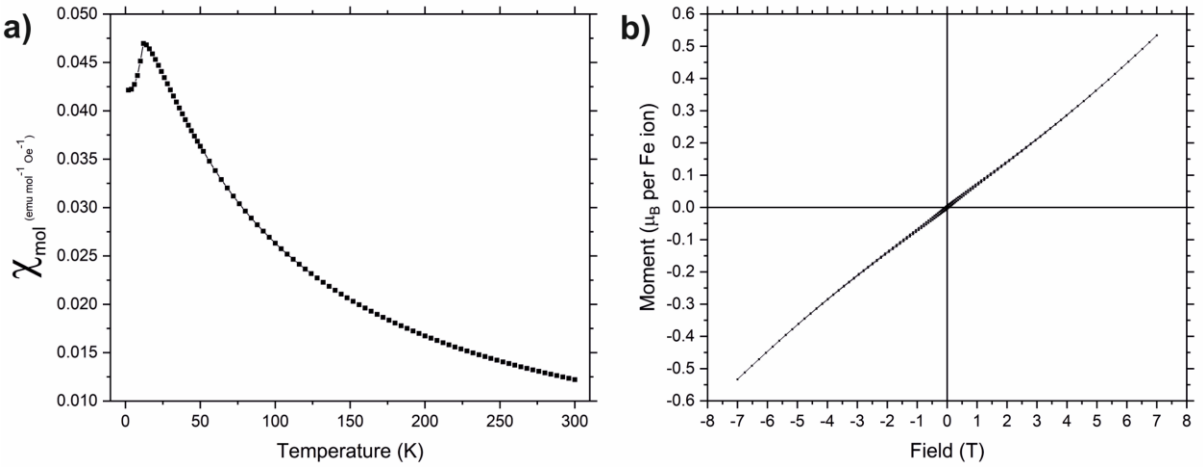


Figure 6.5: Magnetometry results for the Ba_2FeSbS_5 compound showing data from **a)** the magnetic susceptibility and **b)** the magnetisation isotherm measured at 5 K.

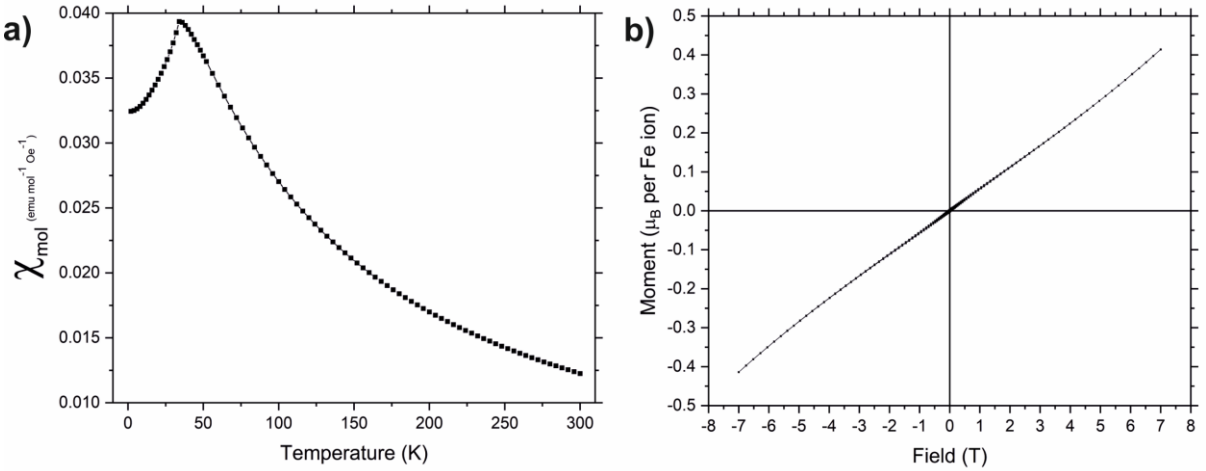


Figure 6.6: Magnetometry results for the Ba_2FeBiS_5 compound showing data from **a)** the magnetic susceptibility and **b)** the magnetisation isotherm measured at 5 K.

Curie-Weiss fits for the magnetometry data predict values for the effective magnetic moment, μ_{eff}, on the Fe site to be 6.061(3) μ_B and 5.983(6) μ_B for Ba_2FeSbS_5 and Ba_2FeBiS_5 respectively (see Figures 6.7 and 6.8). These values are close to the spin-only moment predicted for a high spin d^5 ion, which is μ_{eff} = 5.92 μ_B. Therefore, it is highly likely that Fe^{3+} exists on the Fe sites. The Weiss constants indicate strong antiferromagnetic interactions for both compounds and may indicate some degree of magnetic frustration as they are higher than the ordering temperatures. This is particularly significant in the case of the Sb analogue, where the Weiss temperature is approximately 6 times greater than T_N. This potential magnetic frustration will be discussed further in section 6.3.3.

Magnetometry data for the Ba_3FeS_5 high-pressure phase – which is isostructural with Ba_2FeMS_5 (M = Sb, Bi) but with Ba on the M site – show that it is paramagnetic between 300 K and 800 K with an effective magnetic moment of 5.1 μ_B.[2] This value of μ_{eff} is around 1 μ_B less than the values for Ba_2FeSbS_5 and Ba_2FeBiS_5, as expected from the incorporation of Fe^{4+} d^4 and Fe^{3+} d^5 respectively. These results for Ba_3FeS_5 do not rule out the possibility of low temperature transitions like the ones observed for the Ba_2FeMS_5 (M = Sb, Bi) phases.

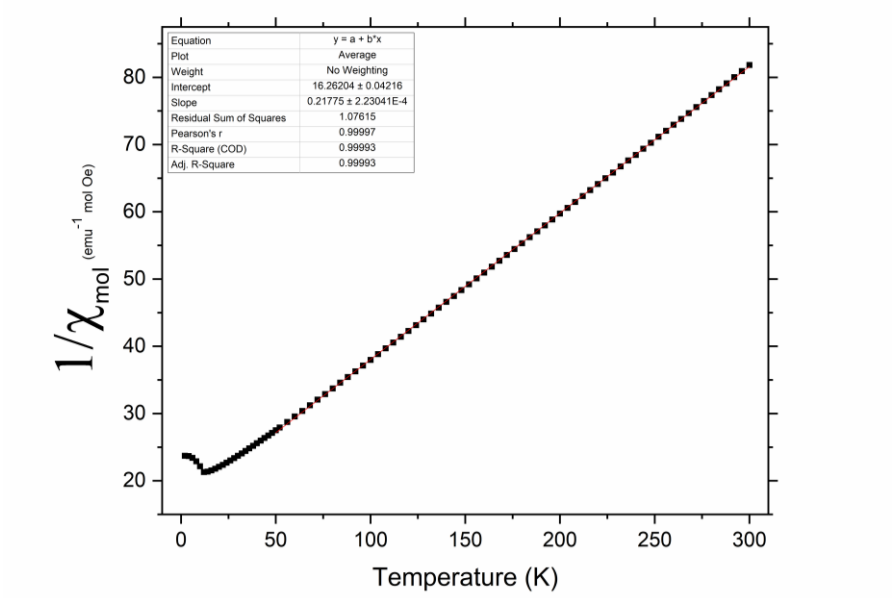


Figure 6.7: Curie-Weiss fit for the magnetometry data collected on the Ba_2FeSbS_5 compound. The fit uses data from 50 K to 300 K, where the curve is linear. The Curie constant, C = 4.592(5) and the effective magnetic moment, μ_{eff} = 6.061(3) μ_B. The Weiss constant, θ = -74.7(4) K.

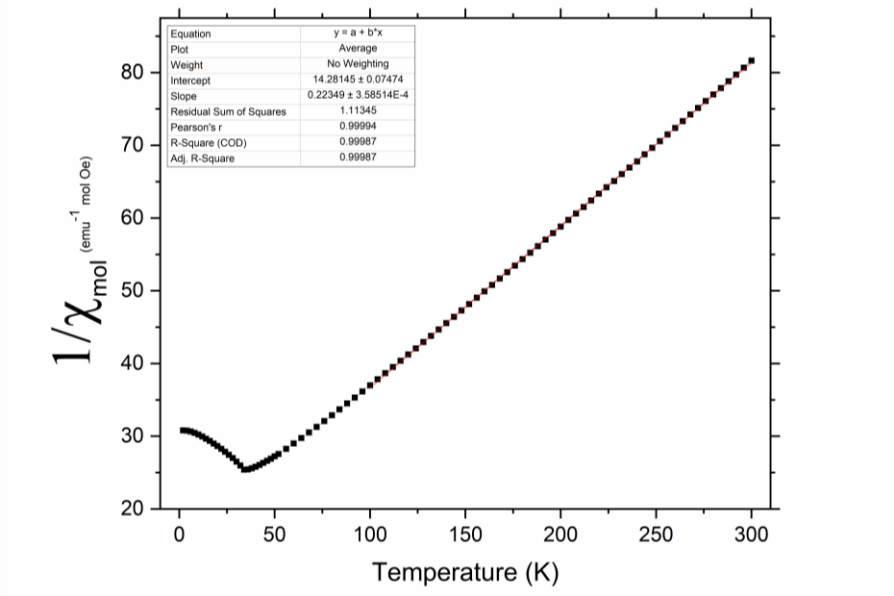


Figure 6.8: Curie-Weiss fit for the magnetometry data collected on the Ba_2FeBiS_5 compound. The fit uses data from 100 K to 300 K, where the curve is linear. The Curie constant, C = 4.474(8) and the effective magnetic moment, μ_{eff} = 5.983(6) μ_B. The Weiss constant, θ = -63.9(5) K.

6.3.3 Variable Temperature NPD

Variable temperature NPD data were gathered on the D1B and D2B instruments at the ILL.

Low temperature NPD studies performed on Ba_2FeSbS_5 show the presence of reflections at high *d*-spacings which cannot be accounted for by the nuclear model alone. Instead, these peaks can be explained by long-range antiferromagnetic ordering of the Fe moments. The vast majority of these peaks are positioned on a *k*-vector with $k = (^1/_2\ 0\ ^1/_2)$ and these are denoted by the black triangles in Figures 6.9 and 6.10. Two peaks of lower intensity are present in Figure 6.9 too (labelled by black squares) however these cannot be accounted for using magnetic modes represented by commensurate *k*-vectors. It should be pointed out here that these two weak peaks are only visible when collecting diffraction data on the extremely high signal/noise D1B instrument (Figure 6.9) which focuses on the long *d*-spacing region and that they are not visible in the diffraction pattern collected on D2B (Figure 6.10). In the D2B data, a large background signal is present up to approximately $2\theta = 10^{\circ}$, which prevents the lower angle nuclear Bragg peaks from being easily identifiable and hence why the refinement in Figure 6.10 begins at $2\theta = 9^{\circ}$.

To a first approximation, the long-range magnetic ordering in Ba_2FeSbS_5 can be represented by the model in Figures 6.11 and 6.12, where this model gave the best fit to the magnetic reflections and is the result of simultaneous refinement of two mU2-U3- (a,b) modes. In the refinement all Fe sites were assumed to have the same moment as they are crystallographically identical. The model can be described as a collinear arrangement of antiferromagnetically aligned moments, which are directed along the *c*-axis.

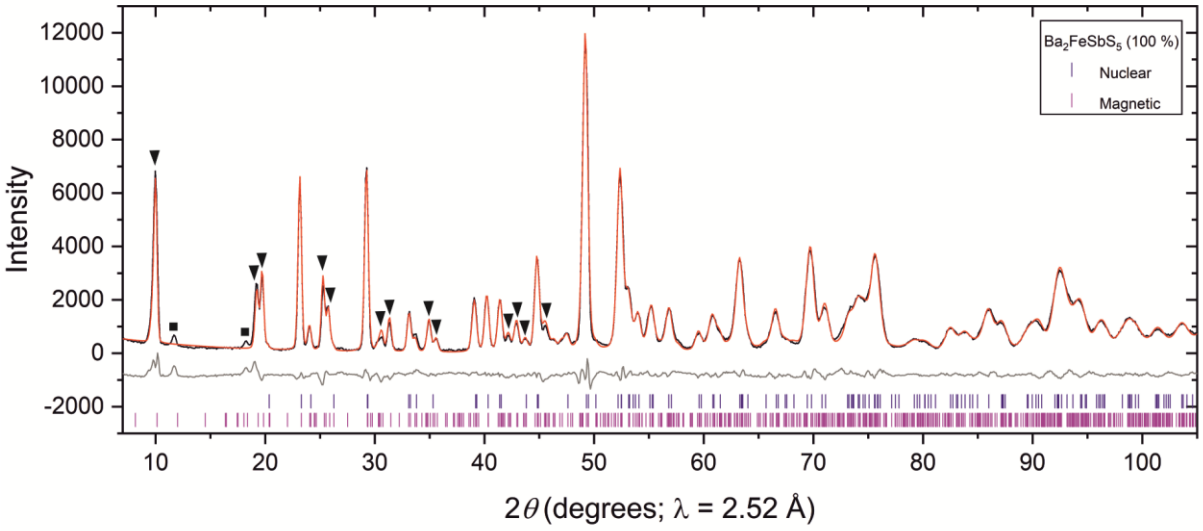


Figure 6.9: NPD pattern of Ba_2FeSbS_5 measured at 1.9 K on the D1B instrument at the ILL showing the observed (black), calculated (red) and difference (grey) curves. The black triangles denote magnetic reflections with $k = (^1/_2\ 0\ ^1/_2)$ and the black squares indicate two low intensity magnetic reflections which cannot be accounted for by commensurate magnetic ordering. R_{wp}: 4.504%.

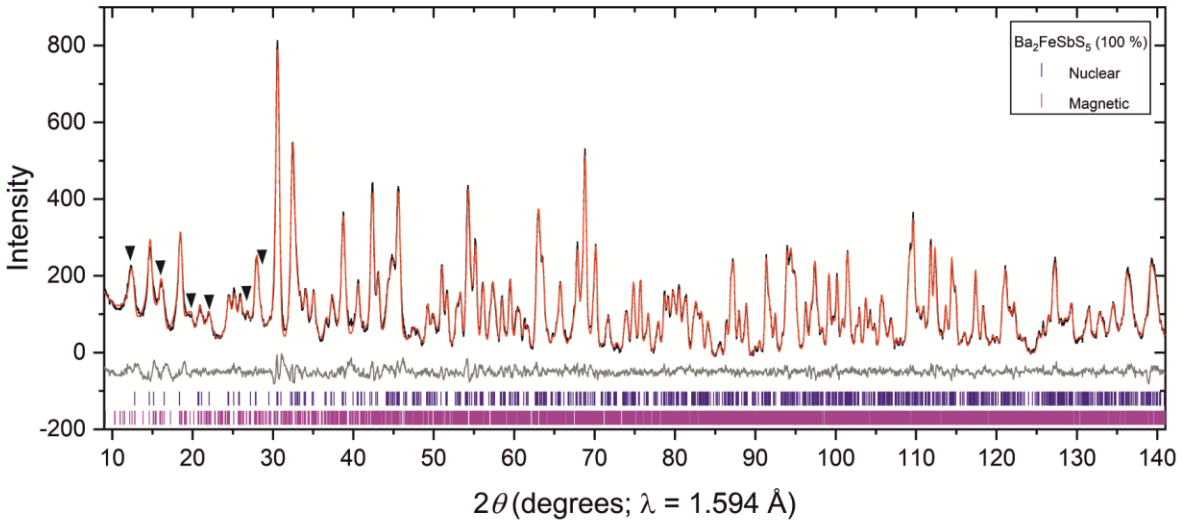


Figure 6.10: NPD pattern of Ba_2FeSbS_5 measured at 2 K on the D2B instrument at the ILL showing the observed (black), calculated (red) and difference (grey) curves. The black triangles denote magnetic reflections with $k = (^1/_2\ 0\ ^1/_2)$. R_{wp}: 2.650%.

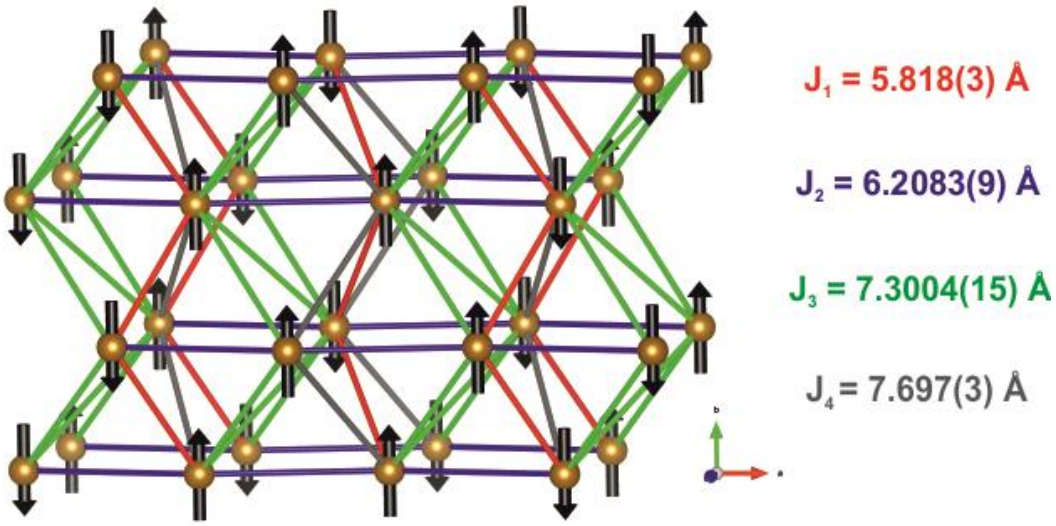


Figure 6.11: Magnetic model for Ba_2FeSbS_5, where the distances given for the magnetic interactions have been refined from the NPD data collected at 2 K on the D2B instrument.

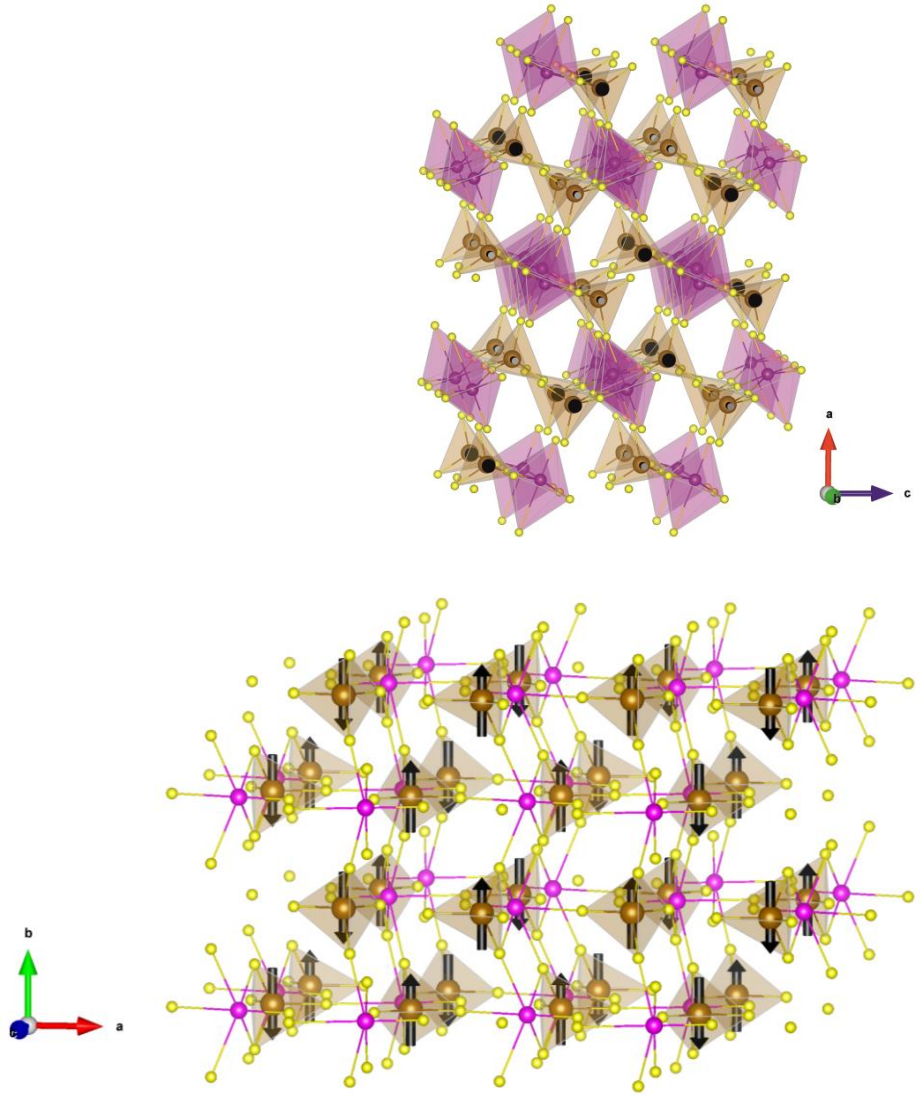


Figure 6.12: Magnetic model for Ba_2FeSbS_5 with the FeS_4 (brown) and MS_6 (purple) polyhedra highlighted.

All magnetic peaks decrease in intensity until a Néel temperature of 12.1(10) K, as shown in Figure 6.13a), which considers all magnetic Bragg peaks apart from the two small peaks which arise from the incommensurate ordering. The saturated moment is approximately 3.6 μB and this decrease from the expected 5 μB for a high-spin d^5 localised moment is likely to be due to covalency in the Fe-S bonds. The critical exponent determined using the plot in Figure 6.13b) is 0.27(2). This is an unusually low value for the critical exponent (values are typically between 0.3 and 0.36) may arise due to the magnetic frustration present in the system (discussed later in this section). It can be seen in Figure 6.14 that all magnetic Bragg peaks appear simultaneously below T_N = 12.1(10) K, whether they arise due to the commensurate or incommensurate ordering, and that there is no obvious shift in the *d*-spacing values of these peaks with temperature (beyond that expected for thermal expansion). As a note, the plot at the top of Figure 6.14 highlights the two small peaks, labelled by the black squares in the main plot, which are difficult to see in the main plot due to their very low intensity.

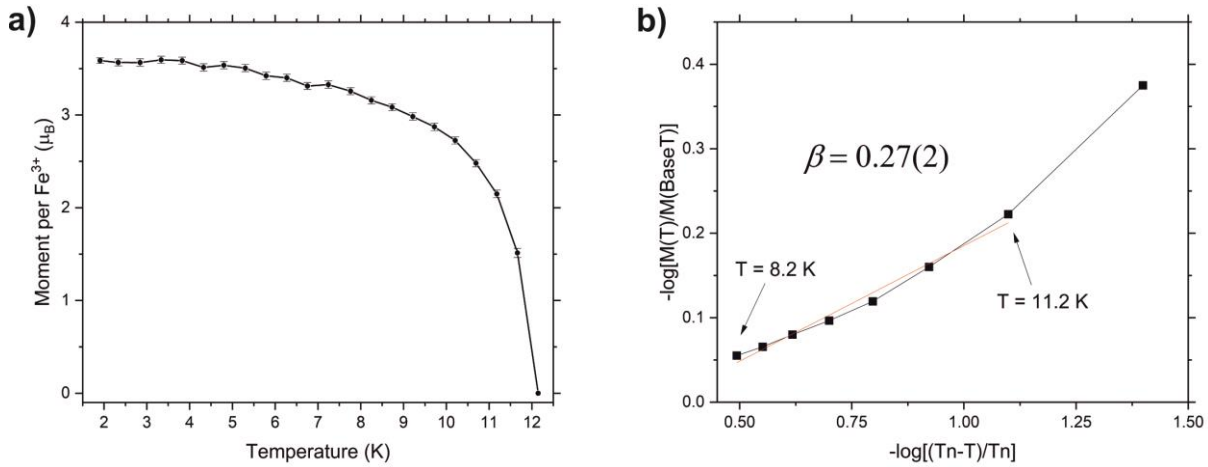


Figure 6.13: Plots depicting **a)** the thermal evolution of the ordered Fe^{3+} magnetic moment in Ba_2FeSbS_5 refined from data collected on the D1B instrument at the ILL and **b)** the determination of the critical exponent, β, of this magnetic transition using the equation $\left[\frac{M(T)}{M(BaseT)}\right] = \left[\frac{T_N - T}{T_N}\right]^{\beta}$ where *M* is the magnetic moment, T_N is the Néel temperature and *T* is the temperature. The Néel temperature used is 12.15 K and base temperature is 1.91 K.

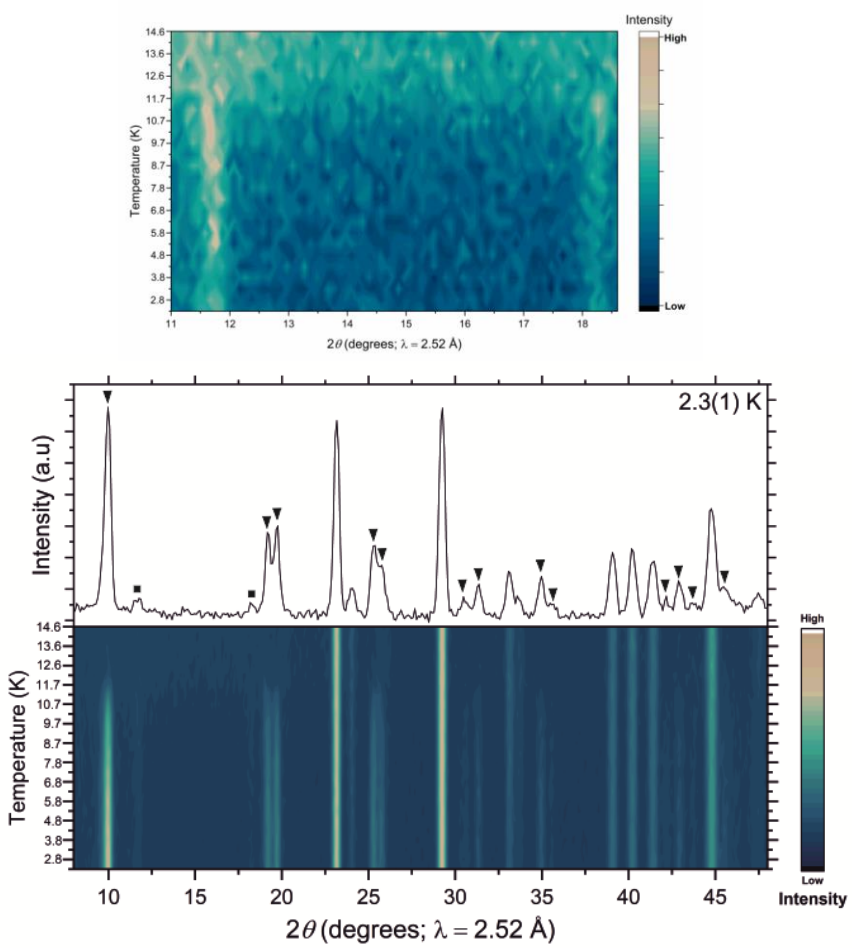


Figure 6.14: Plot of the NPD data collected for Ba_2FeSbS_5 from 2 K to 15 K on the D1B instrument at the ILL. The black triangles denote magnetic reflections with $k = (^1/_2\ 0\ ^1/_2)$ and the black squares indicate two low intensity magnetic reflections which cannot be accounted for using a commensurate magnetic ordering model (a closer view of the evolution of these peaks is given in the top plot).

Refinements of various incommensurately modulated models against the D1B data were performed by Dr Stanislav Savvin at the ILL. A good fit to the data, as illustrated in Figure 6.15, can be achieved by introducing a spin-density wave which is superimposed on the commensurate antiferromagnetic order of the Fe spins. An example of such a model is shown in Figure 6.16. This is ongoing work with the aim of obtaining a model for the magnetic ordering which best fits the D1B data. Given the small number of these additional peaks, there may not be a single unique solution to the nature of the incommensurate structure.

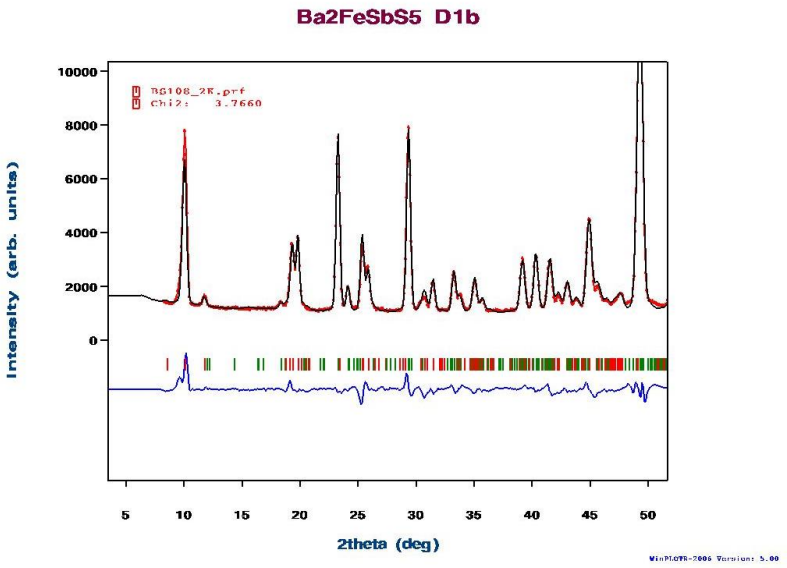


Figure 6.15: NPD pattern of Ba_2FeSbS_5 measured at 1.9 K on the D1B instrument at the ILL showing the observed (black), calculated (red) and difference (blue) curves. An incommensurately modulated spin-density wave has been introduced so that the small magnetic Bragg peaks are accounted for.

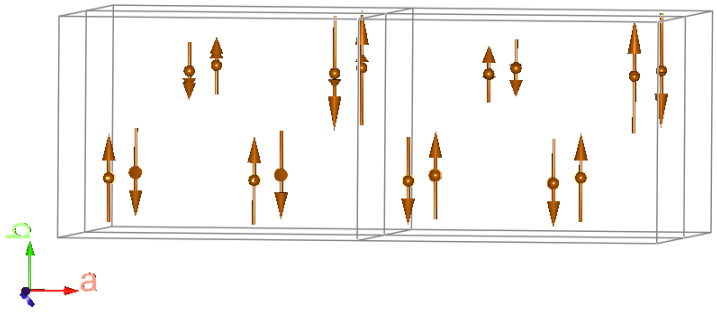


Figure 6.16: Example of a magnetic model for Ba_2FeSbS_5 which includes an incommensurately modulated spin-density wave superimposed on the commensurate antiferromagnetic ordering.

Low temperature NPD studies carried out on Ba_2FeBiS_5 also reveal reflections at high *d*-spacings, again due to long-range antiferromagnetic ordering of the Fe moments. Simultaneous refinement of two mU1-U4- (a,b) modes accounts for all the magnetic reflections. These are denoted by the black triangles in Figures 6.17 and 6.18 and once again located on a *k*-vector with $k = (^1/_2\ 0\ ^1/_2)$. The best fitting model for these data is given in Figures 6.19 and 6.20, where there is a collinear arrangement of the moments which are antiferromagnetically aligned and directed along the long *a*-axis – perpendicular to the moments in the Ba_2FeSbS_5 analogue described above. As for Ba_2FeSbS_5, all Fe sites were assumed to carry similar moments as they are crystallographically identical.

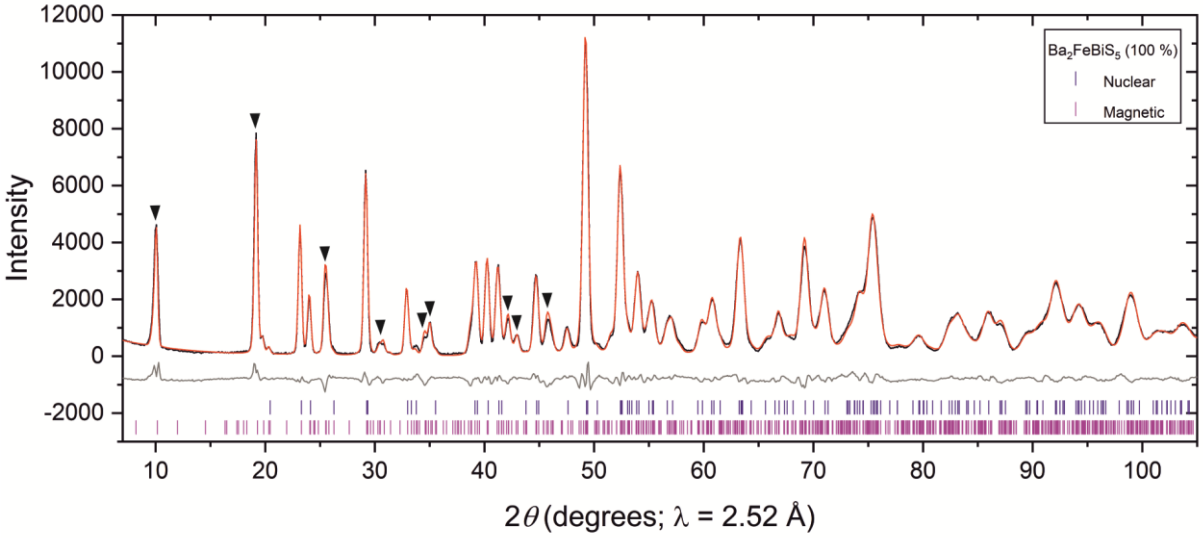


Figure 6.17: NPD pattern of Ba_2FeBiS_5 measured at 1.9 K on the D1B instrument at the ILL showing the observed (black), calculated (red) and difference (grey) curves. The black triangles denote magnetic reflections with $k = (^1/_2\ 0\ ^1/_2)$. R_{wp}: 4.216%. Note that unlike in the case of Ba_2FeSbS_5 there are no peaks left unindexed by the commensurate magnetic model.

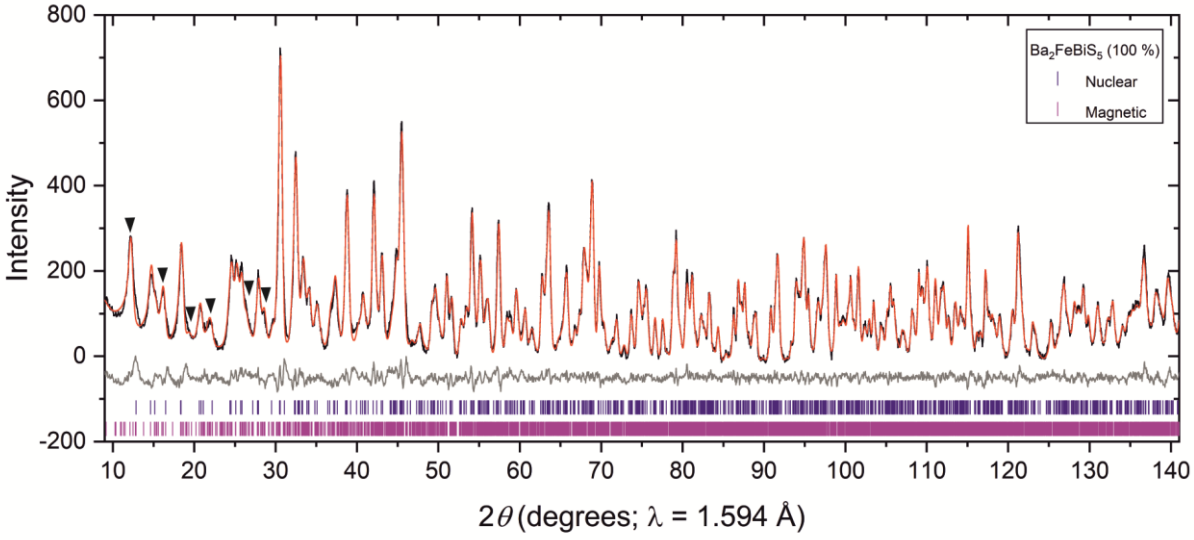


Figure 6.18: NPD pattern of Ba_2FeBiS_5 measured at 2 K on the D2B instrument at the ILL showing the observed (black), calculated (red) and difference (grey) curves. The black triangles denote magnetic reflections with $k = (^1/_2\ 0\ ^1/_2)$. R_{wp}: 2.936%.

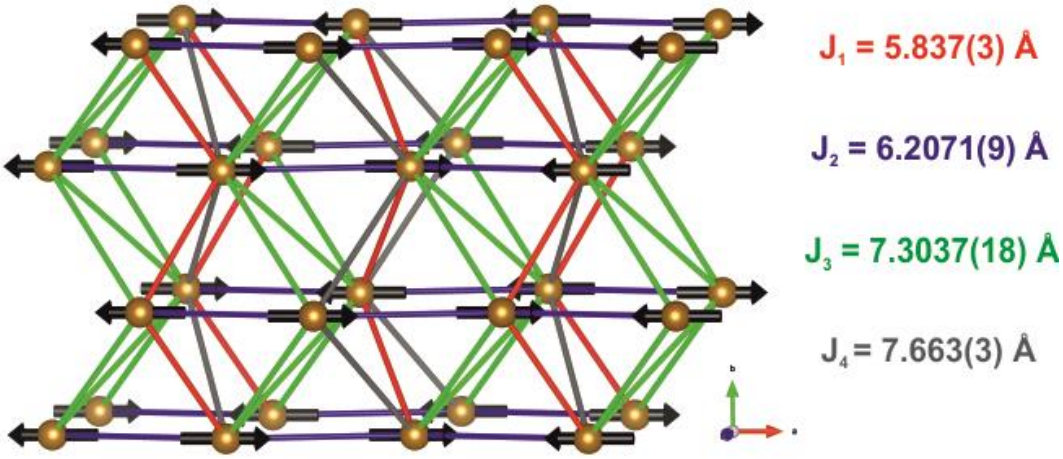


Figure 6.19: Magnetic model for Ba_2FeBiS_5, where the distances given for the magnetic interactions have been refined from the NPD data collected at 2 K on the D2B instrument.

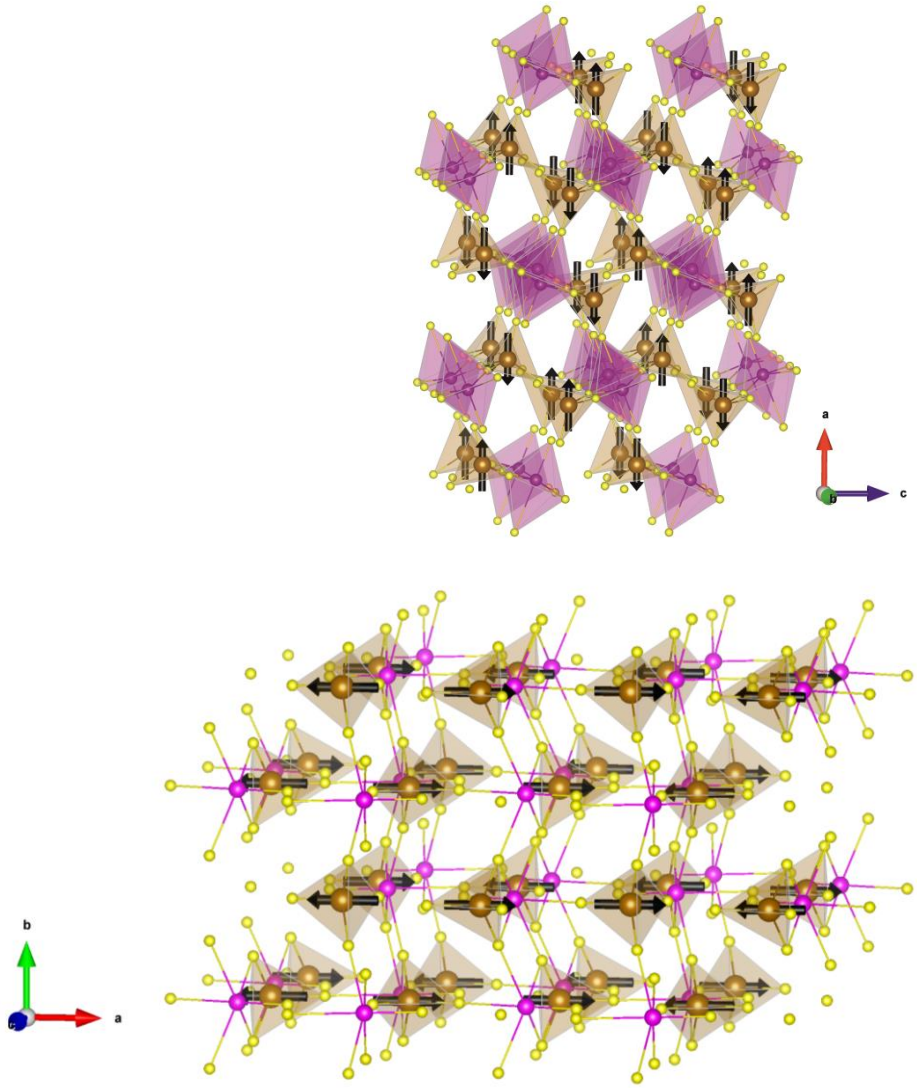


Figure 6.20: Magnetic model for Ba_2FeBiS_5 with the FeS_4 (brown) and MS_6 (purple) polyhedra highlighted.

The magnetic peaks decrease in intensity until a Néel temperature of 34.5(10) K and the saturated moment can be approximated as 3.8 μ_B, as illustrated by the plot in Figure 6.21a). As for Ba_2FeSbS_5 (ordered moment of 3.6 μ_B), the reduction of this localised magnetic moment from the expected 5 μ_B is likely to be due to covalency in the Fe-S bonds. For comparison, the Fe moment in $CuFeS_2$, which contains Fe^{3+} ions in FeS_4 tetrahedra, is reported to be 3.85 μ_B[5] (and later proposed to be 3.42(7) μ_B[6]) whereas the Fe moment in $KFeO_2$, which contains Fe^{3+} ions in FeO_4 tetrahedra, is reported to be 3.99 μ_B[7] (and later proposed to be 3.910(18) μ_B[8]). These examples show how the greater degree of covalency in the Fe-S bonds compared to Fe-O bonds leads to a lower saturated magnetic moment on the Fe^{3+} ions and the values of approximately 3.6 μ_B and 3.8 μ_B – obtained for Ba_2FeBiS_5 and Ba_2FeBiS_5 respectively – are reasonable. The critical exponent was determined using the plot in Figure 6.21b) to be a value of 0.35(1), which indicates a 3D lattice dimensionality and a 3D spin dimensionality. It can be seen in Figure 6.22 that all magnetic Bragg peaks appear simultaneously below T_N = 34.5(10) K and that again there is no obvious shift in the *d*-spacing values of these peaks with temperature (beyond that expected for thermal expansion).

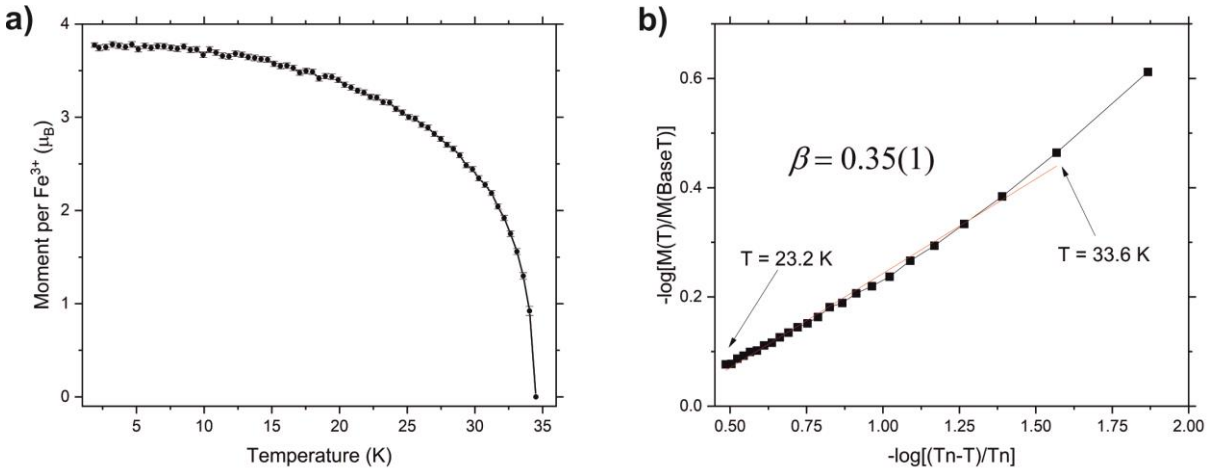


Figure 6.21: Plots depicting **a)** the thermal evolution of the ordered Fe^{3+} magnetic moment in Ba_2FeBiS_5 refined from data collected on the D1B instrument at the ILL and **b)** the determination of the critical exponent, β, of this magnetic transition using the equation $\left[\frac{M(T)}{M(BaseT)}\right] = \left[\frac{T_N - T}{T_N}\right]^{\beta}$ where *M* is the magnetic moment, T_N is the Néel temperature and *T* is the temperature. The Néel temperature used is 34.51 K and base temperature is 1.90 K.

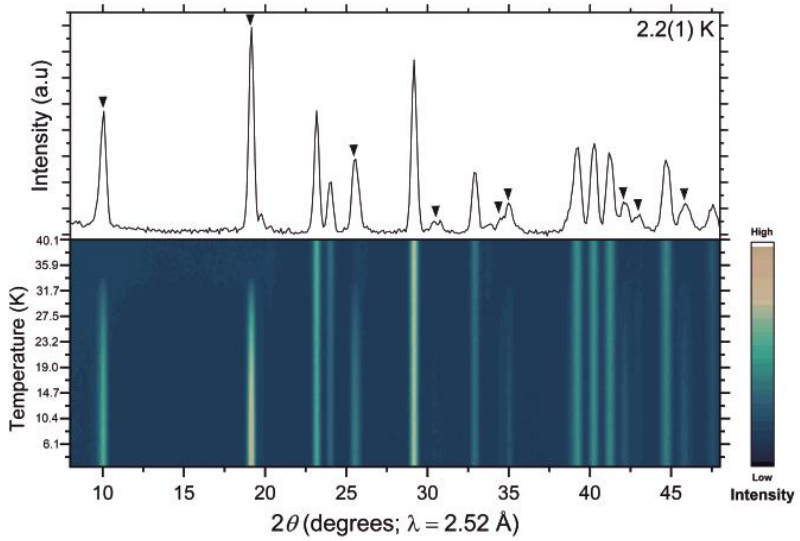


Figure 6.22: Plot of the NPD data collected for Ba_2FeBiS_5 from 2 K to 40 K on the D1B instrument at the ILL. The black triangles denote magnetic reflections with $k = (^1/_2\ 0\ ^1/_2)$.

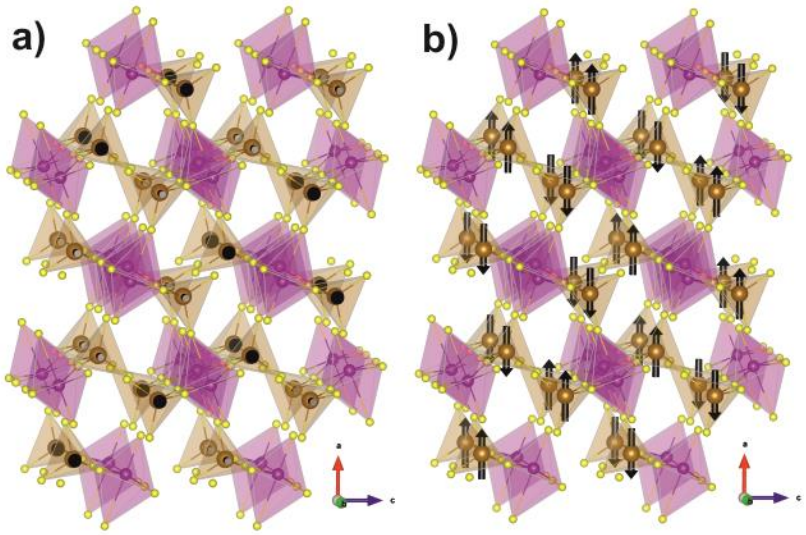


Figure 6.23: Magnetic models for **a)** Ba_2FeSbS_5 and **b)** Ba_2FeBiS_5. In **a)** moments coloured black are directed towards the reader and moments coloured grey are directed away from the reader.

The arrangement of the Fe^{3+} spins, as summarised in Figure 6.23, is dictated by a number of magnetic interactions. In Figures 6.11 and 6.19 the magnetic interactions acting over the four shortest distances are shown. It can be seen in these diagrams that the distances over which the interactions act have lengths where $J_1 < J_2 < J_3 < J_4$. Koo and Whangbo[9] concluded from their computational studies on these two materials that the strongly interacting spin exchange pathways are J_1, J_2 and J_3, therefore these interactions should dictate the long-range magnetic ordering to the greatest degree. The J_1

interactions, which act over the shortest distance, are always antiferromagnetic and they form 1D chains which run along the *b*-direction. All three of the J_1, J_2 and J_3 exchanges are predicted to preferably be antiferromagnetic exchanges, therefore there exists magnetic frustration in (J_1 J_2 J_3) exchange triangles, an example of which is highlighted by the black triangle in Figure 6.24. Koo and Whangbo[9] also conclude that the lower T_N for Ba_2FeSbS_5 arises due to a greater extent of spin frustration in the (J_1 J_2 J_3) triangles in this material compared to Ba_2FeBiS_5, originating from their finding that J_2 and J_3 are much closer in magnitude to J_1 in the Ba_2FeSbS_5 case compared to the Ba_2FeBiS_5 case. Furthermore, thinking about the findings from the NPD data, it could be the case that the additional incommensurate ordering observed in the Ba_2FeSbS_5 material could be a means of easing these highly frustrated (J_1 J_2 J_3) triangles.

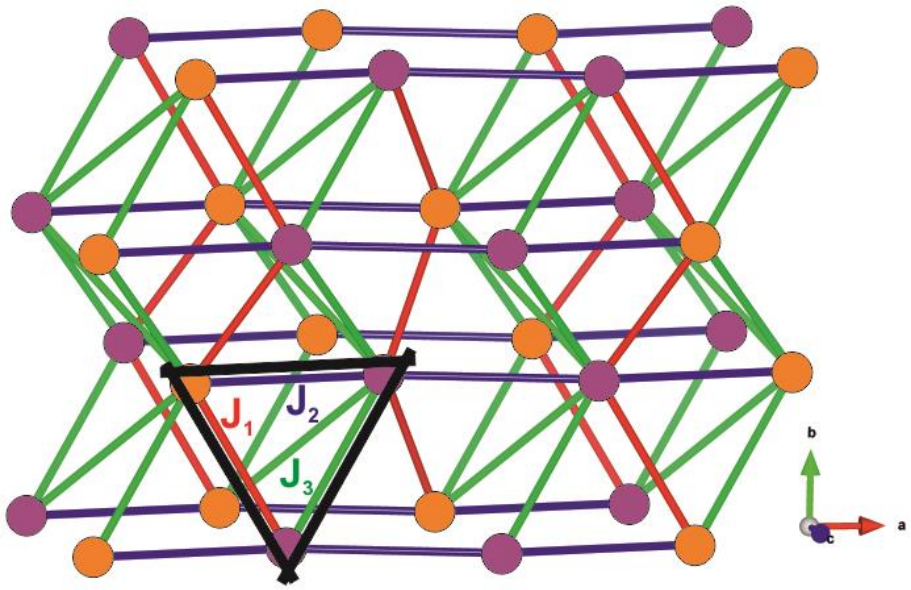


Figure 6.24: Magnetic model for the Ba_2FeMS_5 (M = Sb, Bi) materials. The three shortest Fe-Fe distances are J_1: red; J_2: blue; J_3: green, and where $J_1 < J_2 < J_3$. The black triangle highlights an example of a (J_1 J_2 J_3) exchange triangle. The purple and orange dots indicate Fe moments which are collinear and parallel (if they are labelled by the same colour) or collinear and antiparallel (if they are labelled by different colours).

The J_1 pathways operate via Fe-S…S-Fe super-superexchange, involving Fe 3*d* orbitals (occupied by one electron) and S 3*p* orbitals, which result in an exchange that is antiferromagnetic in nature as depicted in Figure 6.25. The arrangement of the atoms and bonds in this super-superexchange interaction operating along the J_1 pathways, as well as those operating along the J_2 and J_3 pathways, are shown in Figure 6.26. The J_2 pathways also operate over similar Fe-S…S-Fe super-superexchange pathways, as depicted in Figure 6.26b). The J_3 pathway can either be viewed once again as similar Fe-S…S-Fe super-superexchange or as a Fe-S-M-S-Fe super-superexchange, as illustrated in Figure 6.26c). Initial findings on Ba_2FeMSe_5 (M = Sb, Bi) presented by Wang *et al*.[10] give T_N = 58(1) K for $Ba_2FeSbSe_5$ and T_N = 79(2) K for $Ba_2FeBiSe_5$ which are much higher than for either sulfide compound, owing to the stronger super-superexchange interactions along the J_1 Fe-Se…Se-Fe pathways compared to Fe-S…S-Fe pathways. This arises because of the greater degree of covalency in the selenide compound as the Se 4*p* orbitals are more radially extended than the S 3*p* orbitals.

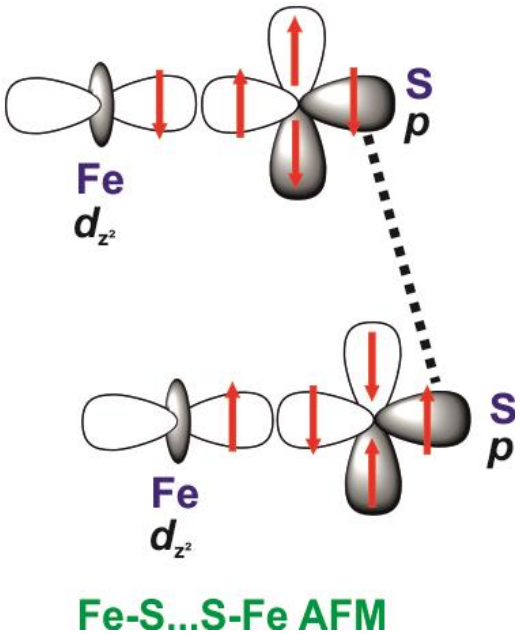


Figure 6.25: The Fe 3*d* and S 3*p* orbitals involved in the Fe-S…S-Fe super-superexchange interactions. These interactions acting along the J_1 pathway are likely to be the driving force for the antiferromagnetic ordering observed in the Ba_2FeMS_5 (M = Sb, Bi) materials. The diagram depicts these orbitals in their relative arrangements as they exist in the structures.

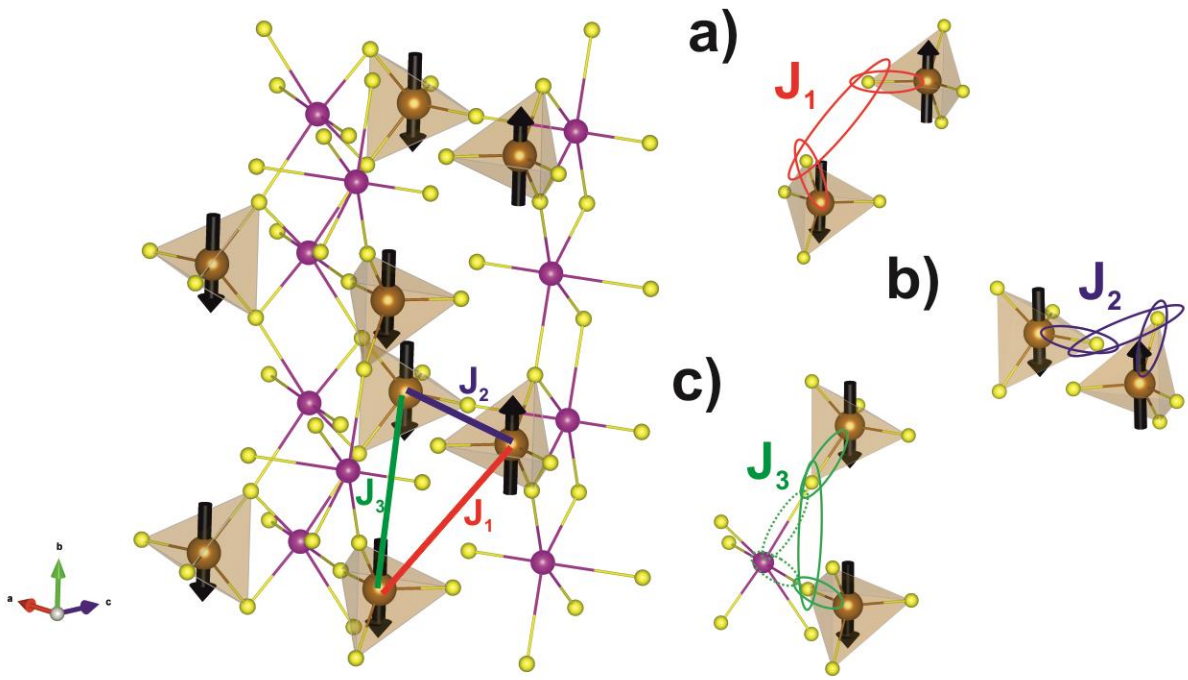


Figure 6.26: Magnetic model for Ba_2FeSbS_5, showing the connecting Sb (purple) and S (yellow) atoms between the Fe (brown) centres. The super-superexchange interactions, as discussed by Koo and Whangbo,[9] highlighted are **a)** the Fe-S…S-Fe J_1 pathway (solid red ovals) **b)** the Fe-S…S-Fe J_2 pathway (blue solid ovals) and **c)** the Fe-S…S-Fe J_3 pathway (solid green ovals) and the Fe-S-Sb-S-Fe J_3 pathway (via dashed green ovals).

The arrangement of antiferromagnetic and ferromagnetic exchanges we find in our magnetic model for Ba_2FeBiS_5 (Figure 6.23b)) is predicted to be the most energetically stable for all values of the on-site repulsion, U, according to the aforementioned computational studies performed by Koo and Whangbo[9] (where the values of U considered were 1.5, 2.5, 3.0, 4.0 and 5.0 eV). In contrast, for Ba_2FeSbS_5, Koo and Whangbo[9] predict competition between the model we have found (Figure 6.23a)) and a model with an alternative spin arrangement - one where not all J_1 are antiferromagnetic but instead every J_2 is antiferromagnetic. The model we find experimentally in Figure 6.23a) is favoured when U is larger (4.0 and 5.0 eV) and the competing model is favoured when U is small (1.5, 2.5 and 3.0 eV). It is perhaps the case here that our model is further stabilised by the incommensurate ordering (which would not have been considered in the computational calculations) or maybe the value of U in this compound is closer to 4.0 - 5.0 eV.

6.4 Discussion

6.4.1 Crystal Structure

As previously discussed in section 1.3.2, compounds with the general formula $Ae_2M_AM_BCh_5$ have been known to crystallise in both the centrosymmetric *Pnma* structure, as exhibited by the compounds studied in this chapter as well as Ba_2GaBiS_5,[11] and the non-centrosymmetric $Cmc2_1$ structure, as exhibited by Ba_2InBiS_5.[11] Both structures are composed of the same transition metal/triel sulfide tetrahedra and pnictogen sulfide distorted octahedra, however they each contain these polyhedra in different arrangements. Using the Ba_2GaBiS_5 and Ba_2InBiS_5 compounds studied by Geng *et al*.[11] as examples, Figure 6.27 shows how the infinite 1D chains are in a 'trans' arrangement for $[GaBiS_5]^{4-}$ chains but are in a 'cis' arrangement for $[InBiS_5]^{4-}$ chains. This results in the centrosymmetric structure type being non-polar and the non-centrosymmetric structure being polar, due to these arrangements of the lone pair local dipole moments. Interestingly, Cassidy *et al*.[12] report the coexistence of two polymorphs of CaFeSeO which adopt the same two space groups- *Pmcn* and $Cmc2_1$.

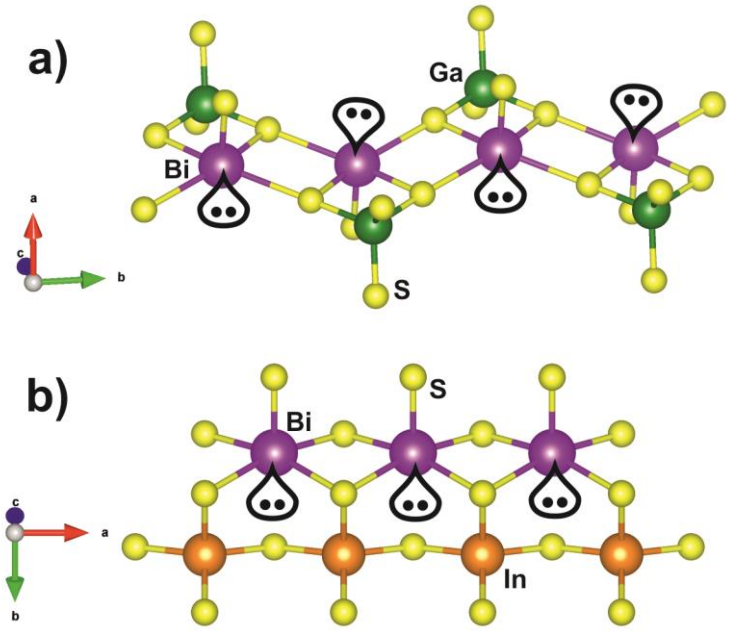


Figure 6.27: The arrangement of the polyhedra which form the 1D chains in **a)** centrosymmetric Ba_2GaBiS_5 and **b)** non-centrosymmetric Ba_2InBiS_5. The likely position of the electron lone pair on the Bi^{3+} cation is shown, highlighting the non-polar nature of 'trans' Ba_2GaBiS_5 and the polar nature of 'cis' Ba_2InBiS_5, due to the relative orientations of these lone pairs.

The lone electron pair on the pnictogen cation in Ba_2FeSbS_5 and Ba_2FeBiS_5 may be most accurately described as being 'partially stereoactive' rather than 'fully stereoactive'. This is because the coordination around the pnictogen cation contains some shorter (primary) bonds and some longer (secondary) bonds, as discussed in section 1.3.2. Considering valence shell electron pair repulsion (VSEPR) theory, it seems highly probable that the lone pair should be directed in the apparent 'space' created by the three longest bonds in the coordination sphere- the two M-S1b bonds and the M-S3 bond. This is summarised in Figure 6.28.

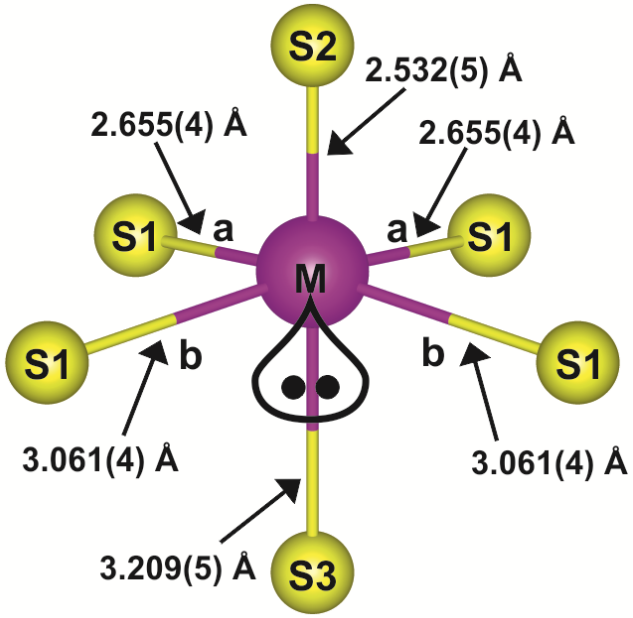


Figure 6.28: The coordination of the sulfide anions around the pnictogen, M, cation centre in the Ba_2FeMS_5 (M = Sb, Bi) compounds. The lone electron pair is likely to be positioned between the three longer bonds (the two M-S1b bonds and the M-S3 bond) due to VSEPR theory. The bond lengths detailed here are those refined for Ba_2FeBiS_5, as given in Table 6.1 in section 6.3.1.

Table 6.2 compares the bond lengths of the M*Ch*$_6$ environments in the Ba_2FeMS_5 and Ba_2FeMSe_5 (M = Sb, Bi) compounds. The ratio of M-*Ch*2/M-*Ch*3 can be used as a way of comparing the degree of distortion in this environment away from perfectly octahedral, as this is the ratio of the shortest M-*Ch* bond to the longest M-*Ch* bond. The Bi analogues are less distorted than the Sb analogues, presumably because the Bi 6*s* orbital is lower in energy than the Sb 5*s* orbital energy, which means the lone pair in the *s*-orbital is less stereoactive. It should be made clear though that the degree of distortion does not differ very significantly between the Sb and Bi analogues.

Compound	M-*Ch*1[a] (Å)	M-*Ch*1[b] (Å)	M-*Ch*2 (Å)	M-*Ch*3 (Å)	M-*Ch*2/M-*Ch*3
Ba_2FeSbS_5	2.499(3)	3.136(3)	2.424(4)	3.241(4)	0.748(3)
Ba_2FeBiS_5	2.655(4)	3.061(4)	2.532(5)	3.209(5)	0.789(3)
$Ba_2FeSbSe_5$	2.6514(6)	3.2467(6)	2.5740(9)	3.3128(9)	0.777(1)
$Ba_2FeBiSe_5$	2.7767(7)	3.2008(7)	2.669(1)	3.301(1)	0.809(1)

Table 6.2: The M-*Ch* bond lengths for the Ba_2FeMS_5 and Ba_2FeMSe_5 (M = Sb, Bi) compounds. The data for $Ba_2FeSbSe_5$ and $Ba_2FeBiSe_5$ are reported by Wang *et al*.[10]

6.4.2 Magnetic Structure

The long-range magnetic ordering in these materials appears to be driven by Fe-S…S-Fe super-superexchange pathways, rather than the Fe-O-M-O-Fe super-superexchange interactions (where such pathways are also seen in the Sr_2FeWO_6[13] and Sr_2MgOsO_6[14] double perovskites). This interaction occurs over a relatively long distance, which means the electron coupling between the two Fe^{3+} centres is weak, and this is likely to be the reason behind the very low Néel temperatures. The potential onset of metamagnetism displayed in the 5 K magnetisation isotherms at high field shown in Figure 6.5b) and Figure 6.6b) in section 6.3.2 may also be a consequence of the weak antiferromagnetic coupling. Perhaps the super-superexchange interactions begin to be overcome when high magnetic fields (approximately greater than 3 T, inferred from the upturn in magnetic susceptibility in Figures 6.5b) and 6.6b)) are applied to the sample, forcing more of the spins to align with the field. This could be explored further using magnetometry and neutron powder diffraction in high magnetic fields.

One major difference between the Ba_2FeSbS_5 and Ba_2FeBiS_5 magnetic models is that the moment orientations differ in the two systems reflecting the fact that the Fe^{3+} d^5 S = 5/2 ion has a magnetic moment with a weak directional preference. Whangbo *et al*.[15] use spin-orbit coupling arguments to predict the preferred moment directions of magnetic ions and they suggest that high-spin d^5 ions only possess a very small orbital momentum which results in these ions exhibiting only weakly preferred spin directions. It appears to be the case that subtle structural differences between the two crystal structures result in one orientation being preferred over the other in such a finely balanced system.

The long-range magnetic ordering which exists in the analogous $Ba_2FeSbSe_5$ selenide compound has been probed using NPD studies by Maier *et al*.[16] They find a magnetic model similar to that shown in Figure 6.23a) for Ba_2FeSbS_5, where the Fe^{3+} moments are aligned along the *b*-axis. However, in the case of the selenide, there is no evidence from the data[16] for an incommensurately modulated component to the ordering of the moments. This would have been observed if present as the data

were gathered using a diffractometer with comparable *d*-spacing coverage, resolution and signal-to-noise ratio to D1B (beamline G4.1, Saclay, France; neutron wavelength, $\lambda = 2.426$ Å). Perhaps the longer Fe-Fe distances in $Ba_2FeSbSe_5$[16] compared to Ba_2FeSbS_5 result in less spin frustration in the (J_1 J_2 J_3) triangles and therefore the incommensurate ordering is lost.

Table 6.3 summarises the Fe-*Ch* and *Ch*…*Ch* distances present in the Ba_2FeMS_5 and Ba_2FeMSe_5 (M = Sb, Bi) compounds, along with the total Fe-*Ch*…*Ch*-Fe distances which are involved in the J_1 super-superexchange pathways. It can be seen for both the sulfide and selenide cases that the antiferromagnetic ordering temperature, T_N, is higher in the Bi analogue compared to the Sb analogue. This can be attributed to the shorter Fe-*Ch*…*Ch*-Fe overall distance and especially the *Ch*…*Ch* distance, which is likely to increase orbital overlap between the chalcogenide 3*p*/4*p* orbitals and therefore result in stronger Fe-*Ch*…*Ch*-Fe super-superexchange interactions. The greater difference in T_N between the sulfide and selenide analogues, when comparing compounds containing the same pnictogen cation, is likely to arise due to the higher degree of covalency in the Fe-Se bonds compared to the Fe-S bonds involved the Fe-*Ch*…*Ch*-Fe pathways, in addition to the shorter *Ch*…*Ch* distances present in the J_1 pathway. This higher degree of covalency in the selenide case compared to the sulfide case means that the J_1 exchanges would be predicted to be stronger for the selenides, thus increasing T_N.

Compound	Fe-*Ch* for J_1 (Å)	*Ch*…*Ch* for J_1 (Å)	Fe-*Ch*…*Ch*-Fe for J_1 (Å)	T_N (K)
Ba_2FeSbS_5	2.193(5), 2.286(3)	3.734(4)	8.213(12)	12.1(10)
Ba_2FeBiS_5	2.170(6), 2.289(4)	3.694(5)	8.153(15)	34.5(10)
$Ba_2FeSbSe_5$	2.3351(13), 2.4106(8)	3.6846(8)	8.430(3)	58(1)
$Ba_2FeBiSe_5$	2.3360(16), 2.4065(11)	3.6626(10)	8.405(4)	79(2)

Table 6.3: The Fe-*Ch*, *Ch*…*Ch* and Fe-*Ch*…*Ch*-Fe distances involved in the J_1 pathway, along with the T_N, for the Ba_2FeMS_5 and Ba_2FeMSe_5 (M = Sb, Bi) compounds. The data for $Ba_2FeSbSe_5$ and $Ba_2FeBiSe_5$ are reported by Wang *et al*.[10]

6.5 Conclusions

This study has investigated the structure and long-range magnetic ordering of the Ba_2FeSbS_5 and Ba_2FeBiS_5 quaternary sulfides.

Ba_2FeSbS_5 and Ba_2FeBiS_5 have been synthesised as black powders with extremely high purity. They contain Fe^{3+} in FeS_4 tetrahedra and M^{3+} (M = Sb, Bi) in MS_6 distorted octahedra. The MS_6 polyhedra are edge-sharing and also share edges with the FeS_4 polyhedra, which are positioned in an alternating manner along the MS_6 polyhedral chains. The unusual coordination of the sulfide anions around the Sb and Bi centres is a product of the lone electron pair on these cations possessing some degree of stereoactivity, which arises due to a 2nd order Jahn-Teller distortion involving n*s*/n*p* mixing mediated by the anion valence orbitals.

High-resolution NPD data gathered on Ba_2FeSbS_5 and Ba_2FeBiS_5 reveal that both of these compounds exhibit long-range antiferromagnetic ordering with Néel temperatures of 12.1(10) K and 34.5(10) K respectively. The magnetic Bragg peaks are positioned with a k-vector of $k = (1/2\ 0\ 1/2)$. The Fe^{3+} ordered moments in these two materials are directed perpendicular to each other- in Ba_2FeSbS_5 spins order parallel to the *b*-axis and in Ba_2FeSbS_5 spins order parallel to the *a*-axis. The arrangement of the Fe^{3+} moments in the magnetic models can be rationalised by considering that J_1 – the strongest magnetic interaction (as predicted by computation[9]) and the interaction which acts over the shortest Fe-Fe distance – is always antiferromagnetic. This interaction acts along Fe-S…S-Fe (M = Sb, Bi) super-superexchange pathways. There is an incommensurately modulated addition to the commensurate long-range magnetic ordering in Ba_2FeSbS_5, suggested by the presence of two low intensity magnetic reflection in the D1B data. Such reflections were not seen for the Ba_2FeBiS_5 material. These reflections can be accounted for by introducing an additional, incommensurately modulated spin-density wave to the commensurate antiferromagnetic ordering of the Fe^{3+} spins. These peaks also appear to share a common Néel temperature with the commensurate magnetic Bragg peaks. The origin of this extra modulation in the magnetic ordering in Ba_2FeSbS_5 is unclear and requires further investigation,

although it may be related to the fact that the magnetic structure is inherently frustrated, and that computation suggests some competition between different magnetic ground states in that compound.

References

(1) Geng, L.; Cheng, W. D.; Zhang, H.; Lin, C. S.; Zhang, W. L.; Li, Y. Y.; He, Z. Z. Syntheses, Crystal and Electronic Structures, and Characterizations of Quaternary Antiferromagnetic Sulfides: Ba_2MFeS_5 (M = Sb, Bi). *Inorg. Chem.* **2011**, *50* (6), 2378–2384. https://doi.org/10.1021/ic102597y.

(2) Lemley, J. T.; Jenks, J. M.; Hoggins, J. T.; Eliezer, Z.; Steinfink, H. $Ba_{15}Fe_7S_{25}$ and Ba_3FeS_5: Crystal Structures, Mössbauer, Magnetic, and Electrical Behavior. *J. Solid State Chem.* **1976**, *16* (1–2), 117–128. https://doi.org/10.1016/0022-4596(76)90013-X.

(3) Brown, I. D.; Altermatt, D. Bond-valence Parameters Obtained from a Systematic Analysis of the Inorganic Crystal Structure Database. *Acta Crystallogr. Sect. B* **1985**, *41* (4), 244–247. https://doi.org/10.1107/S0108768185002063.

(4) Payne, D. J.; Egdell, R. G.; Walsh, A.; Watson, G. W.; Guo, J.; Glans, P. A.; Learmonth, T.; Smith, K. E. Electronic Origins of Structural Distortions in Post-Transition Metal Oxides: Experimental and Theoretical Evidence for a Revision of the Lone Pair Model. *Phys. Rev. Lett.* **2006**, *96* (15). https://doi.org/10.1103/PhysRevLett.96.157403.

(5) Donnay, G.; Corliss, L. M.; Donnay, J. D. H.; Elliott, N.; Hastings, J. M. Symmetry of Magnetic Structures: Magnetic Structure of Chalcopyrite. *Phys. Rev.* **1958**, *112* (6), 1917–1923. https://doi.org/10.1103/PhysRev.112.1917.

(6) Woolley, J. C.; Lamarche, A. M.; Lamarche, G.; Quintero, M.; Swainson, I. P.; Holden, T. M. Low Temperature Magnetic Behaviour of $CuFeS_2$ from Neutron Diffraction Data. *J. Magn. Magn. Mater.* **1996**, *162* (2–3), 347–354. https://doi.org/10.1016/S0304-8853(96)00252-1.

(7) Tomkowicz, Z.; Szytuła, A. Crystal and Magnetic Structure of $KFeO_2$. *J. Phys. Chem. Solids* **1977**, *38* (10), 1117–1123. https://doi.org/10.1016/0022-3697(77)90037-3.

(8) Sheptyakov, D.; Ali, N. Z.; Jansen, M. A Neutron Diffraction Study of Structural and Magnetic Transformations in $AFeO_2$ (A = K, Rb and Cs). *J. Phys. Condens. Matter* **2010**, *22* (42), 426001. https://doi.org/10.1088/0953-8984/22/42/426001.

(9) Koo, H. J.; Whangbo, M. H. Density Functional Investigation of Why Ba_2BiFeS_5 and Ba_2SbFeS_5 Differ in Their Magnetic Properties. *J. Magn. Magn. Mater.* **2014**, *360*, 152–156. https://doi.org/10.1016/j.jmmm.2014.02.024.

(10) Wang, J.; Greenfield, J. T.; Kovnir, K. Synthesis, Crystal Structure, and Magnetic Properties of Quaternary Iron Selenides: $Ba_2FePnSe_5$ (Pn=Sb, Bi). *J. Solid State Chem.* **2016**, *242*, 22–27. https://doi.org/10.1016/j.jssc.2015.12.030.

(11) Geng, L.; Cheng, W. D.; Lin, C. S.; Zhang, W. L.; Zhang, H.; He, Z. Z. Syntheses and Characterization of New Mid-Infrared Transparency Compounds: Centric Ba_2BiGaS_5 and Acentric Ba_2BiInS_5. *Inorg. Chem.* **2011**, *50* (12), 5679–5686. https://doi.org/10.1021/ic2004358.

(12) Cassidy, S. J.; Batuk, M.; Batuk, D.; Hadermann, J.; Woodruff, D. N.; Thompson, A. L.; Clarke, S. J. Complex Microstructure and Magnetism in Polymorphic CaFeSeO. *Inorg. Chem.* **2016**, *55* (20), 10714–10726. https://doi.org/10.1021/acs.inorgchem.6b01951.

(13) Kawanaka, H.; Hase, I.; Toyama, S.; Nishihara, Y. Electronic State of Fe in Double Perovskite Oxide Sr_2FeWO_6. *J. Phys. Soc. Japan* **1999**, *68* (9), 2890–2893. https://doi.org/10.1143/JPSJ.68.2890.

(14) Yuan, Y.; Feng, H. L.; Ghimire, M. P.; Matsushita, Y.; Tsujimoto, Y.; He, J.; Tanaka, M.; Katsuya, Y.; Yamaura, K. High-Pressure Synthesis, Crystal Structures, and Magnetic Properties of 5d Double-Perovskite Oxides Ca_2MgOsO_6 and Sr_2MgOsO_6. *Inorg. Chem.* **2015**, *54* (7), 3422–3431. https://doi.org/10.1021/ic503086a.

(15) Whangbo, M. H.; Gordon, E. E.; Xiang, H.; Koo, H. J.; Lee, C. Prediction of Spin Orientations in Terms of HOMO-LUMO Interactions Using Spin-Orbit Coupling as Perturbation. *Acc. Chem. Res.* **2015**, *48* (12), 3080–3087. https://doi.org/10.1021/acs.accounts.5b00408.

(16) Maier, S.; Gaultois, M. W.; Matsubara, N.; Surta, W.; Damay, F.; Hebert, S.; Hardy, V.; Berthebaud, D.; Gascoin, F. Sb-5s Lone Pair Dynamics and Collinear Magnetic Ordering in $Ba_2FeSbSe_5$. *Phys. Rev. B* **2021**, *103* (5), 54115. https://doi.org/10.1103/PhysRevB.103.054115.

Chapter 7

7 Final Conclusions

This thesis explores the synthesis and characterisation of the $Ca_2FeO_2Fe_{1.6}OS_2$, $Ca_2FeO_2Fe_{1.65}OS_{1.5}Se_{0.5}$, $Ca_2FeO_2Fe_{1.7}OSSe$ and $Ca_2FeO_2Fe_{1.75}OS_{0.5}Se_{1.5}$ oxychalcogenides; $Sr_2CrO_2Cr_2OAs_2$ oxypnictide; and Ba_2FeMS_5 (M = Sb, Bi) chalcogenides.

Chapter 3 discusses the problematic determination of the $Ca_2FeO_2Fe_{1.6}OS_2$ superstructure, where the final solution contains Fe vacancies in the Fe2 FeO_2S_4 layer accompanied by distortion of the neighbouring Fe and O atoms in the *ab*-plane, all in *Aea*2 symmetry. Low temperature NPD data reveal a subtle distortion of the FeO_4 sheets in the Fe1 FeO_4S_2 layer, the nature of which can be described as 'antiphase twisting' and is similar to that seen in perovskite compounds. This distortion is likely to have complicated the structure solution, as well as twinning exhibited in the crystals measured using SCXRD and ED. Bond valence sums strongly suggest that the vertex-sharing FeO_4S_2 distorted octahedra contain Fe^{3+}, whereas the face-sharing FeO_2S_4 distorted octahedra host Fe^{2+}. A number of results- including those from XRPD refinements, NPD refinements, TEM-EDX data and the presence of low amounts of impurities- suggest that the stoichiometry of Fe in the Fe2 FeO_2S_4 layer is less than the 1.6 proposed by Zhang *et al.*[1] and is more likely to be closer to 1.5. Two long-range antiferromagnetic ordering transitions are apparent in the NPD data. The higher temperature transition occurs at 330(10) K and involves concurrent ordering of the Fe moments in the Fe1 and Fe2 layers, with $k = (0,0,0)$ with respect to the supercell. The ordering pattern on both Fe sublattices contains moments directed in the *ab*-plane and ensures that all Fe-O-Fe superexchange pathways are antiferromagnetic. The lower temperature ordering transition occurs at 70 K and is proposed to arise due to canting of all the Fe moments in the system. The moments per Fe at 5 K refine to 3.77(7) μ_B in the Fe1 layer and 2.53(8) μ_B in the Fe2 layer suggesting these contain high spin Fe^{3+} d^5 and high spin

Fe^{2+} d^6 respectively. A structural signature which accompanies this ordering transition may be due to a small degree of electron transfer from the Fe^{2+} in the Fe2 layer to the Fe^{3+} in the Fe1 layer.

Chapter 4 focusses on the solid solution phases $Ca_2FeO_2Fe_{1.65}OS_{1.5}Se_{0.5}$, $Ca_2FeO_2Fe_{1.7}OSSe$ and $Ca_2FeO_2Fe_{1.75}OS_{0.5}Se_{1.5}$. XRPD data show no evidence of long-range ordering of the Fe vacancies in the Fe2 layer (agreeing with the initial report by Zhang *et al.*[1]) and as the proportion of the larger Se^{2-} anion included in the structure increases, more Fe is incorporated into this layer, resulting in fewer Fe vacancies and a slight reduction of the Fe^{3+} in the Fe1 layer, as seen in the bond valence sum trend. The average structure of these materials can be described by a basic unit cell with *P*4/*mmm* symmetry. The low temperature magnetic models are comparable to each other and that proposed for $Ca_2FeO_2Fe_{1.6}OS_2$ in Chapter 3 (see Figure 7.1) with ordering in both Fe layers satisfying the condition of antiferromagnetic Fe-O-Fe superexchange pathways. As the ratio of S:Se varies towards a higher proportion of Se, the Fe1 saturated moment decreases due to the slight reduction of the Fe^{3+} ions as more Fe is incorporated into the structure, whereas the Fe2 saturated moment increases due to the decreasing vacancy concentration in this layer which results in stronger long-range magnetic interactions. The $Ca_2FeO_2Fe_{1.75}OS_{0.5}Se_{1.5}$ material is particularly interesting as it exhibits spin-reorientations of the moments on the Fe1 sublattice, both between 5 K and 100 K upon loss of the long-range ordered moments in the Fe2 layer and then between 100 K and 200 K, with the moments orienting fully into in the *ab*-plane from temperatures at and above 200 K.

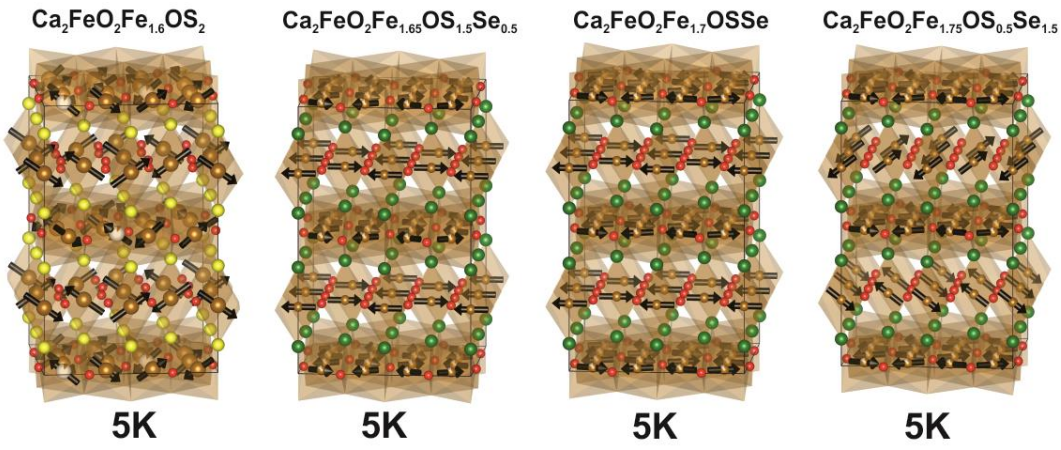


Figure 7.1: The 5 K magnetic models proposed for the compounds studied in Chapters 3 and 4.

Chapter 5 details the initial characterisation of the novel compound $Sr_2CrO_2Cr_2OAs_2$ which proved challenging to obtain in high purity, most likely due to a number of competing phases such as $Sr_2CrO_2Cr_2As_2$, Sr_2CrO_3CrAs and CrAs. Although a mixture of reagents targeting $Sr_2Cr_3O_{2.85}As_2$ was employed, there was no evidence of non-stoichiometry in the final phase. $Sr_2CrO_2Cr_2OAs_2$ is isostructural to the materials investigated in Chapters 3 and 4 however, in contrast to these Fe compounds, the Cr compound contains Cr^{2+} in the oxide-rich CrO_4As_2 environment and Cr^{3+} in the oxide-poor CrO_2As_4 coordination. The Cr^{3+} moments order slightly above 600 K and then the Cr^{2+} moments order at 530(10) K. Moments on both Cr sublattices are directed along the *c*-axis and propagate either along $k = (^1/_2\ ^1/_2\ 0)$ for the case of the Cr1 layer or $k = (0\ 0\ 0)$ for the case of the Cr2 layer. The long-range magnetic order in the Cr1 CrO_4As_2 layer ensures all Fe-O-Fe superexchange pathways are antiferromagnetic, whereas ordering in the Cr2 CrO_2As_4 layer is thought to be dominated by antiferromagnetic direct exchange via the neighbouring Cr^{3+} d_{xz} and d_{yz} orbitals. A subtle structural distortion between 400 K and 500 K could be caused by a small degree of electron transfer from the Cr^{2+} in the Cr1 layer to the Cr^{3+} in the Cr2 layer, comparable to that suspected for $Ca_2FeO_2Fe_{1.6}OS_2$ in Chapter 3.

Chapter 6 furthers the initial study on the quaternary sulfides Ba_2FeSbS_5 and Ba_2FeBiS_5 by Geng *et al*.[2] These crystallise in the *Pnma* space group, where infinite $[FeMS_5]^{4-}$ (M = Sb, Bi) chains are formed, comprising edge-sharing FeS_4 tetrahedra and MS_6 distorted octahedra. The coordination of the sulfide anions around the Sb and Bi centres is likely to be dictated by the lone pair of electrons on these ions and arises due to a 2nd order Jahn-Teller distortion involving n*s*/n*p* mixing mediated by the anion valence orbitals. Ba_2FeSbS_5 and Ba_2FeBiS_5 exhibit long-range antiferromagnetic ordering of the Fe^{3+} moments with Néel temperatures of 12.1(10) K and 34.5(10) K respectively. The magnetic Bragg peaks in the NPD data propagate along $k = (^1/_2\ 0\ ^1/_2)$ and moments in Ba_2FeSbS_5 order along the *b*-direction, whereas moments in Ba_2FeBiS_5 order along the *a*-direction. In both cases, the Fe^{3+} spins order so that the shortest Fe-Fe distances, which act over Fe-S…S-Fe super-superexchange (SSE)

pathways, contain antiferromagnetic Fe moments. In the Ba_2FeSbS_5 case there are small, additional magnetic Bragg peaks which lie on an incommensurate *k*-vector. These can be modelled by superimposing an incommensurately modulated spin-density wave on the commensurately modulated long-range magnetic ordering and may arise due to the greater degree of magnetic frustration in this compound compared to Ba_2FeBiS_5.

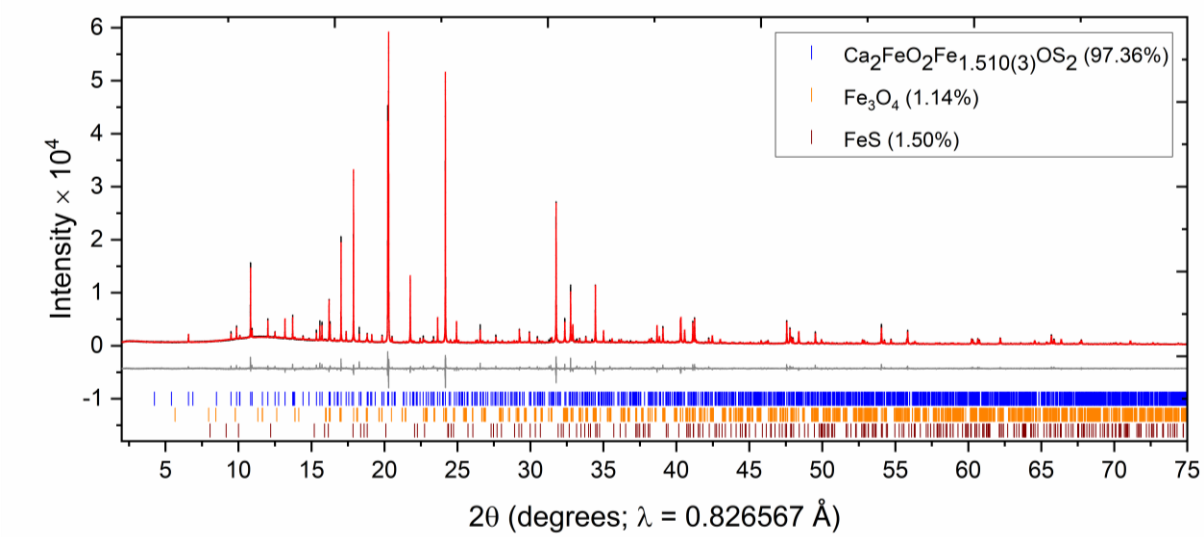
This work emphasises the importance of structure-property relationships in solid-state materials and in particular highlights the influence of crystal structure on long-range magnetic ordering. The findings presented here not only demonstrate the pivotal role that superexchange and super-superexchange pathways often have on the ordering of 3*d* transition metal cation spins, but also that other mechanisms of interaction such as direct exchange cannot be ignored when assessing possible magnetic interactions in a system. These results show how detailed studies into the structure, characterisation and properties of materials are key to a greater understanding of these materials and how they behave.

References

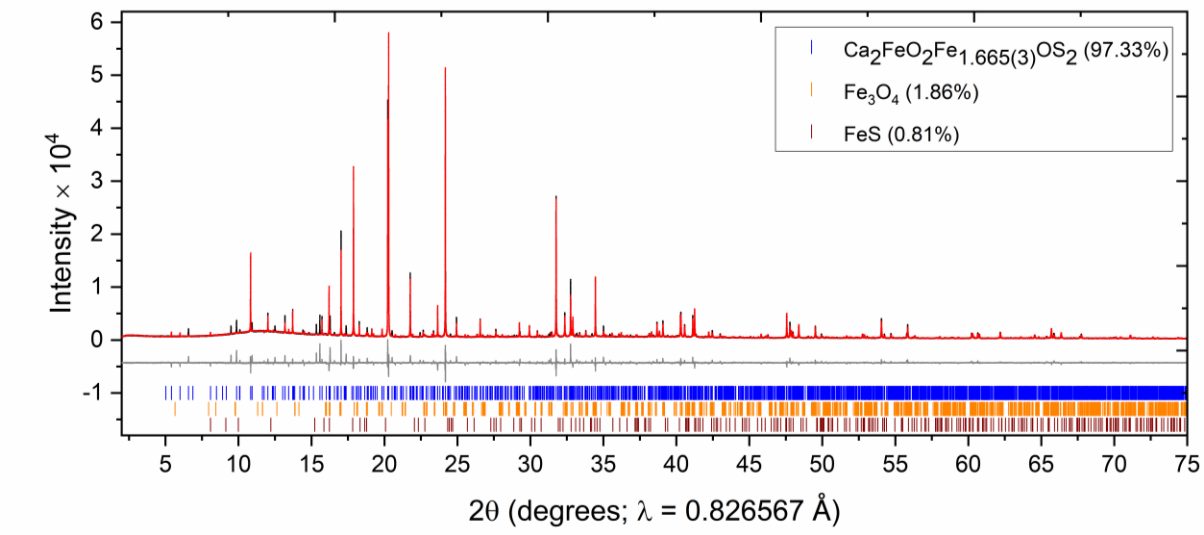
(1) Zhang, H.; Wu, X.; Li, D.; Jin, S.; Chen, X.; Zhang, T.; Lin, Z.; Shen, S.; Yuan, D.; Chen, X. $Ca_2O_3Fe_{2.6}S_2$: An Antiferromagnetic Mott Insulator at Proximity to Bad Metal. *J. Phys. Condens. Matter* **2016**, *28* (14), 145701. https://doi.org/10.1088/0953-8984/28/14/145701.

(2) Geng, L.; Cheng, W. D.; Zhang, H.; Lin, C. S.; Zhang, W. L.; Li, Y. Y.; He, Z. Z. Syntheses, Crystal and Electronic Structures, and Characterizations of Quaternary Antiferromagnetic Sulfides: Ba_2MFeS_5 (M = Sb, Bi). *Inorg. Chem.* **2011**, *50* (6), 2378–2384. https://doi.org/10.1021/ic102597y.

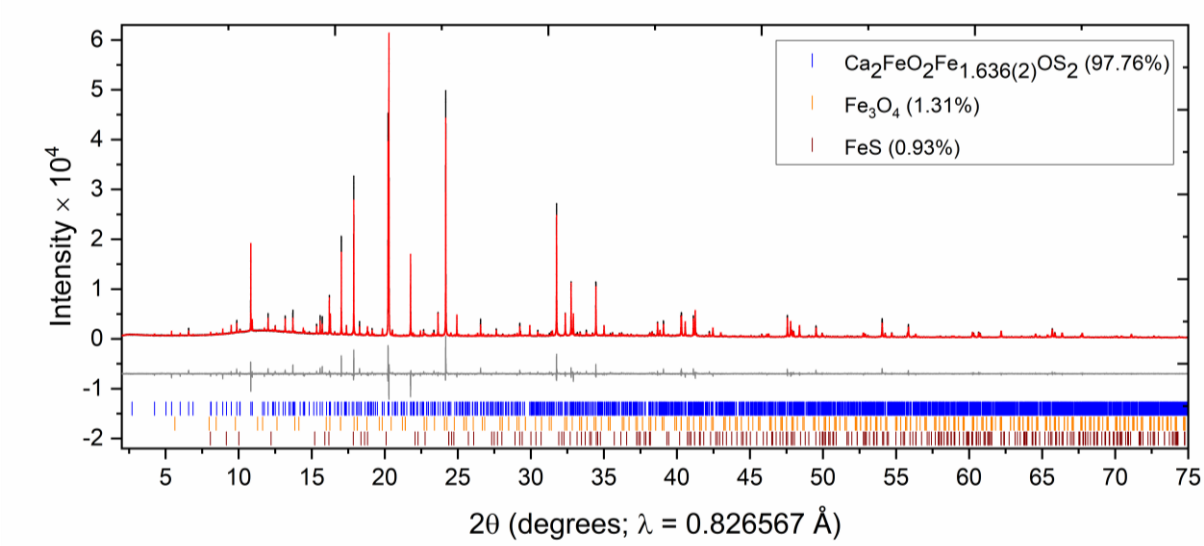
Appendix



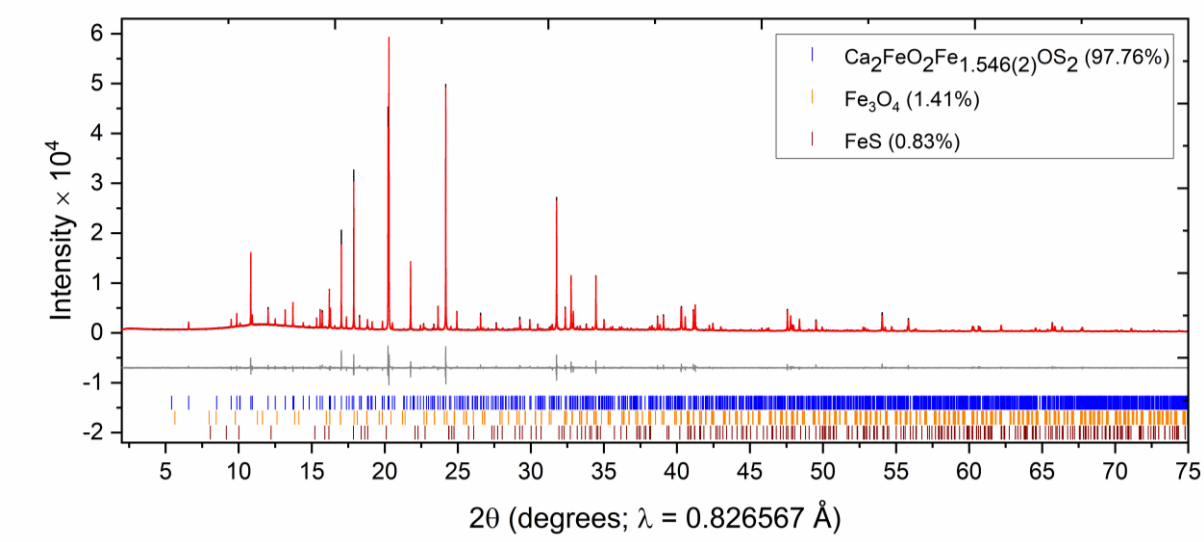
Appendix A.1: Refinement of the *Bmem* superstructure, as suggested by the TEM results, against the XRPD pattern of $Ca_2FeO_2Fe_{1.6}OS_2$ measured at 300 K on the MAC detector at I11 showing the observed (black), calculated (red) and difference (grey) curves. R_{wp}: 7.641%. The fit to the data is good, however in order to achieve this fit the model is refining the occupancies of 3 of the 4 Fe2 sites while the other Fe2 site is fixed to fully occupied. Refinement of only one Fe2 site occupancy gives a poorer fit to the data and also gives a total Fe stoichiometry of 2.705(2) which is unexpectedly high.



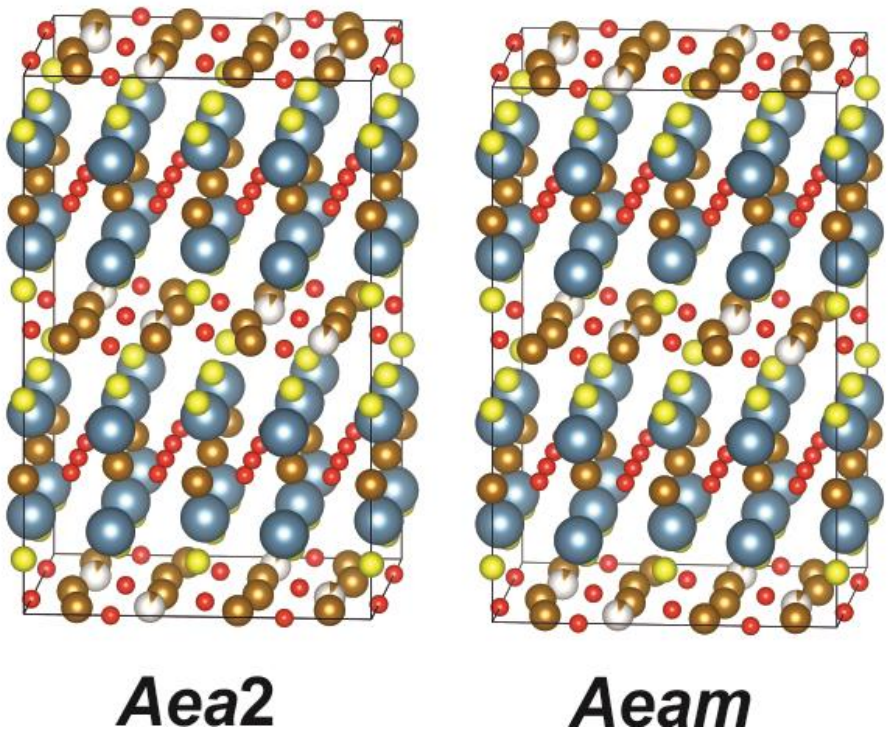
Appendix A.2: Refinement of the *Pnnm* superstructure, as suggested by the SCXRD results, against the XRPD pattern of $Ca_2FeO_2Fe_{1.6}OS_2$ measured at 300 K on the MAC detector at I11 showing the observed (black), calculated (red) and difference (grey) curves. R_{wp}: 10.701%. Compared to models of the supercell in different space groups, the fit of this model to the data is relatively poor.



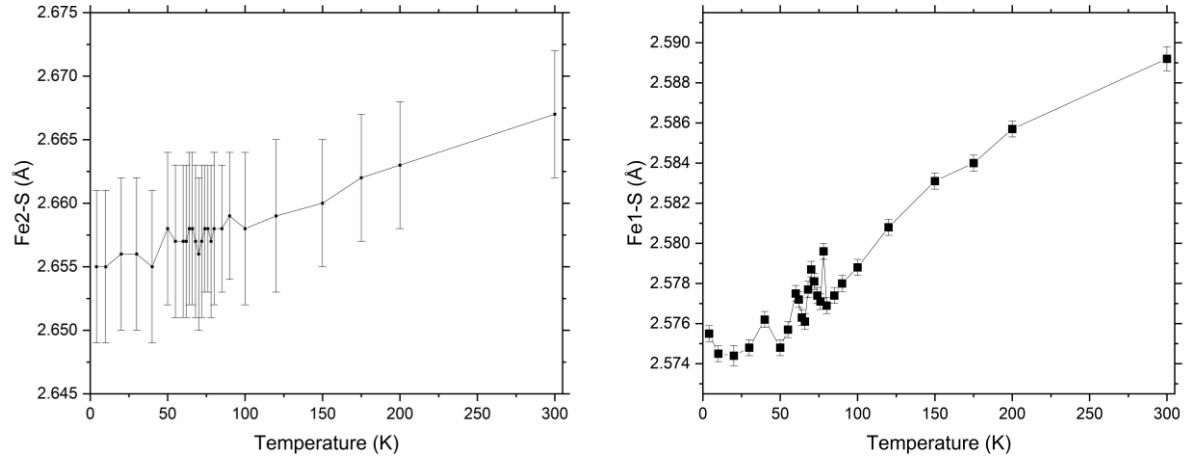
Appendix A.3: Refinement of the superstructure containing the 'theoretically' favoured arrangement of Fe vacancies against the XRPD pattern of $Ca_2FeO_2Fe_{1.6}OS_2$ measured at 300 K on the MAC detector at I11 showing the observed (black), calculated (red) and difference (grey) curves. R_{wp}: 8.714%. The supercell model refined against the data is in *P*1 symmetry with the 'theoretical' arrangement of vacancies in the Fe2 layers, where the pattern of vacancies in adjacent Fe2 layers are translated by (0 ¼ 0) relative to one another. This fit is poorer than the *Aea*2 and *Bmem* models with another issue of this model being that the refined atomic positions are unrealistically far from their starting sites.



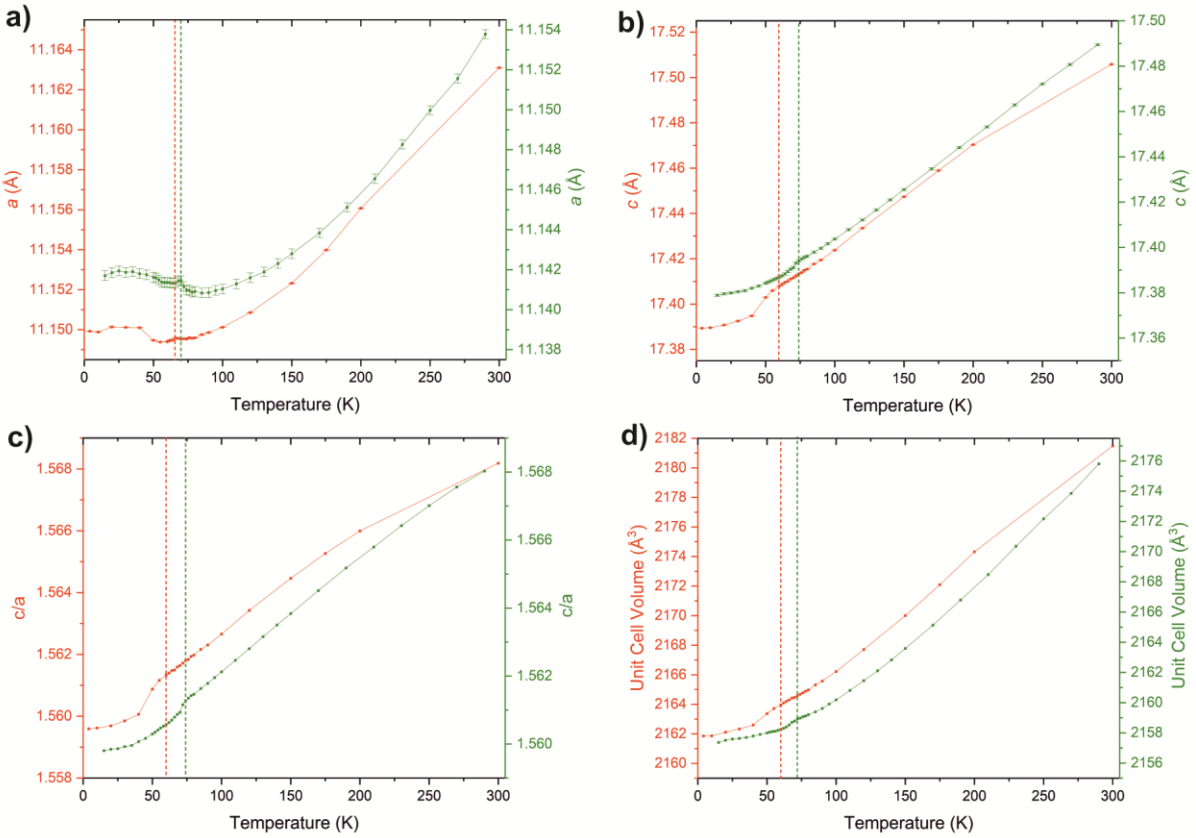
Appendix A.4: Refinement of the *Aeam* superstructure against the XRPD pattern of $Ca_2FeO_2Fe_{1.6}OS_2$ measured at 300 K on the MAC detector at I11 showing the observed (black), calculated (red) and difference (grey) curves. R_{wp}: 6.497%. This is a preliminary refinement where the Fe2 atoms are free to move in the *ab*-plane, the Ca and S are free to move along the *c*-direction and one Fe2 site occupancy is freely refining. Therefore, the quality of this refinement can be directly compared to that of the *Aea*2 refinement given in Figure 3.8 and Table 3.1. The fit to the data is as good as that for the *Aea*2 superstructure and so it is difficult to tell which space group best describes the supercell. In this thesis, *Aea*2 is the supercell symmetry that is used.



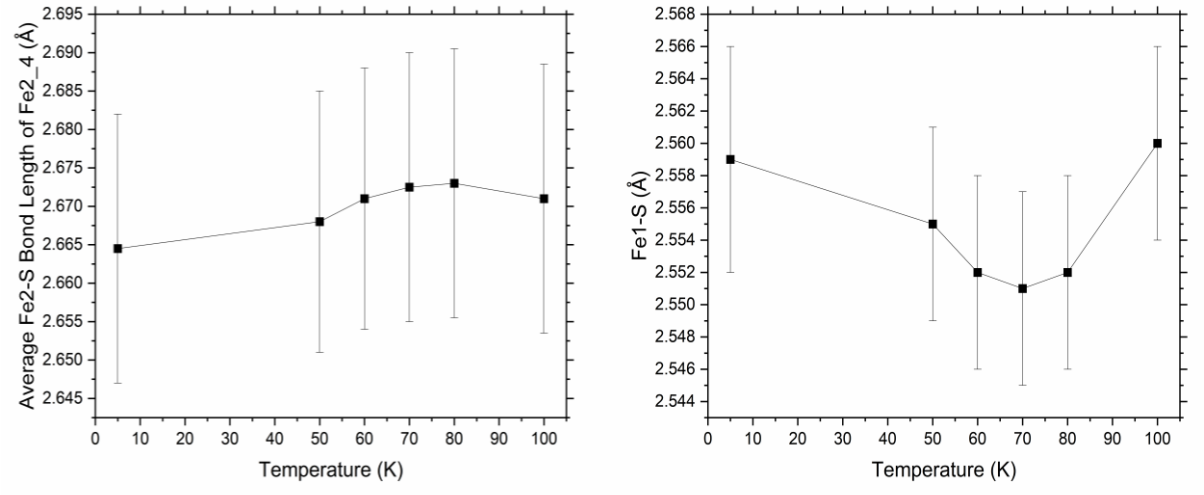
Appendix A.5: Structural models for the $Ca_2FeO_2Fe_{1.6}OS_2$ supercell, refined from the XRPD data gathered on the MAC detector at I11. The models in the two space groups are almost identical, therefore given these two space groups give the best fits to the XRPD data, this arrangement of atoms and Fe2 vacancies is presented as the best structural solution in this thesis.



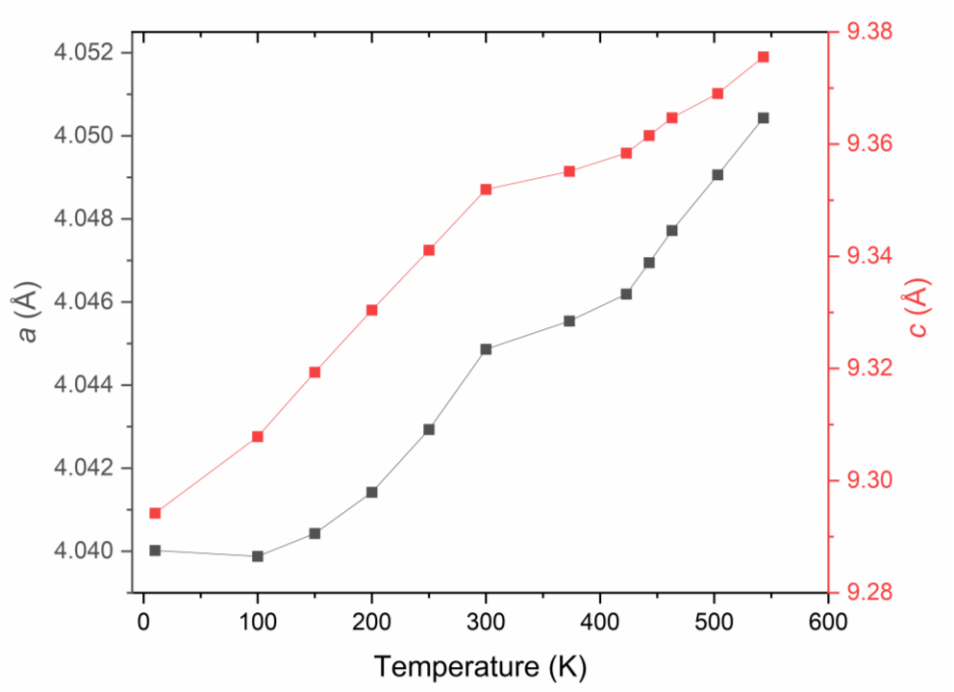
Appendix A.6: The Fe2-S and Fe1-S bond lengths, refined from variable temperature XRPD patterns of $Ca_2FeO_2Fe_{1.6}OS_2$ gathered on the ID22 instrument at the ESRF. The average Fe2-S bond length has been calculated and plotted here. There is significant error on the Fe2-S values and it is perhaps the case that no clear trend is seen for the Fe1-S values because of the many parameters which are allowed to refine in the supercell model (especially the freedom with which the Fe, O and S can move within the Fe2 FeO_2S_4 layers). The errors from these refinements are usually an underestimate too.



Appendix A.7: The variation with temperature of **a)** the *a* lattice parameter **b)** the *c* lattice parameter **c)** the *c*/*a* ratio and **d)** the unit cell volume, refined from variable temperature XRPD patterns of $Ca_2FeO_2Fe_{1.6}OS_2$ gathered on the Malvern Panalytical Empyrean Mo diffractometer with PheniX cryostage (green) and ID22 (red). The features highlighted by the dashed lines occur at lower temperatures for the ID22 results which is likely due to beam heating of the sample.



Appendix A.8: The Fe2-S and Fe1-S bond lengths, refined from variable temperature NPD patterns of $Ca_2FeO_2Fe_{1.6}OS_2$ gathered on the D2B instrument at the ILL. The Fe2-S bond length of the Fe2_4 site has been plotted here as an example. There is significant error on all these Fe1-S and Fe2-S values.



Appendix A.9: The *a* and *c* lattice parameters, refined from NPD data collected at different temperatures on the WISH instrument at ISIS. The error on each value of the lattice parameters is smaller than the width of the corresponding data point. The apparent dip in the value of the moments at 300 K is likely to be an artefact of the different instrument environments upon changing from low temperature data collection to high temperature data collection on the WISH instrument.

Further Rietveld Refinement Details

	$Ca_2FeO_2Fe_{1.6}OS_2$
Diffractometer	D2B (ILL)
Wavelength (Å)	1.594
Temperature (K)	5
Space Group	$P2_12_12$
a (Å)	11.15334(6)[+]
b (Å)	11.15334(6)[+]
c (Å)	17.3957(3)
V (Å^3)	2163.97(4)

$Ca_2FeO_2Fe_{1.6}OS_2$

Atom	Site	*x*	*y*	*z*	Occupancy	U_{iso} (Å^2)
Ca1_1	4*c*	0.25	0	0.15543(16)	1	0.0001(8)
Ca1_2	4*c*	0	0.25	0.15543(16)	1	0.0001(8)
Ca1_3	4*c*	0.5	0.25	0.15543(16)	1	0.0001(8)
Ca1_4	4*c*	0.25	0.5	0.15543(16)	1	0.0001(8)
Ca1_5	4*c*	0.25	0	0.34457(16)	1	0.0001(8)
Ca1_6	4*c*	0	0.25	0.34457(16)	1	0.0001(8)
Ca1_7	4*c*	0.5	0.25	0.34457(16)	1	0.0001(8)
Ca1_8	4*c*	0.25	0.5	0.34457(16)	1	0.0001(8)
Fe1_1	2*a*	0	0	0.25	1	0.0000(6)
Fe1_2	2*b*	0	0.5	0.75	1	0.0000(6)
Fe1_3	4*c*	0.25	0.25	0.25	1	0.0000(6)
Fe1_4	4*c*	0.75	0.25	0.25	1	0.0000(6)
Fe1_5	2*b*	0	0.5	0.75	1	0.0000(6)
Fe1_6	2*a*	0	0	0.25	1	0.0000(6)
Fe2_1	4*c*	0.122(19)	0.107(22)	0	0.093(22)	0.0000(6)
Fe2_2	4*c*	0.138(2)	0.356(3)	0	1	0.0000(6)
Fe2_3	4*c*	0.133(3)	0.626(3)	0	1	0.0000(6)
Fe2_4	4*c*	0.105(2)	0.886(2)	0	1	0.0000(6)
Fe2_5	4*c*	0.151(2)	0.127(2)	0.5	1	0.0000(6)
Fe2_6	4*c*	0.107(2)	0.395(2)	0.5	1	0.0000(6)
Fe2_7	4*c*	0.065(11)	0.694(12)	0.5	0.093(22)	0.0000(6)
Fe2_8	4*c*	0.124(3)	0.866(2)	0.5	1	0.0000(6)
O1_1	4*c*	0.130(5)	0.123(6)	0.25	1	0.0000(8)
O1_2	4*c*	0.114(5)	0.364(8)	0.25	1	0.0000(8)
O1_3	4*c*	0.137(5)	0.611(5)	0.25	1	0.0000(8)
O1_4	4*c*	0.114(4)	0.864(5)	0.25	1	0.0000(8)
O1_5	4*c*	0.380(5)	0.126(6)	0.25	1	0.0000(8)
O1_6	4*c*	0.364(5)	0.386(6)	0.25	1	0.0000(8)
O1_7	4*c*	0.392(4)	0.642(5)	0.25	1	0.0000(8)
O1_8	4*c*	0.372(6)	0.881(5)	0.25	1	0.0000(8)
O2_1	4*c*	0.260(3)	0.987(3)	0	1	0.0000(13)
O2_2	4*c*	0.992(3)	0.254(4)	0	1	0.0000(13)
O2_3	4*c*	0.247(4)	0.997(3)	0.5	1	0.0000(13)
O2_4	4*c*	0.008(3)	0.249(4)	0.5	1	0.0000(13)
S1_1	2*a*	0	0	0.1029(4)	1	0.0040(12)
S1_2	2*b*	0	0.5	0.8971(4)	1	0.0040(12)
S1_3	4*c*	0.25	0.25	0.1029(4)	1	0.0040(12)
S1_4	4*c*	0.25	0.75	0.1029(4)	1	0.0040(12)
S1_5	2*b*	0	0.5	0.1029(4)	1	0.0040(12)
S1_6	2*a*	0	0	0.8971(4)	1	0.0040(12)
S1_7	2*a*	0	0	0.3971(4)	1	0.0040(12)
S1_8	2*b*	0	0.5	0.6029(4)	1	0.0040(12)
S1_9	4*c*	0.25	0.25	0.3971(4)	1	0.0040(12)
S1_10	4*c*	0.25	0.75	0.3971(4)	1	0.0040(12)
S1_11	2*b*	0	0.5	0.3971(4)	1	0.0040(12)
S1_12	2*a*	0	0	0.6029(4)	1	0.0040(12)

For Figure 3.25- Rietveld fit for the NPD pattern of $Ca_2FeO_2Fe_{1.6}OS_2$ measured at 5 K on the D2B instrument at the ILL, using the nuclear model in $P2_12_12$ symmetry. [+]The *a* and *b* lattice parameters were refined together using one variable.

	$Ca_2Fe_{2.65}O_3S_{1.5}Se_{0.5}$
Diffractometer	D2B (ILL)
Wavelength (Å)	1.594
Temperature (K)	5
Space Group	*P*4/*mmm*
a (Å)	3.95643(7)
c (Å)	8.8410(3)
V (Å^3)	138.391(6)

						$Ca_2Fe_{2.65}O_3S_{1.5}Se_{0.5}$
Atom	Site	*x*	*y*	*z*	Occupancy	U_{iso} (Å^2)
Ca	2*h*	0.5	0.5	0.1857(5)	1	0.0070(11)*
Fe1	1*a*	0	0	0	1	0.0002(7)*
Fe2	2*e*	0.5	0	0.5	0.822*	0.0298(11)*
O1	2*f*	0.5	0	0	1	0.0128(8)*
O2	1*d*	0.5	0.5	0.5	1	0.0099(12)*
S	2*g*	0	0	0.2997(6)$^+$	0.770*	0.0014(13)*
Se	2*g*	0	0	0.2997(6)$^+$	0.230*	0.0014(13)*

For Figure 4.19- Rietveld fit for the NPD pattern of $Ca_2FeO_2Fe_{1.65}OS_{1.5}Se_{0.5}$ measured at 5 K on the D2B instrument at the ILL, using the nuclear model in *P*4/*mmm* symmetry. $^+$The positions of the chalcogenides were refined together as one variable. *These values were fixed from the 300 K D2B NPD refinement.

	$Ca_2Fe_{2.7}O_3SSe$
Diffractometer	D2B (ILL)
Wavelength (Å)	1.594
Temperature (K)	5
Space Group	*P*4/*mmm*
a (Å)	3.96867(7)
c (Å)	8.9689(4)
V (Å^3)	141.264(7)

						$Ca_2Fe_{2.7}O_3SSe$
Atom	Site	*x*	*y*	*z*	Occupancy	U_{iso} (Å^2)
Ca	2*h*	0.5	0.5	0.1821(4)	1	0.0086(11)*
Fe1	1*a*	0	0	0	1	0.0055(8)*
Fe2	2*e*	0.5	0	0.5	0.809*	0.0235(9)*
O1	2*f*	0.5	0	0	1	0.0127(7)*
O2	1*d*	0.5	0.5	0.5	1	0.0189(17)*
S	2*g*	0	0	0.2990(4)$^+$	0.525*	0.0019(9)*
Se	2*g*	0	0	0.2990(4)$^+$	0.475*	0.0019(9)*

For Figure 4.21- Rietveld fit for the NPD pattern of $Ca_2FeO_2Fe_{1.7}OSSe$ measured at 5 K on the D2B instrument at the ILL, using the nuclear model in *P*4/*mmm* symmetry. $^+$The positions of the chalcogenides were refined together as one variable. *These values were fixed from the 300 K D2B NPD refinement.

	$Ca_2Fe_{2.75}O_3S_{0.5}Se_{1.5}$
Diffractometer	D2B (ILL)
Wavelength (Å)	1.594
Temperature (K)	5
Space Group	*P*4/*mmm*
a (Å)	3.98265(4)
c (Å)	9.0712(3)
V (Å^3)	143.883(4)

						$Ca_2Fe_{2.75}O_3S_{0.5}Se_{1.5}$
Atom	Site	*x*	*y*	*z*	Occupancy	U_{iso} (Å^2)
Ca	2*h*	0.5	0.5	0.1776(4)	1	0.0031(9)
Fe1	1*a*	0	0	0	1	0.0018(7)
Fe2	2*e*	0.5	0	0.5	0.807*	0.0103(7)
O1	2*f*	0.5	0	0	1	0.0166(8)
O2	1*d*	0.5	0.5	0.5	1	0.0172(14)
S	2*g*	0	0	0.2982(3)$^+$	0.260*	0.0000(7)$^+$
Se	2*g*	0	0	0.2982(3)$^+$	0.740*	0.0000(7)$^+$

For Figure 4.23- Rietveld fit for the NPD pattern of $Ca_2FeO_2Fe_{1.75}OS_{0.5}Se_{1.5}$ measured at 5 K on the D2B instrument at the ILL, using the nuclear model in *P*4/*mmm* symmetry. $^+$The positions and isotropic displacement parameters of the chalcogenides were refined together as one variable. *These values were fixed from the 300 K D2B NPD refinement.

	$Sr_2CrO_2Cr_2OAs_2$
Diffractometer	WISH (ISIS)
Wavelength (Å)	white beam TOF
Temperature (K)	10
Space Group	*P*4/*mmm*
a (Å)	4.04002(7)
c (Å)	9.29417(18)
V (Å^3)	151.697(6)

								$Sr_2CrO_2Cr_2OAs_2$
Atom	Site	*x*	*y*	*z*	Occupancy	U_{11} (Å^2)	U_{22} (Å^2)	U_{33} (Å^2)
Sr	2*h*	0.5	0.5	0.1772(3)	1	0.0053(13)	=U_{11}	0.016(3)
Cr1	1*a*	0	0	0	1	0.005(4)	=U_{11}	0.053(6)
Cr2	2*e*	0.5	0	0.5	1	0.0063(19)	=U_{11}	0.010(3)
O1	2*f*	0.5	0	0	1	0.0139(14)	=U_{11}	=U_{11}
O2	1*d*	0.5	0.5	0.5	1	0.013(3)	=U_{11}	=U_{11}
As	2*g*	0	0	0.3207(3)	1	0.0023(13)	=U_{11}	0.024(3)

For Figure 5.8- Rietveld fit for the NPD pattern of $Sr_2CrO_2Cr_2OAs_2$ measured at 10 K on the WISH instrument at ISIS, using the nuclear model in *P*4/*mmm* symmetry.

	Ba_2FeSbS_5
Diffractometer	D2B (ILL)
Wavelength (Å)	1.594
Temperature (K)	2
Space Group	*Pnma*
a (Å)	12.0828(3)
b (Å)	8.83773(15)
c (Å)	8.88054(17)
V (Å^3)	948.31(3)

					Ba_2FeSbS_5
Atom	Site	*x*	*y*	*z*	U_{iso} (Å^2)
Ba	8*d*	0.32260(17)	0.0072(3)	0.3776(3)	0.0000(5)
Sb	4*c*	0.0228(3)	0.25	0.5175(4)	0.0000(7)
Fe	4*c*	0.09487(12)	0.25	0.1695(2)	0.0000(5)
S1	8*d*	0.0537(3)	0.0474(5)	0.3212(5)	0.0020(9)
S2	4*c*	0.2108(5)	0.25	0.6186(7)	0.0036(12)
S3	4*c*	0.2762(5)	0.25	0.1127(7)	0.0034(13)
S4	4*c*	0.4923(5)	0.25	0.5387(6)	0.0009(12)

For Figure 6.10- Rietveld fit for the NPD pattern of Ba_2FeSbS_5 measured at 2 K on the D2B instrument at the ILL, using the nuclear model in *Pnma* symmetry.

	Ba_2FeBiS_5
Diffractometer	D2B (ILL)
Wavelength (Å)	1.594
Temperature (K)	2
Space Group	*Pnma*
a (Å)	12.0945(3)
b (Å)	8.89801(15)
c (Å)	8.81197(17)
V (Å^3)	948.32(3)

					Ba_2FeBiS_5
Atom	Site	*x*	*y*	*z*	U_{iso} (Å^2)
Ba	8*d*	0.32224(18)	0.0087(3)	0.3827(3)	0.0001(6)
Bi	4*c*	0.01707(16)	0.25	0.5324(3)	0.0005(5)
Fe	4*c*	0.09456(14)	0.25	0.1706(3)	0.0007(5)
S1	8*d*	0.0547(4)	0.0449(5)	0.3173(6)	0.0007(9)
S2	4*c*	0.2162(6)	0.25	0.6260(8)	0.0012(16)
S3	4*c*	0.2781(6)	0.25	0.1148(7)	0.0019(16)
S4	4*c*	0.4943(6)	0.25	0.5394(8)	0.0049(13)

For Figure 6.18- Rietveld fit for the NPD pattern of Ba_2FeBiS_5 measured at 2 K on the D2B instrument at the ILL, using the nuclear model in *Pnma* symmetry.